Thrust Fault Evolution and Hydrocarbon Sealing Behaviour, Qaidam Basin, China

Yangwen Pei

Submitted in accordance with the requirements for the degree of
Doctor of Philosophy

The University of Leeds
School of Earth and Environment

September, 2013

The candidate confirms that the work submitted is his own and that appropriate credit has been given where reference has been made to the work of others.

Acknowledgements

With this thesis finished, I want to say many thanks to those who have given me so much help in my four PhD years. Without their kind help and support, the past four years would be much harder.

Firstly, I will say thanks to my wife Ms Liujuan Xie for her countless love and support in the past years. Without her, the process would be much tougher for me. Also thanks my parents Mr Dingguo Pei and Ms Fanmei Kong for their long-lasting support and care.

Then, I will give my sincere appreciation to my supervisors Prof Rob Knipe and Dr Douglas Paton. They have given me countless supports, scientifically and financially. Their guides have helped me follow the right way all the time. Particularly, my scientific research skills have been significantly improved in the past four years, which will highly impact my future career.

The two periods of fieldwork in this research were carried out by a team that has included Yangwen Pei, Dr Henry Lickorish, Mr Will Bradbury. My own contributions, fully and explicitly indicated in the thesis, have been fieldwork management, measuring dips/stratigraphy, constructing transects, mapping the outcrops and rock sampling. The other members of the group and their contributions have been as follows: tracing the faults, mapping normal fault arrays and detailed mapping.

The SEM experiments were carried out by a team that has included Yangwen Pei and Dr Anren Li from RDR. My own contributions, fully and explicitly indicated in the thesis, have been rock sample cutting, polishing, preparation and SEM investigation. The other members of the group and their contributions have been as follows: preparing chemical reagent for sample preparation, cutting, polishing and SEM investigation.

Thanks will also be given to the Qinghai Oilfield Company (PetroChina) who supported the transports and accommodations for the two periods of fieldwork in Qaidam basin. Also, thank Mr Ian Pollock and Ms Jayne Harnett from RDR who helped with the financial managements for the two periods of fieldwork.

Abstract

In the past, fault seal analysis has been focused on extensional systems. However, fault behaviour in terms of fault sealing is also critical within compressional thrust systems. The results of an evaluation of thrust fault evolution and hydrocarbon sealing behaviour in the Lenghu5 thrust belt of the Qaidam basin of NW China are reported. A multi-scale methodology, ranging from regional- to micro-scale, is utilized in this work to identify the detailed thrust fault architecture and its effect on hydrocarbon sealing properties.

Regional-scale sections and 3D modelling are used to evaluate the evolution of faults within this thrust system and as a platform for detailed seal analysis. The results allow assessment of the timing of deformation, shortening and shortening strain rate. Trishear models are used to assess deformation in the Lenghu5 thrust belt. Based on trishear propagation geometric models, the Lenghu5 deformation history is simulated using forward trishear modelling. A range of trishear modelling parameters is used to interpret the various structural styles presented. This provides new insights to the potential application of trishear mechanism in complex natural structures developed in different environments.

Meso-scale detailed structural maps of exceptionally well-exposed outcrops are used to extract information on local fault geometry. Main thrust faults, minor thrust faults and accommodation normal faults are all mapped in detail, making it possible to evaluate the differences of fault architectures between different types of faults. Models are proposed to define the elements of fault zones. Fault zone evolution models are constructed in order to understand the dynamic process of the fault development.

Micro-structural analysis (e.g., SEM) of rock samples is used for assessment of the deformation mechanisms associated with fault zone development. The vital influence of micro-scale deformation mechanisms on hydrocarbon sealing properties has been evaluated, in order to reveal the relationship between the deformation mechanism and hydrocarbon sealing behaviour.

This work illustrates the value of a regional- to micro-approach on thrust fault evolution and hydrocarbon sealing behaviour, and aims to identify the critical parameters that contribute to improving fault seal analysis in thrust systems.

Table of Contents

List of Tables

List of Figures

List of Abbreviations

M - A	migration - accumulation
CSP	clay smear potential
SSF	shale smear factor
SGR	shale gouge ratio
SSGR	scale shale gouge ratio
p/s ratio	propagation versus slip ratio
SRTM	Shuttle Radar Topography Mission
DEM	Digital Elevation Model
QN	Qilian Shan - Nan Shan
QE	Qimen Tagh - Eastern Kunlun
S	shortening
TS	total shortening
SR	shortening rate
ASR	average shortening rate
FC	fault core
IDZ	inner damage zone
ODZ	outer damage zone
SEM	Scanning Electron Microscope
SE	Secondary Electron
BSE	Back-Scattered Electron
CL	Cathode Luminescence
EDX	Energy Dispersive X-ray Spectrometer
HR	host rock
FR	fault rock
PFFR	phyllosilicate-framework fault rock
TFG	through-going fault
CS	clay smear

Chapter 1
Introduction

The hydrocarbon sealing capacity of faults has attracted interests of geologists over the past 30 years. Many studies have evaluated the sealing properties of faults, by considering the effects of fault juxtaposition (Allan, 1989; Knipe, 1997), fault geometry and fault population (e.g., Cowie and Scholz, 1992; Caine et al., 1996; Childs et al., 1996a; Childs et al., 1996b), clay smear continuity (e.g., Bouvier et al., 1989; Lindsay et al., 1993; Fulljames et al., 1997; Yielding et al., 1997; Childs et al., 2007; Ciftci et al., 2013), and generation of low permeable fault rocks within fault zones (e.g., Knipe et al., 1997; Fisher and Knipe, 1998; Knipe et al., 1998; Ottesen Ellevset et al., 1998; Childs et al., 2007; Jolley et al., 2007; Tueckmantel et al., 2010). Previous studies on fault seal analysis have focused on extensional systems for two aspects of reasons, which are (i) a normal fault zone normally presents lower complexity than a thrust fault zone with a similar fault throw and (ii) it is easier to continue further research based on the previous studies focusing on normal faults. However, this is despite of the importance of fluid flow properties associated with faults located within contractional thrust domains.

In this research, we aim to answer the following questions associated with the fault zone evolution and the hydrocarbon sealing behaviour within contractional thrust systems, which are:

(i). What is the geometry of a thrust fault zone? How does the thrust fault zone evolve with geological time?

(ii). What are the key parameters controlling the thrust fault zone architecture, e.g., the host rock lithology, the bed thickness and the mechanical heterogeneity?

(iii). What is the effects of fault zone geometry and evolution on the fluid flow properties across the fault zones?

(iv). What workflows are best to evaluate the hydrocarbon sealing properties of thrust fault zones?

In order to understand the thrust fault evolution and evaluate its effects on the hydrocarbon sealing behaviour, we have used a study area in the Lenghu5 structure of Qaidam basin in NW China. The Qaidam basin, developed in a contractional environment, is an active hydrocarbon province where seismic datasets, well data, together with well-exposed outcrops are available. With support from both PetroChina and RDR Group, two periods of fieldwork have been successfully completed, to provide key field data for this PhD research programme. A multi-scaled methodology has been used to assess the fault zone architecture and its effects on the fault zone sealing processes:

(1). Regional-scale (1km-10km)

Cross section analysis, balance restoration and 3D modelling are used to evaluate the evolution of faults at a thrust system scale and as a platform for detailed fault seal analysis. The results allow assessment of the timing of deformation, shortening and shortening strain rate.

Conceptual models of fold-fault relationships are considered with trishear models in particular being used to assess the deformation of the Lenghu5 structure. With implications from the trishear propagation geometric models, the Lenghu5 deformation history can be simulated using forward trishear modelling. A range of trishear modelling parameters can also be used to interpret the various structural styles present in natural structures. This provides insights to the potential application of trishear mechanism in complex structures developed in different environments.

The field data, e.g., stratigraphy, fault maps and cross sections, are used to investigate the detailed fault zone architecture, and also to test the application of trishear algorithms on the Lenghu5 structure.

(2). Meso-scale (10cm-1km)

Meso-scale detailed structural maps of exceptionally well-exposed outcrops are used to extract information on the local fault geometry. Main thrust faults, minor thrust faults and accommodation normal faults are all mapped in detail, in order to understand the fault zone architecture of different fault types.

The fault zone evolution is constructed in order to understand the dynamic process of the fault development. A fault zone model is then proposed to define the elements of the thrust fault zones. The controlling parameters, such as the host rock lithology, the bed thickness and the mechanical heterogeneity, on the fault zone architectures has also been evaluated.

(3). Micro-scale (10μm-10cm)

Micro-structural analysis (Scanning Electron Microscope studies) of key rock samples is employed for the identification of the micro-scale deformation mechanisms associated with the fault zone development. As the micro-scale deformation mechanisms have a vital influence on the hydrocarbon sealing properties, the fault rock porosity and permeability are evaluated in order to reveal the relationship between the deformation mechanisms and potential hydrocarbon sealing behaviour. The parameters that control fault sealing capacity have also been evaluated, e.g., the host rock composition, the fault displacement and the bed thickness.

The chart in Figure 1.1 delineates the overall structure of this PhD research.

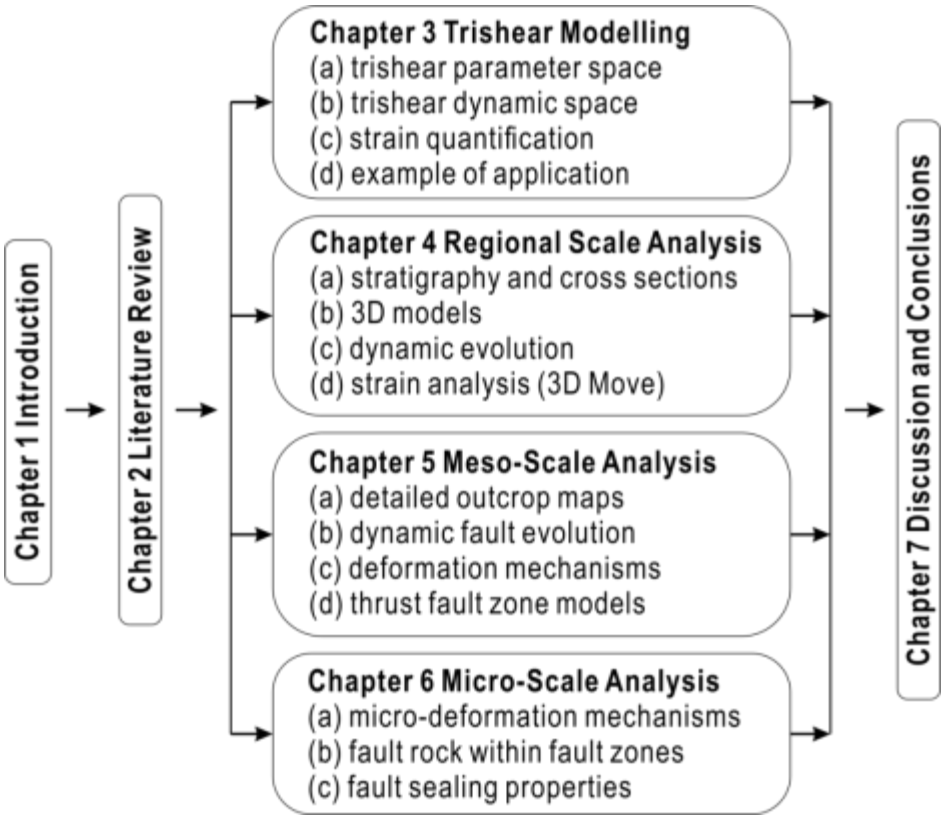

Figure 1.1 A chart delineates the overall structure of this research on thrust fault evolution and hydrocarbon sealing behaviour in the Lenghu5 structure, Qaidam basin, China**.**

Chapter 2
Literature Review

This thesis aims to understand the thrust fault evolution and its effects on the hydrocarbon sealing behaviour. This review chapter, therefore, has two components. The first is to review the geological evolution of the Qaidam basin, northern margin of the Tibetan Plateau, NW China (Figure 2.1); and the second component is a summary of the fault zone architecture and fault seal analysis.

2.1. Geology Settings of the Qaidam Basin

The Qaidam basin, an oil/gas-bearing Mesozoic-Cenozoic sedimentary basin, is located in the northern edge of the Tibetan Plateau, NW China (Figure 2.1).

Topographically, the Qaidam basin covers an area of ~120,000km^2 and has an average altitude of ~3km (based on the SRTM DEM data). In map view, the Qaidam basin is a rhombic shaped basin, and its N-S width changes from ~150km in the east to ~300km in the west (Yin et al., 2007; Yin et al., 2008a; Yin et al., 2008b). Tectonically, the Qaidam basin is constrained by the Qilian Shan-Nan Shan Thrust Fault to the northeast (e.g. Burchfiel et al., 1989; Tapponnier et al., 1990; Meng et al., 2001; Yin et al., 2008a); the left-lateral strike-slip Altyn Tagh Fault to the northwest (e.g. Meyer et al., 1998; Cowgill et al., 2000; Cowgill et al., 2003; Cowgill et al., 2004a; Cowgill et al., 2004b; Yue et al., 2004; Cowgill, 2007; Yin et al., 2007); and the Eastern Kunlun Thrust Belt to the southwest (e.g. Chen et al., 1999; Meng et al., 2001; Jolivet et al., 2003; Yin et al., 2007; Craddock et al., 2012).

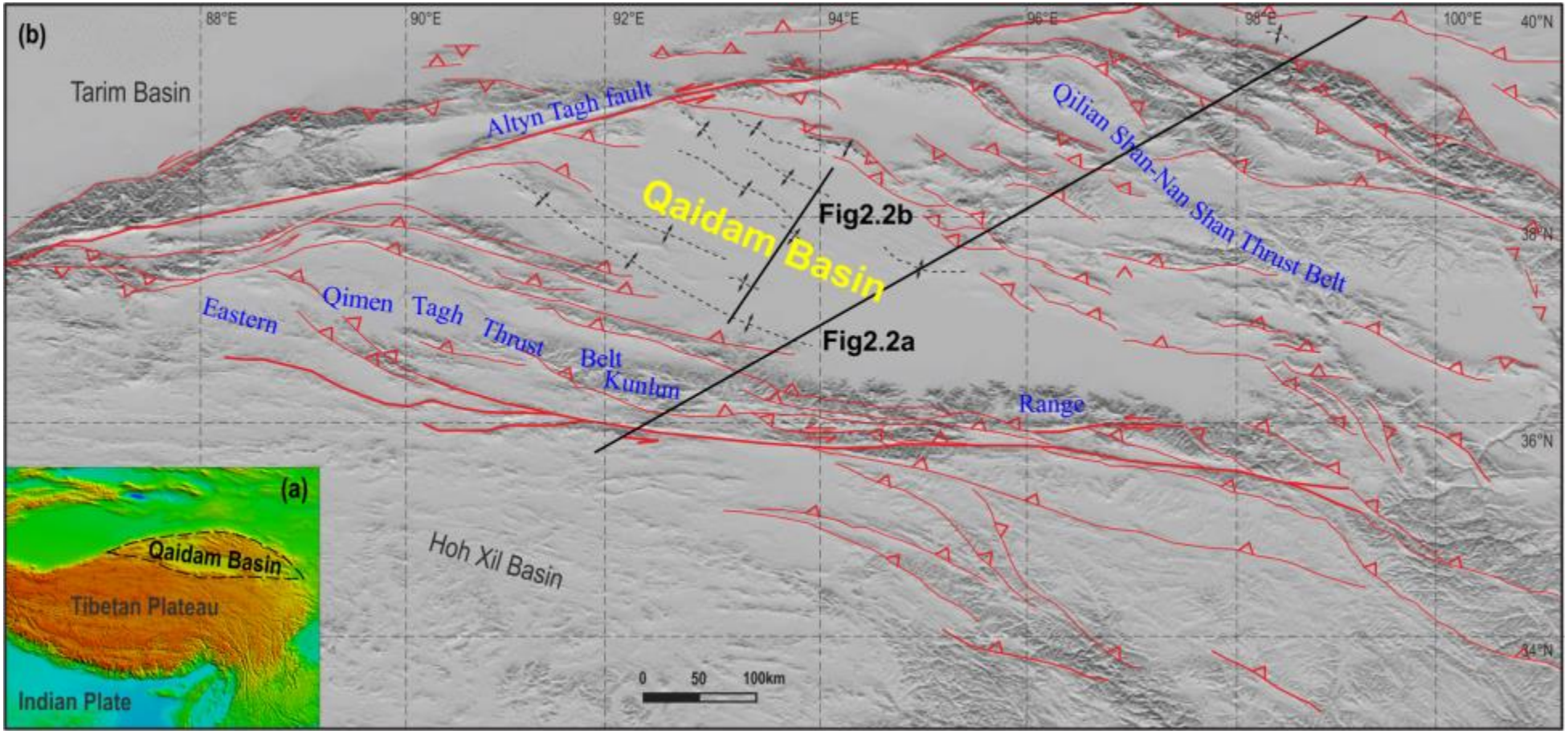

Figure 2.1 Elevation maps showing the position of Qaidam basin (a) and the basic structural interpretation (b) (modified from Yin et al., 2008b).

2.1.1. Basement, Stratigraphy, Structural Geometry and Petroleum Systems of the Qaidam Basin

The nature of the basement is critical for interpreting the tectonic evolution of a sedimentary basin (Allen and Allen, 2005). Based on the magnetotelluric sounding and deep seismic refraction data, a continental crust consisting of Precambrian metamorphic and granitic rocks has been identified beneath the sedimentary fills in the Qaidam basin (Xia et al., 2001). According to the changes of P-wave velocity and resistivity, the lithosphere of the Qaidam basin can be divided into the four subunits (Cui et al., 1995; Deng et al., 1995; Gao et al., 1995): upper crust (15-25km), middle crust (25-35km), lower crust (35-50/60km), and the lithospheric mantle (50/60-95/125km). It was suggested the burial depth of crust is shallower in the central basin than the rim (Xia et al., 2001).

The basin-scale cross sections based on well data and seismic reflection data suggest that the Qaidam basin has been filled by a huge accumulation of Mesozoic-Cenozoic sedimentary rocks above the basin basement (Xia et al., 2001). The thickness of the Mesozoic-Cenozoic sediments in the Qaidam basin reaches up to 15,000m (Huang et al., 1996). The Mesozoic-Cenozoic stratigraphic division and age assignments are based on various studies, e.g., correlation between outcrops and subsurface data, terrestrial fossils, stratigraphic correlation by a network of seismic sections, magnetostratigraphic studies, fission-track, and $^{40}Ar/^{39}Ar$ dating of detrital micas, (Huo, 1990; Yang et al., 1992; Song and Wang, 1993; Huang et al., 1996; Rieser et al., 2006a; Rieser et al., 2006b; Wang et al., 2007).

As listed in Table 2.1 and Table 2.2, the Mesozoic-Cenozoic sediments of the Qaidam basin are divided into ten formations, which are:

(i). the Jurassic and locally distributed Cretaceous sediments (Jr; 206-65Ma);

(ii). the Palaeocene to early Eocene Lulehe Formation (E_{1+2}; 65–49 Ma) (Huo, 1990; Yang et al., 1992; Rieser et al., 2006a; Rieser et al., 2006b);

(iii). the middle and late Eocene Lower Xiagancaigou Formation (E_{3-1}; 49–37 Ma) (Yang et al., 1992; Sun et al., 2005);

(iv). the early Oligocene Upper Xiagancaigou Formation (E_{3-2}; 37–28.5 Ma) (Sun et al., 1999);

(v). the late Oligocene Shanggancaigou Formation (N_1; 28.5–23.8 Ma) (Sun et al., 1999);

(vi). the early to middle Miocene Xiayoushashan Formation (N_{2-1}; 23.5–11.2 Ma) (Sun et al., 1999);

(vii). the late Miocene Shangyoushashan Formation (N_{2-2}; 11.2–5.3 Ma) (Sun et al., 1999);

(viii). the Pliocene Shizigou Formation (N_{2-3}; 5.3–1.8 Ma) (Sun et al., 1999);

(ix). the Pleistocene Qigequan Formation (Q_1; 1.8–0.01 Ma) (Sun et al., 1999);

(x). the Holocene Dabuxun Yanqiao Formation (Q_2) (Yang et al., 1997).

It is suggested that unconformities are widely developed in the Qaidam basin (Xia et al., 2001). As shown in Figure 2.2b, the Cenozoic sedimentary rocks of the Qaidam basin are unconformable on the underlying Mesozoic strata. T_R, the boundary between Mesozoic and Cenozoic sediments, is a regional unconformity throughout the Qaidam basin; the Cenozoic Qaidam basin develops above this unconformity. The youngest unconformity of the Qaidam basin is a tectonic unconformity (T_0) formed in the earliest Pleistocene. Between these two unconformities, four other unconformities are identified in the cross sections of the basin (Figure 2.2b), which are T_5, T_2, T_2' and T_1. Because the four erosional unconformities are indicators of geological events, these unconformities have already been accepted in seismic interpretation by the Qinghai Oilfield Company (PetroChina).

Table 2.1 The Mesozoic and Cenozoic stratigraphic classification and age assignment of the Qaidam basin (modified from Yin et al., 2008a).

Units (formation)	Symbol		Geologic time	Lithology	Age (Ma)
Dabuxun Yanqiao	Q_2		Holocene	yellow, brownish-grey conglomerates with grey mudstones	< 0.01
Qigequan	Q_1	T_0	Pleistocene		1.8-0.01
Shizigou	N_{2-3}	T_1	Pliocene	interbedded grey, brownish-grey conglomerates and brownish-red mudstones	5.3-1.8
Shangyoushashan	N_{2-2}	T_2'	late Miocene		11.2-5.3
Xiayoushashan	N_{2-1}	T_2	early-middle Miocene	brownish-red mudstones	23.8-11.2
Shangganchaigou	N_1	T_3	late Oligocene	grey, dark-grey mudstones with siltstones	28.5-23.8
Upper Xiaganchaigou	E_{3-2}	T_4	early Oligocene	grey, dark-grey mudstones	37-28.5
Lower Xiaganchaigou	E_{3-1}	T_5	middle and late Eocene	red muddy siltstones	49-37
Lulehe	E_{1+2}	T_R	Palaeocene–early Eocene	brownish-red, brown sandy mudstones	65-49
Jurassic and locally distributed Cretaceous sediments	J_r	T_6	Jurassic - Cretaceous	conglomerates, sandstones, mudstones, and coals	206-65

Table 2.2 Thickness and facies of the Cenozoic sediments in the Qaidam basin (modified from Huang et al., 1996; Yin et al., 2008b).

Geological time		Southern Qaidam basin		
		Units	Thickness	Facies
Pliocene		Shizigou Formation	>1500m	Lacustrine
Miocene	Late	Shangyoushashan Fm.	>822m	Lacustrine
	Middle	Xiayoushashan Fm.	1243m	Lacustrine/ Fluvial
	Early			
Oligocene	Late	Shangganchaigou Fm.	848m	Fluvial/ Lacustrine

Eocene	Early	Lower and Upper Xiaganchaigou Fm.	1011m	Fluvial/ Lacustrine
	Late			
	Middle			
	Early	Lulehe Formation	1043m	Alluvial/ Fluvial
Palaeocene				

A series of studies have focused on the thrust-fold systems of the Qaidam basin, to identify the structural styles and its dynamic evolution. The basin-scale section in Figure 2.2a shows two orogens constrain the two ends of the Qaidam basin, which are the Eastern Kunlun thrust belt to the south and the Qilianshan thrust belt to the north. The deep-seated Eastern Kunlun thrust system and the Qilianshan thrust belt account for the uplift of the two orogens in the two ends of the Qaidam basin. Consequently, the Qaidam basin has been developed since the Mesozoic-Cenozoic sediments started filling the intermountain space. Based on the cross sections and geomagnetic analysis (Yin et al., 2008b), the maximum shortening of this system (including the two orogens) has been calculated to be 140-170km, although no consensus on the shortening amount has been reached yet.

As shown on the basin-scale cross section in Figure 2.2b, the Qaidam basin is characterized by a synclinorium (Bally et al., 1986). The sediments of the Qaidam basin are composed of the Mesozoic and the Cenozoic sediments, with thickness of up to 15km (Huang et al., 1996; Yin et al., 2008a; Yin et al., 2008b), and are distributed throughout the whole Qaidam basin. However, the thickness of the Mesozoic-Cenozoic sediments varies significantly across the basin. The studies suggest that the deformation of the Qaidam basin is controlled by deep-seated thrust faults; while the accommodation faults are developed in the shallower domains, including the thrust faults, the normal faults and the reactivated normal faults (Xia et al., 2001). The cross section (Figure 2.2b) indicates the deposition of the Mesozoic sediments was initially controlled by the normal faults and the Cenozoic sediments have been controlled by the thrust faults (Zhou et al., 2006; Yin et al., 2008b; Liu et al., 2009). Therefore, it is speculated that the Qaidam basin has experienced an inversion from the Mesozoic extension to the later Cenozoic compression (e.g., Xia et al., 2001; Yin et al., 2002; Wang and Burchfiel,

2004; Zhou et al., 2006; Zhu et al., 2006; Yin et al., 2008a; Yin et al., 2008b; Liu et al., 2009).

The Figure 2.2c section is our interpreted seismic reflection profile of the Lenghu5 structure. The evidence of structural inversion can also be identified here, i.e., the thickened hanging wall of the lower controlling fault F_2. The lower part of this structure is controlled by a series of SW-directing thrust faults; while the upper part is controlled by a NE-directing thrust fault. The interaction between the lower faults and the upper fault determines the current geometry of the Lenghu5 structure.

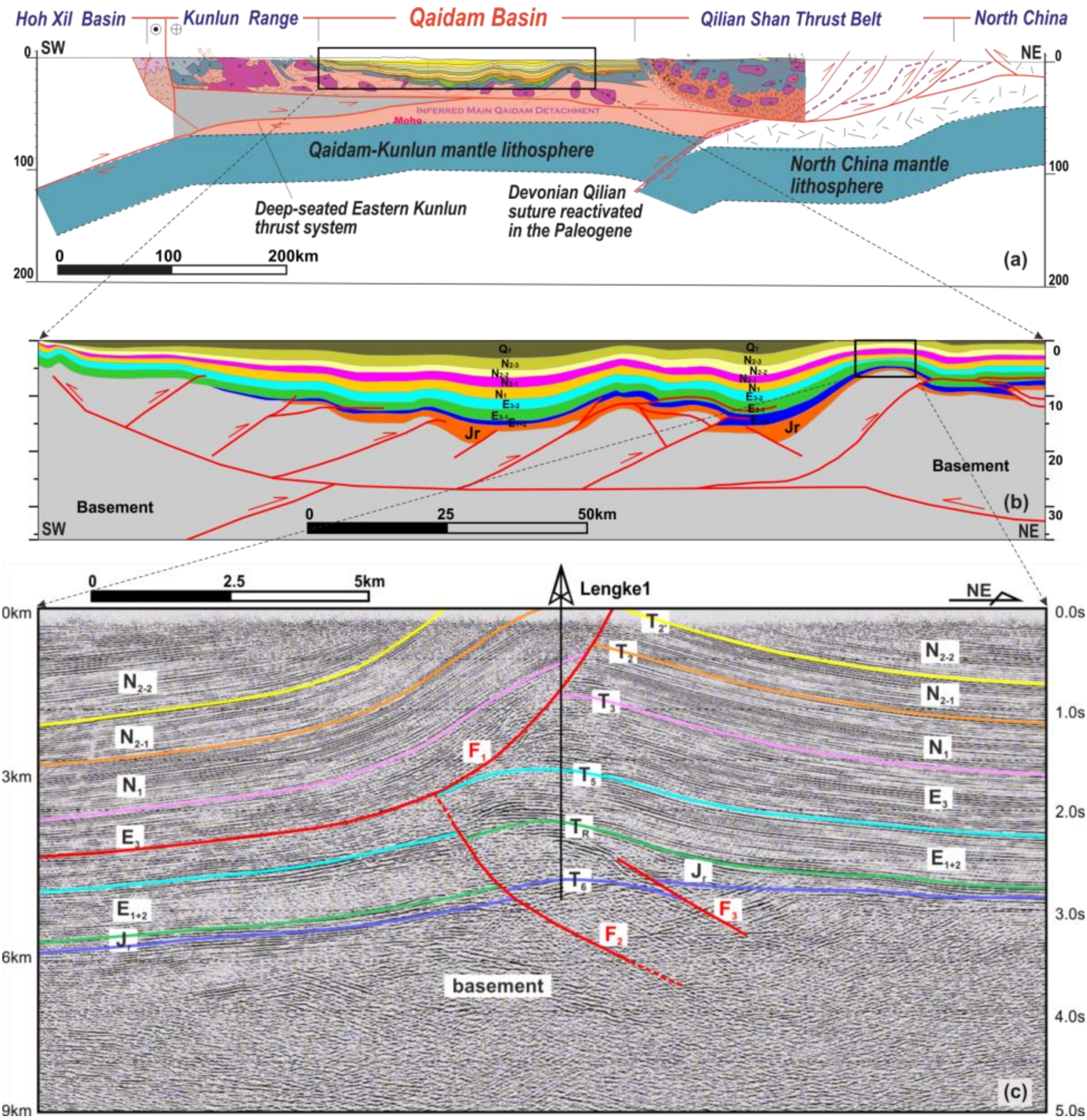

Figure 2.2 The multi-scale cross sections (position in Figure 2.1) demonstrate the fundamental tectonic settings and the structural geometry of the Qaidam basin: (a) macro-scale tectonic settings (modified from Yin et al., 2008b); (b) basin-scale structural geometry (modified from Yin et al., 2008b); and (c) regional-scale geometry of the Lenghu5 structure.

Based on the occurrence and abundance of the organic-rich source rocks, previous studies (Wang, 2001; Pang et al., 2004) have identified three main petroleum systems in the Qaidam basin; these are the Jurassic petroleum system in north-western Qaidam basin, the Tertiary petroleum systems in western Qaidam basin and the Quaternary petroleum system in the eastern Qaidam basin (Figure 2.3). Pang et al. (2004) also reported four types of hydrocarbon migration and accumulation (M-A) models for the Qaidam basin, e.g., (i). the superficial thrust fault M-A model; (ii). the combined syn-depositional reverse fault-strike-slip fault M-A model; (iii). the recoil fault M-A model; and (iv). the superficial thrust fault and lower strike-slip fault complex M-A model.

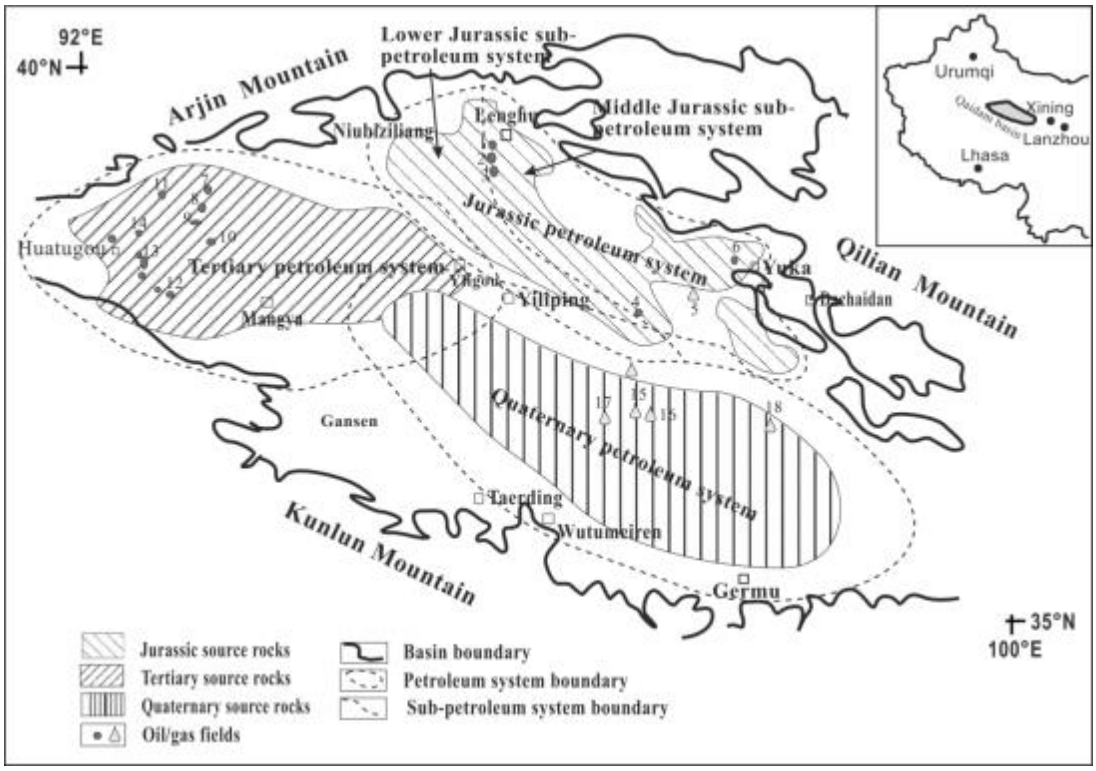

Figure 2.3 The distribution of source rocks and petroleum systems in the Qaidam basin, NW China (Pang et al., 2004).

2.1.2. Structural Geometry and Tectonic Evolution

The Tibetan plateau resulted from the compression that has been induced by the collision between the Indian plate and the Eurasian plate. It is suggested that the north-south convergence between the two plates is partially accommodated by the eastward extrusion of the Tibetan crust along the left-lateral Altyn Tagh strike-slip fault (Molnar and Tapponnier, 1975). Along this left-lateral strike-slip fault, the NE Tibetan plateau has moved northeastward

towards the North China Craton (Figure 2.2). The strain of the Indian-Eurasian collision, especially along the left-lateral Altyn Tagh fault, resulted in the NE-SW compression, which gives rise to the orogens in the northern margin of the Tibetan Plateau. The Qaidam basin, associated with the NE-SW compression, is an intermountain basin resulting from the Qilian Shan-Nan Shan belt to the north and the East Kunlun range to the south (Wang et al., 2006b). In the study of Wang and Burchfiel (2004), the Altyn Tagh fault and the Wenquan fault are treated as conjugate structures; as the slip rate of Altyn Tagh fault is definitely larger than that of the right-lateral Wenquan fault, it indicates that the Qaidam basin has experienced a clockwise rotation, which gives rise to a gradual decrease in shortening from west to east.

The study of Xia et al. (2001) suggests that the Qaidam basin experienced a two-phased structural inversion that is composed of an initial extension stage and a later compression. The extensional stage (Cretaceous-Oligocene, 75.0-23.3Ma) is caused by the rise of the mantle plume, while the following compressional stage is induced by the northeastward propagation of compressional stress produced by the Indian-Eurasian collision. Many other studies also held similar views that the Qaidam basin has experienced an inversion from an initial extension to later compression (e.g., Pang et al., 2004; Zhou et al., 2006; Yin et al., 2008b; Liu et al., 2009). Specifically, Zhu et al. (2006) investigated the Cenozoic evolution of the Qaidam basin based on the lateral changes of the Cenozoic sediment fill within the Qaidam basin and suggested a three-stage division: the strike-slip basin stage in the earlier period (60-46Ma); the foreland basin development (46-2.4Ma); and the intermountain basin stage in the later period (2.45-0Ma).

As the Qaidam basin is dominated by the Cenozoic compression, the shortening-related quantification has attracted the interest of geological studies (e.g., Zhou et al., 2006; Yin et al., 2008b; Liu et al., 2009). Zhou et al. (2006) analysed the Cenozoic deformation history of the Qaidam basin by means of the balance cross-section restoration of six geological sections, in which two fast shortening periods were identified: 42.8-40.5Ma and 2.8Ma-present. Yin et al. (2008b) restored the interpreted seismic sections and then calculated the shortening amounts and rates of each section. According to the present

section lengths and the corresponding shortening rates, the Qaidam basin is reconstructed in map view, which allows the estimation of the maximum shortening of the Qaidam basin to be 140-170km (along the Altyn Tagh fault). Liu et al. (2009) investigated the Cenozoic stratigraphy deformation history in the central and eastern Qaidam basin by balance section restoration and then quantitatively evaluated the geologic events of the Indian-Eurasian collision since ~55Ma.

2.2. Fault Zone Architecture and Fault Seal Analysis

In petroleum exploration and production, as faults can be either conduits or retarders for hydrocarbon migration, the presence of faults increases the risks for hydrocarbon drilling, exploration and development. In order to avoid or minimise the risks, the way in which faults and fractures affect the hydrocarbon migration has attracted the interest of geologists. Previous research (e.g., Smith, 1966; Schowalter, 1979; Smith, 1980; Watts, 1987; Allan, 1989; Bouvier et al., 1989) has studied the fault behaviour and proposed many fundamental principles that control the fault sealing properties within oil/gas reservoirs. In the recent 20 years, the abundance of data, including seismic reflection data, structural and micro-structural analysis from both core and field rock samples, wellbore and production data of oil/gas fields, makes it possible to conduct fault seal analysis to predict fault-sealing properties.

The progress in understanding the faulting processes (Caine et al., 1996; Childs et al., 1996b; Childs et al., 2009), the fault rock development (Knipe, 1989; Knipe et al., 1997; Fisher and Knipe, 1998), the fault geometry (Peacock and Sanderson, 1991, 1992, 1994) and the fault population (Cowie and Scholz, 1992; Cowie et al., 1993; Cowie et al., 1996) has provided a platform for improving the accuracy of fault sealing analysis. Knipe (1992a, b, 1994) also highlighted the importance of the fault zone complexity and the petrophysical properties of the fault rocks in the evaluation of fault-sealing capacity. Firstly, the fault zone development can involve strain being accommodated by a complex array of faults not just a single, through-going fault; secondly, the sealing capacity of the fault zones may vary significantly

depending on the composition of the host rocks that are entrained into the fault zones.

2.2.1. Fault Zone Architecture

In natural structures, it is common to observe a mechanically layered sequence of beds subject to stress. In previous studies focusing on the deformation mechanisms of the mechanically layered sequence, it has been reported that the faults tend to form first in the brittle beds (e.g. cemented sandstones or carbonates); while the weak/ductile beds (e.g. clay beds) deform by distributed shear to accommodate the overall strain (Eisenstadt and De Paor, 1987; Peacock and Sanderson, 1992; McGrath and Davison, 1995; Childs et al., 1996a; Schöpfer et al., 2006). Several quantitative dynamic models have been presented (e.g., Egholm et al., 2008; Welch et al., 2009) to analyse the mechanics of clay/shale smearing along faults in layered sand and shale/clay sequences. These models predict that the isolated initial faults formed within the brittle beds will grow until eventually they link up with increasing strain, by propagating across the ductile intervals to create a complex fault zone architecture (Peacock and Sanderson, 1991; Childs et al., 1996a; Walsh et al., 1999; Walsh et al., 2003). Many natural examples support those previous studies on detailed fault zone architecture, e.g., the deformed interbedded sandstones and shales derived from the Cutler Formation juxtaposed against limestone from the Honaker Trail Formation near the entrance to Arches National Park (Davatzes and Aydin, 2005); the outcrop studies from a minor normal-fault array exposed within Gulf of Corinth rift sediments, Central Greece (Loveless et al., 2011); and the multilayer systems in the South-Eastern basin, France (Roche et al., 2012). Fault zone models defining the fault zone architecture have also been proposed, e.g., the fault zone model in crystalline rocks (Caine et al., 1996); the fault zone model in poorly lithified sediments (Heynekamp et al., 1999; Rawling and Goodwin, 2003, 2006); and the dynamic fault zone models within poorly consolidated sediments by Loveless et al. (2011). The effects of fault zone geometry and fault population on the fluid flow properties have also been considered in previous studies (e.g., Caine et al., 1996; Rawling et al., 2001; Faulkner et al., 2010).

2.2.2. Fault Seal Process

Knipe (1989, 1992a, 1993a, b) reviewed the fundamental fault seal processes that give rise to the occurrence of fault related permeability barriers. Five types of fault seal processes have been identified, which are: (i) clay/phyllosilicate smearing; (ii) cementation; (iii) cataclasis; (iv) diffusive mass transfer by pressure solution or quartz cementation; and (v) porosity reduction by disaggregation or mixing. However, as Knipe (1997) pointed, these five fault seal processes can either perform individually during deformation or combine interactively with each other.

(1). Clay/Phyllosilicate Smearing

As continuous clay/phyllosilicate smear has very low porosity and permeability (Smith, 1966, 1980), it performs as an extremely effective fluid flow barrier and therefore many studies have focused on this fault seal process.

Deformation induced shearing of clays/phyllosilicates has been discussed in previous studies (e.g., Bouvier et al., 1989; Gibson, 1994; Fulljames et al., 1997; Yielding et al., 1997; Aydin and Eyal, 2002). Three principle means of clay/phyllosilicate smearing are proposed by Lindsay et al. (1993), which are: (i). by abrasion of clay/phyllosilicate when it is moving past sandstones; (ii). by shearing and ductile deformation of beds (with high clay/phyllosilicate content, e.g. shale or mudstone beds) between hanging wall and footwall; and (iii). by injection of clay/phyllosilicate materials during fluidisation. It is suggested that the continuity of clay/phyllosilicate smearing is determined by a series of parameters including the sedimentary lithification state, the effective stress, the confining pressure, the strain rate and the mineralogy (Fisher and Knipe, 1998).

Several algorithms have been proposed to evaluate the fault sealing properties quantitatively, either based on the continuity of clay/phyllosilicate smears or average clay content within the fault zones, e.g., Clay Smear Potential (CSP) (Bouvier et al., 1989; Fulljames et al., 1997), Shale Smear Factor (SSF) (Lindsay et al., 1993), Shale Gouge Ratio (SGR) (Yielding et al., 1997) and Scaled Shale Gouge Ratio (SSGR) (Ciftci et al., 2013). These algorithms evaluate the fault sealing properties by considering the re-distribution of mudstone/shale beds or the clay/phyllosilicate content of the beds in faults.

Empirically, the stacking sequences with high clay/phyllosilicate content are likely to form fault zones with low permeability. During the deformation of fault rocks, there can be two competing compaction mechanisms which are (i) the mechanical compaction and (ii) chemical compaction (Fisher and Knipe, 2001). This results in the relationship between clay/phyllosilicate content and fault sealing properties (e.g. porosity, permeability, capillary pressure) being highly complicated and can even lack correlation. Therefore, the algorithms, such as CSP, SSF, SGR and SSGR, should be used with caution when evaluating the fluid flow properties of the fault zones.

(2). Cementation

The most common result of deformation related cementation includes cemented faults or fractures (Fisher and Knipe, 1998). The microstructures of these features provide important evidence for studying the mechanisms and timing of the cementation processes. As faults/fractures may perform as conduits for fluid flow, the flow behaviour of faults/fractures is sensitive to quartz precipitation because within the fault zones there are both quartz sources (from dissolution) and nucleation sites for potential cementation. The source for cementation can be internal or external, but Fisher and Knipe (1998) pointed that natural oil/gas field examples do not always require that an external fluid source controls the sealing properties of the fault zones, especially at a large scale where the external fluids may not promote continuous cementation for extensive sealing.

As there may be impure sandstones containing clay minerals, it is important to understand the effects of clay minerals on the quartz cementation, which has been well established in previous studies (e.g., Heald, 1955; Dewers and Ortoleva, 1991; Bjorkum, 1996; Oelkers et al., 1996). It is suggested that small concentrations of clay/phyllosilicate minerals in sandstones increase the potential of cementation as the clay/phyllosilicate minerals can act as a local source for cementation (Heald, 1955; Dewers and Ortoleva, 1991; Oelkers et al., 1996); however, high clay/phyllosilicate contents can lead to the clay/phyllosilicate-coating on the quartz grains (Cecil and Heald, 1971; Tada and Siever, 1989), which decreases the effective quartz grain surface area available for cementation (Walderhaug, 1996).

(3). Cataclasis

Cataclasis involves grain fracturing and can reduce the porosity and the permeability as well as increase the capillary threshold pressure of rocks within fault zones (e.g., Borg et al., 1960; Engelder, 1974; Knipe, 1989; Antonellini and Aydin, 1994, 1995). During the process of cataclasis, the porosity and permeability are reduced because the cataclasis results in the collapse of porosity, the reduction of grain size and the grain-sorting is becoming poorer by fracturing (Fisher and Knipe, 1998). Micro-structural analysis is an effective tool to study the cataclasis processes of fault rocks. Such studies undertaken (Blenkinsop, 1991; Antonellini et al., 1994; Fisher and Knipe, 1998) suggest that the concentration of clay/phyllosilicate materials in host rocks can inhibit the probability of occurrence of cataclasis. Therefore, the sandstones with high clay/phyllosilicate content are likely to be resistant to the cataclasis during faulting deformation, as the clay/phyllosilicate-rich sandstones tend to deform more easily by grain sliding and rotation rather than by grain fracturing.

(4). Diffusive Mass Transfer by Pressure Solution and Quartz Cementation

Diffusive mass transfer, a process of mass transfer from high-pressure sites to low-pressure sites, happens when materials are dissolved at the grain contacts and then transported by diffusion to free pore spaces where the dissolved materials reprecipitate (Rutter, 1983; Spiers and Schutjens, 1990; Knipe et al., 1997). Diffusive mass transfer is actually a redistribution of soluble materials from their original sites with high pressure, by means of dissolution, transport and reprecipitation (Dewers and Ortoleva, 1990; Knipe et al., 1997; Fisher et al., 2009); and can alter the porosity and permeability of fault rocks.

Based on the micro-structural analysis, Fisher and Knipe (1998) found the extent of diffusive mass transfer is dominated by the clay/phyllosilicate content and its distribution at the time of deformation. For example: (i). for clean sandstones with clay/phyllosilicate contents of <5%, the fault zones experience enhanced quartz cementation within fault zones but can occur with no enhanced pressure solution (i.e. an external source is involved); (ii). for

clean sandstones with higher clay/phyllosilicate content of 5-15%, there is evidence for both enhanced pressure solution and quartz cementation (i.e. an internal source is involved); (iii). for impure sandstones with clay/phyllosilicate contents of 15-25%, the fault zones can experience enhanced pressure solution but no extensive enhanced quartz cementation; (iv). for impure sandstones with clay/phyllosilicate content of >25%, the porosity and permeability of the fault zones may not be significantly affected by either pressure solution or quartz cementation. The reason for these observations is that diffusive mass transfer needs a catalyst (clay/phyllosilicate) for pressure solution as well as nucleation sites for quartz cementation.

The rate of diffusive mass transfer is especially determined by the presence and distribution of clay/phyllosilicate. For example, the presence of small concentration of clay/phyllosilicate minerals at the grain-contact points promotes the occurrence of pressure solution (e.g. Odling et al., 2004); while clay/phyllosilicate-coating on the quartz grains inhibits the quartz cementation (e.g. Tada and Siever, 1989), because the coating clay/phyllosilicate minerals reduce the effective surface area of quartz grains available for precipitation.

(5). Porosity Reduction by Disaggregation and Mixing

In this fault seal process, there is no extensive grain fracturing but just disaggregation and mixing of grains, which means this process results in the reorganisation of distribution of detrital grains and clay/phyllosilicate minerals without a universal reduction of grain size (Knipe et al., 1997; Fisher and Knipe, 1998; Ottesen Ellevset et al., 1998). This fault process is common in sedimentary units that are unconsolidated or unlithified, as in this situation there is enough space for grains and clay/phyllosilicate minerals to be redistributed during faulting deformation. The sedimentary units that are buried at shallow depths tend to experience disaggregation and mixing to reduce the rock porosity. The distribution of both detrital grains and clay/phyllosilicate minerals can be heterogeneous when initially deposited and then becomes more homogeneous after the disaggregation and mixing during faulting deformation, thus altering permeability pathways.

The permeability of fault rocks produced by disaggregation and mixing varies within a big range, depending on the clay/phyllosilicate content of the host rocks (Knipe et al., 1997; Fisher and Knipe, 1998). For clean sandstones, because the grain size and grain sorting of the fault rock do not change considerably after the reorganization of detrital grains, the fault rock porosity and permeability are not changed significantly. In contrast, for impure sandstones, as well as the reorganization of detrital grains, the fine-grained clay/phyllosilicate minerals are also mixed with these detrital grains, resulting in the occupation of micro-porosity between the detrital grains by the fine-grained clay/phyllosilicate minerals. In this scenario, barriers for fluid flow can be produced and the sealing capacity is effectively increased. According to Fisher and Knipe (1998), the low permeability gouges with intermediate clay content can promote sealing and form when the sedimentary units contain more than 15% clay/phyllosilicate minerals, where enough clay/phyllosilicate minerals are present to fill the porosity within the fault gouge; and moreover, a lower content of clay/phyllosilicate minerals may be required if grain fracturing aids the porosity reduction.

2.2.3. Fault Seal Types and Generated Fault Rocks

Although there have not been universal agreements reached on the fault seal classifications, two types of fault seals have already been recognized, which are juxtaposition seals and fault rock seals (Knipe, 1992a; Knott, 1993; Knipe et al., 1997; Cerveny et al., 2004).

(1). Juxtaposition Seals

Juxtaposition seals are associated with cases where cross fault juxtaposition with low permeability non-reservoir units occurs and have been well described in previous studies (Allan, 1989; Knipe, 1997). When a sequence of beds is cut by faults, the hanging wall can be considered to move downward for normal faults; upward for thrust faults; and laterally for strike slip faults. The relative movement between the two walls of the faults gives rise to the occurrence of juxtaposition between the rocks with different lithologies or petrophysical properties in the hanging wall and the footwall. As rocks with different lithologies usually have different petrophysical properties (e.g. different porosity, permeability, capillary entry pressure), there will be a perme-

ability gradient between different rocks juxtaposed between the hanging wall and the footwall. Juxtaposition seals between the hanging wall and the footwall can be produced by this process. For instance, it is possible to form juxtaposition seals when a sandstone bed is juxtaposed with a mudstone/shale bed; in contrast, it may not form a juxtaposition seal when a sandstone bed juxtaposes with a sandstone bed.

Figure 2.4 is a schematic diagram demonstrating the occurrence of the juxtaposition seals. As the hanging wall moves downward relative to the footwall, different stratigraphic units (A: mudstone; B: sandstone; C: mudstone) from the hanging wall and the footwall juxtapose against each other. For example, the mudstone bed (A) of the hanging wall juxtaposes against the sandstone bed (B) of the footwall (polygon I); B of the hanging wall juxtaposes against B of the footwall (polygon II); and B of the hanging wall juxtaposes against C of the footwall (polygon III). As sandstone presents higher permeability and lower capillary entry pressure than mudstone, the juxtaposition seals can happen in polygon I and polygon III, but do not happen in polygon II.

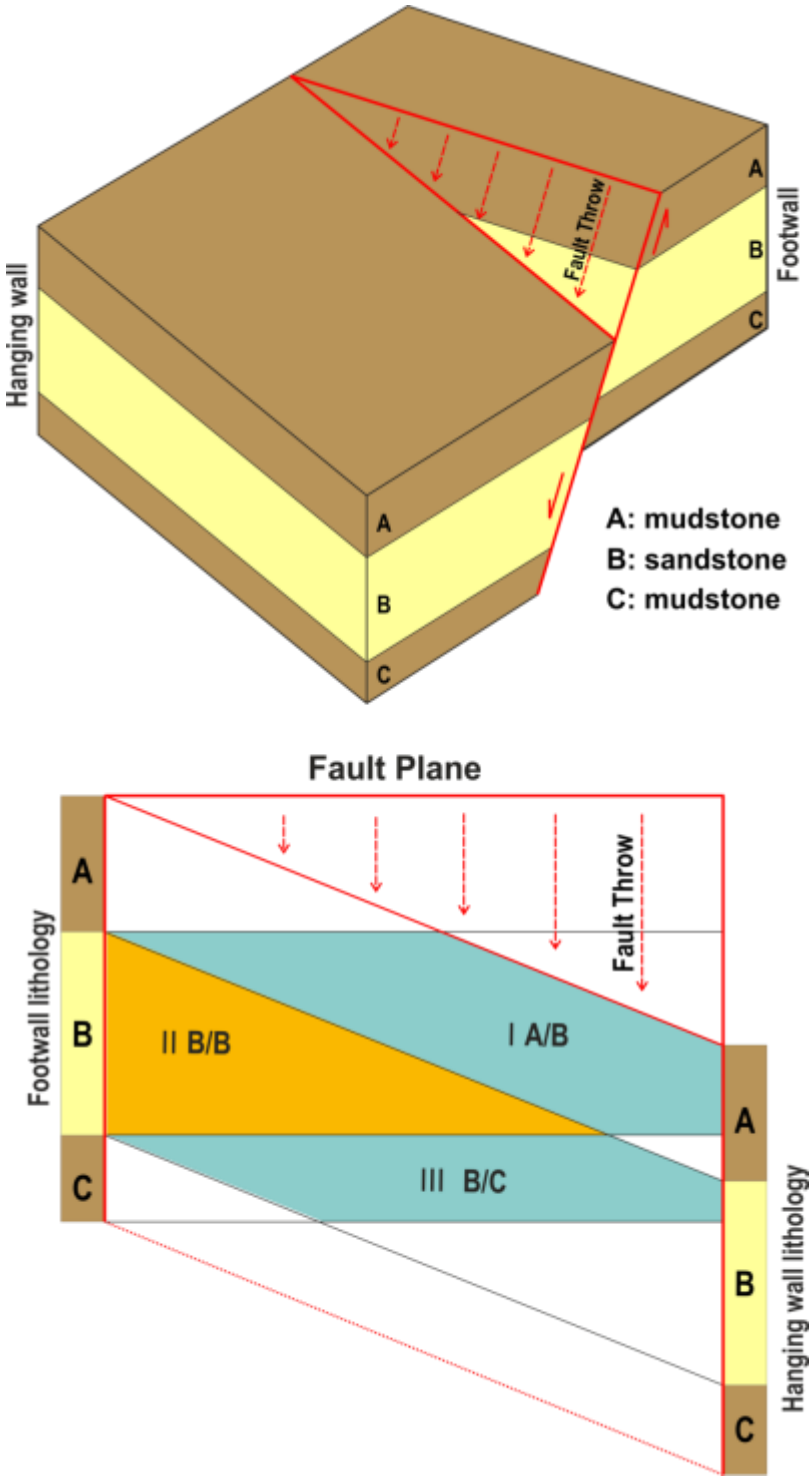

Figure 2.4 A schematic diagram shows how juxtaposition seals happen (modified from Knipe et al., 1997). In the Fault Plane, polygons I, II and III demonstrate three different types of juxtaposition. I: mudstone (hanging wall) juxtaposing against sandstone (footwall); II: sandstone (hanging wall) juxtaposing against sandstone (footwall); III: sandstone (hanging wall) juxtaposing against mudstone (footwall).

(2). Fault Rock Seals

Many faults in nature are not single-plane faults but composed of a series of fault planes that form fault zones (Caine et al., 1996; Childs et al., 1996a; Childs et al., 1996b). Different fault rocks are then generated when different types of host rocks are entrained into the complex fault zones during faulting (Knipe et al., 1997; Fisher and Knipe, 1998; Knipe et al., 1998; Ottesen Ellevset et al., 1998). The study of Watts (1987) highlighted that most faults/fault zones were membranes or flow retarders with different properties of transmissibility or permeability. As the sealing properties of fault rocks can be evaluated by the permeability and the capillary threshold pressure (Watts, 1987; Fisher and Knipe, 2001; Fisher and Jolley, 2007), the fluid flow across the fault zones will not happen unless the capillary threshold pressure is reached. Therefore, the petrophysical properties of the fault rocks, such as the capillary threshold pressure and permeability control the hydrocarbon sealing properties of faults/fault zones.

As pointed (Knipe et al., 1997; Fisher and Knipe, 1998), the composition of the host sediments at the time of deformation determines the deformation mechanisms, microstructures and petrophysical properties of the fault rocks within the fault zones; and fault rock seals may occur if fault rocks with low permeability and high capillary threshold pressure are generated within the fault zones. Fisher and Knipe (2001) suggested that fluid flow properties of faults are significantly influenced by the presence of clay/phyllosilicate in three ways: (i). the high concentrations of clay/phyllosilicate can produce fault rocks within which most of the original porosity is occupied by the fine grained clay/phyllosilicate minerals and the micro-porosity (Fisher and Knipe, 1998); (ii). there is a higher potential for clay/phyllosilicate smearing within the sedimentary units with high clay/phyllosilicate contents (Lindsay et al., 1993); and (iii). the existence of clay/phyllosilicate materials between framework-silicate grains promotes pressure solution and quartz cementation (Fisher and Knipe, 1998). Therefore, if the faults maintain self-juxtaposition of these units, the fault rock types related to the fault rock seals can be classified according to the composition (especially the clay/phyllosilicate content) of the host rocks from which the fault rocks are produced. Where faulting exceeds the thickness of the host units, the resulting clay content of the fault

rock (from smearing and mixing of the host rocks involved in the faulting), grain size reduction processes and the potential for cementation can impact on the fault rock flow properties

Fault rocks can therefore be classified into the following groups (Knipe et al., 1997; Fisher and Knipe, 1998; Ottesen Ellevset et al., 1998): the cemented faults/fractures; the clay/phyllosilicate smears; the phyllosilicate-framework fault rocks (PFFRs); the cataclasites; and the disaggregation zones (Figure 2.5). This classification is based on the relationship between the clay/phyllosilicate content and fault rock types.

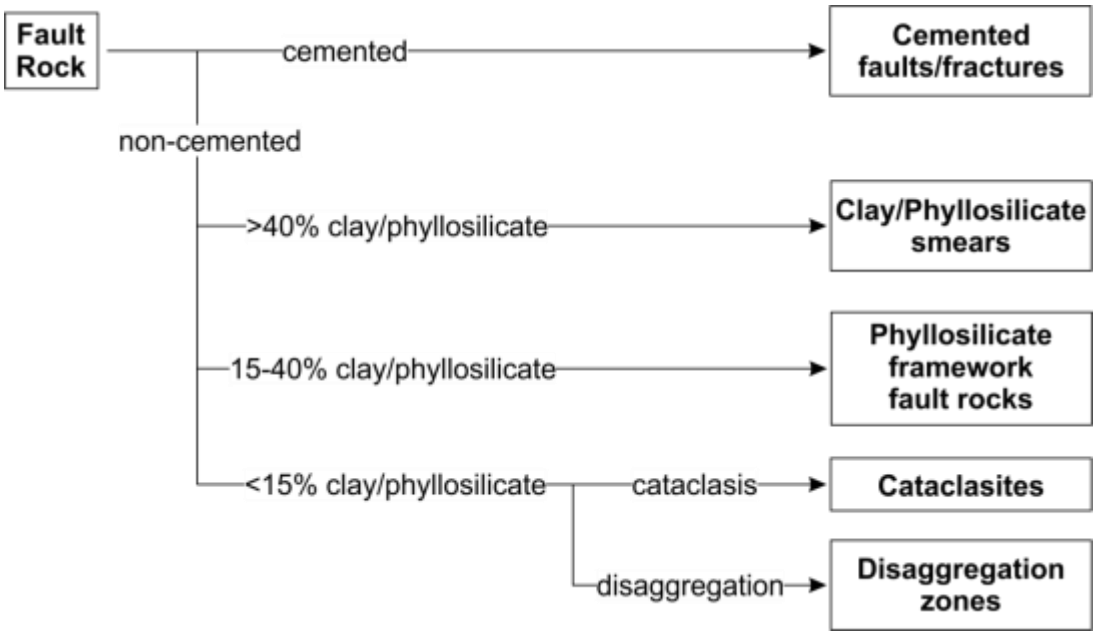

Figure 2.5 Illustration of typical fault rocks and their clay/phyllosilicate contents, showing the important control of the clay/phyllosilicate content on the fault rock development (Knipe et al., 1997; Fisher and Knipe, 1998; Ottesen Ellevset et al., 1998).

(i). Cemented faults/fractures

Fault seal analysis based on the prediction of fault rock clay contents can be invalidated if cemented fault zones are extensively developed (Knipe, 1993a; Knipe et al., 1997). However, in most cases, the cementation is not extensive enough to influence the sealing properties of the fault zones (Ottesen Ellevset et al., 1998), as the cementation can rarely form continuous seals but is often restricted to limited areas of the fault zone or between the footwall and the hanging wall cut offs of units prone to cementation.

Generally, cement seals only happen in fault zones where the sealing properties are dominated by the minerals' dissolution-reprecipitation process or where new minerals' precipitation is promoted (Knipe, 1997). Therefore, the cement seals are mostly associated with the sites where local dissolution and reprecipitation happen during deformation or along the invasion paths of fluids in the faults. For cemented faults and fractures, Knipe et al. (1997) found that cementation is the dominant mechanism of porosity reduction within the fault zones. There are probably two main sources of cements: the local soluble minerals within the fault zones; and the invaded fluids along the fault planes. Because of the high density of nucleation sites on the fault planes, both the local soluble minerals and invaded fluids can be easily precipitated along or adjacent to the fault planes. Ottesen Ellevset et al. (1998) suggested that the cementation extent along the fault planes may be limited to three times the thickness of the unit that acts as a source unit for the cementation.

(ii). Clay/Phyllosilicate Smears

As shown in the fault rock classification (Figure 2.5), fault rocks with clay/phyllosilicate contents >40% are defined as clay smears. These can develop from the deformation of a host shale rock with >40% clay/phyllosilicate content at the time of deformation (Knipe, 1997; Knipe et al., 1997; Ottesen Ellevset et al., 1998). In this situation, a continuous clay material zone with low-permeability along fault planes can be produced during the faulting deformation. The factors controlling the clay/phyllosilicate smear continuity are the content and distribution of clay/phyllosilicate-rich units, fault throw (Bouvier et al., 1989; Lindsay et al., 1993; Fulljames et al., 1997; Yielding et al., 1997), and the lithification state (Heynekamp et al., 1999; Egholm et al., 2008; Loveless et al., 2011). Empirically, Knipe (1997) found that the clay/phyllosilicate smears often become discontinuous once the fault throw is larger than three times the thickness of clay/phyllosilicate-rich stratigraphic units.

(iii). Phyllosilicate-Framework Fault Rocks (PFFRs)

As shown in the fault rock classification (Figure 2.5), phyllosilicate-framework fault rocks (PFFRs) contain 15-40% clay/phyllosilicate minerals.

These can develop from impure sandstones containing 15-40% clay/phyllosilicate at the time of deformation or from the mixing of high and low clay content units (Knipe, 1992a; Knipe et al., 1997; Fisher and Knipe, 1998). An impure sandstone, with a mixture of phyllosilicates and framework silicates, can produce PFFRs where the petrophysical properties are dominated by the generation of anastomosing networks of the micro-smears around the framework fragments or clasts (Knipe, 1997). These micro-smears may have similar properties to the clay smears; thus, as pointed by Knipe (1992a), it is not necessary to have clay units for creating PFFRs if the sealing properties are determined by the continuity and the structure of deformed phyllosilicates.

Ottesen Ellevset et al. (1998) pointed that the occurrence of PFFRs has great effects on the sealing behaviour in two areas, which are the area where the impure sandstones directly juxtapose against the fault zones; and the area along fault planes between the hanging wall and footwall cut-offs of impure sandstone units. The latter scenario is to some extent similar to the behaviour of clay/phyllosilicate smears. The continuity of the PFFRs determines the effectiveness of PFFRs to form effective retarders for fluid flow (Knipe et al., 1997; Fisher and Knipe, 1998; Ottesen Ellevset et al., 1998).

(iv). Cataclasites

Cataclasites dominate seal development in clean sandstones containing <15% clay content at the time of deformation (Knipe et al., 1997; Fisher and Knipe, 1998; Ottesen Ellevset et al., 1998). Because of the low clay content within such host rocks, the main mechanisms of porosity and permeability reduction are the cataclasis and the post-deformation quartz cementation (Fisher and Knipe, 1998). During the process of cataclasis, the grain size decreases by means of grain fracturing and frictional grain sliding, resulting in the porosity reduction and potential cementation. The granulation seams or deformation bands, which are discussed in many studies (Knipe, 1992a, 1993a, b; Antonellini and Aydin, 1994), are cataclasites.

Previous research has pointed out that the permeability of cataclasites varies over a large range; this depends on the lithification state of the host rocks (Knipe et al., 1997; Fisher and Knipe, 1998). According to the lithification

state, the cataclasites can be divided into three types: (i). poorly lithified cataclasites, which show little or even no compaction or cementation (post-deformation) and point contacts are maintained between grains; (ii). partially lithified cataclasites, which have some compaction and cementation; and (iii). lithified cataclasites, which comprise grains interlocked by post-deformation dissolution and/or cementation (Knipe, 1992a, 1993b; Knipe et al., 1997).

(v). Disaggregation Zones

The disaggregation zones are fault rocks generated by deformation without fracturing. They can also be produced from pure, low clay-content (<15%) sandstones (Figure 2.5), similar to the generation of the cataclasites (Knipe et al., 1997; Fisher and Knipe, 1998; Ottesen Ellevset et al., 1998). However, the host rocks of disaggregation zones are normally poorly lithified rocks. In the process of disaggregation, the grains move by way of particulate flow to accommodate the strain during faulting deformation, with no extensive grain fracturing (Knipe et al., 1997; Fisher and Knipe, 1998). The permeability of disaggregation zones is usually higher than that of the other types of fault rocks. It is difficult for disaggregation to form effective seals to prevent fluid flow, because there are not sufficient clays/phyllosilicates within the disaggregation zones to act as a source for either the cementation or the clay/phyllosilicate smears.

2.2.4. Factors Affecting Petrophysical Properties of Fault Rocks

The petrophysical properties of fault rocks are mainly determined by the clay/phyllosilicate content, the level of cataclasis and the amount of cementation. However, in some natural oil/gas fields, the fault rocks, generated from sandstones with identical clay/phyllosilicate contents, can have different porosity and permeability characteristics (e.g. Fisher and Knipe, 2001; Fisher et al., 2003). This can be attributed to the interaction between the temperature history and the stress history, which can alter the petrophysical properties of fault rocks within the fault zones (Fisher and Knipe, 2001). Therefore, as well as the clay/phyllosilicate content of host rocks, the effects of temperature history and stress history need to be taken into account when evaluating the fault sealing properties.

(i). Temperature history

It has been commonly accepted that the temperature history of fault rocks has a significant effect on the rate of meso-diagenesis, e.g., quartz cementation and pressure solution (e.g., Walderhaug, 1996). The rate usually increases as a function of temperature (Fisher and Knipe, 2001; Fisher et al., 2003; Fisher et al., 2009), e.g., the quartz cementation and pressure solution occurs at rapid rate when the temperature exceeds ~90°C.

(ii). Stress History

Many studies tried to identify the effects of confining pressure on the deformation behaviour of faults/fault zones in sandstones. These studies suggest that: the sandstones at low confining pressures are likely to experience brittle faulting (failure occurs along single slip planes) (e.g. Handin et al., 1963; Scott and Nielsen, 1991); while the sandstones at high confining pressures prefer more distributed ductile deformation without the generation of discrete slip planes (e.g. Handin et al., 1963; Scott and Nielsen, 1991). The experimental studies indicate that the grain size and the permeability of faults/fault zones decrease with increasing confining pressure and temperature (e.g. Engelder, 1974; Zhu and Wong, 1997; Crawford, 1998; Fisher and Knipe, 2001).

2.2.5. Methods to Evaluate Fault Sealing Properties

In the recent 20 years, geologists have developed and used several methods to evaluate the fault sealing properties. Although all methods have their own shortcomings, the methods have been improved to become more and more effective and useful for evaluation of the fault sealing properties.

Allan (1989) introduced a model to relate faults to hydrocarbon migration and entrapment, suggesting the influence of faults on the hydrocarbon migration and the entrapment is determined by the lithologies of juxtaposed stratigraphic units on different sides of fault and the fault throws between the hanging wall and the footwall cut-offs. The model provides a 3D overview and understanding on the architecture of the fault juxtapositions, the stratigraphic units and the fault throws, which can help to understand the stratigraphic contacts, the fault geometry and the structure/closure style.

Knipe (1997) presented an updated technique of triangle juxtaposition diagram to judge what types of fault seals can be formed based on the final and evolution of stratigraphic juxtapositions across faults (Figure 2.6).

It is known that reservoir stratigraphic units (e.g., permeable sandstones) juxtaposing against impermeable stratigraphic units (with high concentration of clay/phyllosilicate materials, e.g., shales/mudstones) probably form fault seals; while leaking windows are more likely if reservoir sand stratigraphic units are juxtaposed against each other. By using the triangle juxtaposition diagram, it is possible to make an initial judgement and prediction of fault sealing properties, particularly when seeking possible leaking windows. Moreover, in the triangle juxtaposition diagram, the sidewall charts can also be attached to provide more details of the stratigraphy, such as the sand net/gross ratio, the clay/phyllosilicate content, the host rock lithology and the host rock permeability (e.g., Knipe, 1997; Knipe et al., 1997; Cerveny et al., 2004). These details contribute to allow a more reliable assessment and prediction of sealing properties on the faults. Different types of juxtapositions between different stratigraphic units can be identified on this diagram; and these different juxtaposition types provide important clues for estimating the fault sealing properties of different places on the fault plane with various fault throws.

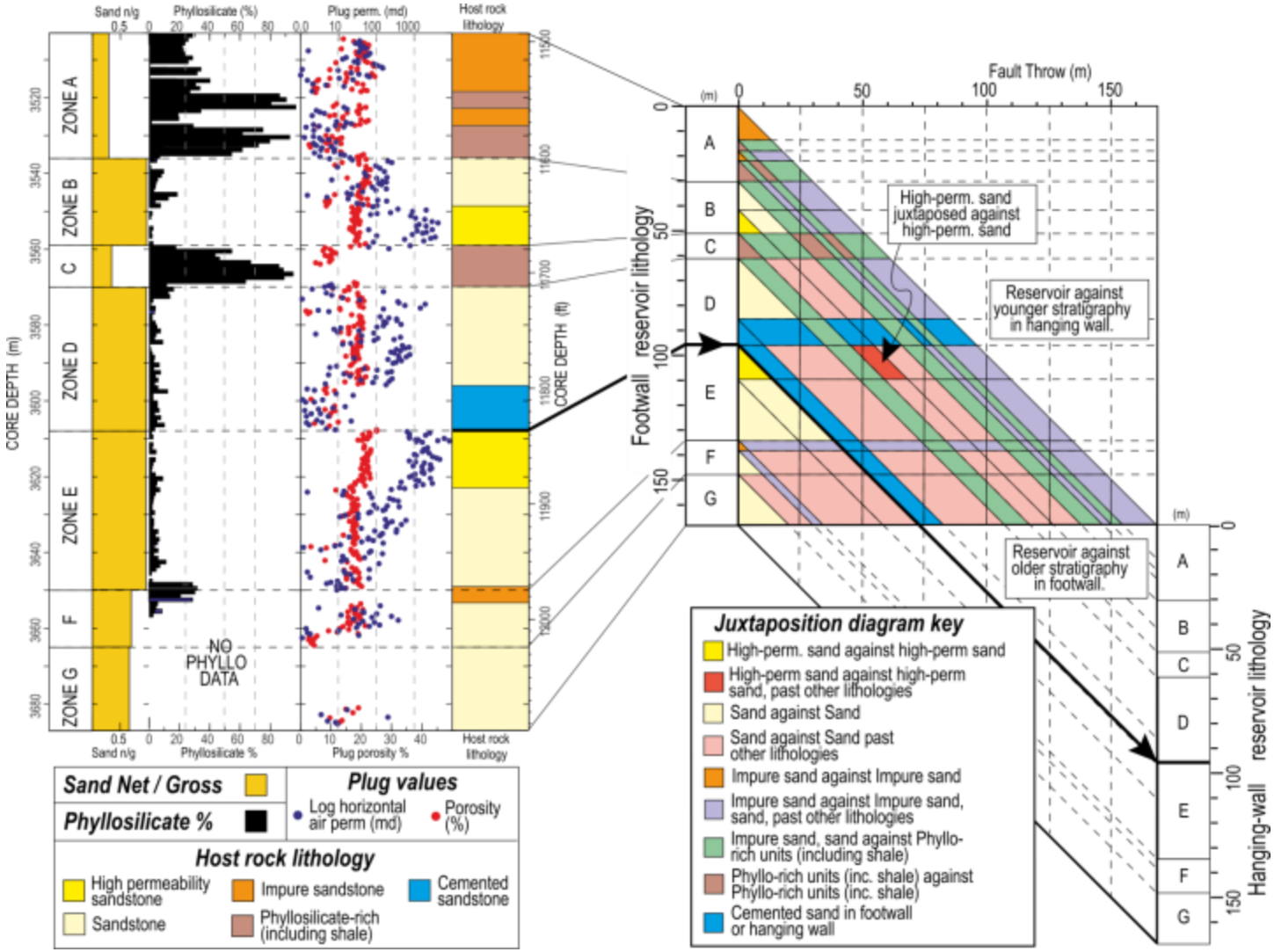

Figure 2.6 The triangle juxtaposition diagram uses sidewall chart input to identify the leaking windows and the fault seals resulting from the stratigraphic juxtapositions between the hanging wall and the footwall (Knipe, 1997).

Bouvier et al. (1989) employed Clay Smear Potential (CSP) to estimate the potential of occurrence of clay smearing based on studies in Nigeria. The CSP was then expressed more explicitly by Fulljames et al. (1997) (Figure 2.7a). The CSP represents the total amount of clay/phyllosilicate that has been smeared from every stratigraphic unit with high clay/phyllosilicate content along the fault planes. The value of CSP increases with increasing thickness of shale/mudstone beds and the number of stratigraphic units with high concentrations of clay/phyllosilicate; and the CSP decreases with increasing fault throw.

$$\mathrm{CSP} = \sum \frac{(\text{Shale bed thickness})^2}{\text{Distance from source bed}}$$

Lindsay et al. (1993) introduced another algorithm Shale Smear Factor (SSF, Figure 2.7b) to estimate the magnitude of fault seals formed by smearing of clay/phyllosilicate-rich units, e.g., shales and mudstones. The SSF value is proportional to the fault throws and inversely proportional to the thickness and the number of source units of clay/phyllosilicate. Using the SSF algorithm to estimate the extent of clay/phyllosilicate smears, there is increasing potential to form a continuous clay/phyllosilicate smears with increasing thickness and number of source unites of clay/phyllosilicate and decreasing fault throws, and vice versa.

$$\mathrm{SSF} = \frac{\text{Fault throw}}{\text{Shale layer thickness}}$$

The algorithm Shale Gouge Ratio (SGR, Figure 2.7c) was proposed (Yielding et al., 1997) to estimate the clay content in faults from the mixing of units with different clay contents in the throw interval. This helps evaluate fault seals in more complex stacking sequences. The SGR is proportional to cumulative thickness of shale beds within a scale of a distance equal to fault throw and inversely proportional to fault throw.

$$\mathrm{SGR} = \frac{\sum(\text{Shale bed thickness})}{\text{Fault throw}} \times 100\%$$

Furthermore, the definition of SGR was extended for a package of sediments (Figure 2.7d). In this situation, SGR is considered to be the percentage of clay present in all units in the throw interval.

$$\mathrm{SGR} = \frac{\sum[(\text{Zone thickness}) \times (\text{Zone clay fraction})]}{\text{Fault throw}} \times 100\%$$

As a summary, the algorithms of CSP and SSF estimate the fault sealing properties by considering the continuity of smearing of shale/mudstone beds; while the SGR algorithm calculates the average mixture of clays likely to be present at different point on a fault.

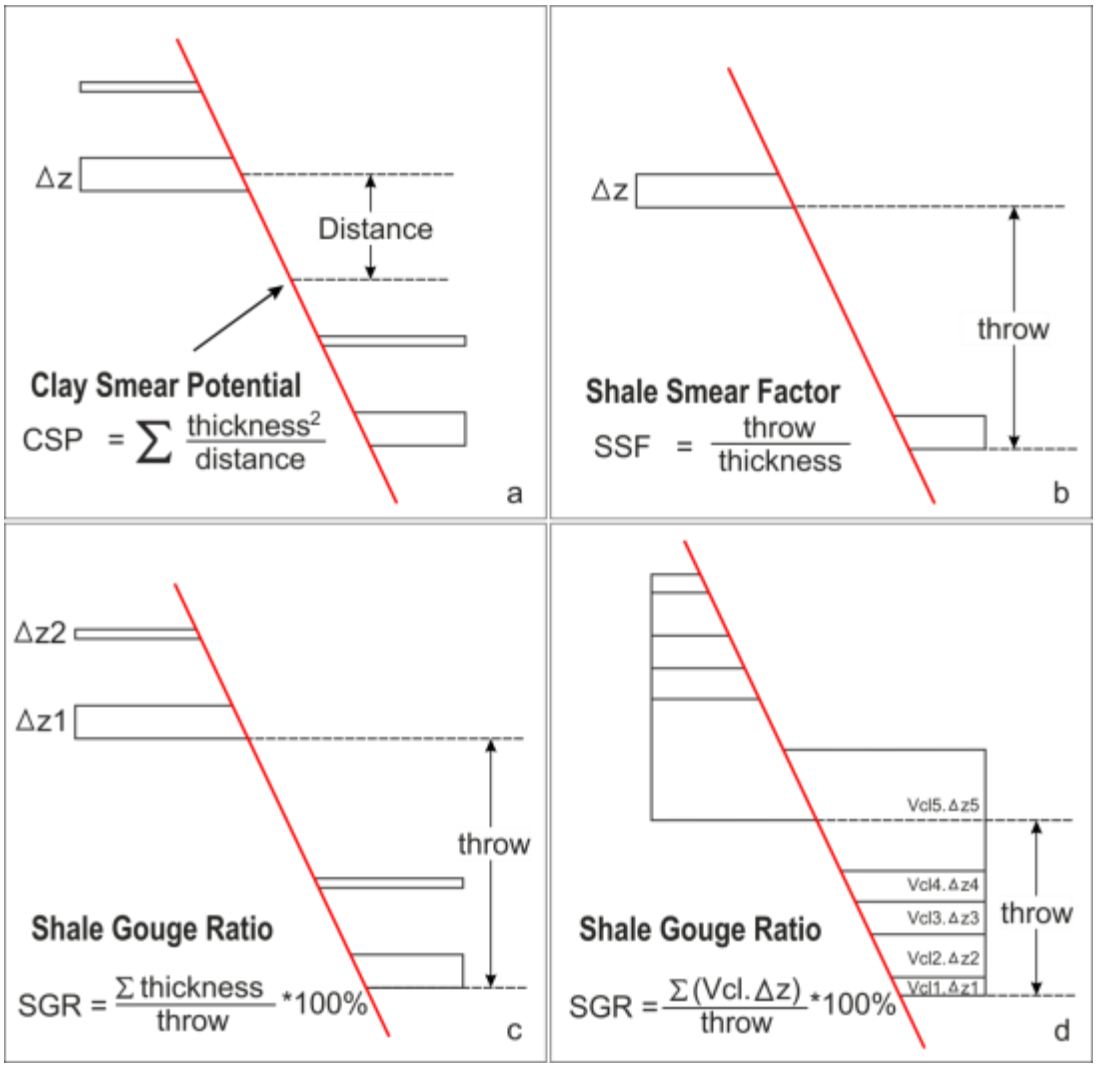

Figure 2.7 Diagram and calculation of methods for estimation of fault seals (especially fault seals formed by clay/phyllosilicate smearing): (a) Clay Smear Potential (CSP) (Bouvier et al., 1989; Fulljames et al., 1997); (b) Shale Smear Factor (SSF) (Lindsay et al., 1993); (c, d) Shale Gouge Ratio (SGR) (Yielding et al., 1997).

Knipe (1992a) found that the fault sealing properties (e.g. fault seal processes, fault rock types, petrophysical properties and fluid flow behaviour) vary because of the impact of the geological conditions and history during and after deformation, e.g., the temperature history (Fisher and Knipe, 2001; Fisher et al., 2003; Fisher et al., 2009) and stress history (Handin et al., 1963; Scott and Nielsen, 1991; Fisher and Knipe, 2001).

As introduced above, the fault rocks are generated when the sedimentary units are entrained into the fault zones. The detailed evaluation of different types of fault rocks can be achieved by integrating micro-structural analysis on the deformation mechanisms and the porosity and permeability data. The Scanning Electron Microscope (SEM) was employed in Knipe (1992a) to investigate the micro-structures of fault rocks. The following studies (e.g., Fisher and Knipe, 1998; Ottesen Ellevset et al., 1998; Fisher and Knipe, 2001; Fisher et al., 2003; Fisher et al., 2009) integrated the fault rock petrophysical sealing properties with the micro-structural analysis on the fault rocks developed within the fault zones.

The micro-structural analyses undertaken are laboratory based that aim to characterise the microstructures and the petrophysical properties of fault rocks and compare these to their host rocks, in order to estimate the deformation mechanisms and the fault seal processes that the fault rocks experienced, and to identify the relative timing of deformation during diagenesis.

The petrophysical properties of the fault rocks have been measured to evaluate the sealing capacity of the fault rocks quantitatively in many previous studies (e.g., Fisher and Knipe, 1998; Ottesen Ellevset et al., 1998; Fisher and Knipe, 2001; Jolley et al., 2007; Tueckmantel et al., 2010). A case study in the North Sea and Norwegian Continental Shelf plotted the permeability of fault rocks against the clay content of the host rocks for various fault rock types (Figure 2.8) (Fisher and Knipe, 2001). The case study suggests that for low throw faults with self-juxtaposition, the clean sandstones (clay content <15%) tend to form cataclasites that do not always represent effective fluid flow barriers; the impure sandstones (clay content 15%-40%) experience significant porosity and permeability reduction; while the mudstones or shales form continuous clay smears with very low permeability that can be

effective barriers for fluid flow across the fault zones. It also highlights that the permeability of the fault rocks is not only determined by the clay content of host rocks, but also related to their burial history (Figure 2.8).

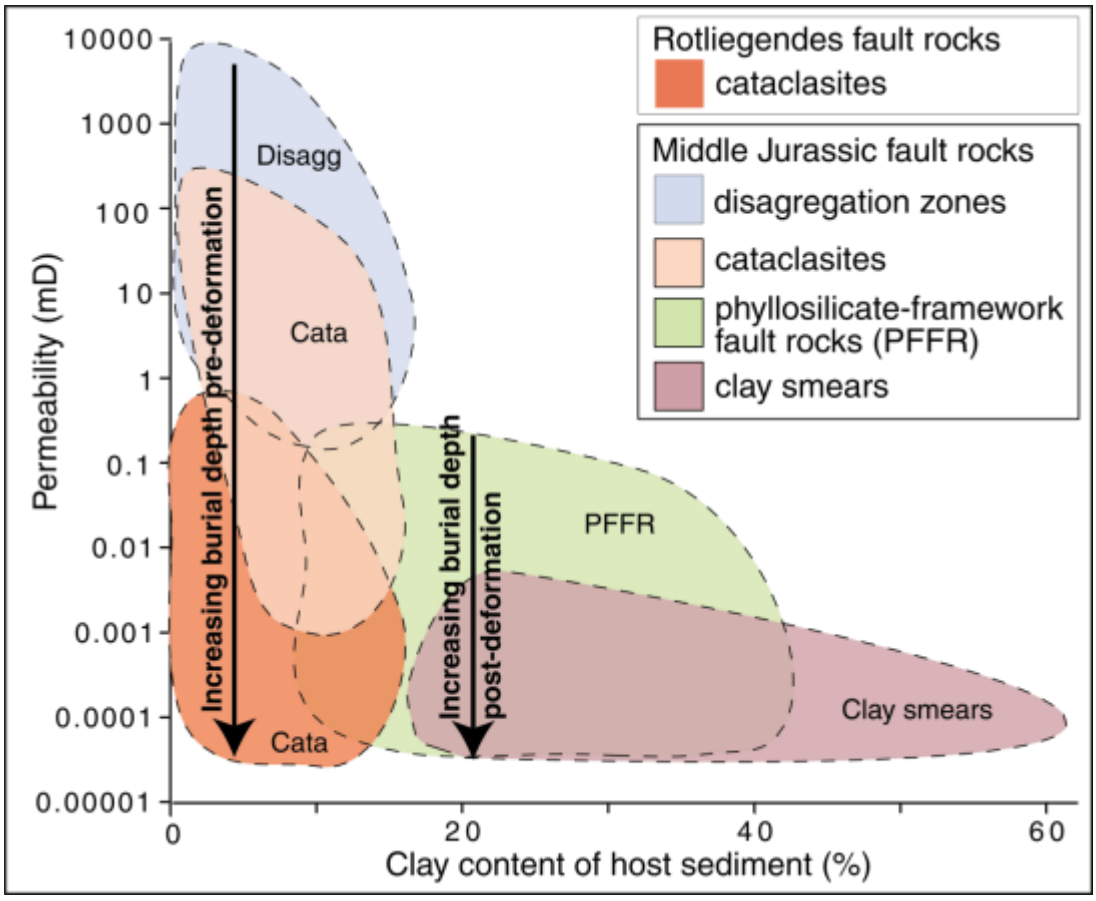

Figure 2.8 Summary of the fault rock permeability from the North Sea and Norwegian Continental Shelf (modified from Fisher and Knipe, 2001). The permeability of various fault rocks is plotted against the clay content of the host rocks. The chart also describes the control of the burial depth on the fault rock permeabilities.

2.2.6. Summary

Although there are many effective methods, they have mostly been used to study the fault zone architecture and fault sealing properties in extensional regimes. Many case studies have realized that faults/fractures can play important control on the hydrocarbon migration in contractional regimes, e.g., the study in Kentucky, USA (Lewis et al., 2002), the New Guinea Fold Belt (Hill et al., 2004), the North West Borneo (Ingram et al., 2004), the Qaidam basin (Pang et al., 2004), etc. However, the detailed thrust fault architecture (particularly the meso- to micro-scale deformation features) and its effect on the fault sealing behaviour have not been well studied in contractional systems.

Having reviewed the geological settings of Qaidam basin and the background of fault zone architecture and fault seal analysis, the next chapter will demonstrate the trishear parameter/dynamic spaces and trishear strain quantification that can be used to assist the application of trishear algorithm to natural structures. An example in the Lenghu5 structure of Qaidam basin is presented to demonstrate an effective workflow of applying trishear algorithm to natural structures.

Chapter 3
Trishear Parameter/Dynamic Spaces and Strain Quantification to Assist the Application of Trishear Algorithm to Natural Structures

3.1. Introduction

It has been established that there is often an intimate relationship between folding of sedimentary sequence and underlying faults. In the previous studies based upon fieldwork data, seismic reflection and well logging, etc., examples of well-established models include fault-bend folds (Suppe, 1983; Jamison, 1987; Medwedeff and Suppe, 1997; Tavani et al., 2005), fault-propagation folds (Jamison, 1987; Mitra, 1990; Suppe and Medwedeff, 1990) and detachment folds (Jamison, 1987; Dahlstrom, 1990; Poblet and McClay, 1996; Mitra, 2003). Many of these models are based upon the kink band method (Figure 3.1a, b) to predict uniform dips and homogeneous deformation in limbs of folds resulting from fault-bend and fault-propagation (Suppe, 1983; Suppe and Medwedeff, 1990). The kink band method usually keeps constant layer thickness and line-length during structural deformation (Suppe, 1983; Suppe and Medwedeff, 1990). However, this kink band method is not always applicable to all fault/fold systems. Many experimental analogue studies (Ellis et al., 2004; McQuarrie, 2004; Bose et al., 2009; Miller and Mitra, 2011), numerical models (e.g., Erslev, 1991; Hardy and Ford, 1997; Allmendinger, 1998; Cristallini and Allmendinger, 2001) and natural geological structures (e.g., Erslev, 1991; Erslev and Rogers, 1993; Erslev and Mayborn, 1997; Allmendinger, 1998; Cristallini and Allmendinger, 2001) show non-uniform dips in the same limb and inhomogeneous deformation within the fault zone (Figure 3.1c), which are not predicted by the kink band method. In these scenarios, the layer thickness and length within strain zones change during deformation so the kink band method is inapplicable here. For these structures, the trishear model was initially proposed by Erslev (1991), with a precondition that the section area is kept constant during deformation (Figure 3.2).

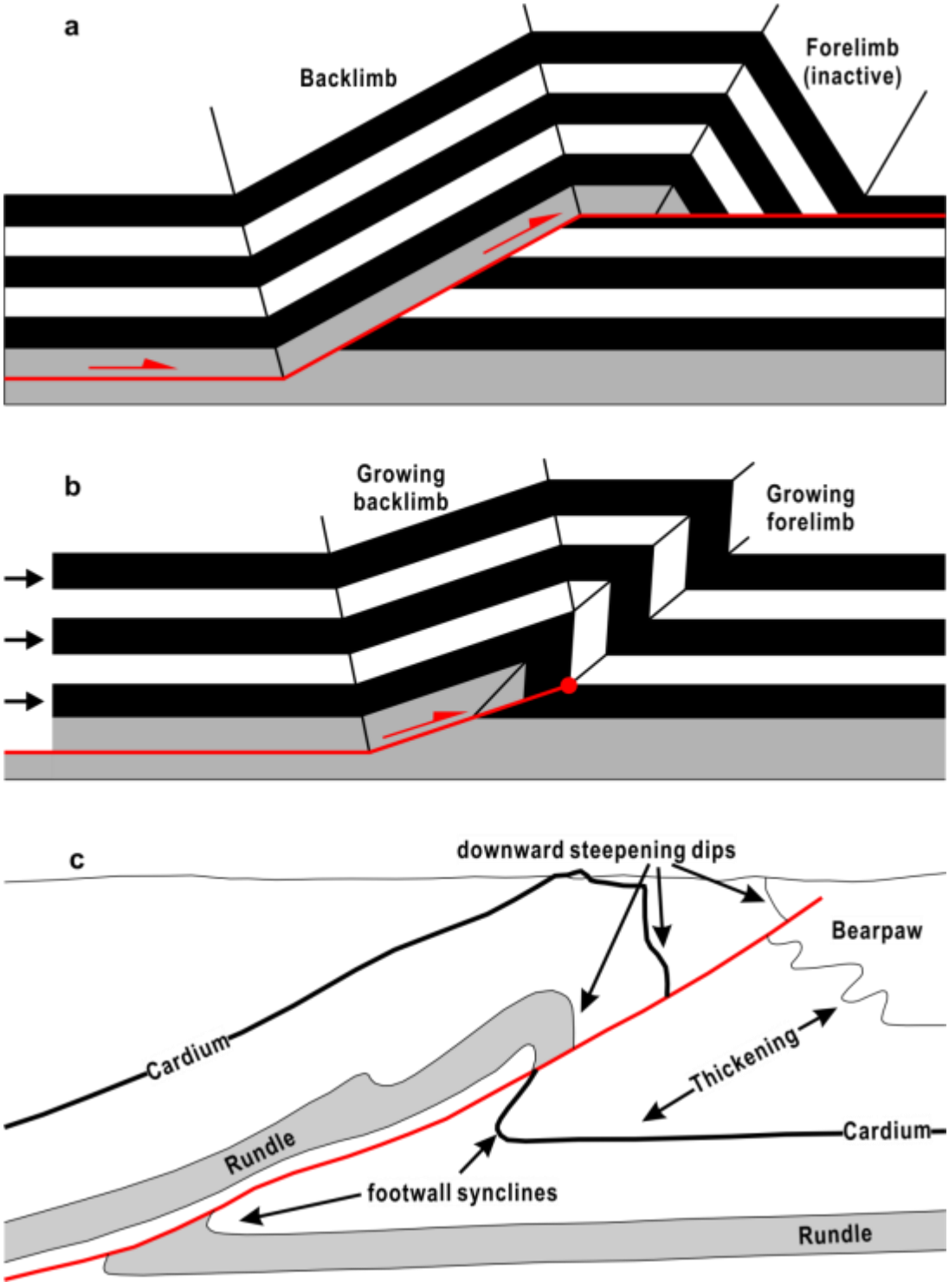

Figure 3.1 Fault-bend fold and fault-propagation fold based on kink bend method (a, b) (Suppe, 1983; Suppe and Medwedeff, 1990) and a natural example showing variable layer thickness (c) (Allmendinger, 1998).

Within the trishear model (Figure 3.2), the deformation is concentrated within a triangle zone in front of the propagating fault tip. Compared with the simple shear algorithm (Withjack and Peterson, 1993), the particles in the triangle zone no longer migrate parallel to the fault trace, but with a displacement component from the hanging wall side to the footwall side. The migration velocity within the triangle zone decreases from a maximum on the hanging wall trishear boundary to zero on the footwall trishear boundary. This non-uniform migration within the triangle zone allows the layer thickness and length to change during the trishear deformation. However, the section area is kept constant. There are three controlling parameters in the trishear algorithm, which are the trishear p/s ratio (the fault propagation/slip ratio); the trishear apical angle; and the fault dip. For example, when the fault slips from point A to point B, the fault tip propagates from point A to point C (Figure 3.2). The ratio between the length of AC and AB is the trishear p/s ratio. The conceptual trishear model of Erslev (1991) has subsequently been quantified to account for definition of the parameters controlling the trishear geometry by the later studies (e.g., Hardy and Ford, 1997; Zehnder and Allmendinger, 2000; Cristallini and Allmendinger, 2001; Cristallini et al., 2004). By varying the controlling parameters, further modifications also allow a spectrum of trishear models, including basic (homogeneous) trishear models (Hardy and Ford, 1997); heterogeneous trishear models (Erslev, 1991); asymmetric trishear models (Zehnder and Allmendinger, 2000); extensional trishear models (Jin and Groshong, 2006); reverse trishear models (Cruden and McCaffrey, 2001); evolving apical angle trishear models (Allmendinger, 1998); and quadshear models (Welch et al., 2009) where propagation of two pre-existing faults towards each other is used to model fault development in mechanically heterogeneous sequences. The simplest trishear model and its potential application has been discussed in many studies (Allmendinger et al., 2004; Cardozo, 2005; Cardozo et al., 2005; Gold et al., 2006; Jin and Groshong, 2006; Lin et al., 2007; Cardozo, 2008; Cardozo and Aanonsen, 2009; Jin et al., 2009; Cardozo et al., 2011). Allmendinger (1998) demonstrated the geometric complexities resulting from varying parameters associated with a single fault, while Allmendinger et al. (2004) considered the resulting geometry when multiple faults with opposing dips are modelled.

Despite these studies, there has been little attention to the spectrum of potential trishear geometry, which limits the application of the trishear mechanism in understanding natural structures, especially in the complex thrust-and-fold belts in compressional systems.

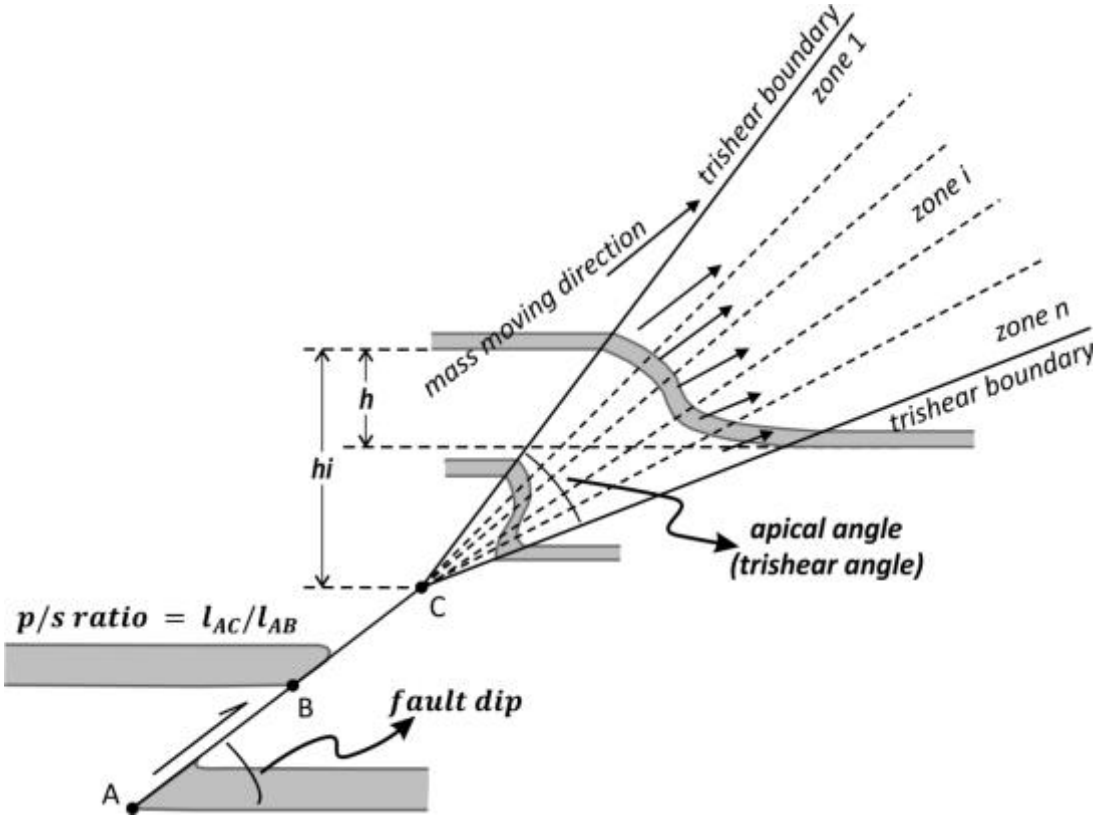

Figure 3.2 Conceptual model of trishear algorithm, based on Hardy and Ford (1997).

This chapter focuses on the trishear deformation associated with reverse faults. Given the significant degrees of freedom available with the trishear parameters, it is difficult to find unique solutions to define appropriate parameters for natural structures. Therefore, the effect of varying each parameter on the resultant geometry is evaluated by defining a three-dimensional parameter space (Figure 3.3), where the three controlling parameters (the p/s ratio, the trishear apical angle and the fault dip) can vary independently of each other. A range of published examples is then considered in terms of where they plot onto the parameter space (Figure 3.4). A cluster of natural examples is found and helps to constrain the best-fit parameters for natural structures. As an important element of the trishear model is the temporal evolution of the structure, having outlined the static parameter space a three-dimensional dynamic space is built to consider how

the structures most represented in natural systems evolve with time (Figure 3.5). The relationship between the key parameters controlling trishear geometries is quantified (Figure 3.6), in order to predict the ranges of trishear parameters for natural structures. Those natural examples that are not adequately described by our static or dynamic parameter space are also considered and alternative parameters are also proposed, e.g., the fault-dip change and pre-existing faults. Finally, a natural example from the Lenghu5 structure (Qaidam Basin, NW China) is interpreted by the trishear parameter/dynamic space and the strain quantification, which provides a new workflow of applying trishear algorithm to the complex natural structures.

3.2. 3D Parameter Space and Clusters of Natural Examples

As introduced above, the three principle controlling parameters for the trishear algorithm are the trishear p/s ratio, the trishear apical angle and the reverse fault dip. In order to evaluate the effects of the parameters on the resulting geometry, a three-dimensional parameter space is created, with three axes representing each of the parameters (Figure 3.3). By varying the three parameters, the parameter space is constructed, allowing the construction of a variety of trishear models with different geometries (models generated in 2D MOVE in Midland Valley).

As described in previous studies, part of the final geometry is a consequence of the general algorithm and is therefore common to all trishear models. This includes the development of a monocline in front of the fault tip. As shown in Figure 3.3, a constant layer thickness is not maintained during deformation. For example, in all the trishear models and published natural examples, the hanging wall strata are thinned while the footwall strata are thickened. These features are consistent with the observations in natural trishear examples, e.g., rotation structures (Figure 3.1c). Although these geometries are common to all examples, Figure 3.3 shows how in detail these geometries vary significantly, dependent upon the specific parameters that are used. For example, with same trishear apical angles and reverse fault dips, low trishear p/s ratio leads to high magnitude of hanging wall thinning and footwall thickening. By comparing the trishear models distributed in the

parameter space, the effects of the parameter selection on the geometry of trishear models are summarized below:

(i). With a constant fault slip, the amplitude of the hanging wall uplift has a positive correlation function of fault dip that is unaffected by p/s ratio or apical angle; while the fault tip propagation is positively correlated with high p/s ratio and unaffected by apical angle or fault dip.

(ii). Parameters of low fault dip, low p/s ratio and high apical angle result in a high magnitude of hanging wall thinning and footwall thickening.

(iii). Parameters of low fault dip, low p/s ratio and high apical angle form a wide monocline.

(iv). The monocline in front of the fault tip can be overturned with parameters of high fault dip, high p/s ratio and low apical angles.

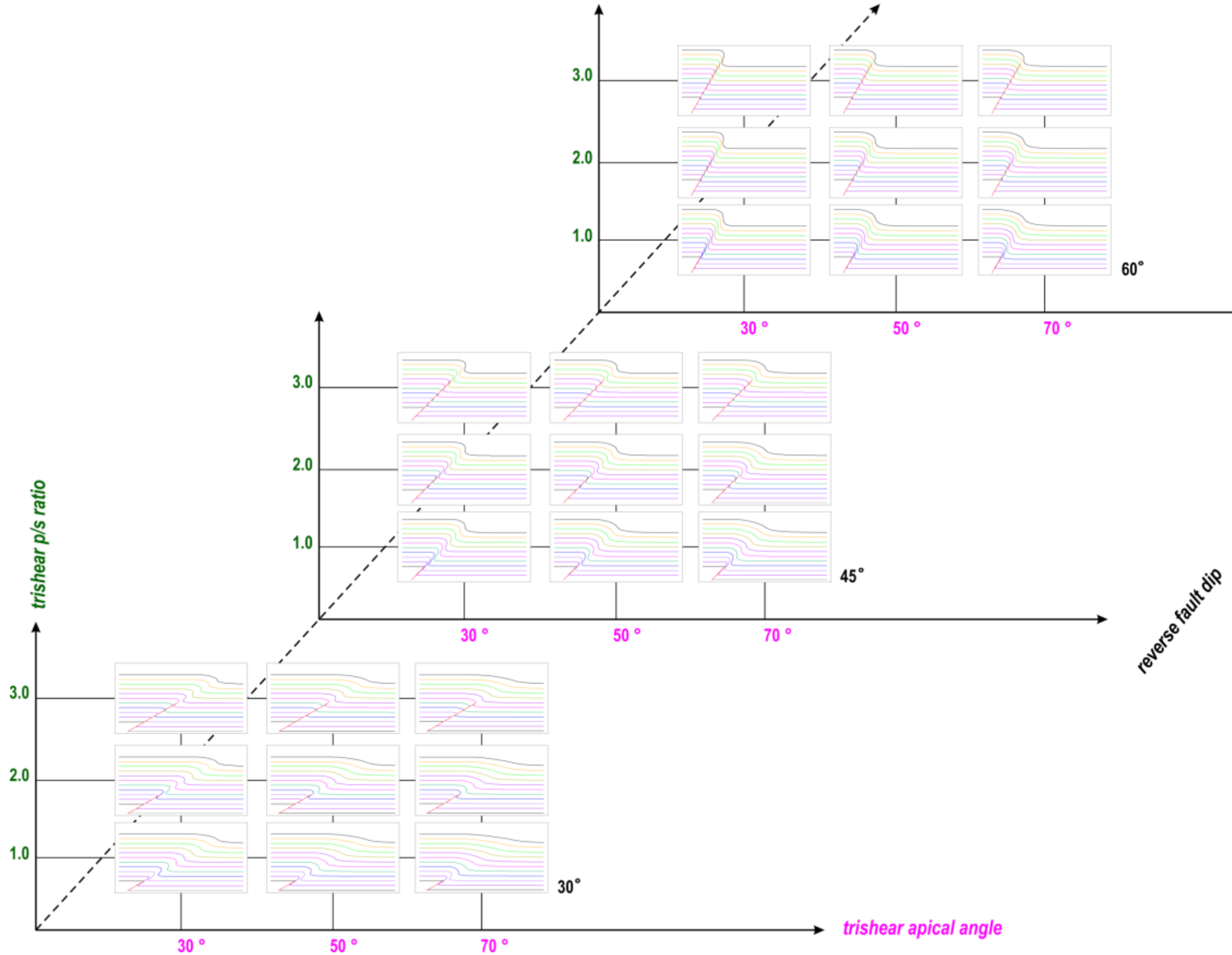

Figure 3.3 Three-dimensional parameter space with corresponding trishear models. The three axes represent the trishear p/s ratio, the trishear apical angle and the reverse fault dip, respectively.

Many natural structures have been explained by the application of trishear algorithm (e.g., Hardy and Ford, 1997; Allmendinger, 1998; Champion et al., 2001; Allmendinger et al., 2004; Cardozo, 2005; Cardozo et al., 2005; Gold et al., 2006; Lin et al., 2007; Cardozo and Aanonsen, 2009). Thirteen published examples of trishear are characterised according to their trishear parameters. The thirteen natural trishear examples are plotted in the parameter space according to their best-fit parameters (Figure 3.4). Two clusters of the natural trishear examples are observed, although there are several examples located outside of the clusters. The two clusters are best described by two sets of trishear parameters: (i) p/s ratios of 2-3, apical angle of 30°-35°, fault dip of ~30° and (ii) p/s ratios of 2-3, apical angle of 70°-75°, fault dip of ~30°. These findings can be used to estimate the best-fit trishear parameters when applying trishear algorithm to natural structures. As it is also important to highlight the relatively small sample set, more natural trishear examples need to be added in this parameter space in the future to define more reliable clusters. As noted in previous studies (Hardy and Finch, 2007; Loveless et al., 2011; Roche et al., 2012), competent packages are likely to develop steep faults while incompetent packages can develop shallow or even bedding-parallel faults. In the parameter space, the trishear models associated with high angle reverse faults, which are not well-described by the clusters, may correspond to the steep faults developed in competent packages.

Table 3.1 A cluster of natural trishear examples in published studies and their corresponding best-fit parameters.

Ref No.	Structure names	Basement-involved	p/s ratio	apical angle	fault dip	Scale, fault slip or stratigraphy	Example Sources
1	Turner Valley, Rocky Mountain	No	2.0+	37	25	Scale: 12km*30km (section width*depth); fault slip: 10km;	Hardy and Ford (1997)
2	Tejerina Fault, Spain	No	3.0+	35	30	Scale: 0.8km*1.2km; fault slip: 250m; stratigraphy: conglomerates with thin shales;	Hardy and Ford (1997)
3	Broad Haven, Pembrokeshire	No	3.0+	35	24	Scale: 6m*10m; fault slip: 2m;	Hardy and Ford (1997)
4	Hudson Valley, New York	No	2.5	30-35	36	Scale: 2km*3km; fault slip: 0.3km;	Allmendinger (1998)
5	Rangely anticline, W US	No	2.3	76	38	Scale: 6km*12km; fault slip: 4.2km;	Allmendinger (1998)
6	Reelfoot Fault, Proctor, US	Yes	0.9	36	80	Scale: 0.5km*0.8km; fault slip: 52m;	Champion et al. (2001)
7	Filo Morado structure, W Neuquen basin	No	1.9	35	30-40	Scale: 4km*10km; fault slip: 8.7km; stratigraphy: thick units (evaporates & shales)	Allmendinger et al. (2004)
8	Waterpocket anticline, S Utah	No	2.25	105	35	Scale: 5km*10km; fault slip:3.8km;	Cardozo (2005)
9	Rip Van Winkle anticline, New York	No	1.5	90	25	Scale: 5km*8km; fault slip:43m; stratigraphy: wackstone, packstone and grainstone;	Cardozo et al. (2005)
10	Dalong fault, Gansu, China	Yes	1.5	30	50	Scale: 5km*10km; fault slip:669m; stratigraphy: basement + cover (terrestrial clastic sediments);	Gold et al. (2006)
11	Chelungpu fault, Taiwan	No	2.5	80	35	Scale: 5m*40m; fault slip: 6m; stratigraphy: clay, silt clay with sand;	Lin et al. (2007)
12	Hudson Valley, New York	No	2.4	36	35	Scale: 2km*3km; fault slip: 0.3km;	Cardozo and Aanonsen (2009)
13	Santa Fe Springs anticline, Los Angeles basin	No	2.52	1	29	Scale: 7km*12km; fault slip:6.7km;	Cardozo and Aanonsen (2009)

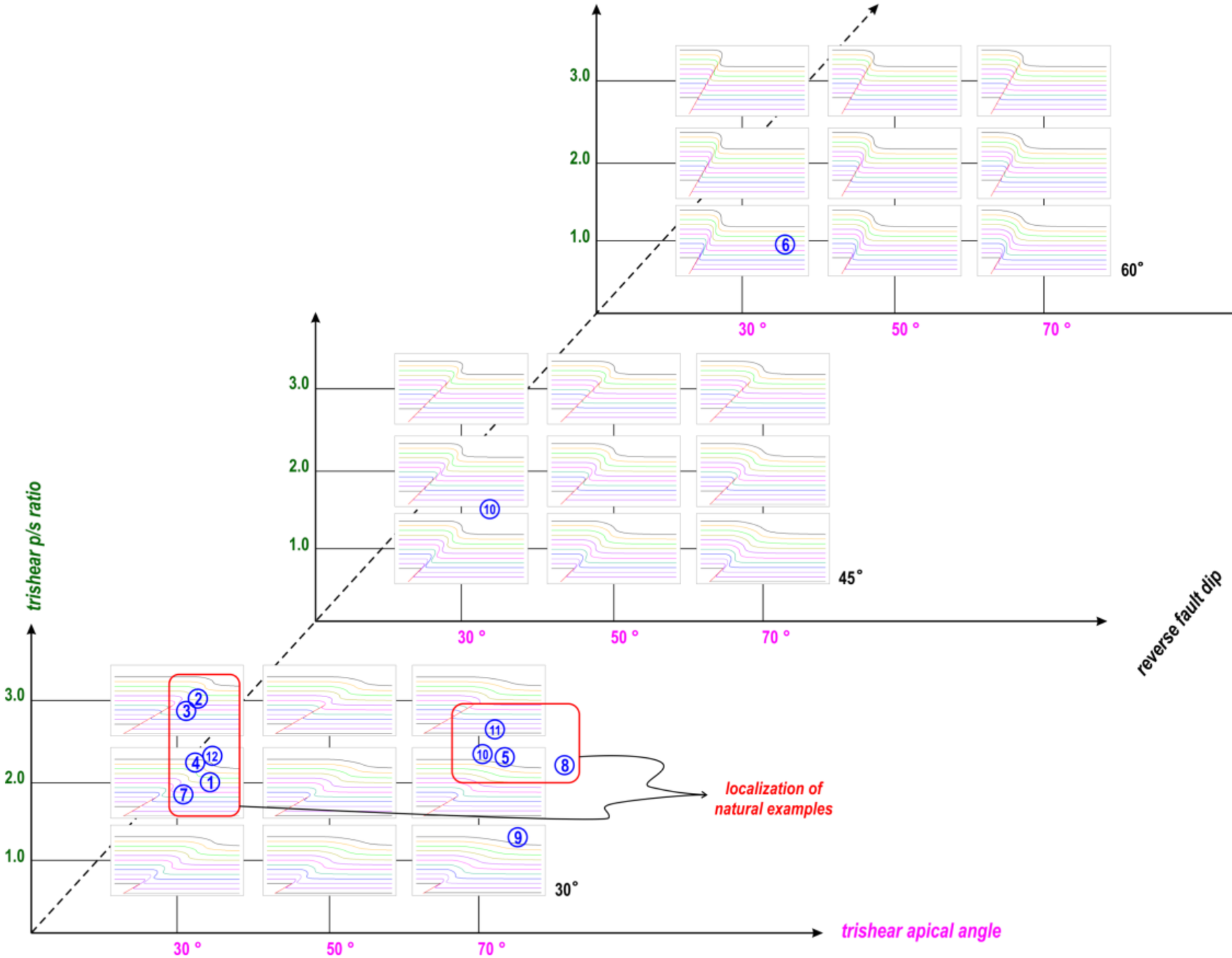

Figure 3.4 Clusters of natural trishear examples in the 3D parameter space. In the parameter space, 13 natural examples are plotted in and two clusters are observed. The clusters suggest that the most applicable trishear p/s ratio is 2-3 and the trishear apical angle varies from 30° to 100°. The majority of these natural trishear examples show shallow fault dips of 25°-45°.

3.3. Dynamic Space of Trishear Models

In the previous section, the clustering of natural examples in the parameter space was considered. However, it is important to consider how the temporal evolution impacts on the resulting geometry. To illustrate this temporal evolution the **deformation stage R_i** is defined for a reference horizon by the following equation:

$$\mathrm{R}_i = \mathrm{h}/h_i \qquad \textbf{(Equation 3.1)}$$

In the above equation, h is the hanging wall uplift and h_i is the depth from hanging wall to the fault tip (Figure 3.2).

However, the deformation stage parameter R_i is not unique within a trishear model, but is variable for different horizons at different levels in the structure. Therefore, the R_i value depends on the selection of the reference horizon used for calculation. In Figure 3.5, a trishear model (left) with the parameters p/s ratio of 2.5, fault dip of 30° and apical angle of 50° is used to illustrate the impact of the selection of the reference horizon. The R_i values are calculated for the horizons that have not been propagated through by the underlying fault. The diagram (right) suggests a decreasing R_i value from h_8 to h_1 upward through the model.

One of the clustered points on the parameter space (p/s ratio of 2.5) is taken to consider how varying trishear apical angle (30°, 50°, 70° and 100°) and reverse fault dip (30° and 45°) alter the resultant geometry. A three-dimensional dynamic space is generated here, with two horizontal axes representing the trishear apical angle and the reverse fault dip, and the vertical axis representing the **deformation stage R_i** (Figure 3.6). Given the variability of the R_i value for different horizons, here the top horizon is selected as the reference for the calculation. In the dynamic space, three R_i values are set, which are 0.2, 0.5 and 0.8.

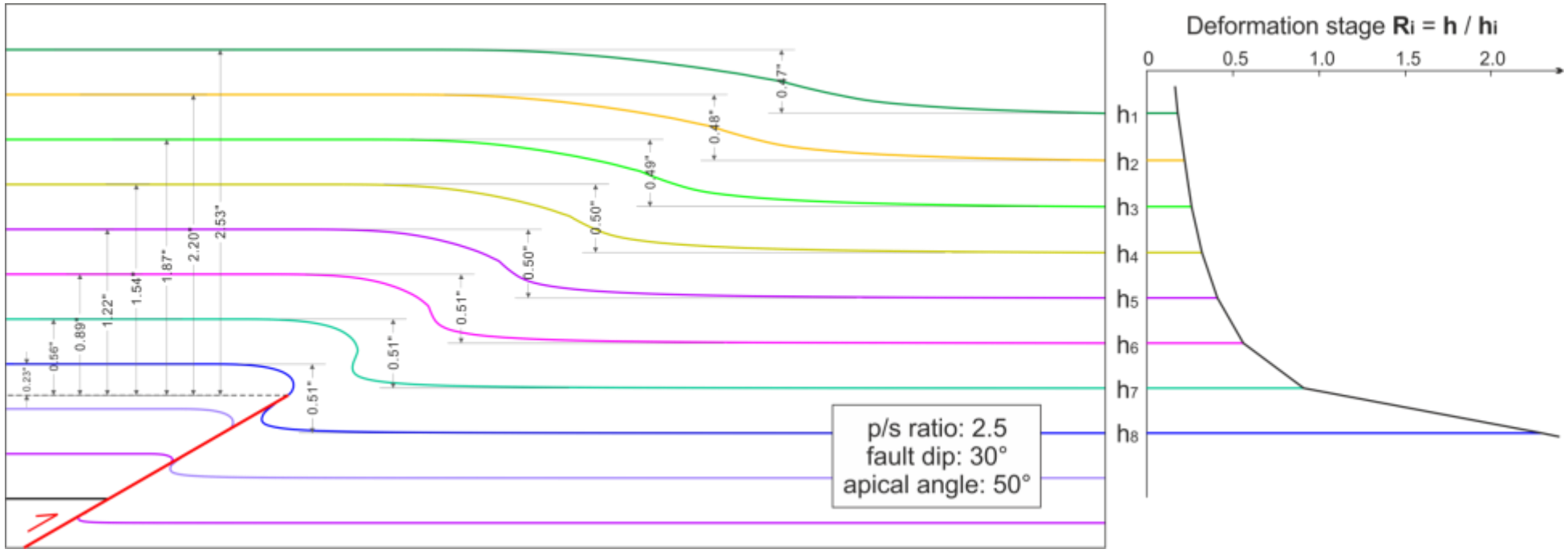

Figure 3.5 Diagram delineating the impact of the selection of the reference level, i.e., the horizon used to calculate the deformation stage $\boldsymbol{R_i}$. Here a trishear model (left) with the parameters p/s ratio of 2.5, fault dip of 30° and apical angle of 50° is selected, in which the $\boldsymbol{R_i}$ of the horizons that have not been propagated through by the underlying fault are calculated. The deformation stage $\boldsymbol{R_i}$ is not unique for a trishear model, but is variable for different horizons. The right diagram suggests a decreasing $\boldsymbol{R_i}$ value from h8 to h1 upward through the model.

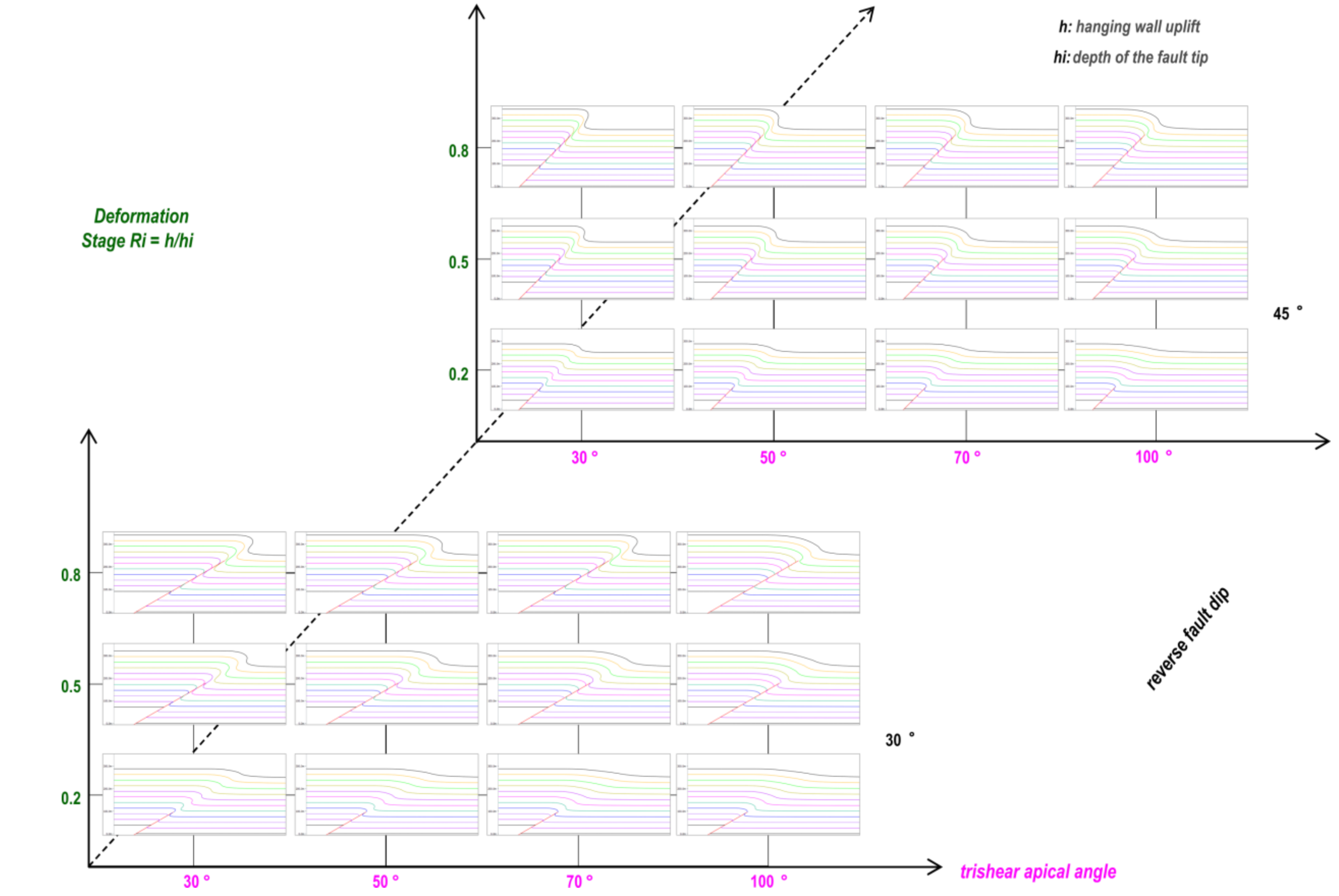

Figure 3.6 Dynamic space of trishear models with suggested parameters from the clusters of natural trishear examples.

The parameter space and dynamic space of trishear models introduced above provide a platform for the application of trishear algorithms to natural structures. Although it is still difficult to identify unique solutions for the natural structures because of the significant degrees of freedom available with the trishear parameters, the range of the parameters can be narrowed to estimate the temporal evolution of the structure by using the parameter space and dynamic space. For example, with a natural structure, by comparing the first-order structural geometry with the trishear models in the parameter space, the range of best-fit parameters for this structure can be determined. With the best-fit parameters suggested by the parameter space, the deformation stage can be identified by comparing the hanging wall geometry of the natural structures with the trishear forward models in the dynamic space.

3.4. Strain Quantification Associated with Trishear Algorithm

As the deformation associated with the trishear algorithm is always constrained within the triangle zone in front of the fault tip, it is possible to calculate the strain of the folded beds, which is the ratio of the hanging wall uplift ($\boldsymbol{h}$) versus the width of the folded beds ($\boldsymbol{w}$). Figure 3.7a delineates the trigonometric relationship of the key variables, and hereby the **strain** $\boldsymbol{e}$ is defined as Equation 3.2:

$$\boldsymbol{e = h/w} \qquad \textbf{(Equation 3.2)}$$

As

$$\frac{h}{w} = \frac{l_{AB}}{l_{AC}} = \frac{l_{AB}}{l_{AD} - l_{CD}} = \frac{l_{AB}}{l_{BF} - l_{CD}}$$

$$= \frac{l_{AB}}{(l_{DE} - l_{AB}) \times \tan(\pi/2 - \alpha + \theta/2) - l_{DE} \times \tan(\pi/2 - \alpha - \theta/2)}$$

$$= \frac{h}{(h_i - h) \times \cot(\alpha - \theta/2) - h_i \times \cot(\alpha + \theta/2)}$$

$$= \frac{h/h_i}{(1 - h/h_i) \times \cot(\alpha - \theta/2) - \cot(\alpha + \theta/2)}$$

$$= \frac{\boldsymbol{R_i}}{(1 - \boldsymbol{R_i}) \times \cot(\boldsymbol{\alpha} - \boldsymbol{\theta}/2) - \cot(\boldsymbol{\alpha} + \boldsymbol{\theta}/2)}$$

thus,

$$\boldsymbol{e = R_i/[(1 - R_i) \times \cot(\alpha - \theta/2) - \cot(\alpha + \theta/2)]} \qquad \textbf{(Equation 3.3)}$$

In Equation 3.3, the four involved variables are the **strain** $\boldsymbol{e}$, the **deformation stage** $\boldsymbol{R_i}$, the **fault dip** $\boldsymbol{\alpha}$ and the **apical angle** $\boldsymbol{\theta}$. In order to avoid the variability of the $\boldsymbol{R_i}$ value for different reference horizons (see Figure 3.5), a trishear model with only one single layer is selected. The equation demonstrates that the strain increases when the deformation progresses (i.e., increasing deformation stage). Qualitatively, with a fixed deformation stage $\boldsymbol{R_i}$ (e.g., $\boldsymbol{R_i}$ = 0.5), faults with steep dip or narrow apical angle form folds with high strain (Figure 3.7b) earlier, which coincides to the above concluded effects of parameters on the resulting structural geometry. With a given natural structure, the strain $\boldsymbol{e}$ can be calculated by measuring the hanging wall uplift and width of the folded beds in the monocline. Then the corresponding plots with a fixed strain $\boldsymbol{e}$ can be created (e.g., $\boldsymbol{e}$ = 0.5 in Figure 3.7c). If the subsurface data provided possible range of deformation stage $\boldsymbol{R_i}$ and fault dip $\boldsymbol{\alpha}$, then the apical angle $\boldsymbol{\theta}$ can be estimated from the plots. Although it is still difficult to apply the equations to identify the unique solutions for natural structures, these equations and plots can narrow the range of the variables, particularly when the surface and subsurface data provide better constraints to the variables.

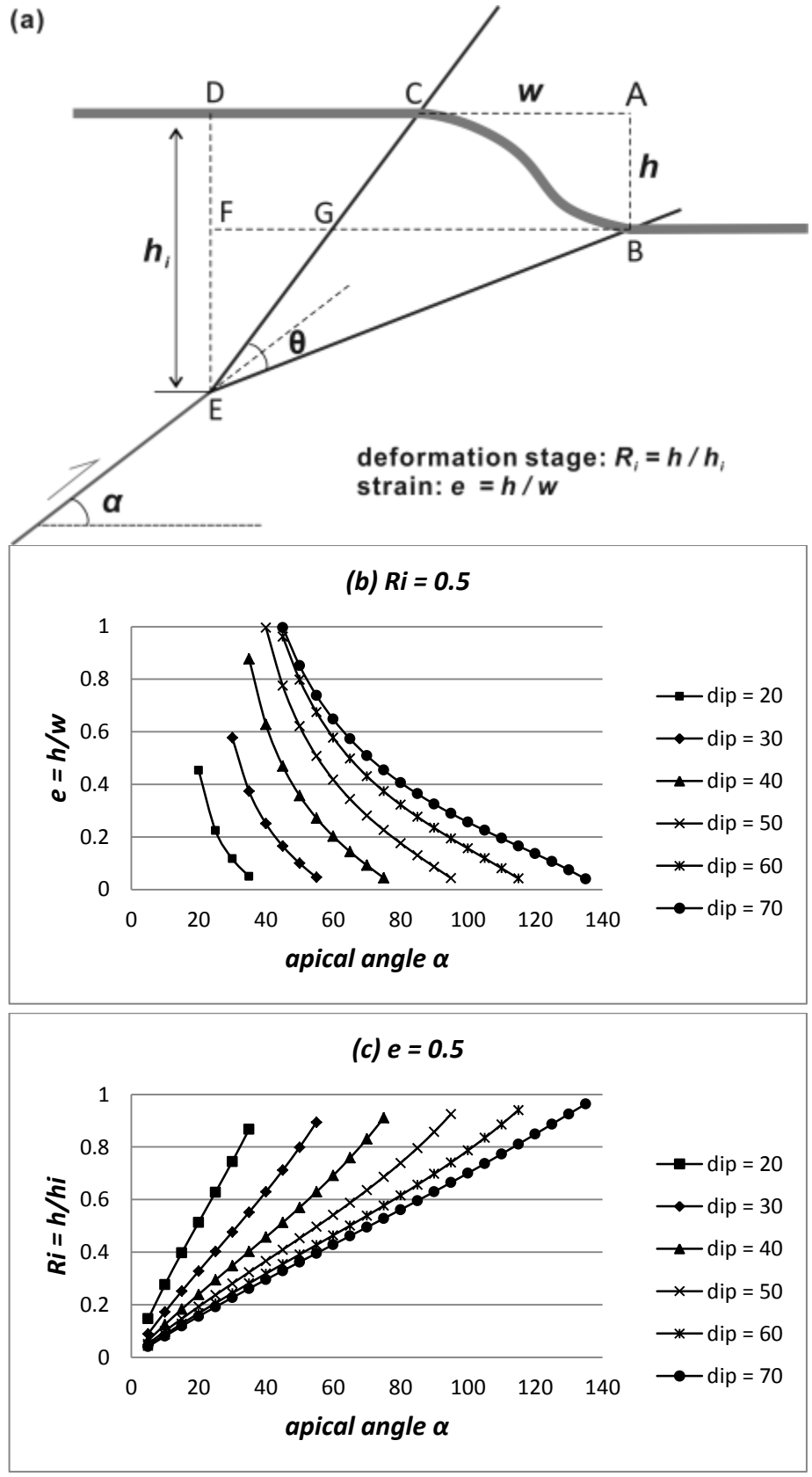

Figure 3.7 Quantification of strain (ratio of hanging wall uplift versus folded bed width) associated with trishear algorithm. The figure (a) delineates the trigonometric relationship among the variables, while two plots are generated with deformation stage $\boldsymbol{R_i}$ = 0.5 in (b) and strain $\boldsymbol{e}$ = 0.5 in (c).

3.5. Complex Trishear Geometry

The above parameter space and dynamic space only show trishear models that are applicable in simple natural structures with one constant-dipping fault and where displacement is not substantial enough to cause overturning. However, in many natural examples, the structures are related to either a more complex faults or a set of related faults (e.g., Allmendinger, 1998; Allmendinger et al., 2004). The complexity of the fault systems obviously inhibits the application of trishear algorithm to natural structures and results in a large population of possible scenarios. Therefore, here the key additional factors that may influence the resultant geometry and promote increased complexity of trishear models are summarized. The three identified factors are: the change in fault dip during propagation, multiple faults and pre-existing faults. Schematic trishear models are created integrating these contributing factors (Figure 3.8 and Figure 3.9). It is anticipated that the generated models are useful for predicting subsurface structures based on high-resolution fieldwork data (surface data, e.g., fault/stratum dips, layer thickness variation, second-order structures), particularly when the subsurface data is insufficient in the study area. The key controls of each of these factors are reviewed individually below.

3.5.1. Fault-Dip Change

In many multi-layer sequences, fault dip of any one layer may be controlled by the thickness or competence of the layer (e.g., Hardy and Finch, 2007; Loveless et al., 2011; Roche et al., 2012) and therefore may change upward through the stratigraphy. In the scenario where there are basement-involved structures, the fault may initially be steep in the competent basement but will become shallower as it propagates through the overlying sedimentary cover that is relatively incompetent (Hardy and Finch, 2007). In contrast, in the scenario where there are only thin-skinned structures, the fault usually initiates parallel to the horizons and then propagates upward to cut through the upper layers (Hardy and Finch, 2007). To represent these two scenarios, two series of trishear forward models are created (Figure 3.8), with the trishear algorithm applied on an upward-steepening reverse fault in Figure 3.8a and an upward-shallowing reverse fault in Figure 3.8b, respectively.

The upward-steepening reverse fault modelled in Figure 3.8(a1-3) initiates with a gentle dip angle of 20° and the stepwise increment of fault-dip is 10° until it reaches 70°, while the upward-shallowing reverse fault modelled in Figure 3.8(b1-3) initiates with a steep dip angle of 70° and the upward stepwise decrement of fault-dip is 10° until it decreases to 20°. For both scenarios, the p/s ratio is set as 2.5 (suggested by the clusters of natural examples in the parameter space), while the trishear apical angle is set as 50° (a medium value of the apical angle range suggested by the clusters of natural examples in the parameter space).

The upward-steepening and upward-shallowing reverse faults form very different hanging wall and footwall geometries. The hanging walls experience more deformation than the footwalls in both scenarios. The hanging walls are uplifted during the deformation while the footwalls stay in the original position. However, the hanging wall and footwall geometries are different in the two series of models. The upward-steepening reverse fault forms an anticline in the hanging wall, with a gentle backlimb and overturned forelimb; while the upward-shallowing reverse fault forms a monocline in the hanging wall and the hanging wall shows downward steepening dips towards the triangle deformation zone. For the footwall geometry, the footwall adjacent to the fault trace shows more thickening in the model of upward-steepening fault than that in the model of upward-shallowing fault.

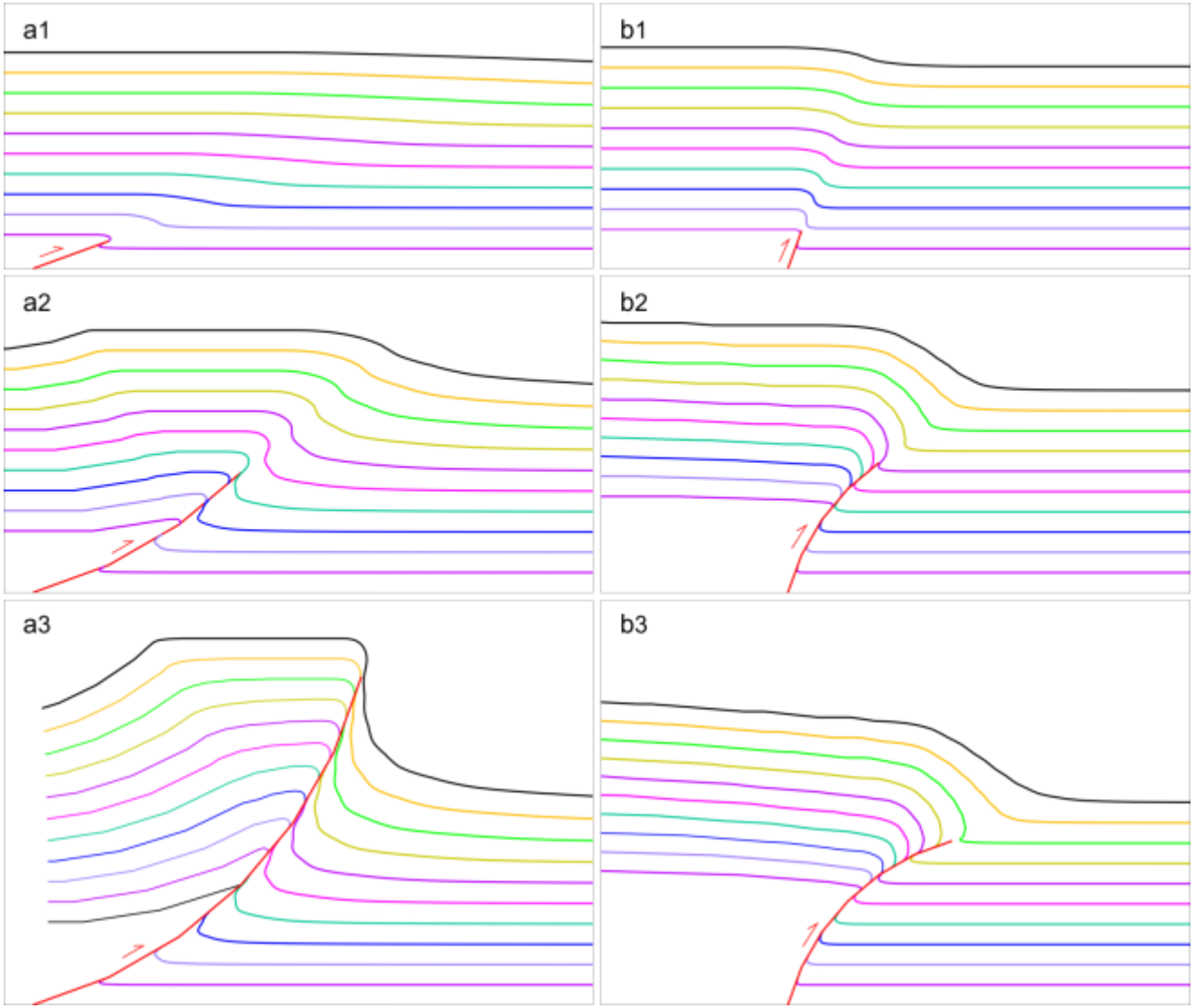

Figure 3.8 (a1-3): Trishear forward models of an upward-shallowing reverse fault. The fault dip changes from 20° to 70° upwards with a stepwise increment of 10°. (b1-3): Trishear forward models of an upward-shallowing reverse fault. The fault dip changes from 70° to 20° upwards with a stepwise decrement of 10°.

In previous studies, according to the level of basement involvement in the deformation, two categories of structures are observed in compressional systems, which are thin-skin fold-and-thrust belts and thick-skin/basement-involved belts. In thin-skin fold-and-thrust belts, the deformation concentrates primarily in the sedimentary cover rather than the basement, e.g., Canadian Rocky Mountain-style foreland fold-and-thrust belts (Bally et al., 1966; Price, 1981; Barclay and Smith, 1992). While in thick-skin/basement-involved belts, the basement rocks are shortened along steep dipping reverse faults, although the rocks are not transported over long distances horizontally (Coward, 1983), e.g., the Laramide uplifts (Schmidt et al., 1993). In Figure 3.8, geometrically, it is likely that the basement is more involved in the trishear model of an upward-shallowing reverse fault (Figure 3.8b) and less involved in the trishear model of the upward-shallowing reverse fault (Figure 3.8a). Therefore, it is assumed that the upward-steepening reverse fault tend to develop in thin-skin deformation while the upward-shallowing reverse fault is likely to develop in thick-skin deformation. However, the thin-skin style and thick-skin style can coexist in a single structure on some scales, as the steep faults that penetrate the basement rocks can change to sub-horizontal when they reach sedimentary cover and then help the horizontal initiation of the thin-skin detachments (Hayward and Graham, 1989). This assumption is supported by the results of physical experiments (McClay and Whitehouse, 2004; Bose et al., 2009).

3.5.2. Pre-Existing Fault(s)

In natural structures, it is common for a single structure to contain a number of discrete faults developed asynchronously (Allmendinger et al., 2004). The reactivation of the pre-existing faults may form complex structural geometries together with the younger faults, which increases the complexity of identifying the subsurface structures based on the surface data. The examples permitting high geometric complexity by allowing the inclusion of multiple faults in a section are demonstrated by Allmendinger et al. (2004). However, it is also vital to understand the surface geometrical control on the complex fault deformation in subsurface. Therefore, it is worth assessing the surface compatibility of high-level subsurface structures by applying the trishear algorithm on multiple reverse faults.

Figure 3.9 shows the schematic evolution of the trishear models in which deeper pre-existing faults are present beneath the upper reverse faults. As discussed above, the reverse faults in these models can be upward-steepening for thin-skinned structures or upward-shallowing for thick-skinned/basement-involved structures. The sets (a) and (b) apply upward-steepening reverse faults in the trishear modelling (Figure 3.9a,b), while the sets (c) and (d) apply upward-shallowing reverse faults (Figure 3.9c,d). Both the same and opposite thrusting direction are modelled (same direction in Figure 3.9a,c and opposite direction in Figure 3.9b,d). The trishear models in Figure 3.9a,b show similar geometries to the anticlines formed in Sub-Andean belt of southern Bolivia (Belotti et al., 1995) where the middle weak layer can decouple the shallow depth strain from the deep subsurface (e.g., Willingshofer and Sokoutis, 2009; Burliga et al., 2012). Figure 3.9c&d delineate the highly basement-involved structures with upward-shallowing faults when propagating into the sedimentary cover, which is commonly observed in many studies in thick-skinned structures (e.g., Butler et al., 2004; Bose et al., 2009). Particularly, the Figure 3.9c shows an analogue model that may represent the bifurcation of an early single reverse fault or the splay faults coming off from a single reverse fault, to form a triangular strain confined by the multiple faults. In nature, a single reverse fault may initiate within a propagation fold and subsequently bifurcate or form splays when propagating through the upper sedimentary cover, e.g., the Absaroka thrust sheet case (Lamerson, 1982; Mitra, 1990). In this scenario, the earlier formed fold geometry may be modified during the subsequent fault bifurcation or generation of splay faults.

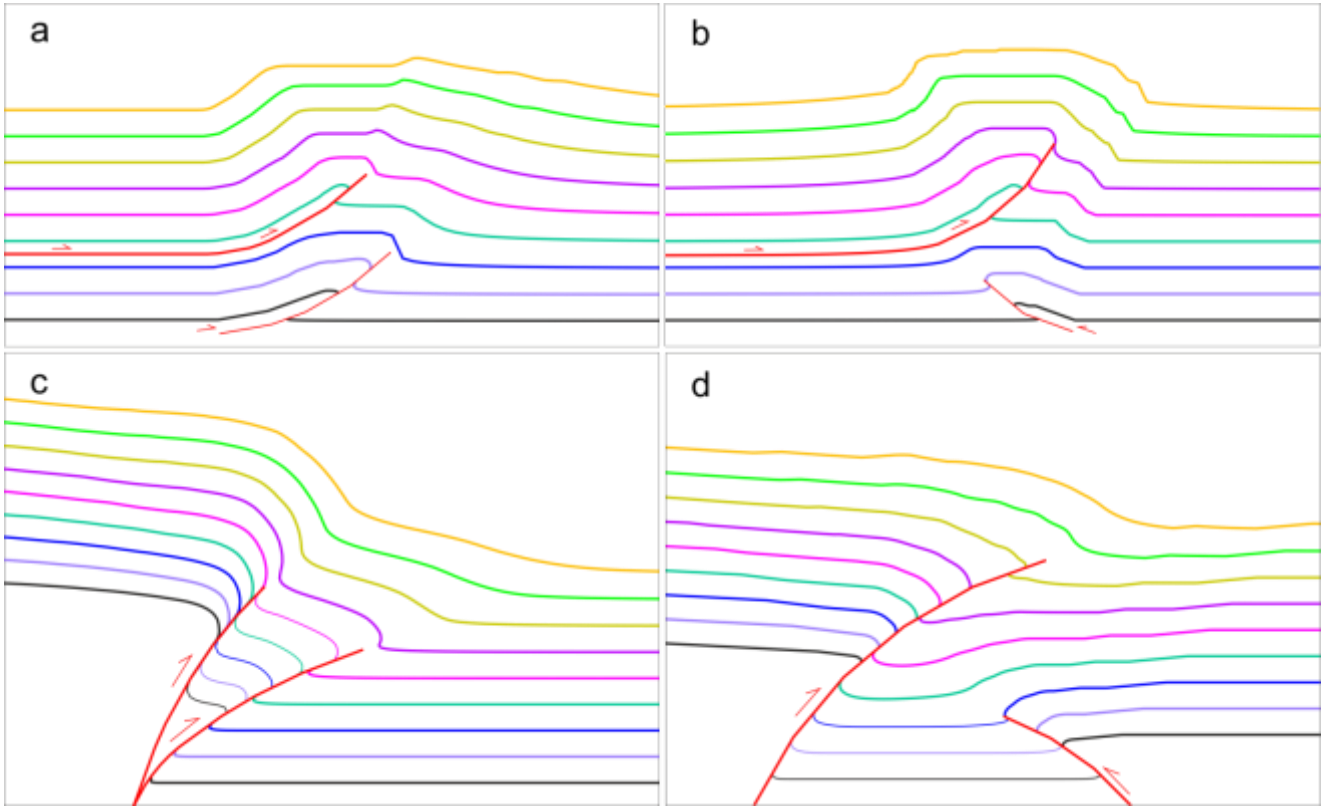

Figure 3.9 Trishear forward models of reverse faults affected by pre-existing faults. (a & b) upward-steepening reverse faults developed above deeper pre-existing reverse faults. (c & d) upward-shallowing reverse faults developed above deeper pre-existing reverse faults. Pre-existing faults with the same or opposite thrusting directions are all simulated.

The models (a) and (b) all form anticlines in the surface. However, different subsidiary structures (i.e., minor anticlines and synclines in the footwall) are developed in (a) and (b). For example, the subsurface minor folds in model (a) has wider wavelength than that in model (b). For the upward-shallowing reverse faults, the models (c) and (d) all form monoclines in the surface, but the hanging wall has a higher uplift in model (c) than in model (d). Moreover, in model (d), minor synclines are developed at both ends of the central common footwall, resulting in a syncline-like geometry. Different combinations of upper reverse faults and lower pre-existing faults can form very different structural styles. However, as the surface geometry is a reflection of subsurface structures, there are still some features that can be used to illustrate the overall structure and predict the subsurface structures. For example, the symmetry, wavelength and amplitude of the folds depend on the subsurface structures and therefore these features can be used to predict the subsurface structures. According to the simulated models in Figure 3.9, the following inferences are drawn:

(i). Reverse faults are implied to be upward-steepening if the fold observed in the surface is an anticline and upward-shallowing if the surface fold is a monocline.

(ii). For upward-steepening reverse faults, asymmetric anticlines suggest reverse faults with the same thrusting direction, while relative symmetric anticlines suggest opposite-directing reverse faults.

(iii). For upward-shallowing reverse faults, opposite-directing reverse faults result in smaller hanging wall uplift.

3.6. Application to the Lenghu5 Structure, Qaidam Basin

The applicability of the trishear algorithms to natural structures in complex thrust system is now discussed. A natural example from the Lenghu5 structure in Qaidam basin of the Northern Tibetan Plateau (e.g., Yin et al., 2008a; Yin et al., 2008b) is selected to test the applicability of trishear modelling. The Figure 3.10a-c delineates the workflow used to apply the trishear algorithm to the Lenghu5 structure. The surface data (Figure 3.10a) suggests that the underlying reverse fault accounts for the development of the anti-

cline in the SW hanging wall. The structures adjacent to the reverse fault cannot be well-described by the kink band model, therefore, here the trishear algorithm is applied to interpret the Lenghu5 structure. In order to apply the trishear algorithm to understand the Lenghu5 structure, the appropriate simplification is conducted to obtain the primary structural geometry (Figure 3.10b). The primary structure is also rotated clockwise to make the footwall horizontal. By comparing the geometry of the blue layer with the trishear models in the parameter space (Figure 3.3), it is suggested that the trishear model in the space with the parameters of p/s ratio of 2.0, reverse fault dip of 45°, and apical angle of 50° shows the most similar geometry with the simplified Lenghu5 structure (Figure 3.10c). The strain $\boldsymbol{e}$ of the best-fit trishear model (Figure 3.10c) can also be measured to compare with that of the Lenghu5 structure. The best-fit trishear model in Figure 3.10c presents strain $\boldsymbol{e}$=0.99, which shows a high similarity to the strain $\boldsymbol{e}$=0.92 presented in the Lenghu5 structure (Figure 3.10b).

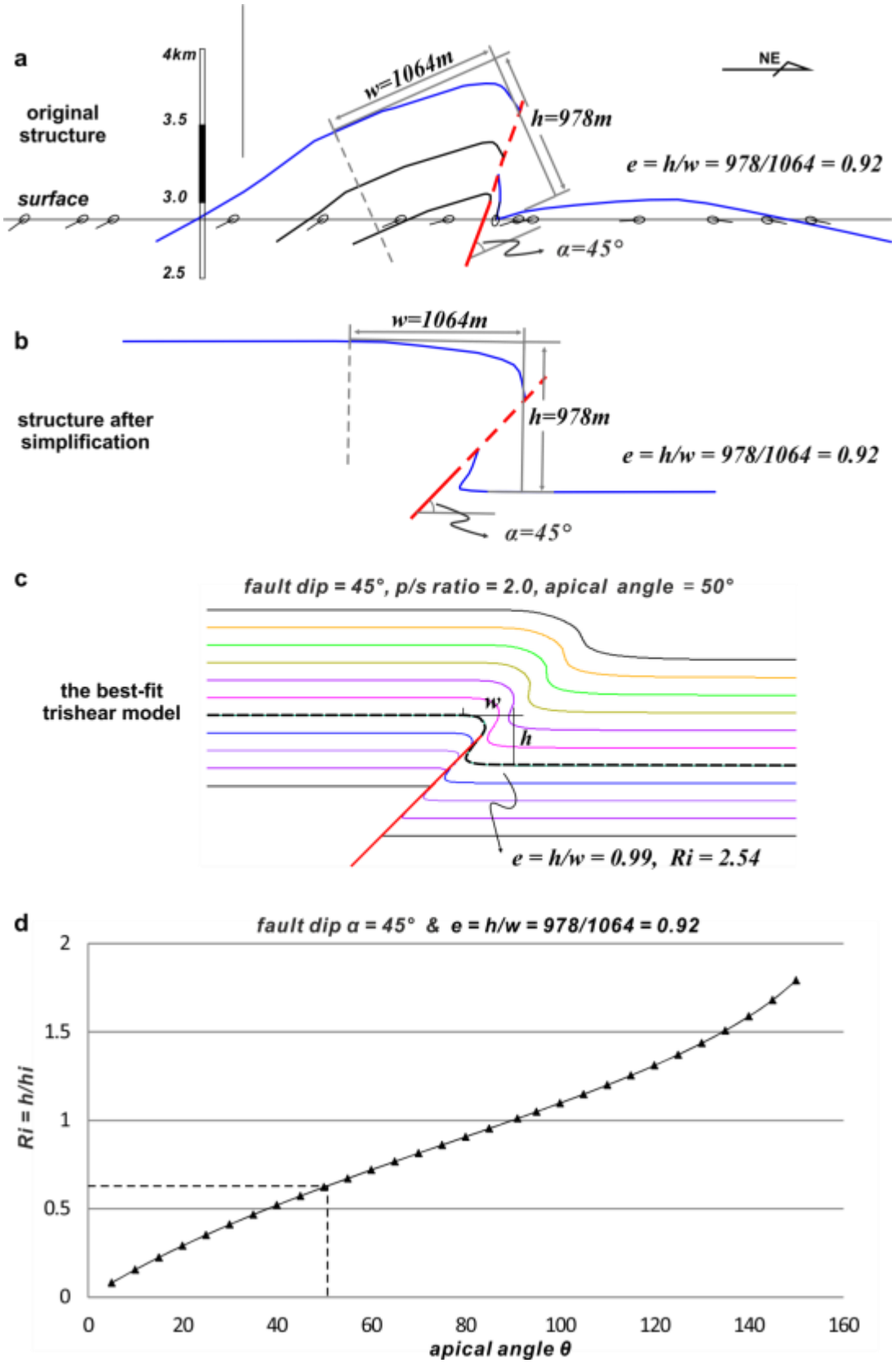

Figure 3.10 The workflow of applying the trishear algorithm to the Lenghu5 structure, Qaidam Basin, Northern Tibetan Plateau.

However, in the plots shown in **Figure 3.10**d created by applying the Equation 3.3 with fault dip $\boldsymbol{\alpha}$=45° and strain $\boldsymbol{e}$=0.92 (measured in Figure 3.10b), the deformation stage $\boldsymbol{R_i}$=~0.7 does not match the measured deformation stage $\boldsymbol{R_i}$=2.54 in the best-fit trishear model (Figure 3.10c). The mismatch of the deformation stage may be caused by the fault complexity that has not been considered above. As shown in the seismic section (Figure 3.11a), the Lenghu5 anticline is mainly controlled by the underlying reverse faults F_1, F_2 and F_3. Two anticlines are observed in this structure: the surface anticline above F_1 and deeper subsurface anticline beneath F_1. The upward decreasing displacement of F_1 suggests a trishear algorithm is applicable in this structure. Moreover, reverse faults F_1 and F_2 all present upward-steepening shapes, which is highly comparable with the complex trishear models shown in Figure 3.9b. Therefore, the trishear algorithm forward modelling is applied to simulate the structural evolution of the Lenghu5 structure by allowing multiple curved faults in a single section. Figure 3.11b-e depicts the progressive development models of the Lenghu5 structure simulated using 2D Move (Midland Valley).

The parameters suggested by the best-fit trishear model in the parameter space are used in the trishear forward modelling (apical angle of 50° and p/s ratio of 2.0, suggested in Figure 3.10c). The comparison between the fault displacement and the fault tip propagation of F_2 also suggests a trishear p/s ratio of 2.0. In order to simulate the upward steepening reverse faults F_1 and F_2, the interpreted F_1 and F_2 are used as templates to decide the stepwise values of upward steepening angles. In Figure 3.11b, normal fault F_2 was developed to form a half-graben in the J_r sediments followed by deposition of post-extension sequence from E_{1+2} to N_{2-1}; in Figure 3.11c-d, the geological environment changed to be compressional which results in the inversion of F_2 and the development of the reverse fault F_1; after uplift and erosion to present, Figure 3.11e presents a good match to the geometry of the Lenghu5 structure. The models in Figure 3.11b-e constrain the structural evolution of the Lenghu5 structure. Furthermore, the forward trishear models can also predict the future geometry of the Lenghu5 structure if strain had continued.

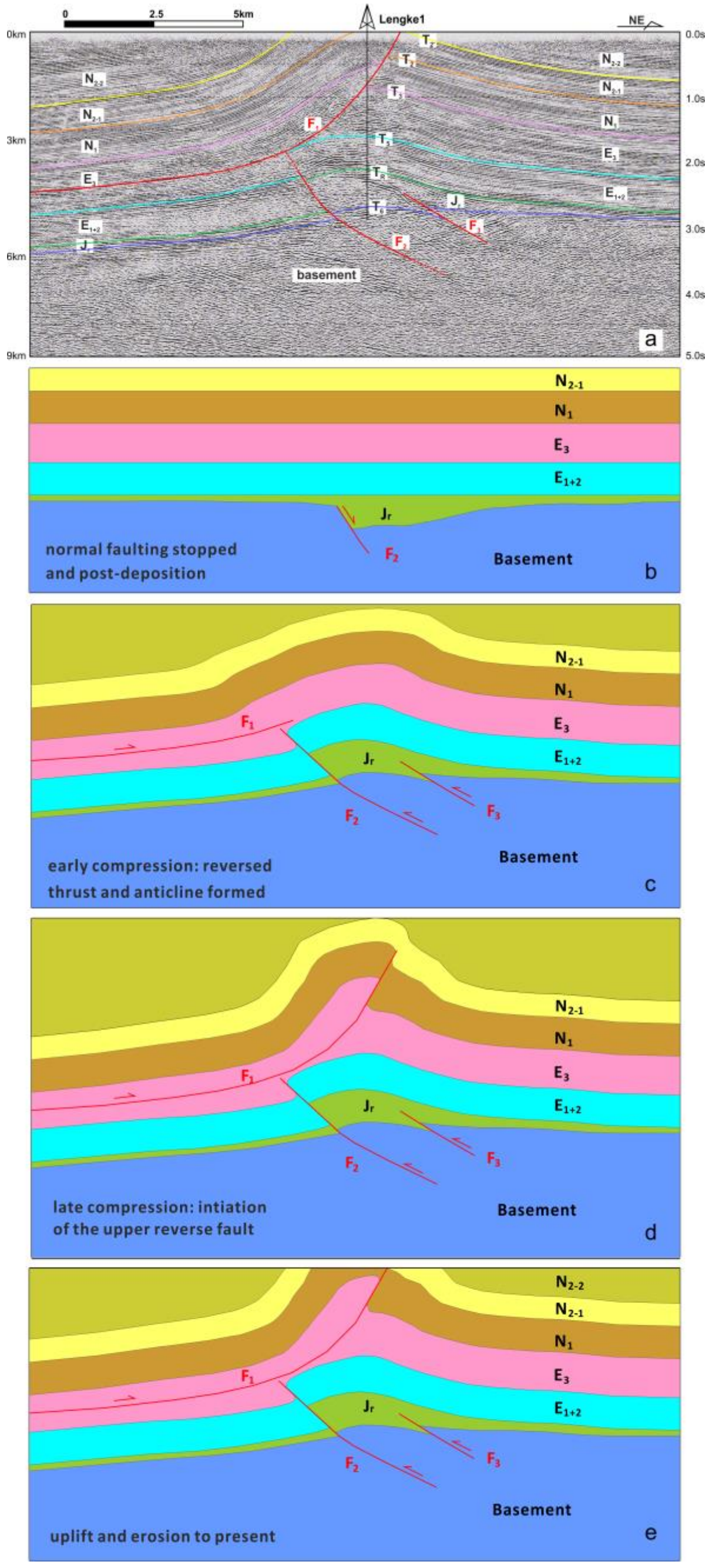

Figure 3.11 The forward trishear models depicting the structural evolution of the Lenghu5 structure by allowing multiple curved reverse faults in trishear forward modelling.

3.7. Discussion

3.7.1. Geometric Constraints of Trishear Algorithm

The trishear algorithms were proposed to understand the geometric evolution of structures which are not well-described by the kink band method (e.g., Erslev, 1991; Hardy and Ford, 1997). However, since there are three controlling parameters for the trishear algorithms, a variety of trishear geometries can be formed by varying the combination of these parameters, which inhibits the application of trishear algorithm directly to natural structures. Therefore, it is vital to identify the most likely parameters before applying trishear algorithm to natural structures. In this study, a simple parameter space is built to evaluate the effect of varying each parameter independently and to help determine the temporal evolution of the natural structures by generating the dynamic space. However, the parameter space and dynamic space are constructed based on trishear models on simple faults (constant dip during deformation) and the factors increasing the complexity of trishear models have not been completely integrated. When the reverse fault dip varies during fault slip and when multiple faults or pre-existing faults are present, the spectrum of structural geometries is much broader and the resulting structures can be more complex. Therefore, some appropriate simplification of natural structures is needed before applying the parameter space and dynamic space. For example, when applying trishear algorithms to natural structures: firstly, the first-order geometry can be used as initial constraints to compare with the trishear models in the parameter space; secondly, the best-fit trishear parameters can be constrained by using the parameter space; and finally, the best-fit trishear parameters can be adopted in the trishear modelling on the required combination of curved reverse faults, multiple faults and pre-existing faults. The previously simplified structural complexity is reproduced in the final trishear models to compare with the original natural structures, which can help test the validity of the application of the trishear algorithm to the natural structures.

As there are only a few natural trishear examples plotted in the parameter space at present, the clusters of natural structures identified in the parameter space might not cover all the possible structural geometries. In Figure

3.4, the clusters of plotted natural examples are concentrated in the space with shallow reverse fault dip. This is because most of these examples are from thin-skin structures, e.g., foreland fold-and-thrust belts in Canadian Rocky Mountain (Bally et al., 1966; Price, 1981; Barclay and Smith, 1992) and Turner Valley anticline in Alberta Foothills (Gallup, 1951; Mitra, 1990). In these structures with thin-skin deformation, the thrusting involves only the sedimentary cover whereas the basement is unaffected in the deformation (Poblet and Lisle, 2011). However, in the trishear parameter space, there are also a series of trishear models with high angle reverse faults. Although the clusters of reported natural examples do not cover these models, the high angle trishear models are very likely to be basement-involved and can be related to thick-skin structural inversion. The contractional inversion of older extensional faults has now been widely recognized in fold-and-thrust belts, for instance, in the Neuquen Basin in Argentina (Rojas et al., 1999), the Spanish Pyrenees (Muñoz, 1992), Alps (Schmid et al., 1996; Pfiffner et al., 2000), Apennine Mountains (Coward et al., 1999), Papua New Guinea (Hill, 1991; Buchanan and Warburton, 1996; Hill et al., 2004), etc. In contrast to thin-skin structures, the basement rocks of thick-skin structures (basement-involved structures) have not been transported over long horizontal distances as the steep faults penetrate the basement and lead to basement uplifts (Poblet and Lisle, 2011). However, the thin-skin fold-and-thrust belts (basement-unaffected) and thick-skin belts (basement-involved) can coexist in a single structure. The coexistence of these different structural styles might be common in many orogenic belts. For example, Hamilton (1988) found the Rocky Mountains-USA Cordillera exhibits thin-skin deformation in the interior and thick-skin deformation in the outer part; the steep faults that penetrate the basement become sub-horizontal when reaching the sedimentary cover and promote the horizontal initiation of the thin-skin detachments such as in the Alps (Hayward and Graham, 1989).

3.7.2. Influence of Stratigraphy on Trishear Algorithm

In this chapter, the parameter space and dynamic space concepts focus on the geometrical constraints of the trishear algorithm. The curved reverse faults, the multiple faults and the pre-existing faults are considered when applying trishear algorithms to natural structures. However, it needs to be rec-

ognised that lithology and mechanical strength also play a role on the trishear models, with the parameters being very different depending upon mechanical stratigraphy (Alonso and Teixell, 1992; Hardy and Ford, 1997; Hardy and Finch, 2007). It was suggested that rocks with high competency present higher trishear p/s ratios than low competent rocks, e.g., sandy units show higher trishear p/s ratios than clay-rich units (Hardy and Ford, 1997). Hardy and Finch (2007) also employed a discrete-element technique (Finch et al., 2003; Finch et al., 2004) to investigate sedimentary cover deformation in response to contractional faulting. The fault zone deformation was simulated with different settings: in the homogeneous weak cover model, a wide and open triangular zone was developed in front of the fault tip and significant thinning and thickening were observed within the triangular zone, which broadly agreed with the predictions of the trishear kinematic models (Erslev, 1991; Hardy and Ford, 1997; Allmendinger, 1998); while in the strongly heterogeneous layered models, a much narrower kink-like triangular zone was observed in front of the fault tip and layer thickness was roughly preserved within the triangular zone. In the physical modelling of Dixon (2004), the relatively homogeneous weak stratigraphy resulted in a trishear-like ductile deformation (low trishear p/s ratio) while the model with strong bedding-controlled heterogeneity is prone to form through-going reverse faults (high trishear p/s ratio). All these mechanical and physical models suggest the important role of stratigraphy and strength in the cover deformation (see also Welch et al., 2009), however, are likely to be second order controls superimposed upon the first order geometry outlined here.

3.8. Conclusion

This chapter presented a three-dimensional parameter space to evaluate the effects of different trishear parameters on the geometries of trishear models. The parameter space associated with the identified clusters of natural structures can be used to constrain the best-fit trishear parameters needed to apply trishear algorithms to natural structures. A dynamic space is then built to evaluate the deformation stage of the structures. The strain of trishear models is also quantified, with the plots providing possible solutions for interpreting natural structures. On the basis of the parameter and dynamic spaces,

fault-dip change, multiple faults and pre-existing faults, are integrated in the trishear models, to understand the possible complex structures that can form. A natural example of application was employed to verify the applicability of trishear algorithm. By applying the trishear forward modelling, an improved structural evolution of the natural structure has been revealed.

Having understood the complex geometry of the Lenghu5 structure using trishear modelling, the next chapter will demonstrate regional-scale structural analysis of the Lenghu5 structure. The regional-scale structural analysis will be primarily based on two periods of fieldwork, in which the detailed stratigraphy, transects and fault maps will be used to understand the 3D thrust fault architecture and dynamic evolution of the Lenghu5 structure.

Chapter 4
Regional Scale Structural Analysis of the Lenghu5 Structure, Qaidam Basin

4.1. Introduction

The Qaidam basin, located in the northern margin of the Tibetan Plateau, is developed in a compressional environment resulting from the collision between the Eurasian and India Plates (e.g., Xia et al., 2001; Pang et al., 2004; Yin et al., 2008b; Liu et al., 2009). The Lenghu5 structure located in the northern Qaidam basin was selected for high-resolution fieldwork. This chapter focuses on the regional-scale structural geometry and fault development based on the high-resolution fieldwork studies, in order to understand the structural geometry, the fault zone development and the dynamic evolution of the Lenghu5 structure.

The high-resolution fieldwork data, e.g., the stratigraphy and the regional structural transects, are used to study the Lenghu5 structure as the detailed deformation features are mostly under seismic resolution. Based on the stratigraphy and transects, 3D models are built to demonstrate the overall geometry of the Lenghu5 structure, particularly the lateral structural variation along the fault zone. The 3D model is then restored to reveal the 3D dynamic evolution of the fault zone. The comparison between the strain analysis and the field observation suggests a useful workflow for the prediction of the subseismic structures.

4.2. Geological Settings

The Qaidam basin shows a triangular shape, with a ~550km NE margin, a ~300km NW margin and a ~700km SW margin (Figure 4.1). The Qaidam basin, with an average elevation of ~2800m, is constrained by the Qilian Shan-Nan Shan Thrust Belt to the northeast (e.g. Burchfiel et al., 1989; Tapponnier et al., 1990; Yin et al., 2008a), the Altyn Tagh Fault to the northwest (e.g. Meyer et al., 1998; Cowgill et al., 2000; Cowgill et al., 2003;

Cowgill et al., 2004a; Cowgill et al., 2004b; Cowgill, 2007; Yin et al., 2007) and the Qimen Tagh-Eastern Kunlun Belt to the southwest (e.g. Jolivet et al., 2003; Yin et al., 2007).

The stratigraphy of the Qaidam basin is divided into three main packages, which are metamorphic basement, late Palaeozoic-Mesozoic sediments and Cenozoic sediments (e.g., Cui et al., 1995; Deng et al., 1995; Gao et al., 1995; Xia et al., 2001). Based on outcrop observations, seismic sections, boreholes, terrestrial fossils, basin-scale stratigraphic correlation, fission-track and $^{40}Ar/^{39}Ar$ dating of detrital micas (Huo, 1990; Yang et al., 1992; Song and Wang, 1993; Huang et al., 1996; Xia et al., 2001; Qiu, 2002; Sun et al., 2005; Rieser et al., 2006a; Rieser et al., 2006b), the division and time assignments of Mesozoic to Cenozoic sediments have been proposed. The sedimentological division and time assignments in Yin's research (Yin et al., 2008a; Yin et al., 2008b) are employed in this research.

In Figure 4.2, a typical NE-SW-directing cross section through central Qaidam basin delineates the present structural geometry of the Qaidam basin (modified from Yin et al., 2008b). The section presents huge thickness of Cenozoic sediments up to 16km (E_{1+2}-Q_1) and locally-distributed thin Mesozoic sediments (Jr). The central thickening of Cenozoic sediments suggests the Qaidam basin is controlled by NE-SW compression resulted from the uplift of Tibetan Plateau, which has been reported in many previous studies (e.g., Molnar and Tapponnier, 1975; Xia et al., 2001; Pang et al., 2004; Wang and Burchfiel, 2004; Wang et al., 2006b; Zhou et al., 2006; Zhu et al., 2006). The ~190km section demonstrates that the Qaidam basin forms different orders of structures: the first-order structure is a large-scale synclinorium composed of a series of tight anticlines and open synclines, with a wavelength of ~380km and amplitude of ~16km; while the second-order structures are regional scale folds/faults. Inversed faults in Mesozoic sediments and thrust faults in Jurassic-Eocene sediments indicate a complex geological history of the Qaidam basin. The growth strata, developed as the response to the fault development, are used to identify the structural deformation time. As the observed fault throws of both inversed faults and shallow thrust faults do not exceed 5km, it is believed deeper and larger thrusts are

required to build a synclinorium with this wavelength and amplitude (Yin et al., 2008b). These deeper thrusts are assumed to be related to the uplift of Qilian Shan-Nan Shan to the northeast and Qimen Tagh-Eastern Kunlun to the southwest.

According to the growth strata analysis and crosscutting relationship between the faults and horizons, the geological history of Qaidam basin can be identified. The normal faults, resulting from Mesozoic extension, led to the syn- sedimentation during the Jurassic (Jr) to form the growth strata in the hanging walls. The extension then ceased no later than the beginning of Palaeocene (E_{1+2}), as there may be erosion of the Mesozoic sediments. In the following Cenozoic compression stage, the reverse faults were developed throughout the Qaidam basin. The shallow reverse faults with maximum displacement of 5km mostly died out in E_{3-1} and E_{3-2}. Then the deep reverse faults with large displacements are developed, to make the QN thrust belt and QE belt uplift rapidly. The uplift of these two belts in the two ends of Qaidam basin resulted in the basin-scale growth strata. After E_{3-2}, the shallow reverse faults almost ceased deformation; and the deep large reverse faults remain active, maintaining the compression to form the synclinorium of Qaidam basin.

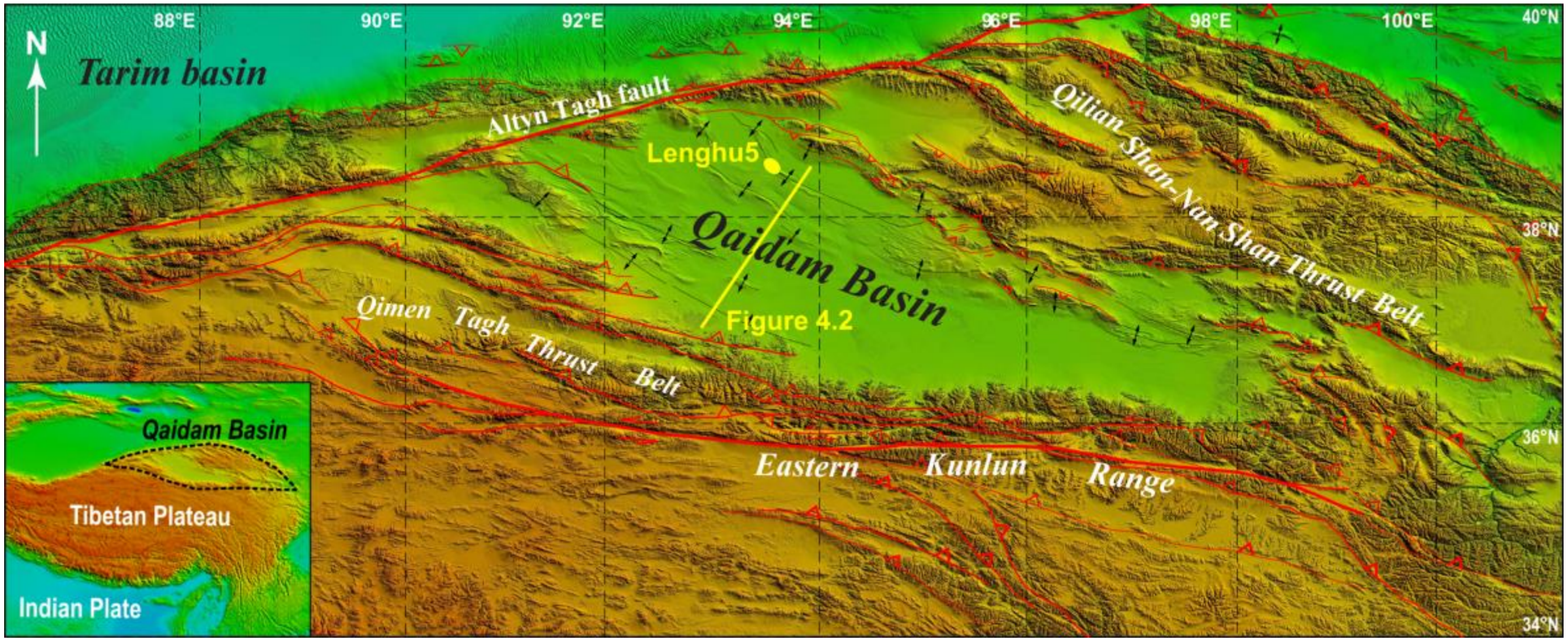

Figure 4.1 The structural map of Qaidam basin, generated based on the geological maps published in previous studies (Yin et al., 2008a; Yin et al., 2008b; Liu et al., 2009). This map is interpreted on a surface of topography (based on SRTM elevation data).

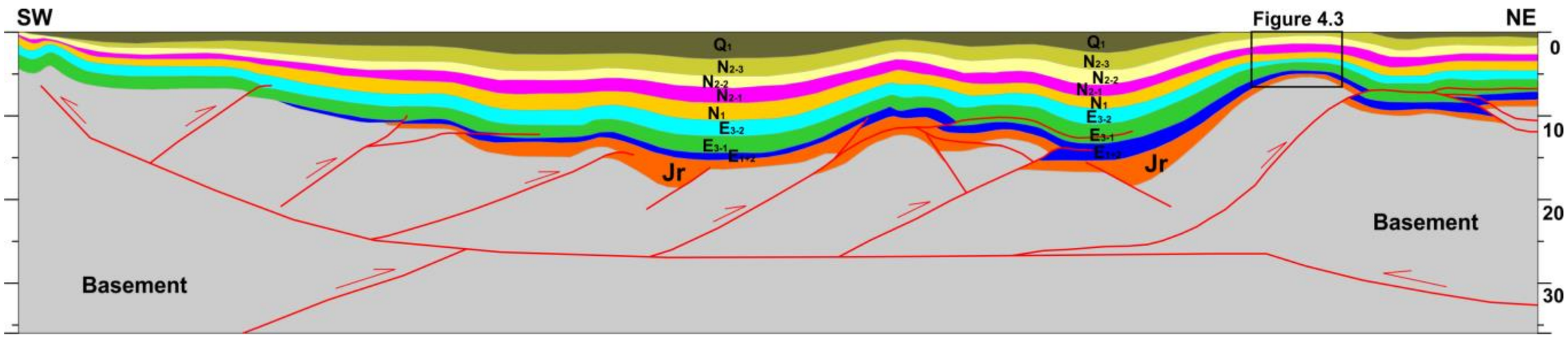

Figure 4.2 A cross section through the central Qaidam basin (modified from Yin et al., 2008b; Liu et al., 2009), delineating the structural geometry of present Qaidam basin developed under a compressional environment. (See section location in Figure 4.1).

In order to understand the detailed structural evolution of the Qaidam basin and compare with the results in previous studies, a cross-section of the Qaidam basin has been reconstructed in 2D MOVE (Midland Valley) in this study (Figure 4.2). With the restoration shown in Figure 4.3, the section restoration presented here is achieved by combining 'UNFOLD' and 'MOVE ON FAULT' functions in 2D MOVE.

As introduced above, the Cenozoic sediments (E_{1+2}-Q: T_R-T_0) are distributed throughout Qaidam basin while the Mesozoic sediments (Jr: T_6-T_R) is just locally present. Thus, the restoration mainly focuses on the Cenozoic sediments, corresponding to E_{1+2}-Q in the section shown in Figure 4.3. The restoration algorithms used in this restoration are Flexural Slip (based on Kane et al., 1997) for 'UNFOLD' and Fault Parallel Flow (based on Egan et al., 1997; Kane et al., 1997) for 'MOVE ON FAULT'. A Pin Line is pre-set in the biggest depocenter of the basin. By using the Flexural Slip algorithm, the horizons are unfolded to a fixed datum from T_0 to T_R. If horizons are cut by faults, the 'MOVE ON FAULT' conduction is used prior to 'UNFOLD', making the hanging walls restored to the original position first. The balancing restoration of the cross section in Figure 4.3 was accomplished by the following steps:

(i). i→h: after removing the layer above T_0, the horizon T_0 was unfolded to be horizontal using 'flexural slip' algorithm;

(ii). h→g→f→e→d: repeat the step (i) for the horizons T_1, T_2', T_2 and T_3;

(iii). d→c: as the horizon T_4 was faulted in the left end of the section, after removing the layer above the horizon T_4, T_4 was firstly reconnected by restoring the hanging walls back to their original positions using 'MOVE ON FAULT' function, and then unfolded using 'flexural slip' algorithm;

(iv). c→b→a: repeat the step (iii) for the horizons T_5 and T_R.

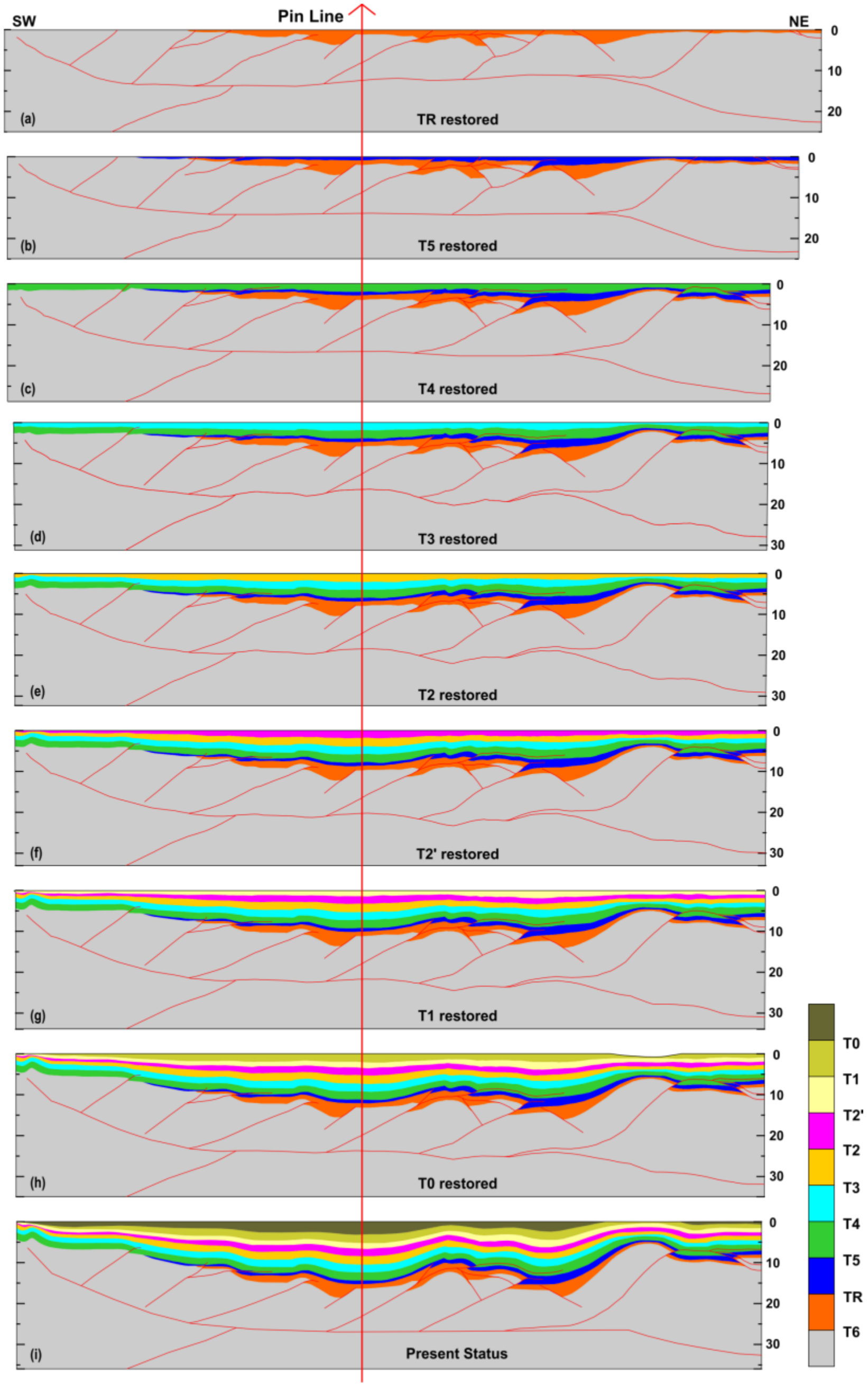

Figure 4.3 The balancing restoration of a cross section through the central Qaidam basin in 2D MOVE, Midland Valley.

After restoring and unfolding horizons, the length of restored section is measured for assessing the shortening amounts presented here. The shortening amounts and the shortening rates during the compression are calculated in this study (Table 4.1), based on the sediment division and age assignments shown in Table 2.1. The plots of these calculated results are then used to generate the statistical shortening plots (Figure 4.5). The total shortening of central Qaidam basin in Cenozoic reached ~20km (Table 4.1). Since T_R (~65Ma), the majority of shortening (~70%) had been reached in a period of 28Ma between T_R (~65Ma) and T_4 (~37Ma). After T_4, the other ~30% shortening was accomplished in the following 37Ma. This indicates that the Qaidam basin experienced a quick shortening episode and then the shortening rate slowed down abruptly after T_4 (~37Ma). The average-shortening rate in Cenozoic was 0.28-0.31mm/a, while there were two shortening rate peaks that appeared in T_5-T_4 (0.61-1.03mm/a) and T_0-Present (0.53-0.54mm/a). This suggests that there was an accelerating shortening from T_5 to T_4 and a second accelerating shortening from T_0 up till now (Figure 4.5c). Thus, it is inferred that the compression slowed down after T_4 but accelerated again after T_0. The results also indicate that the Qaidam basin is still experiencing NE-SW compression.

Compared with the results (Figure 4.5a, c) based on the restoration using ‘Flexural Slip’, the results based on restoration using ‘Line Length’ are also calculated and the corresponding shortening plots have been built (Figure 4.5b, d). Although the calculated shortening amounts and rates are not identical, the lines in the plots show similar positions of highs and lows; there is also a similar trend for the transition between the highs and lows.

Table 4.1 The shortening estimates for the Qaidam basin: calculation of shortening (S), total shortening (TS), shortening rate (SR), average-shortening rate (ASR) and percentage of shortening reached (PS). Two calculating algorithms are used, (a) flexural slip and (b) line length.

(a) algorithm: flexural slip							
Stage	***L (km)***	***T (Ma)***	***S (km)***	***TS (km)***	***SR (mm/a)***	***ASR (mm/a)***	***PS (%)***
T_R	*208.36*	*65.00*	*0.00*	*0.00*	*0.00*	*0.00*	*0*
T_5	*201.85*	*49.00*	*6.51*	*6.51*	*0.41*	*0.41*	*35.4*
T_4	*194.49*	*37.00*	*7.36*	*13.87*	*0.61*	*0.50*	*75.5*
T_3	*192.61*	*28.50*	*1.88*	*15.75*	*0.22*	*0.43*	*87.8*
$T_{2'}$	*192.00*	*23.80*	*0.61*	*16.36*	*0.13*	*0.40*	*90.7*
T_2	*191.58*	*11.20*	*0.42*	*16.78*	*0.03*	*0.31*	*91.7*
T_1	*191.21*	*5.30*	*0.37*	*17.15*	*0.06*	*0.29*	*91.8*
T_0	*190.95*	*1.80*	*0.26*	*17.41*	*0.08*	*0.28*	*95.2*
P	*190.00*	*0.00*	*0.95*	*18.36*	*0.53*	*0.28*	*100*
(b) algorithm: line-length							
Stage	***L (km)***	***T (Ma)***	***S (km)***	***TS (km)***	***SR (mm/a)***	***ASR (mm/a)***	***PS (%)***
T_R	*210.13*	*65.00*	*0.00*	*0.00*	*0.00*	*0.00*	*0.00*
T_5	*208.64*	*49.00*	*1.49*	*1.49*	*0.09*	*0.09*	*7.41*
T_4	*196.32*	*37.00*	*12.3*	*13.81*	*1.03*	*0.49*	*68.6*
T_3	*195.75*	*28.50*	*0.57*	*14.38*	*0.07*	*0.39*	*71.4*
$T_{2'}$	*194.66*	*23.80*	*1.09*	*15.47*	*0.23*	*0.38*	*76.9*
T_2	*193.15*	*11.20*	*1.51*	*16.98*	*0.12*	*0.32*	*84.4*
T_1	*191.68*	*5.30*	*1.47*	*18.45*	*0.25*	*0.31*	*91.6*
T_0	*190.96*	*1.80*	*0.72*	*19.16*	*0.20*	*0.30*	*95.2*
P	*190.00*	*0.00*	*0.96*	*20.13*	*0.54*	*0.31*	*100*

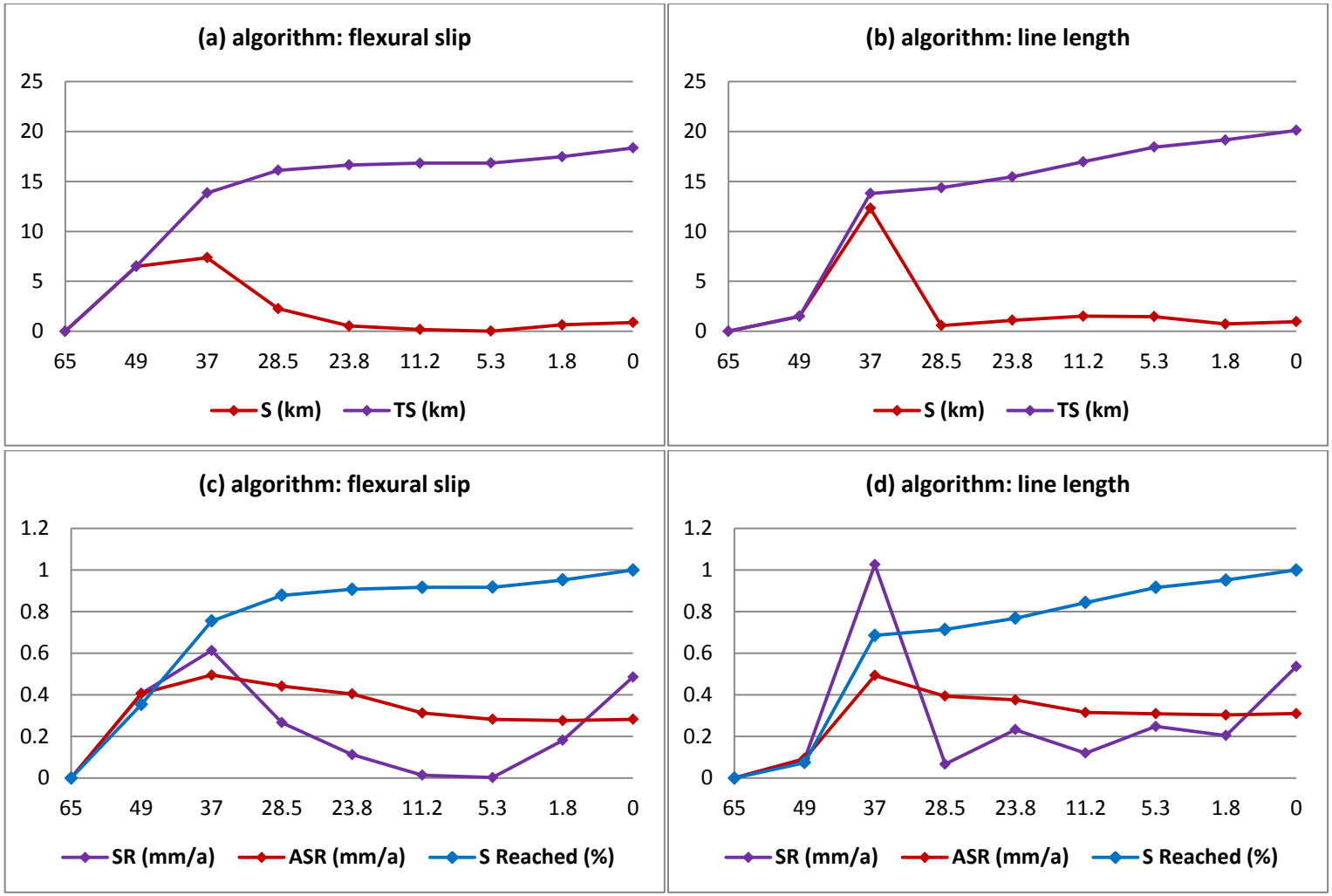

Figure 4.4 The plot diagrams of the deformation and shortening rates. The time axis is not assigned averagely. In diagrams (a) and (b), the shortening and total shortening are calculated versus deformation time, from 65Ma to present. Shortening rate (mm/a), total shortening rate (mm/a) and percentage of shortening reached are displayed in diagram (c) and (d). S: shortening; TS: total shortening; SR: shortening rate; ASR: average-shortening rate; S Reached: shortening reached.

Table 4.2 The comparison of shortening related calculation between this research and results in previous studies (Zhou et al., 2006; Yin et al., 2008b; Liu et al., 2009). *: calculated based on the data in the paper.

		total shortening (km)	shortening rate (mm/a)	
			maximum	average
this research	flexural slip	18.36	0.61	0.28
	line length	20.13	1.03	0.31
Zhou et al. (2006)		18.05	2.42	0.28
Yin et al. (2008b)		41.00		0.63*
Liu et al. (2009)		30.75	4.76	0.47*
Modified from Liu et al. (2009)		22.79*		0.35*

Some shortening-related calculations are reported in previous studies (e.g. Zhou et al., 2006; Yin et al., 2008b; Liu et al., 2009). As the comparison in Table 4.2 shows, no consensus has been reached on the total shortening amounts and shortening rates, particularly on the total shortening amounts and maximum shortening rates.

The calculations in this research (using flexural slip and line length algorithms) are similar to the results of Zhou et al. (2006). The seismic section in Yin et al. (2008b) is also analysed here to understand why the total shortening amount and average-shortening rate are much higher than that in this research. In the section (Figure 7 in Yin's paper), there should be a marked line-length increase from T_4 to T_5, as T_5 is cut by many thrust faults that leads to larger fault displacements. However, the line-length balancing in Yin et al. (2008b) does not present this line-length increase, which may lead to a larger total shortening amount and the higher shortening rate. When it comes to the results in Liu et al. (2009), the profile 2-2' includes the northern Saishiteng Mountains that absorbs a very large shortening (Figure 4 in Liu's paper). The inclusion of the northern Saishiteng Mountains makes the results of total shortening amount and shortening rate much higher. Based on the line-length restoration of profile 2-2' in Liu et al. (2009), if the effects of the northern Saishiteng Mountains are removed from the calculation then the newly calculated total shortening and average-shortening rate are 22.79km

and 0.35mm/a (Table 4.2). These modified results are similar to the results of this research, suggesting the calculations are reliable. As a summary, by integrating the calculations in Zhou et al. (2006), Liu et al. (2009) and this research, the total shortening of the central Qaidam basin since 65Ma is 20±2km, which leads to a shortening rate of 0.30±0.04mm/a.

4.3. 3D Fault Architecture of the Lenghu5 Structure

A seismic section, high-resolution fault system maps and detailed regional transects are employed to study the structural geometry and fault development of the Lenghu5 structure (see position in Figure 4.1). 3D geometric models are then constructed to understand the lateral structural variation of the Lenghu5 structure.

4.3.1. Overall Geometry based on Seismic Interpretation

The Lenghu5 structure, located in northern Qaidam basin, is a ~10km wide asymmetric anticline controlled by reverse faults (see position in Figure 4.1). The anticline is well imaged on a ~7km long seismic section through the Lenghu5 structure (Figure 4.5) and the internal stratigraphy is well constrained by the Lengke1 well (data from Yang et al., 2003; Pang et al., 2004). The Lengke1 well contains lithological boundaries T_6 to T_3 upward and the T_3 repeats a second time because of the existence of the high-angle reverse fault. Apart from the basement, six main stratigraphic units are interpreted according to the well logging data, which are J_r to $N_{2\text{-}2}$ in the stratigraphic younging direction. Three faults are interpreted according to the discontinuous reflections.

The Lenghu5 surface geology shows a broad fold cut by a high-angle reverse fault through the fold axis. However, the seismic section suggests shallowing of the dip of the reverse fault with increasing depth into a decollement above a sequence interpreted as the late Eocene sediments (E_3). The Lenghu5 anticline extends throughout the section continuing below the reverse fault. The origin of the Lenghu5 anticline is attributed to the regional NE-SW oriented compression (e.g., Chen et al., 2005; Wang et al., 2006a).

In the section shown in Figure 4.5, the units E_{1+2} to $N_{2\text{-}1}$ maintain constant thickness, while the hanging wall J_r is about four times thicker compared to

the footwall. The growth strata are developed in unit N_{2-2}. The Lenghu5 anticline is controlled by the lower SW-directing reverse faults (F_2 and F_3 in Figure 4.5b) and the upper younger NE-directing reverse fault (F_1 in Figure 4.5b). The two main faults F_1 and F_2 account for the majority of the fault displacement: ~800m displacement in the unit J_r along F_2 and ~800m in the unit N_1 along F_1. The displacements of F_1 and F_2 all decrease upward along the fault planes. Previous studies have demonstrated that the Qaidam basin comprises an earlier extension stage and a later compression stage (e.g., Xia et al., 2001; Pang et al., 2004; Wang et al., 2006b; Zhu et al., 2006). Therefore, it is inferred that the lower SW-directing reverse fault F_2 formed as a normal fault initially and then inverted to be a reverse fault in the later compression stage, which is justified by the J_r thickness difference between hanging wall and footwall. The constant thickness of E_{1+2}-N_{2-1} in the two limbs suggests the compression starts no earlier than the deposition of N_{2-1}. The growth strata developed in N_{2-2} indicates the initiation of the anticline development. As a summary, the geological history can be inferred as three main stages:

(i). the initial normal faulting in the Jurassic (J_r) NE-SW oriented extension;

(ii). the inverted SW-directing reverse faulting in the early Eocene (E_{1+2}) NW-SE oriented compression;

(iii). the NE-directing reverse faulting from the late Eocene (E_3) to the Neocene (N) compression.

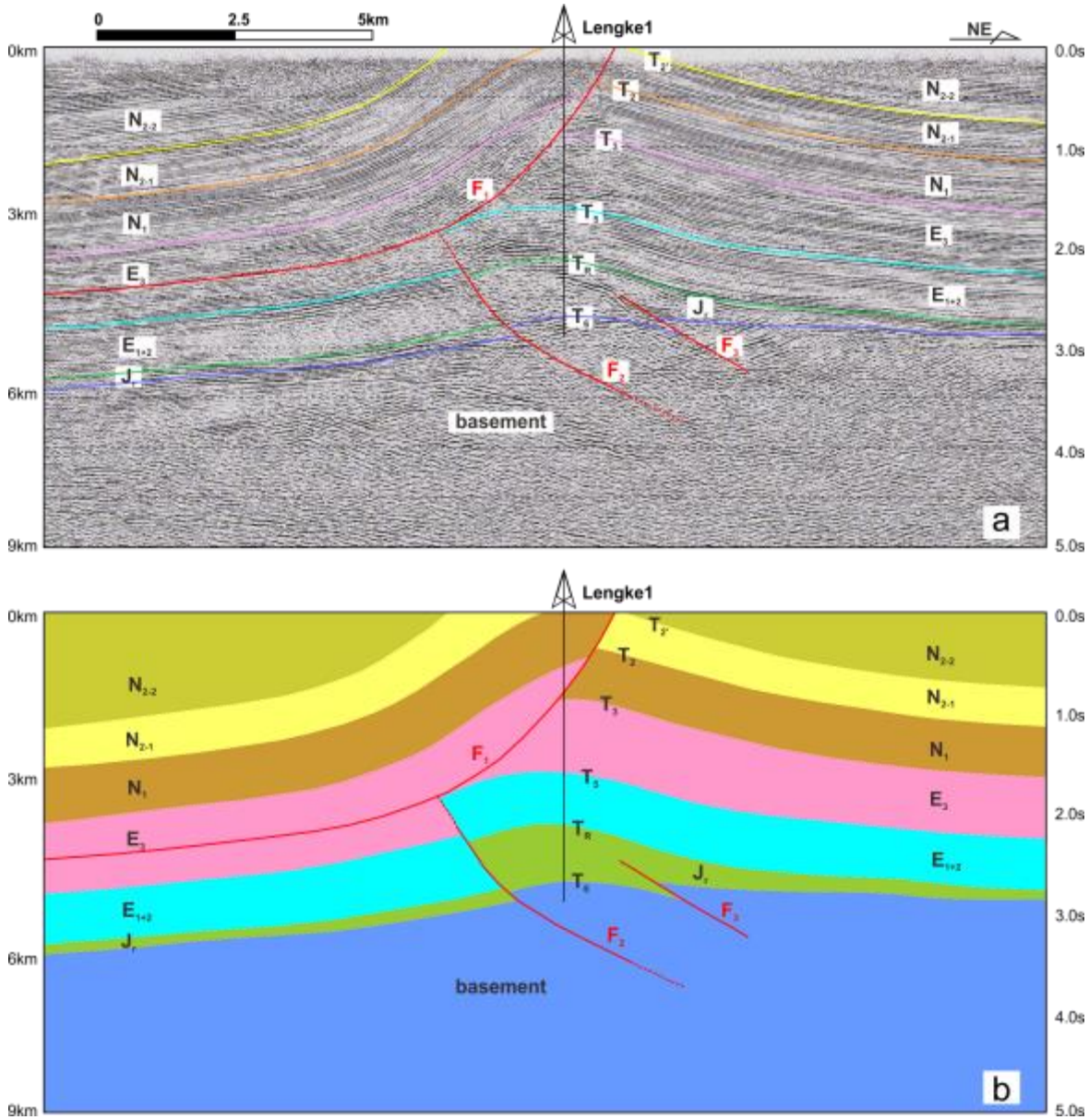

Figure 4.5 The Lenghu5 structure is controlled by the lower inversed faults (F_2 and F_3) and the upper NE reverse fault (F_1).

4.3.2. Detailed Fault Architecture based on High-Resolution Fieldworks in the Lenghu5 Structure

The structural evolution of the Lenghu5 structure is derived from the above seismic section. However, the variability of fault displacements of F_1 and F_2 cannot be properly explained. Given the limitation of seismic resolution, it is inferred that this variation in the fault displacements may be accounted for by the absence of details within the fault zone, e.g. local buckling of the layers, local lateral thickness changes, etc.

(1). Stratigraphy

The detailed stratigraphy of the hanging wall and the footwall were measured on the ground along three traverses sub-perpendicular to strike of the Lenghu5 structure (Figure 4.6): two traverses in the hanging wall (HW1: 3km long through the northern anticline and HW2: 1km long through the southern anticline); and one traverse in the footwall (FW: 3km long through northern end of footwall). The stratigraphic columns, generated from the program 'StratlogH.exe', show that the thicknesses of HW1, HW2 and FW are ~1200m, ~350m and ~650m, respectively. The stratigraphy of HW1 and HW2 is similar to each other, except the extra central part exposed in the southern culmination. The stratigraphic correlation between hanging wall and footwall suggests the division into the following five packages:

(i). $\mathbf{S_a}$ comprises fine sandstones and red/grey/mottled shales/mudstones, with a minimum thickness of 170m in HW1;

(ii). $\mathbf{S_b}$ is fine-medium sandstone interbedded with very few thin red/grey mudstones and its thickness is ~350m;

(iii). $\mathbf{S_c}$ is pure fine sandstone with inconstant thickness (10-30m);

(iv). $\mathbf{S_d}$, ~400m thick, shows a similar lithology as $S_{b,}$ but with thin medium-coarse sandstone interbedded;

(v). $\mathbf{S_e}$ becomes a coarse-very coarse sandstone, of which the thickness exceeds 250m.

The stratigraphic correlation between hanging wall and footwall can be used to estimate the fault displacement of the Lenghu5 structure. According to the stratigraphic correlation, the fault throw is inferred to be ~500m in the northern anticline. Therefore, the main reverse fault has a throw that is large enough to be imaged on seismic reflection data, which may correspond to fault F_1 in the seismic section (Figure 4.5). Given the northern anticline exposes less stratigraphy than the southern anticline and the exposure of footwall stratigraphy decreases southward, it is assumed that the fault displacement increases from the northern anticline to the southern anticline. The lithology of the Lenghu5 structure changes from the coarse/very coarse sandstone in the two walls to the clay-rich fine sandstone towards the central fault zone.

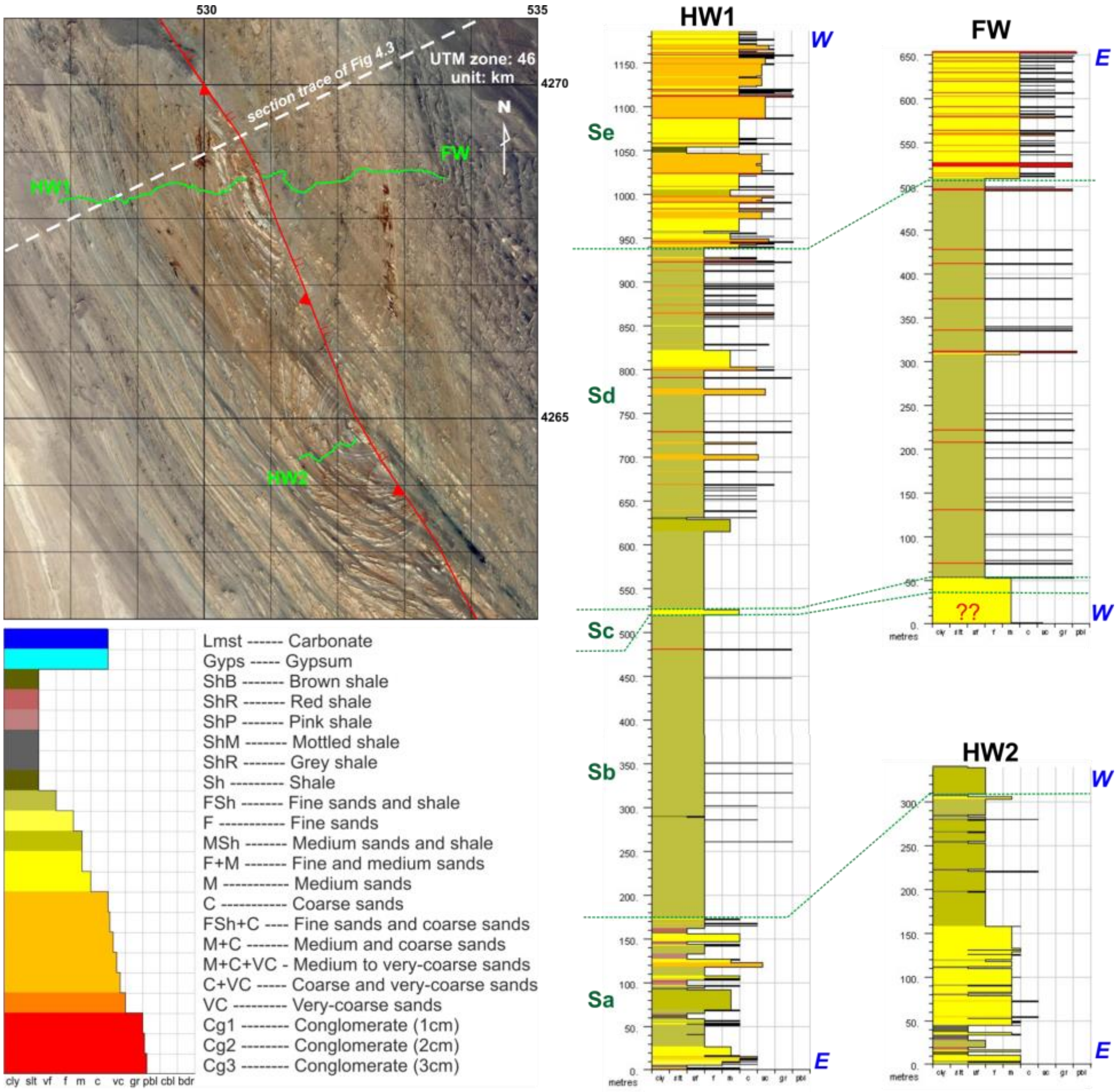

Figure 4.6 Regional stratigraphy of the Lenghu5 structure. Five major stratigraphic units are identified: (S_a) clay-rich fine sandstone; (S_b) fine-medium sandstone; (S_c) fine sandstone; (S_d) medium-coarse sandstone and (S_e) coarse sandstone to conglomerate.

(2). Regional Transects

Topographically, the southern anticline shows a higher elevation change from the hanging wall to the footwall than the northern anticline; and stratigraphically, the southern anticline exposes more stratigraphy in the core than the northern anticline. These observations can be explained by the larger displacement in the southern anticline, which leads to higher uplift of the hanging wall and more exposure of the older units in the surface.

In order to investigate the nonuniform reverse faulting along the Lenghu5 structure, ten parallel transects (Figure 4.7) are created based on the field-work data and satellite Image interpretation. Two high-resolution transects S3 and S9 (Figure 4.8) are used to compare the different geometry in the northern and southern anticlines. The other eight transects are also constructed (Figure 4.9) to build the 3D geometric model, in order to reveal the high degree of lateral variation along the reverse fault zone.

The fold geometries are highlighted in the two transects S3 and S9, with a length of ~6km and a depth of ~1.25km. The detailed stratigraphic columns are projected onto the section surface to assist the stratigraphy construction. The stratigraphic boundaries are also extrapolated above the present topography up to the thrust faults in order to estimate the displacement of the fault zone.

The section S3 through the northern anticline presents a fault zone comprising a main reverse fault and a splay fault in the footwall. Using Sa as the reference unit, the main reverse fault F1 shows a maximum displacement of ~415m that accounts for ~90% of the total fault displacement; while the ~50m displacement of the splay fault F2 is negligible compared with that of the main reverse fault F1. However, the reverse fault F1 does not keep a constant displacement along the fault, but decrease to ~180m in unit Sc-Se (see fault zone in Figure 4.8a). In the hanging wall, the layers experience more clockwise rotation when it goes up fault, resulting in a reducing displacement up fault. In section S9 through the southern anticline, the fault zone still comprises a main reverse fault F1 and a splay fault F2. However, the splay fault F2 changes to be blind rather than exposed in the surface (see S9 in Figure 4.8b). Compared with S3, the hanging wall anticline pre-

sents a relative flat crest adjacent to the main thrust. Moreover, a pair of structures, a small-scale tight syncline and open anticline, are developed in the footwall. A ~850m cumulative fault displacement is present in the fault zone and the main thrust fault F1 accounts for the majority of the displacement in Sa-Sc. Similar to S3, the displacement of the main reverse fault decreases upward as well.

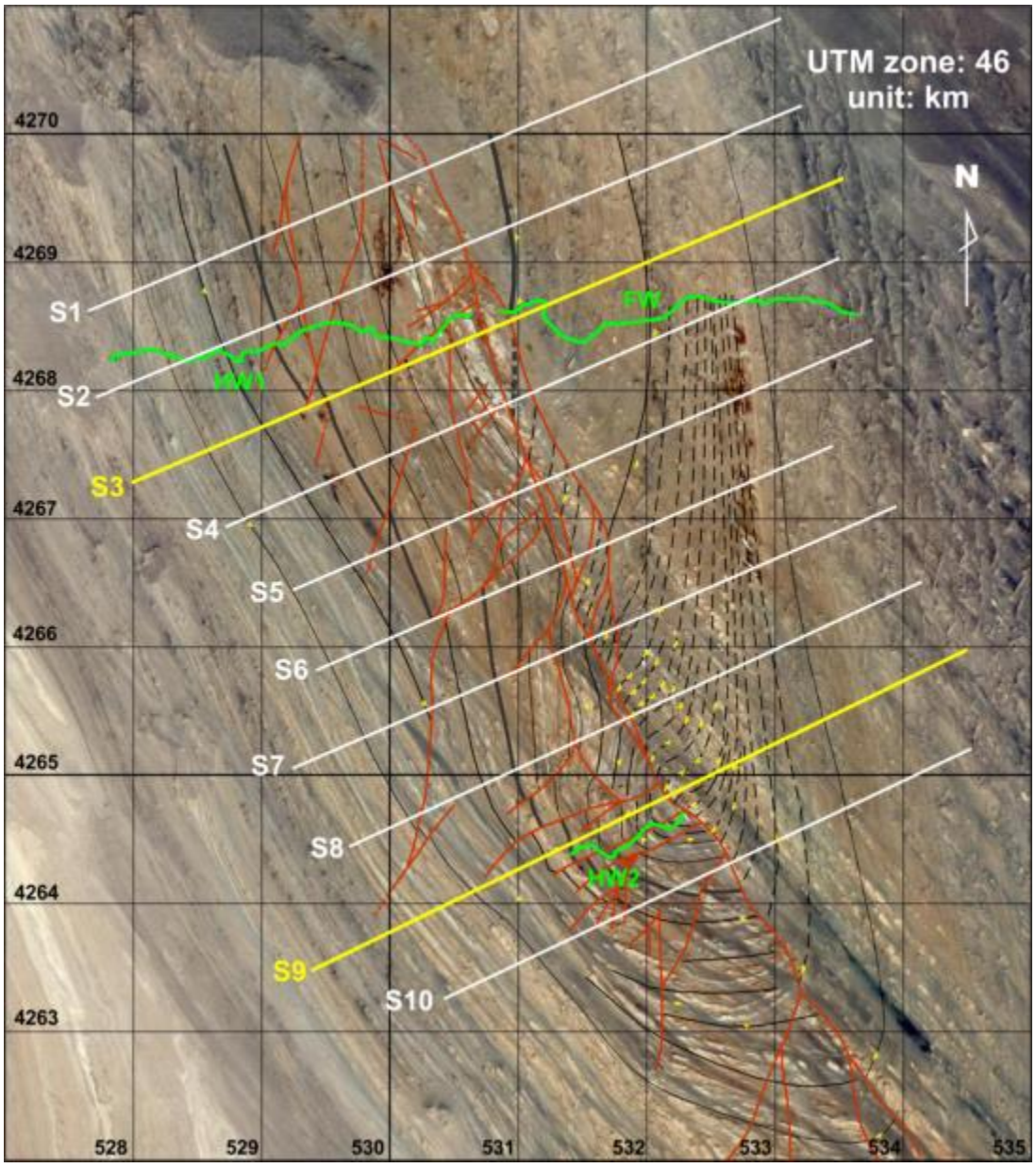

Figure 4.7 The traces of ten regional sections through the Lenghu5 structure: S3 and S9 (yellow) are two key cross sections while other eight sections (white) are constructed to build 3D models of the Lenghu5 structure.

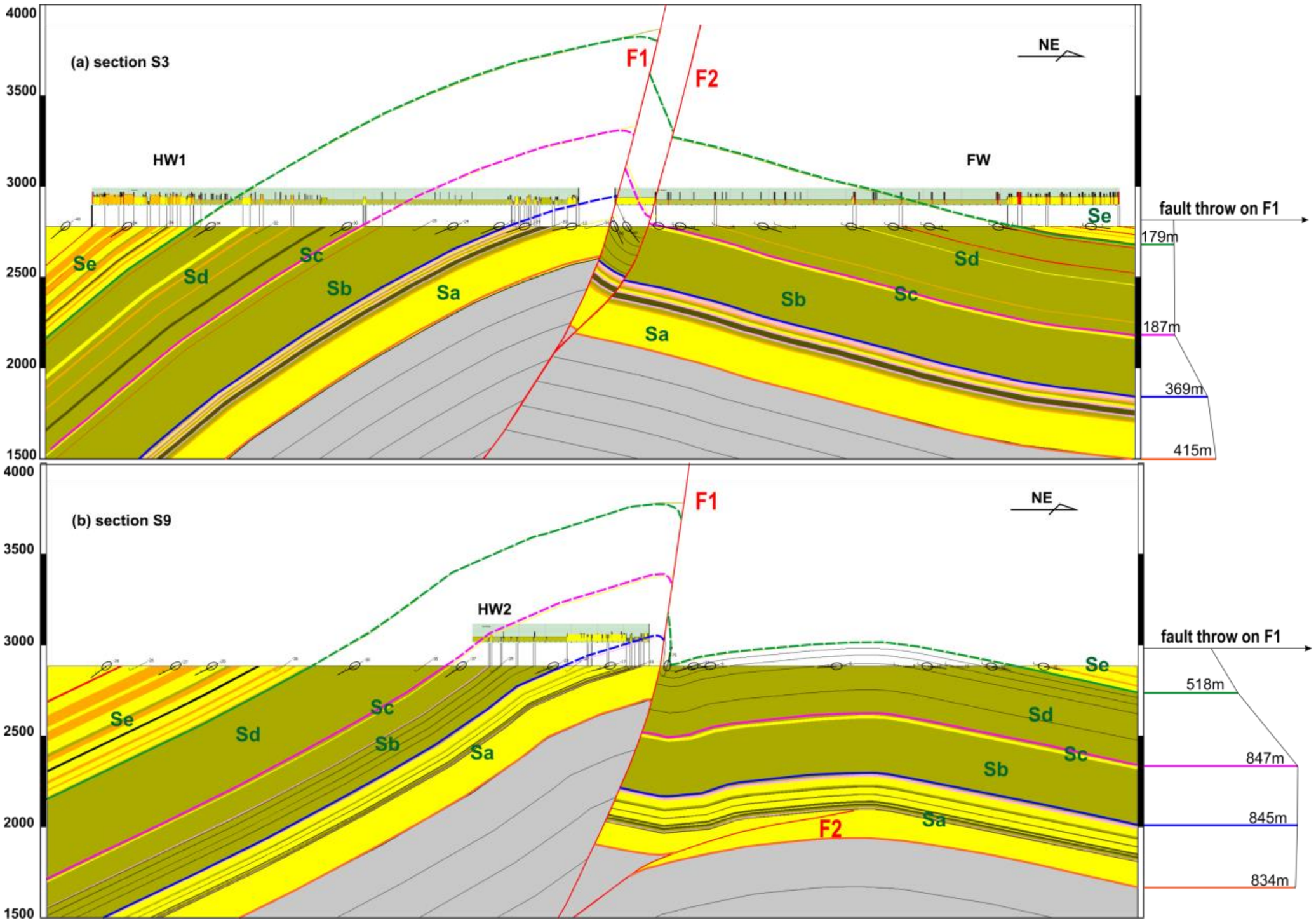

Figure 4.8 Regional sections delineating the fault zones composing a main reverse fault and splay faults. (a): S3 cutting through the northern anticline and (b): S9 cutting through the southern anticline. The fault displacement along the main reverse fault plane increases from north to south, while the footwall splay fault changes to be blind in the southern anticline.

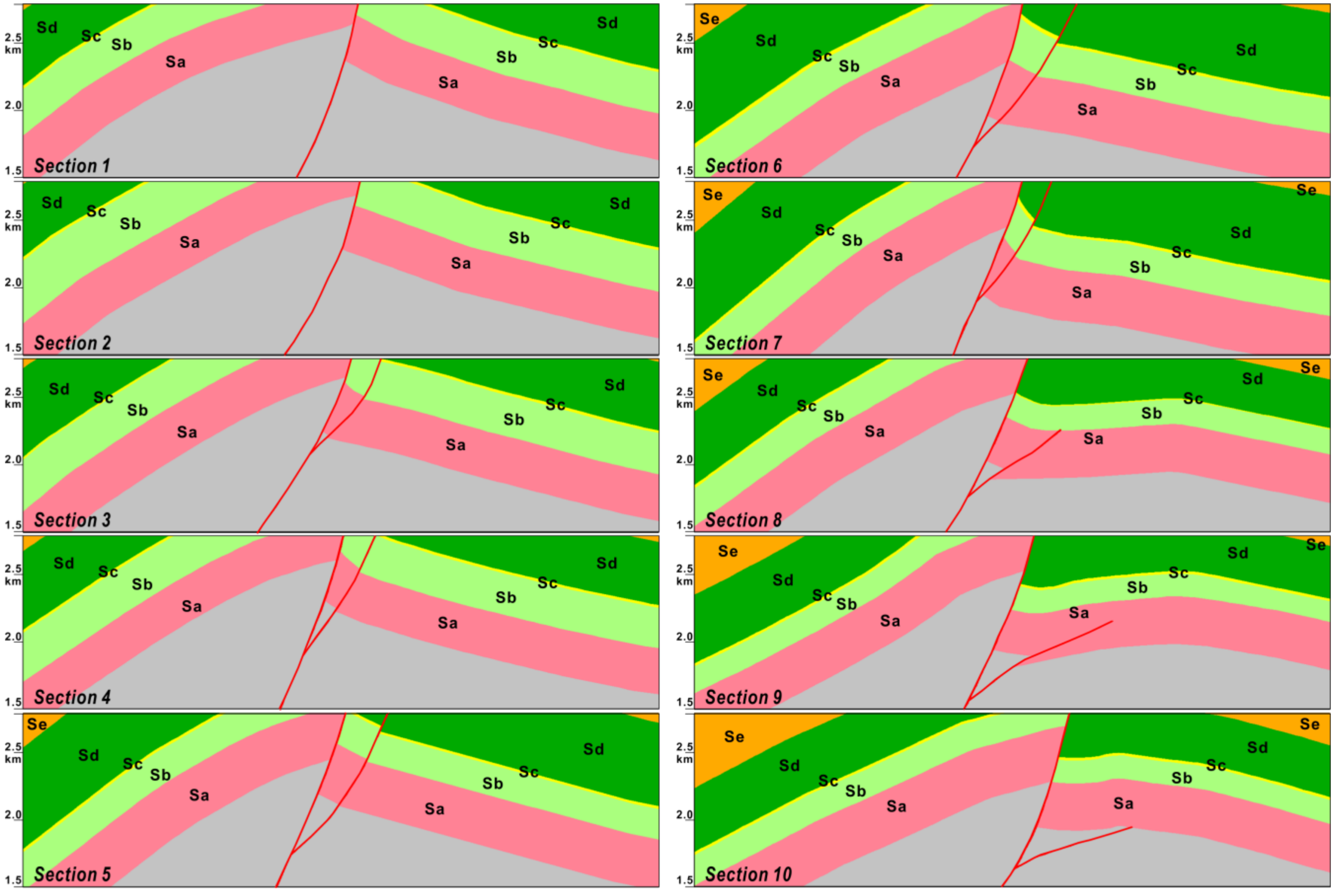

Figure 4.9 The parallel cross sections delineate the lateral structural variation of the Lenghu5 structure.

Based on the structural geometry of the subparallel transects (Figure 4.9), the Lenghu5 structure can be divided into 3 distinct components:

(i). S1-S2: single steep thrust faults (with increasing fault displacement southeastward);

(ii). S3-S7: exposed bifurcating faults (fault displacement decreases from S3 to S5 and then increases from S5 to S7);

(iii). S8-S10: blind bifurcating faults (displacement on main fault increases from S8 to S9 and then decreases from S9 to S10; displacement on minor fault increases and then decreases as it shallows).

(3). Structural Map

Based on the ten structural transects and grounding mapping, the geological structural map of the Lenghu5 structure was generated (Figure 4.10). The main reverse fault is steeply dipping with angles of 60-70SW, spreading ~10km from the northern end to the southern end. Reacting to the NE-SW compression, two anticlines (i.e., the two topographic culminations) are developed in the hanging wall, which indicates the nonuniform deformation along the fault zone. The curved fault trace of the main reverse fault on the ground also suggests variable deformation along the Lenghu5 structure. The fault zone is not a single fault plane, but comprises a main reverse fault and several small splay faults. The main reverse fault accounts for the majority of the displacement of the fault zone. Several splays of the main reverse fault are also observed in the field, in either the hanging wall or the footwall. The splay faults are not pervasively developed, but located in the middle saddle between the two anticlines. It suggests that the middle saddle may have a local strain concentration because of the nonuniform deformation between the two anticlines. The splay faults generate a number of fault lenses in both the hanging-wall and the footwall. About 90% of the second-order structures occur in the fault zone and the hanging wall, suggesting the strain mostly happens to the hanging wall and the central fault zone. Many small reverse faults and normal faults form in the hanging wall to accommodate the overall strain present in the hanging wall. Moreover, the accommodation faults in the hanging wall mostly concentrate in the clay-rich fold cores and the fault density decreases away from the main reverse fault zone.

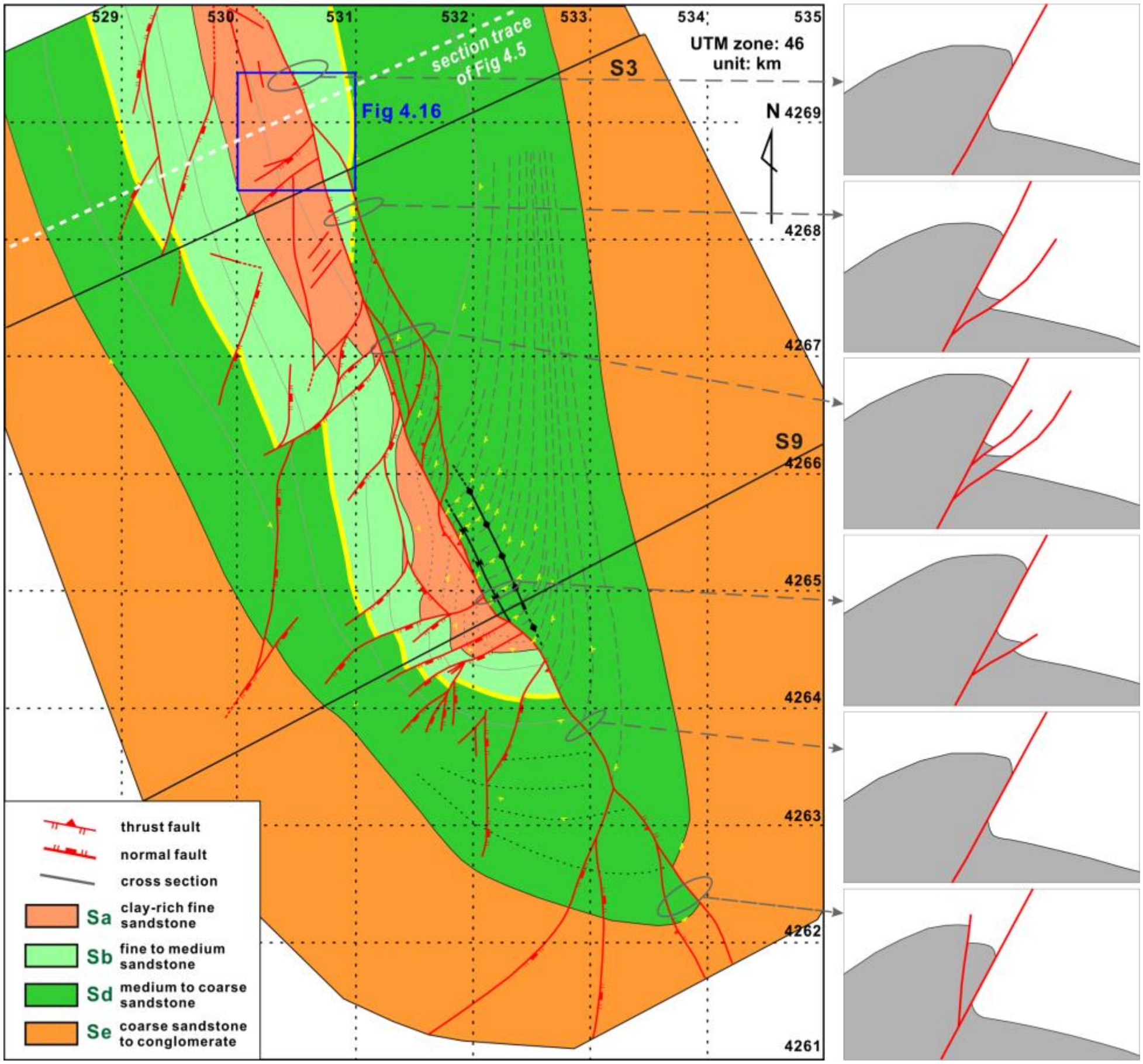

Figure 4.10 The structural map of the Lenghu5 structure based on a combination of satellite imagery and ground mapping. The Lenghu5 structure, an anticline in response to a NE-directing reverse fault, presents high degree of lateral variation along the NW-SE oriented reverse fault.

As a summary, the Lenghu5 structure presents a nonuniform fault displacement along the strike of fault zone. This nonuniform reverse faulting dominates the structural lateral changes along the Lenghu5 structure, e.g.,

(i). The main reverse fault reaches local maximum displacements at two locations corresponding to the two topographic culminations, forming the northern and southern anticlines in the hanging wall.

(ii). The reverse fault beneath the southern anticline shows a maximum fault displacement of ~850m, which is ~450m larger than that shown in the northern anticline (maximum displacement of ~400m). The larger displacement leads to the higher curvature of the hanging wall in the southern anticline than that in the northern anticline.

(iii). The middle saddle between the two anticlines, with locally the smallest fault displacement, acts as a stress-concentrated area because of the rapidly increasing displacement both northward and southward.

In the Lenghu5 structure, the main reverse fault (first-order) controls the regional deformation; while the smaller splay faults together with the second-order accommodation structures increase the meso-scale complexity. Abundant second-order structures are observed in the field, e.g., a pair of tight syncline and open anticline is localized in the footwall against the southern anticline (Figure 4.10 and Figure 4.8); abundant normal faults with displacements of 10cm-10m are developed in the hanging wall, representing an anticline-core-concentrated strain (Figure 4.10). The distribution of these second-order structures demonstrates the local-stress concentration areas, e.g., the anticline cores, the middle saddle between the anticlines and the footwall with the blind splay faults. It is assumed that the second-order structures are mostly developed in response to the lateral strain variation along the Lenghu5 structure. Therefore, in compressional systems, the concentration of second-order structures can be taken as indicators of a high degree of lateral structural variation.

4.3.3. 3D Fault Architecture of the Lenghu5 Structure

Based on the Google image interpretation, stratigraphy, fault system maps and detailed regional transects, the structural geometry of Lenghu5 is visualized in three dimensions (Figure 4.11). The Lenghu5 structure is controlled by the thrust fault zone beneath the northern and southern culminations. The fault zone is composed of a main thrust fault and some splay faults in the hanging wall or footwall. These splay faults generate some lenses, which might affect the hydrocarbon sealing property as compartments are formed in the fault zone.

A good stratigraphic correlation between the hanging wall and footwall suggests the overall Lenghu5 anticline gently plunges southeastward. The hanging wall exposes more stratigraphy because the older stratigraphy is brought upward by the reverse faulting. The second-order structures are also presented in the 3D diagrams, e.g., the normal fault arrays in the hanging wall and the minor folds in both the hanging wall and the footwall. These second-order structures are assumed to accommodate the overall strain in local structures caused by the regional compression in the Lenghu5 structure. For example, the normal faults in the hanging wall mostly concentrate in the cores of the anticlines, accommodating the local extensional strain because of the layers bending, particularly in the crest of the two anticlines in the hanging wall. The pair of second-order syncline/anticline (see the magnified ellipse in Figure 4.11c) developed in the footwall does not spread northward but dies out at the two ends.

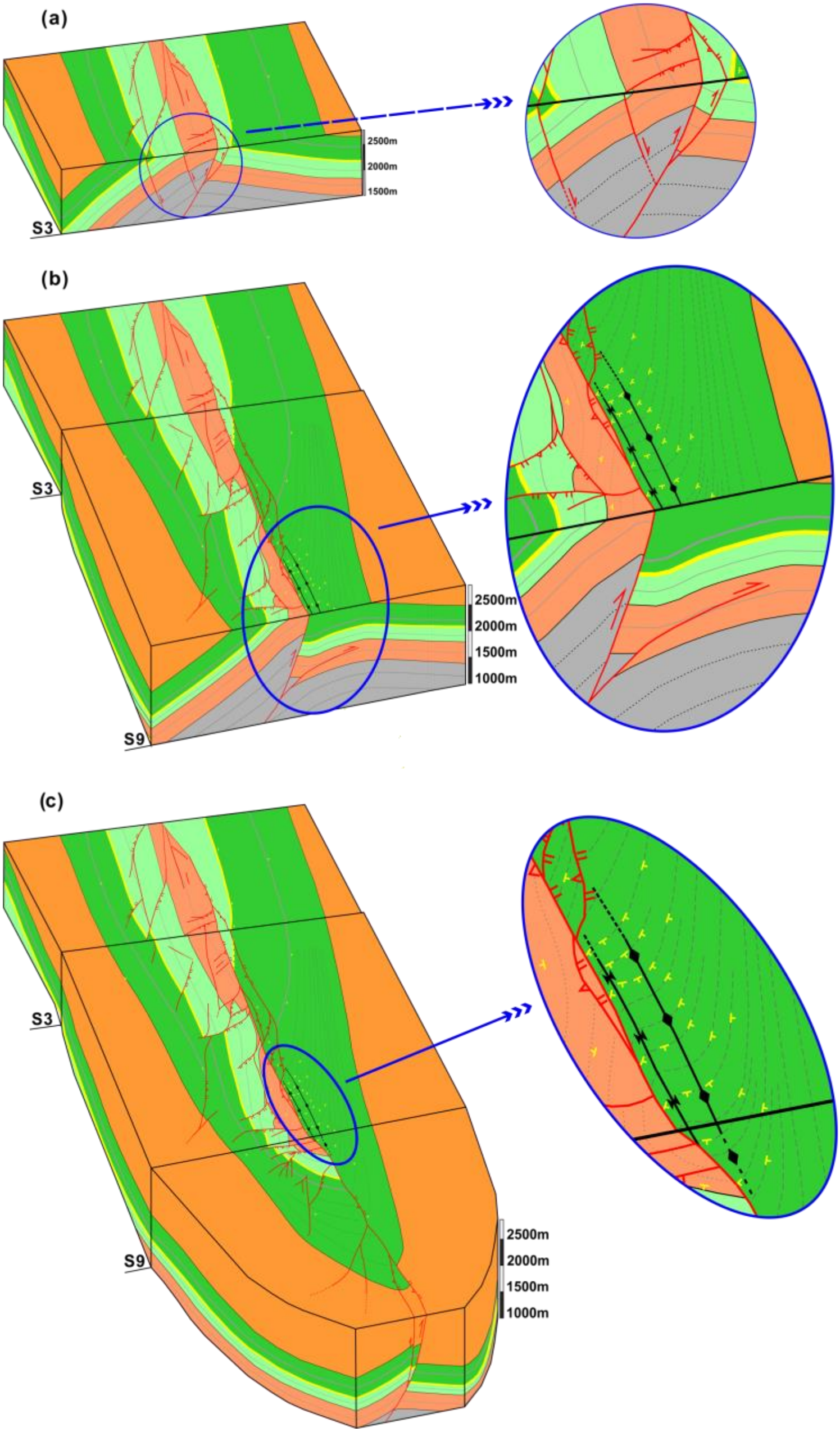

Figure 4.11 3D models depict structural geometry of the Lenghu5 structure. The 3D models are generated by integrating geologic structural maps and the regional transects. (c) is an overview 3D diagram of the whole study area, while (a) and (b) are 3D diagrams with S3 and S9 exposed.

The 3D models in Figure 4.11 demonstrate that both the hanging wall anticlines and the fault zone show lateral variability from NW to SE. The fault zone presents nonuniform combinations of a single-plane reverse fault and multiple splay faults. However, the splay faults concentrate in the middle saddle between the northern and southern anticline, which implies the middle section has a more complex strain distribution, arising from the interaction of the two propagating fold structures.

The two topographic culminations (pink stratigraphy in the surface) correspond to the two anticlines shown in transects S3 and S9 (Figure 4.8). As the anticlines are two primary deformation areas, the second-order accommodation faults (i.e., the normal faults in the hanging wall) present an anticline-core-concentrated distribution. The two anticlines all result in concave stratigraphic boundaries against the fault zone. However, the southern anticline shows relatively steeper beddings in the core than the northern anticline (Figure 4.11a,b), and the southern anticline presents a higher concave magnitude than that of the northern one. This can be explained by the larger fault displacement in the southern anticline than in the northern one.

Normal faults are developed in the hanging wall of the Lenghu5 structure. However, the distribution of the normal faults is not even in the hanging wall, but localised in the cores of the two anticlines. The throw of the normal faults varies from 10cm to 10m, which is negligible compared with the displacement of the main reverse faults. The fault throw is effectively reduced in clay-rich units, i.e., the layers mainly composed of shale/mudstone. The normal faults are mostly truncated by the main reverse fault zone without spreading to the footwall, suggesting the normal faults are not earlier than the main reverse faults and perform as accommodation faults in the hanging wall.

4.4. Dynamic Evolution of the Lenghu5 Structure

4.4.1. Fault Throw Measurement

By using the ten sub-parallel cross sections (Figure 4.9) created based on the fieldwork data, the 3D model of the Lenghu5 structure is built (Figure 4.12a). When constructing the 3D model, the second-order faults are simplified except the main reverse fault F1 and two splay faults F2 and F3. The

horizons B0 to B5 are used to define the fault throws (B1 to B5 are at the base of the main stratigraphic packages Sa, Sb, Sc, Sd and Se).

Allan maps (Allan, 1989) of the horizons on the reverse fault F1 are created in 3D Move to measure F1 displacement along the fault strike. Then the Throw-Distance chart is plotted as Figure 4.12b, with the horizontal axis directing the southeast end of the Lenghu5 structure. This Throw-Distance chart quantitatively demonstrates the nonuniform deformation by faulting along the fault zone of Lenghu5. Two peaks in the Throw-Distance chart represent the areas where the two anticlines are formed; while the middle valley corresponds to the middle saddle between the two anticlines where the throw decreases rapidly. The shape of the Throw-Distance curves suggests a larger fault displacement in the southern culmination, which concurs with the more exposure of the older stratigraphic units in the southern culmination. The rapid decrease of fault throws in the southern end of the Lenghu5 structure indicates the fault is dying out or going to be blind with buried tip line southeastward, suggesting the SE-plunge of the Lenghu5 anticline.

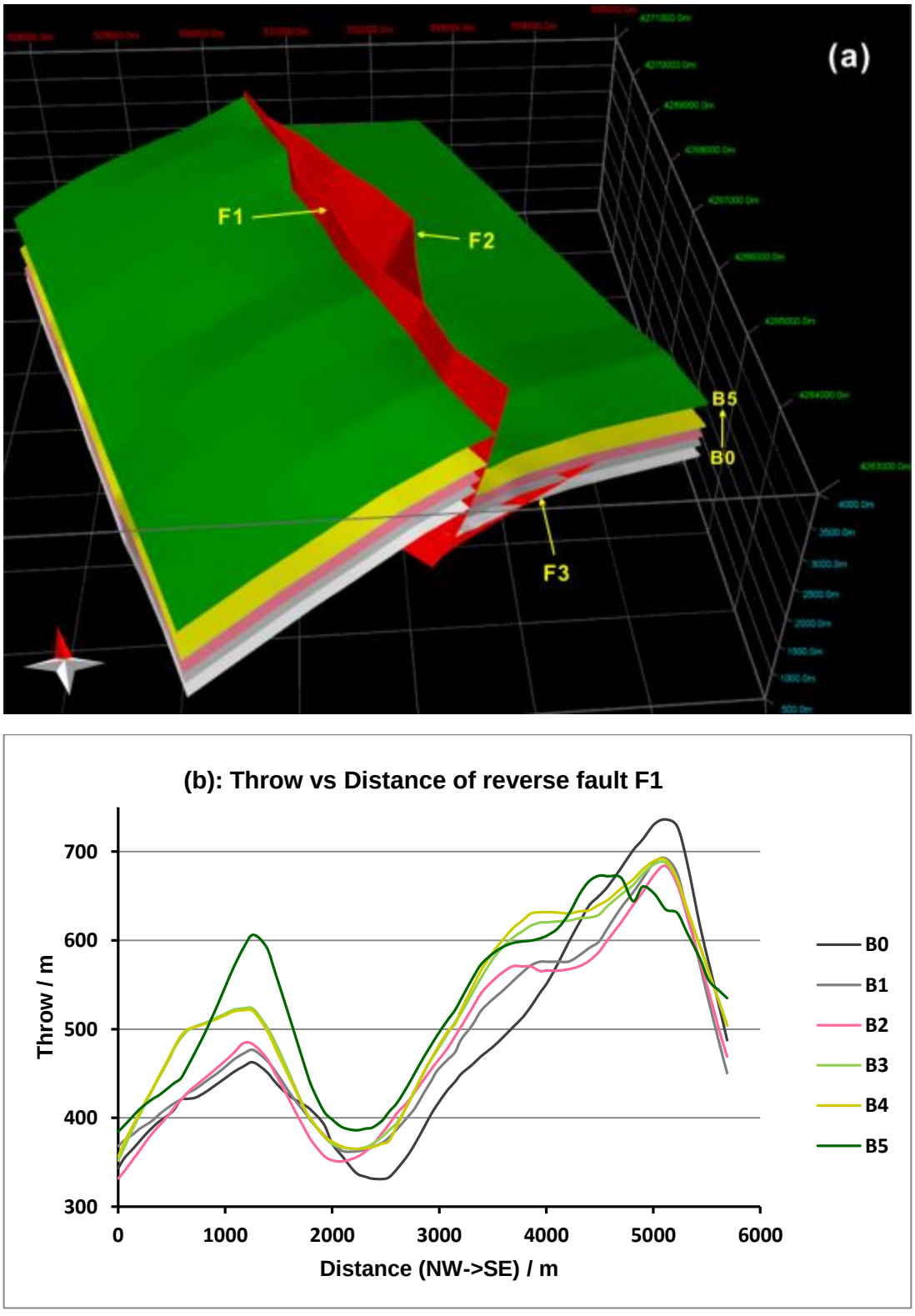

Figure 4.12 The 3D model of the Lenghu5 structure is built based on the parallel transects (a), and the Throw-Distance chart is plotted based on measurements on Allan maps (Allan, 1989) (b).

4.4.2. 3D Restoration

The 3D model is then restored to reveal the dynamic evolution of the Lenghu5 structure (Figure 4.13). The 3D restoration is conducted by using the 'Move on Fault' and 'Unfold' functions in 3D Move (Midland Valley). The calculating algorithms for the two functions are 'Fault Parallel Flow' (based on Egan et al., 1997; Kane et al., 1997) and 'Flexural Slip Unfold' (based on Kane et al., 1997).

The 3D restoration of the Lenghu5 structure is accomplished by the following steps:

(i). Move on Fault along fault F3 (Figure 4.13e→d);

(ii). Move on Fault along fault F2 (Figure 4.13d→c);

(iii). Move on Fault along fault F1 (Figure 4.13c→b);

(iv). Unfold the folded horizons (Figure 4.13b→a).

As these restoration procedures are reversible, the dynamic evolution of Lenghu5 is revealed. The geological history of the Lenghu5 structure is then drawn as below:

(i). the sedimentation of Sa-Se (Figure 4.13a);

(ii). the original Lenghu5 anticline is formed reacting to the early NE-SW regional compression (Figure 4.13b);

(iii). the upward-steepening reverse fault F1 is developed perpendicular to the late NE-SW compression (Figure 4.13c);

(iv). the splay faults F2 and F3 form to accommodate the strain required to the fault zone (Figure 4.13d, e);

(v). the Lenghu5 structure is uplifted and eroded to the present configuration (Figure 4.13f).

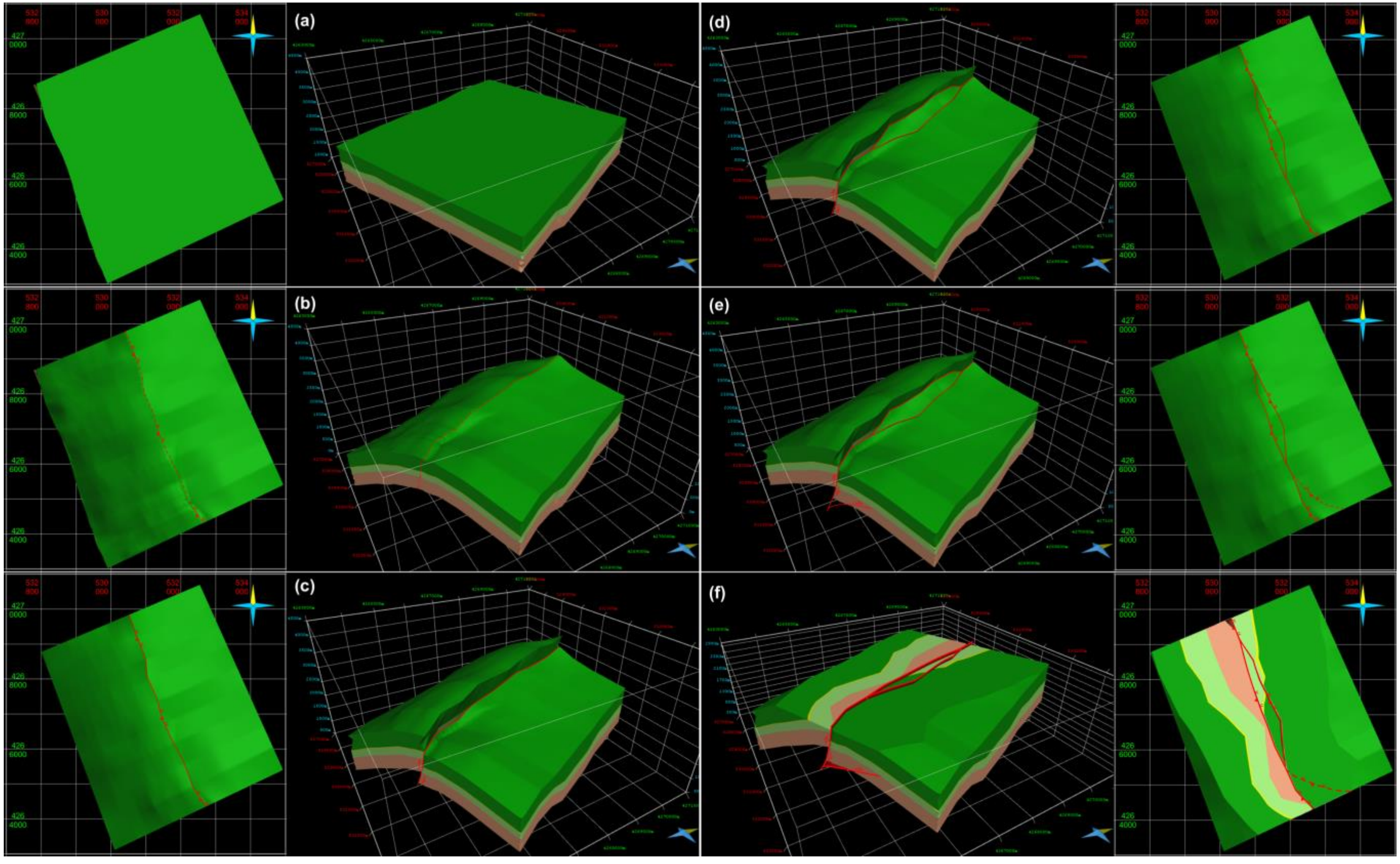

Figure 4.13 Dynamic evolution of Lenghu5 is revealed by 3D restoration in 3D Move (Midland Valley): (a->b): folding; (b->e): reverse faulting F1, F2, F3; (e->f): uplift and erosion to present.

4.5. Strain Analysis to Predict Minor Structures

In the Lenghu5 structure, both primary large reverse fault and second-order small faults are observed. It is assumed that the second-order faults are developed to accommodate the overall strain of the hanging wall. However, the fold-core-concentrated distribution of the normal faults has not been interpreted in detail. Therefore, the Lenghu5 structure is simplified to analyse the strain distribution between the two developing anticlines, in order to understand the factors that control the distribution of second-order faults.

4.5.1. Strain Analysis on Simplified Model

In the simplification, the first-order geometry of the Lenghu5 structure is maintained while the smaller scale features are removed. The simplified model (Figure 4.14) comprises two anticlines in the hanging wall reacting to the nonuniform reverse faulting along the N-S trending fault zone (the top surface). The simplified model is restored to the undeformed status (the bottom surface) using the 'Flexural Slip Unfold' function in 3D Move (based on Egan et al., 1997; Kane et al., 1997). The coloured surface (Figure 4.14a) presents the total straight-line movement of each vertex from the original surface to the deformed surface. The principle strains of the surface during the deformation are tracked (tension positive convention), e.g., extensional strain e1 (Figure 4.14b) and contractional strain e3 (Figure 4.14c). The principle strain ratio (1+e1)/(1+e3) is also shown in Figure 4.14d.

In the simplified model, the footwall presents a uniform high contractional strain (Figure 4.14c); while the hanging wall presents a high extensional strain and low contractional strain (Figure 4.14b, d). However, the strain of the hanging wall is no longer uniform. The strain maps suggest the two anticline-cores are dominated by extensional-strain; while the middle saddle between the two anticlines is contractional-strain dominated. It indicates potential development of extensional structures concentrating in the anticline cores, which concurs with the field observation in Lenghu5 that the second-order normal faults are 90% concentrated within the two anticline cores (Figure 4.10 and Figure 4.11). Rose diagrams and the stereonet plots are also generated to reveal the principle stress azimuth and resultant shear

planes (Figure 4.15), to aid the prediction of second-order structures. The stereonet plots (Figure 4.15e, f) predict potential shear planes that are sub-parallel and sub-perpendicular to the main fault strike.

However, as the model is simplified, the natural complexity has not been fully taken into account. Therefore, it is very difficult to predict the second-order structures directly from these stereonet plots. Thus, a statistical investigation is conducted on the normal faults observed in the Lenghu5 structure, in order to validate the simplified model.

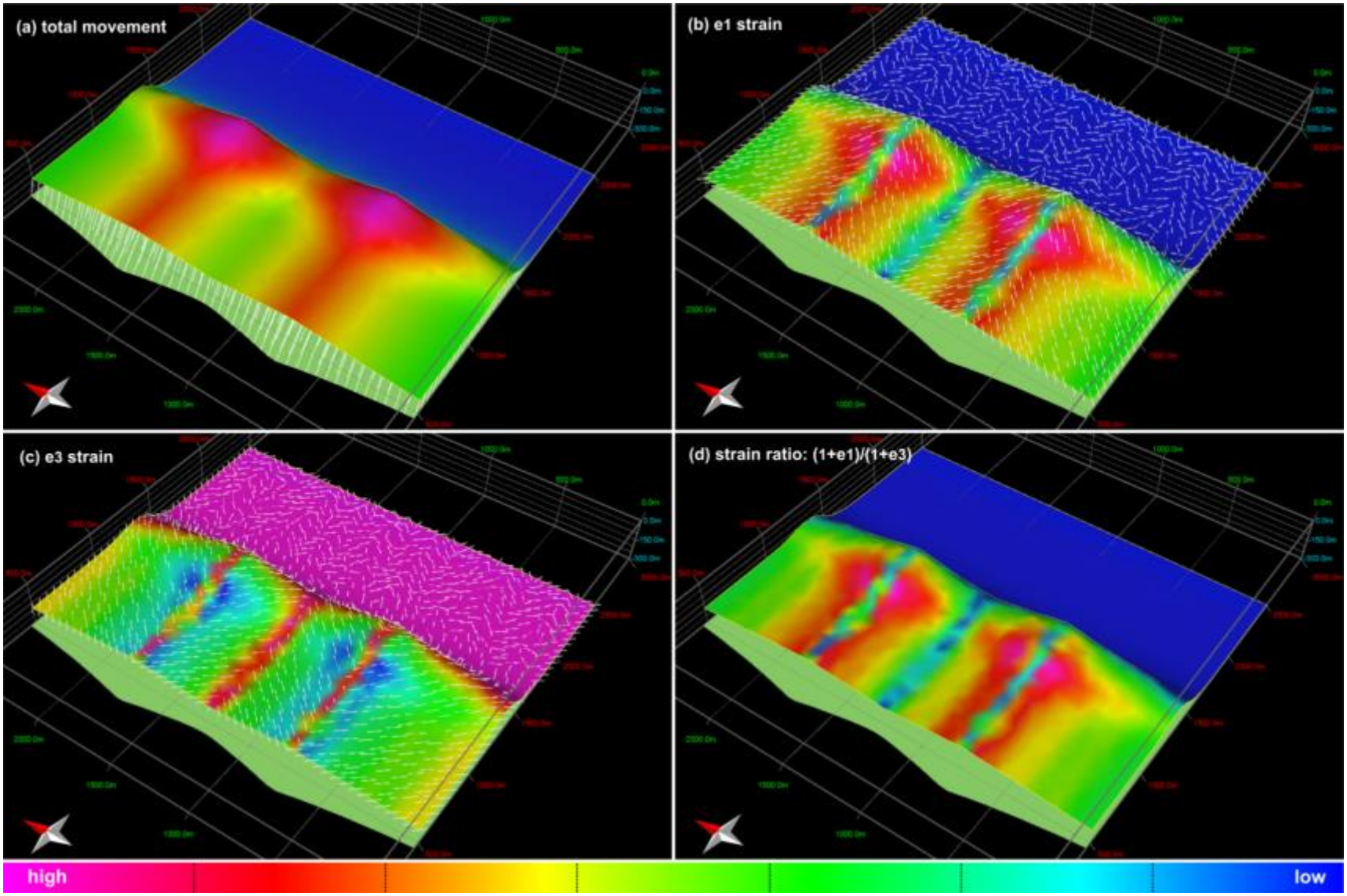

Figure 4.14 Strain analysis on a simplified model of the Lenghu5 structure. The results delineate the total movement (a), the extensional strain e1 (b), the contractional strain e3 (c), and the strain ratio (1+e1)/(1+e3) (d).

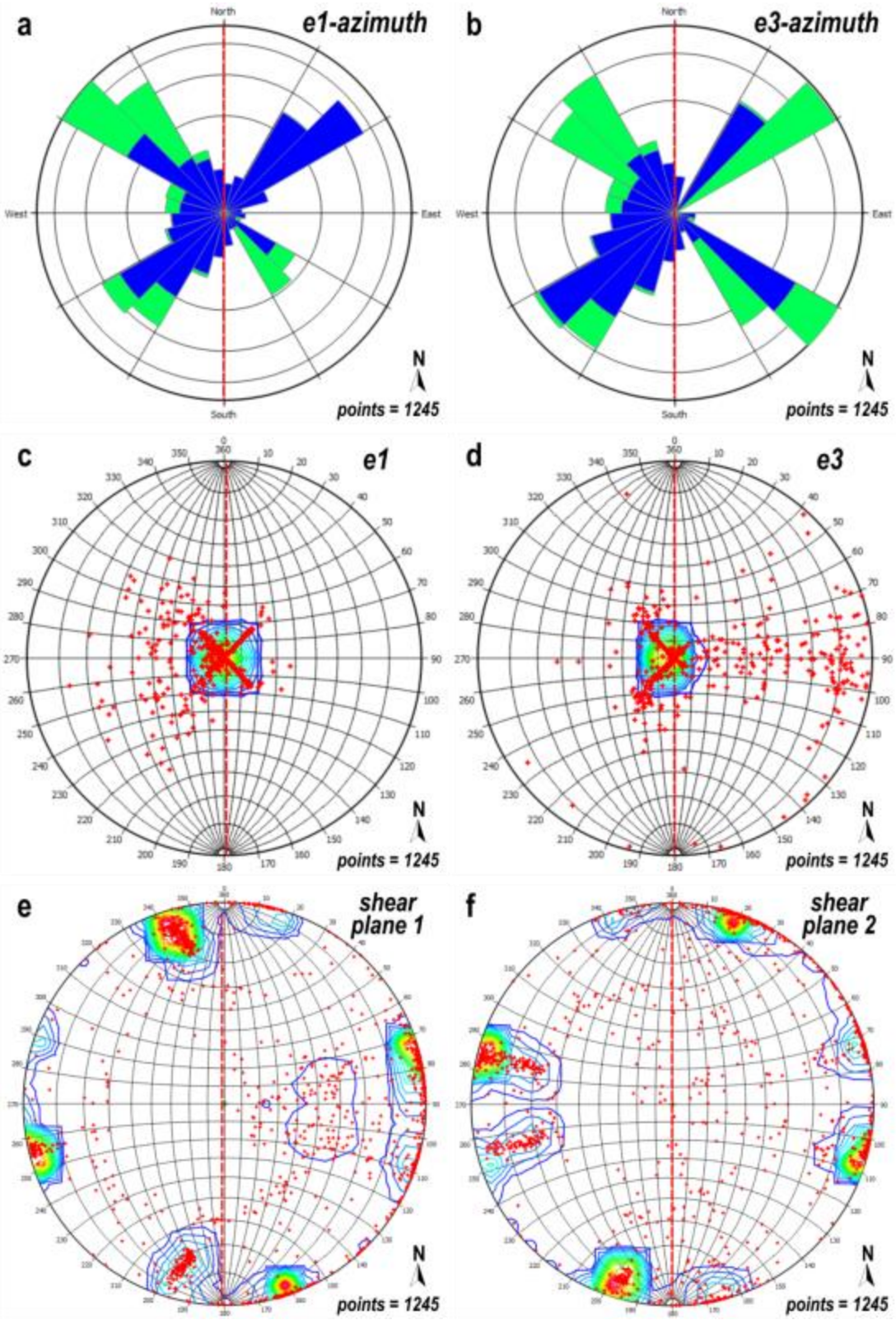

Figure 4.15 The rose diagrams of the principle stress and the stereonet plots of the principle stress, potential joint/shear plane.

4.5.2. Field Data Verification

Normal faults are developed almost exclusively in the hanging wall of the Lenghu5 structure (Figure 4.16). In the hanging wall, the distribution of the normal faults is not even, but localised in the cores of the two anticlines (Figure 4.10).

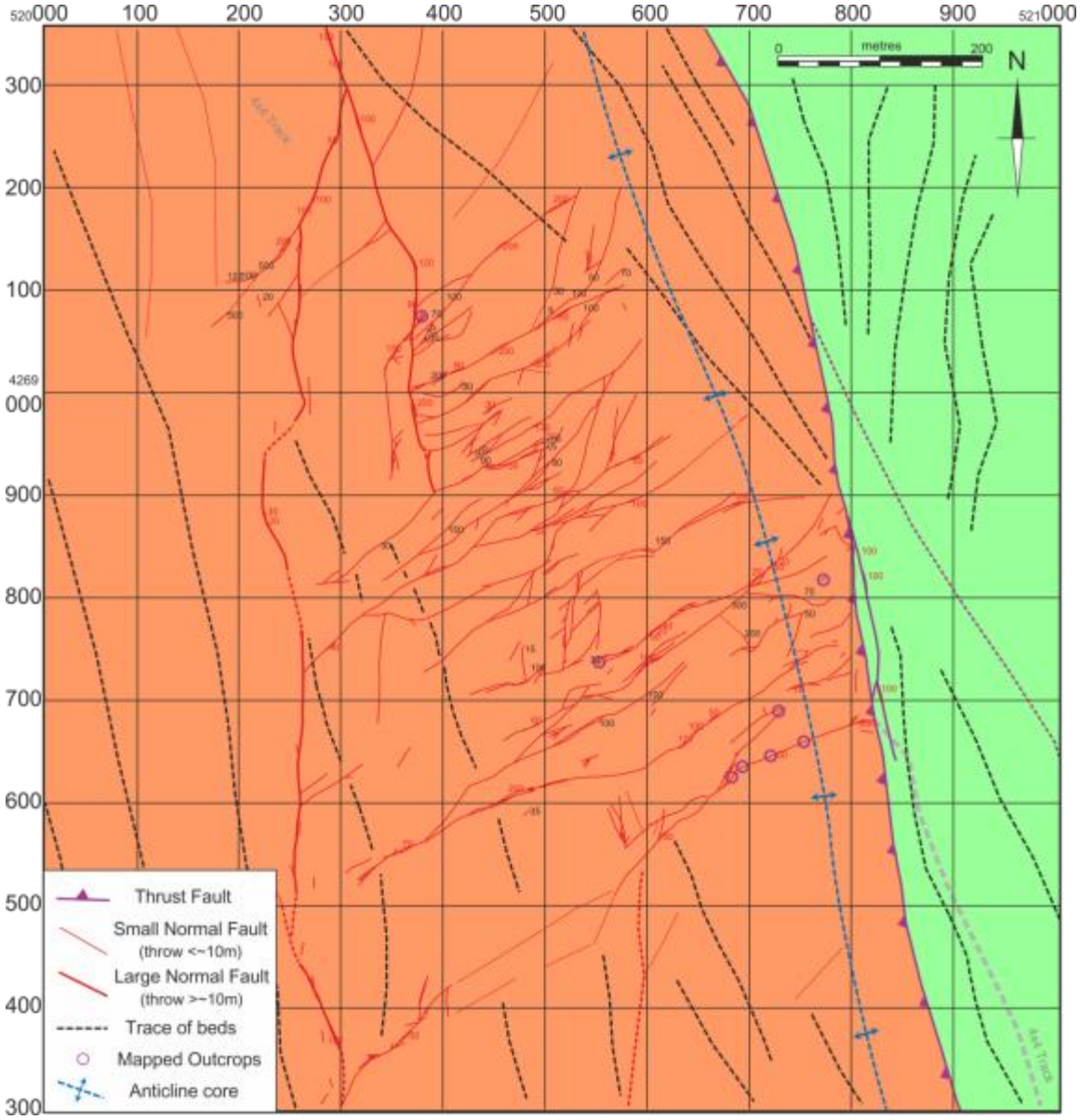

Figure 4.16 Normal fault arrays mapped in a kilometre-square located in the hanging wall of the Lenghu5 structure (See position in Figure 4.10).

Rose diagrams and stereonet plots are created for both the main reverse fault and the second-order normal faults in the hanging wall (Figure 4.17) to assess the relationship between them. In the strike rose diagrams, the main reverse faults show a principal NNW-SSE (~170°/350°) trend (Figure 4.17c). Although the normal faults show various strikes, two main sets of the normal faults are identified in the rose diagram: the N-S (~180°/360°) trending set and the NE-SW (~55°/235°) trending set, respectively (Figure 4.17d). The N-S trending set is sub-parallel to the main reverse faults, while the NE-SW trending set is obliquely truncated by the main reverse faults. The N-S trending set is rarer but has higher fault throws and lengths along strike than the NE-SW trending set. This observation concurs with the potential shear plane directions predicted by the simplified model (Figure 4.15e, f).

Firstly, it is inferred that the N-S trending set is a response to the NNW-SSE extensional strain applied throughout the hanging wall because of the layers' folding when the Lenghu5 anticlines are developed. This inference is proved by the smaller amount but larger fault throws of the N-S trending set. Secondly, the NE-SW trending set presents an anticline-core-concentrated distribution, which suggests the NE-SE trending normal faults are generated as a response to the nonuniform reverse faulting along the fault zone (Figure 4.10).

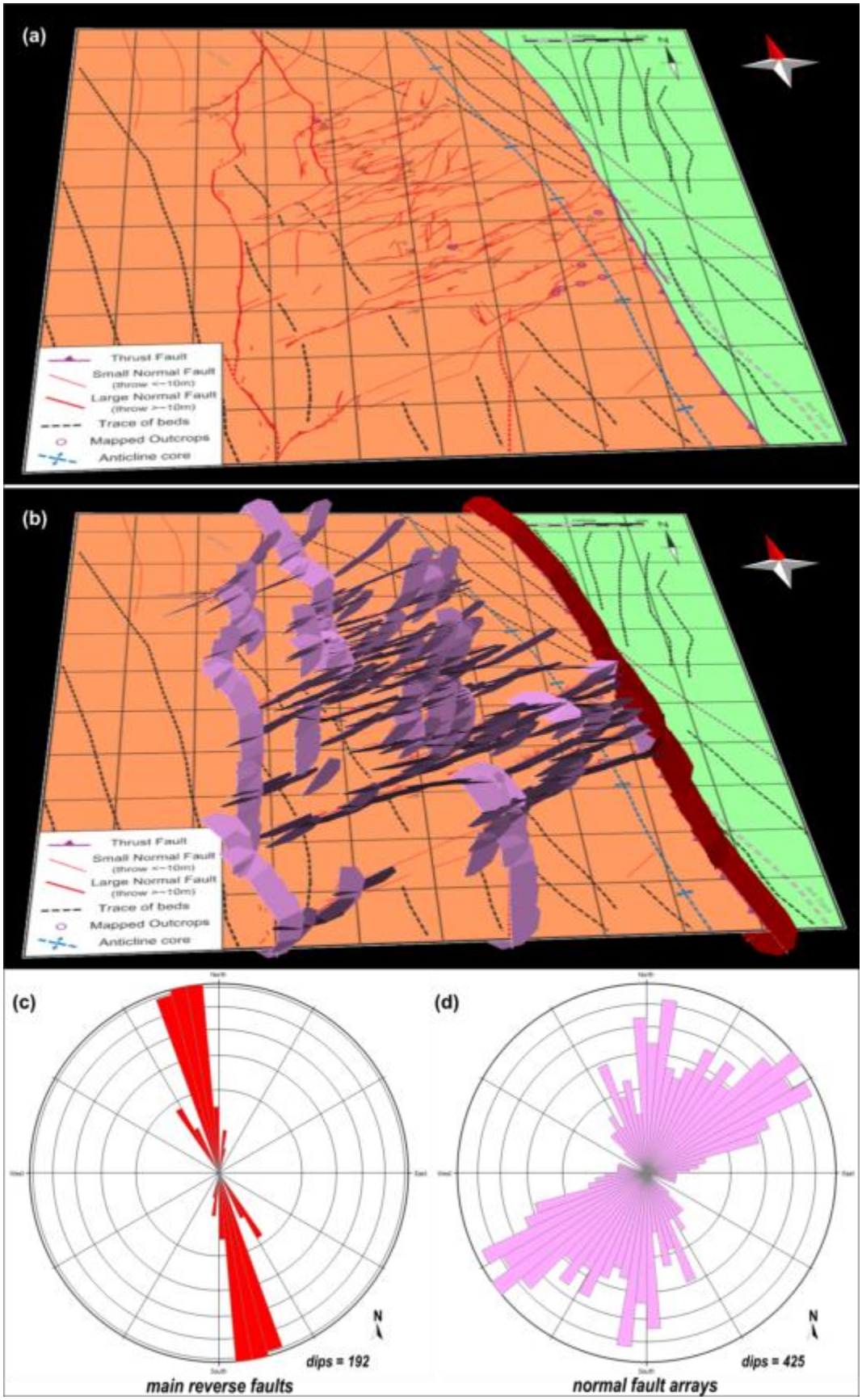

Figure 4.17 (a, b): the distribution of accommodation normal faults within the hanging wall of the Lenghu5 structure; (c, d): strike rose diagrams revealing the relationship between the main reverse faults and the normal faults in the hanging wall.

4.6. Discussion and Conclusions

4.6.1. Effects of Mechanical Stratigraphy on Fault Zone Architecture

The effects of stratigraphy on fault architecture have been widely discussed in previous studies (e.g., Corbett et al., 1987; Couzens and Wiltschko, 1996; Hardy and Finch, 2007; Simpson, 2009). It has been commonly agreed that competent stratigraphy is prone to brittle deformation while weaker stratigraphy inclines to ductile deformation. The detachment folding (e.g., Jamison, 1987; Mitra and Namson, 1989; Homza and Wallace, 1995) and trishear algorithm (e.g., Erslev, 1991; Hardy and Ford, 1997) are related with ductile deformation focused in the stratigraphic units with low competency, in which the bed folding absorbs the majority of the fault displacement (see details in Chapter 3).

Based on the regional transects (S3, S9) and second-order structures (e.g., normal faults in the hanging wall), it is demonstrated that the mechanical stratigraphy plays an important role in controlling the structural styles. In section view, although the displacement is nonuniform along the fault zone, the displacements are decreasing upward in the regional transects S3 and S9 (Figure 4.8). Specifically, the fault displacement decreases when the fault propagates into the clay-rich units (e.g. Sb and Sd, Figure 4.6 and Figure 4.8). This can be attributed to the clay-rich units (e.g., Sb and Sd with low competency) that tend to experience ductile deformation and present lower fault propagation/slip ratios (Hardy and Ford, 1997), which leads to the upward decreasing displacement when a fault propagates from a sandy unit into a clay-rich unit. In plan view, the normal faults also present decreasing throws or even die out when the fault traces propagate into the clay-rich units Sb and Sd (Figure 4.7), because the ductile deformation is accommodated through bedding parallel flexural slip rather than brittle deformation (e.g., Jamison, 1987; Erslev, 1991).

However, in nature, it is uncommon to observe a sequence with completely homogeneous stratigraphy; more commonly are sequences of beds with different lithologies, e.g., inter-bedded mudstone and sandstone. The term mechanical stratigraphy is therefore widely accepted in structural geology as

the subdivision of rocks into discrete mechanical units defined by properties such as tensile strength, elastic stiffness, brittleness and fracture mechanics properties (e.g., Corbett et al., 1987; Cooke, 1997; Laubach et al., 2009). A mechanical stratigraphy with heterogeneity has been shown to increase the complexity of the fault zone architecture in thrust systems (Woodward and Rutherford Jr, 1989; Woodward, 1992; Pfiffner, 1993).

In this study, the regional stratigraphy of the Lenghu5 is divided into five packages, which are Sa to Se. The packages Sb and Sc present lower mechanical heterogeneity than the packages Sa, Sd and Se. Given the package Se is not influenced too much by the fault development, the packages Sa-Sd are used to identify the effects of mechanical stratigraphy on the fault architecture. In the southern anticline (Figure 4.10), a normal fault developed in low heterogeneity package (e.g., Sd) is prone to transfer to be multi-plane normal fault arrays when propagating into high heterogeneity package (e.g., Sb and Sc). Moreover, within the central main thrust fault zone, the splay faults and fault lenses are developed in the footwall where the high heterogeneity package Sd is truncated by the fault zone; while only a single reverse fault is developed where the low heterogeneity package Sb and Sc are truncated in the northern end. Therefore, it is inferred that the fault zone presents a minimal complexity when the faults cut a sequence with low mechanical heterogeneity, while a greater complexity of fault zone is formed when the faults cut a sequence with high mechanical heterogeneity. This observation is in an agreement with the previous studies focusing on fault architecture in a multi-layered sequence (Eisenstadt and De Paor, 1987; Peacock and Sanderson, 1992; McGrath and Davison, 1995; Childs et al., 1996a; Schöpfer et al., 2006).

Schematic models have been built to demonstrate the effects of mechanical heterogeneity on the fault architecture at regional scale (Figure 4.18). The models illustrate the increasing density of splay faults and fault lenses when the mechanical heterogeneity increases, either in the contractional or extensional regimes. The models also present an increasing fault zone width when cutting a sequence with high heterogeneity. Therefore, the mechanical heterogeneity plays a key control on the fault zone architecture, e.g., the

splay faults, the fault lenses, fault zone width, etc. Therefore, in the field, the increasing density of splay faults and fault lenses in a widening fault zone can probably be used as indicators of increasing mechanical heterogeneity.

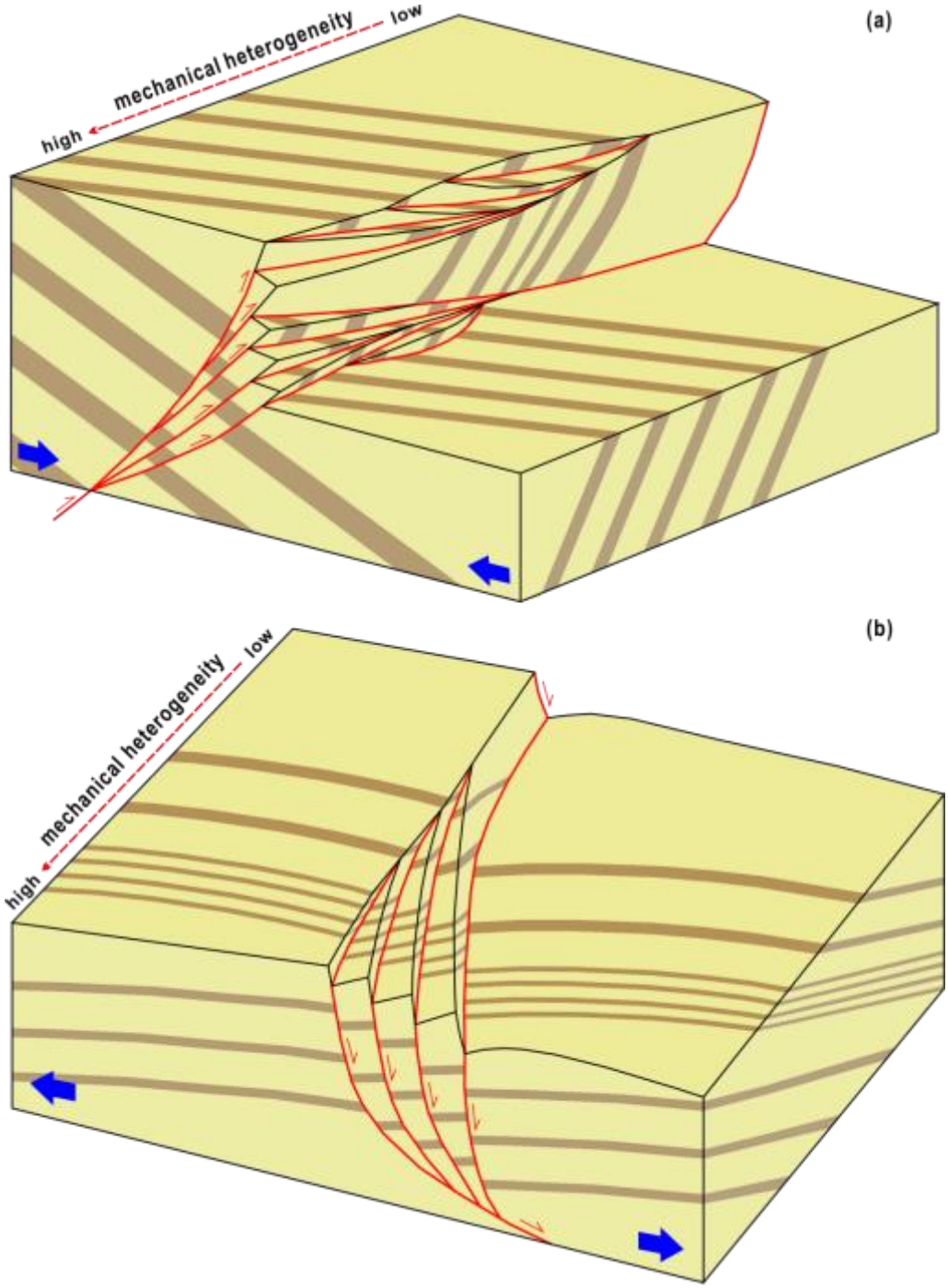

Figure 4.18 Schematic models of reverse faults and normal faults demonstrate the control of mechanical stratigraphy on the fault zone architecture. Single plane faults form in sequences with low mechanical heterogeneity; while complex fault zones form in sequences with high mechanical heterogeneity, generating splay faults and fault lenses.

4.6.2. Predict Second-Order Structures by Strain Analysis on Simplified Model

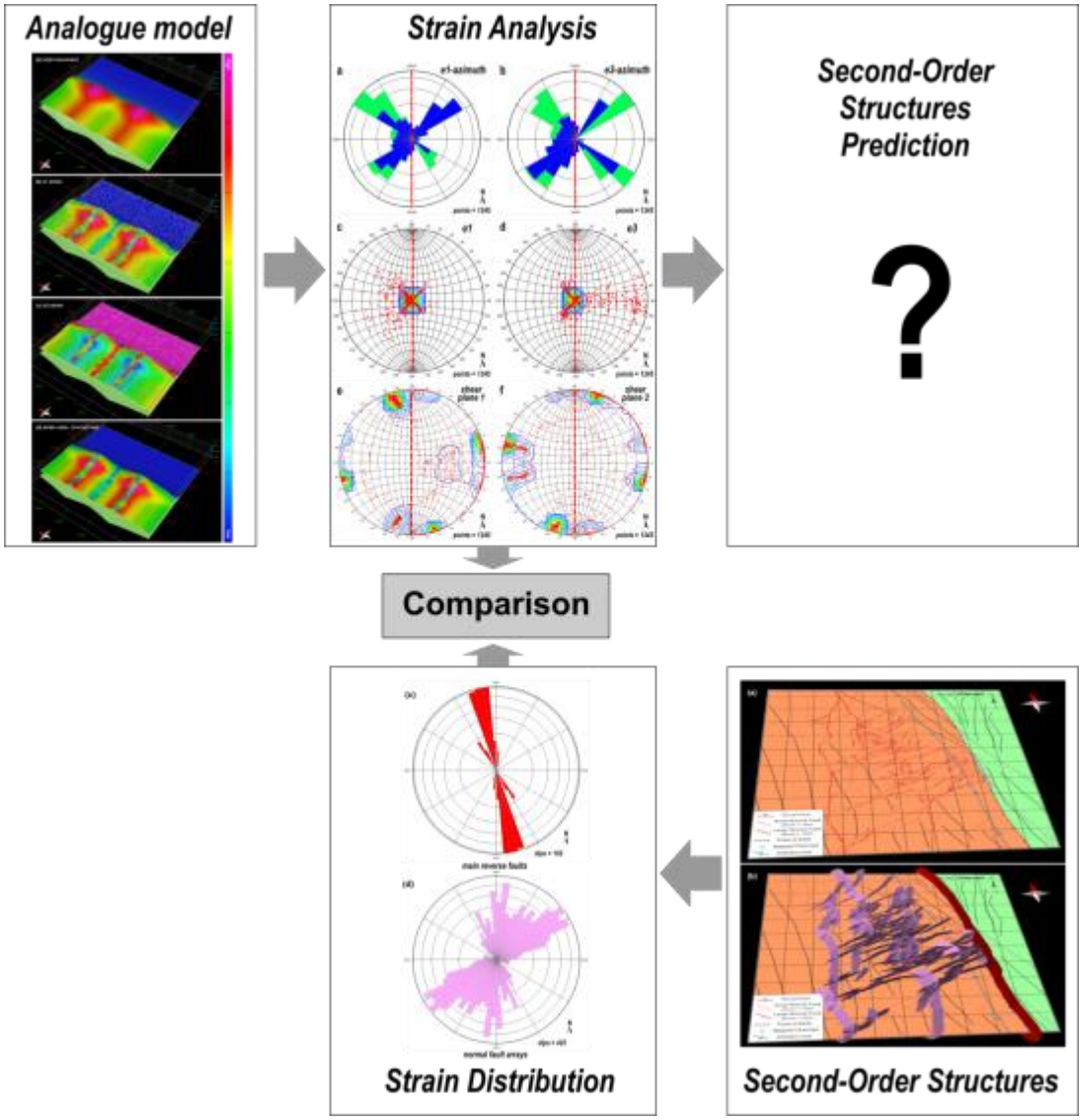

Figure 4.19 Schematic workflow demonstrates application of strain analysis to natural structures.

It is common for geologists to employ simplified models to simulate the strain distribution of natural structures. The strain analysis can be used to predict the resultant structural geometry and even second-order structures, e.g., joints, fractures or faults. In this research, the stereonet plots of potential shear planes are created to predict second-order normal faults observed in the Lenghu5 structure. However, as the simplified model is a simplified example, natural complexity has not been fully considered in strain analysis. Therefore, it is usually very difficult to predict the second-order structures directly from the stereonet plots (Figure 4.19). In this situation, it is useful to study the second-order structures in the field alone. The field results can be

compared with the strain analysis. If the strain distribution and strain analysis results are comparable to each other, it suggests the simplified model can be used to simulate the development of the natural structures.

4.6.3. 3D models Integrating Multi-Scale Structures

By integrating the regional stratigraphy, seismic-scale section, regional transects and meso-scale fault system maps, the 3D models integrate multi-scale structures. The 3D models integrating across multi-scale structures (Figure 4.11) suggest:

(i). The overall structure of Lenghu5 is controlled by the NW-SE striking fault zone comprising a main reverse fault and several splay faults. Two anticlines are developed in the hanging wall corresponding to two topographic culminations. The regional stratigraphic correlation between the hanging wall and the footwall can assist fault displacement estimation of the fault zone.

(ii). The lateral structural variation leads to high complexity in the fault zone and the anticlines in the hanging wall. The fault zone varies from northwest to southeast: (a) main thrust only, (b) main thrust + one footwall splay, (c) main thrust + two footwall splays, (d) main thrust + a blind footwall splay or (e) main thrust + a hanging wall splay (Figure 4.10). The hanging wall anticlines are not continuous along the fault zone, but are linked by the middle saddle where the topography is relatively flat. The southern anticline exposes more stratigraphy in the core than the northern anticline, indicating nonuniform fault displacement along the fault zone. The variability of the fault zone and the discontinuity of the hanging wall anticlines all reveal a nonuniform deformation in the Lenghu5 structure.

(iii). The second-order structures are developed in both hanging wall and footwall. A pair of structures, a tight syncline and an open anticline, are present in the footwall against the southern anticline, which may be attributed to the underlying blind splay fault. The normal faults are primarily developed in the hanging wall and present a fold-core-concentrated strain distribution. These second-order structures are formed to accommodate the overall strain in the Lenghu5 structure, as

the nonuniform deformation in Lenghu5 results in the locally concentrated stress, e.g., the footwall adjacent to the fault zone, the anticline cores, and the middle saddle between the two anticlines. The concentration of second-order structures can be treated as indicators of areas where the structural lateral variation increases.

(iv). The mechanical stratigraphy plays an important control on the structural geometry and the fault architecture. The competent beds (e.g., sandstones) tend to deform by brittle deformation; while the clay-rich sandstones or mudstones are prone to ductile deformation. In section view, the fault zone displacement decreases upward when propagating into clay-rich units; in map view, the displacements of the normal faults also decrease or die out when propagating into clay-rich units.

The multi-scale modelling presented allows us to integrate both the overall structural geometry (e.g., main thrust fault zone, primary folds) and the second-order structures (e.g., minor folds in the footwall, small normal faults in the hanging wall) into a new detailed structural model. The interactive analyses of the multi-scale structures presented have revealed the internal relationship between the regional and the meso-scale structures.

Having understood the regional-scale 3D fault architecture of the Lenghu5 structure, the next chapter will demonstrate meso-scale structural analysis of the Lenghu5 structure. The meso-scale structural analysis will focus on more detailed deformation features within fault zones of different fault types (including main reverse faults, minor reverse faults and normal faults in the Lenghu5 structure) to understand the fault zone evolution and deformation mechanisms.

Chapter 5
Meso-scale Detailed Fault Architecture of the Lenghu5 Structure, Qaidam basin

5.1. Introduction

In natural structures, it is common to observe a mechanically layered sequence of beds subject to stress. In the previous studies focusing on the deformation mechanisms of mechanically layered sequence, it has been reported that faults tend to form first in the brittle beds (e.g. sandstones or carbonates); while the weak/ductile beds (e.g. clay beds) deform by distributed shear to accommodate the overall strain (Eisenstadt and De Paor, 1987; Peacock and Sanderson, 1992; McGrath and Davison, 1995; Childs et al., 1996a; Schöpfer et al., 2006). Several quantitative dynamic models have been presented (e.g., Egholm et al., 2008; Welch et al., 2009) to analyse the mechanics of clay/shale smearing along faults in layered sand and shale/clay sequences. These models predict that the isolated initial faults formed within the brittle beds will grow until eventually they link up with increasing strain, by propagating across the ductile intervals to create a complex fault zone architecture (Peacock and Sanderson, 1991; Childs et al., 1996a; Walsh et al., 1999; Walsh et al., 2003). Many natural examples support those previous studies on detailed fault zone architecture, e.g., the deformed interbedded sandstones and shales derived from the Cutler Formation juxtaposed against limestone from the Honaker Trail Formation near the entrance to Arches National Park (Davatzes and Aydin, 2005); the outcrop studies from a minor normal-fault array exposed within Gulf of Corinth rift sediments, Central Greece (Loveless et al., 2011); and the multilayer systems in the South-Eastern basin, France (Roche et al., 2012). Fault zone models defining the fault zone architecture have also been proposed, e.g., the fault zone model in crystalline rocks (Caine et al., 1996); the fault zone model in poorly lithified sediments (Heynekamp et al., 1999; Rawling and Goodwin, 2003, 2006); and the dynamic fault zone models within poorly consolidated sediments by Loveless et al. (2011). The effects of fault zone

geometry and fault population on the fluid flow properties have also been considered in the previous studies (e.g., Caine et al., 1996; Rawling et al., 2001; Faulkner et al., 2010).

However, most of these previous studies focus on the fault architecture of extensional normal faults. In order to understand the reverse fault architecture and test whether the previous published results associated with extensional faults are applicable to reverse faults, this chapter focuses on the detailed (10cm-1km scale) architecture of reverse faults in the Lenghu5 structure in the northern Qaidam basin that is controlled by compressional deformation (e.g., Yin et al., 2008a; Yin et al., 2008b). The detailed structural maps of well-exposed outcrops are generated based on the data collected in two periods of fieldwork (May/June 2010 and April/May 2011), to understand the detailed meso-scale fault architecture and structural evolution of fault zone in compressional system. This chapter aims to:

(i). document the mapping of fault zone elements of the key outcrops, including reverse and normal faults in low to moderate consolidated sediments with different stratigraphy;

(ii). construct conceptual models to define the reverse fault zone and identify the deformation mechanisms associated with the development of reverse faults;

(iii). understand reverse fault evolution and key parameters that impact the fault zone architecture.

The locations of the outcrops selected for detailed outcrop mapping are marked in the structural map of the Lenghu5 (Figure 5.1). In order to compare and understand the fault zone deformation related to different fault types or fault displacements, the outcrops are classified into three types: main reverse faults (throw >500m, Figure 5.2-Figure 5.10), minor reverse faults (throw <10m, Figure 5.11-Figure 5.14) and normal faults (throw <10m, Figure 5.15 and Figure 5.16). The dynamic fault zone evolution (Figure 5.17 and Figure 5.18) and the deformation mechanisms associated with reverse faults (Figure 5.19 and Figure 5.20) are then considered. Based on the detailed outcrop maps, a new detailed thrust fault zone model is proposed and compared with the previously published fault zone models of normal faults

(Figure 5.21). The effects of these factors on the reverse fault architecture are also evaluated, e.g., the fault displacement, the bed thickness, the stratigraphic heterogeneity and the mechanical heterogeneity (Figure 5.23 and Figure 5.24).

5.2. Methods

5.2.1. Detailed Outcrop Mapping

The detailed structural maps of meso-scale well-exposed outcrops were constructed during fieldwork in order to understand the fault architecture and structural evolution in detail. The resultant detailed outcrop maps not only delineate the geological elements of the fault zones, e.g., faults, fractures and folds, but also present the internal relationship between these elements, e.g., cross-cutting relationships, cataclasis and clay smear.

The specific workflows for the detailed outcrop mapping are:

(1). Select well-exposed outcrops. Outcrops of a high quality are vital to detailed structural outcrop mapping. In the Qaidam basin, some of the outcrops are severely covered by massive weathering materials; therefore, it is important to clean all the weathering covers off to expose a fresh surface of outcrop. When selecting outcrops the following aspects should be considered: firstly, a vertical outcrop is as perpendicular to the strike of the main structure as possible; secondly, the size of the outcrop is between 2m to 10m in order to be able to capture data at an appropriate level of detail (the bigger scale structures have been considered in Chapter 4); thirdly, the fault should be definable in order to quantify deformation detail in the fault zone.

(2). Print high-resolution photos of the outcrops. High-resolution photos of the outcrops are taken and printed on glossy photo papers, including photos of both overall outcrop and zoomed in local parts. The photos are taken perpendicular to the outcrop, in order to minimize angular distortion.

(3). On-site interpretation of the outcrops. Lay a transparent plastic sheet on top of the printed photos and make interpretation on this sheet. The interpretation uses underlying printed photos as templates but does not entirely depend on them such that small scale or poorly imaged details are still cap-

tured on site. The stratigraphic columns are also constructed for the outcrops. Here caution should be given to two aspects in the interpretation. Firstly, in the field, often the exposure surface is not perpendicular to the fault plane, which makes the observed outcrops more difficult to interpret. In this situation, the necessary remarks are attached to the interpretation. Secondly, all the details in and out of the fault zone must be collected as much as possible, as comparison between the fault zone and undeformed layers is vital to understand the deformation in the outcrops during the faulting process.

(4). Construction of detailed outcrop maps based on the on-site outcrop interpretation. The on-site outcrop interpretation are scanned and then digitized in CorelDRAW. There are several kinds of elements in the digitalization, e.g., horizons, faults, labels (name and lithology of horizon), measurements and filling colour. The selected filling colour is similar to that observed in the outcrops to represent lithology of the rocks.

5.2.2. Fault Architecture Characterization

The resultant detailed outcrop maps are used to characterize the fault zone deformation. Both reverse faults and normal faults cutting the same section from the Lenghu5 structure are studied:

(i). well-exposed outcrops of the main reverse fault cutting the Lenghu5 structure are mapped in detail, of which the fault displacements were calculated to exceed 500m in Chapter 4;

(ii). outcrops of minor reverse faults (at 2-10m scale) are mapped to compare with main reverse fault outcrops, in order to identify the effects of fault displacement on the fault zone geometry;

(iii). outcrops of normal faults with displacements of 10cm-10m are also mapped to assess the relationship to thrust faults and deformation mechanisms involved in generating different fault rock types.

The mapped outcrops are located in the hanging wall of the Lenghu5 structure, where a regional-scale anticline is developed and forms the major geometry in the subsurface (see the regional structural map and cross sections in Chapter 4). These outcrops are analysed by integrating geological ele-

ments such as fault displacement, lithology and mechanical stratigraphy, to evaluate the effects on the fault zone deformation.

5.2.3. Deformation Mechanisms and Dynamic Fault Evolution

Based on the fault zone characterization of different types of faults, the deformation mechanisms associated with the reverse faults are assessed. The dynamic fault zone evolution is then considered for both reverse faults and normal faults. The effects of possible controlling factors (e.g., fault displacement, stratigraphy and mechanical heterogeneity) on the fault architecture are also evaluated. For example,

(i). the outcrops with different throws (main reverse faults TF1-TF4 and minor reverse faults F1-F3) are compared to investigate the effects of fault displacement;

(ii). the outcrops with a sequence of beds with different lithologies (mudstone-dominated sequence of F1 and sandstone-dominated sequence of F2) are used to investigate the effects of stratigraphy;

(iii). the outcrops with similar stratigraphy but different vertical heterogeneity (NF1 and NF2) are compared to understand the effect of mechanical heterogeneity.

The outcrop-based fault architecture characterization in the Lenghu5 structure allows us to propose a conceptual model to define the fault elements in contractional structures. In the fault model, the influences of the different parameters on the fault architecture are evaluated, e.g., fault displacement, bed thickness, stratigraphy and mechanical heterogeneity. This allows a comparison between published normal fault models with our observations on reverse faults. This fault model can also provide hints to aid interpretation for the micro-scale analysis in Chapter 6 where the Scanning Electron Microscope is employed to investigate the micro-deformation features of the fault rocks developed within the fault zones.

5.3. Fault Architecture Characterization - Main Reverse Faults within the Fault Zone

Based on the detailed maps of outcrops, the fault architecture are characterized into three types of faults (Figure 5.1): (i). the main reverse faults TF1, TF2, TF3 and TF4; (ii). the minor reverse faults F1, F2 and F3; and (iii). the minor normal faults NF1 and NF2.

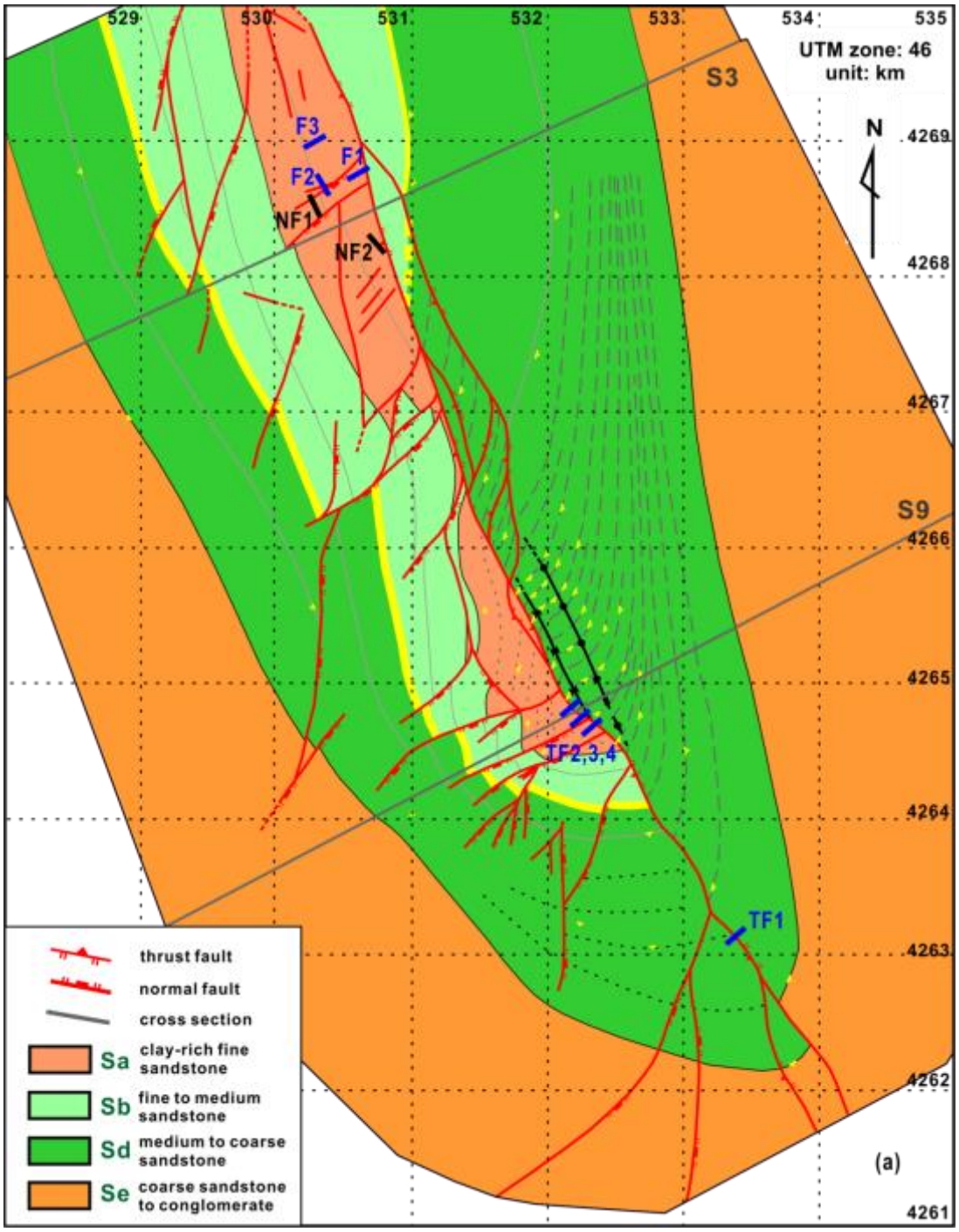

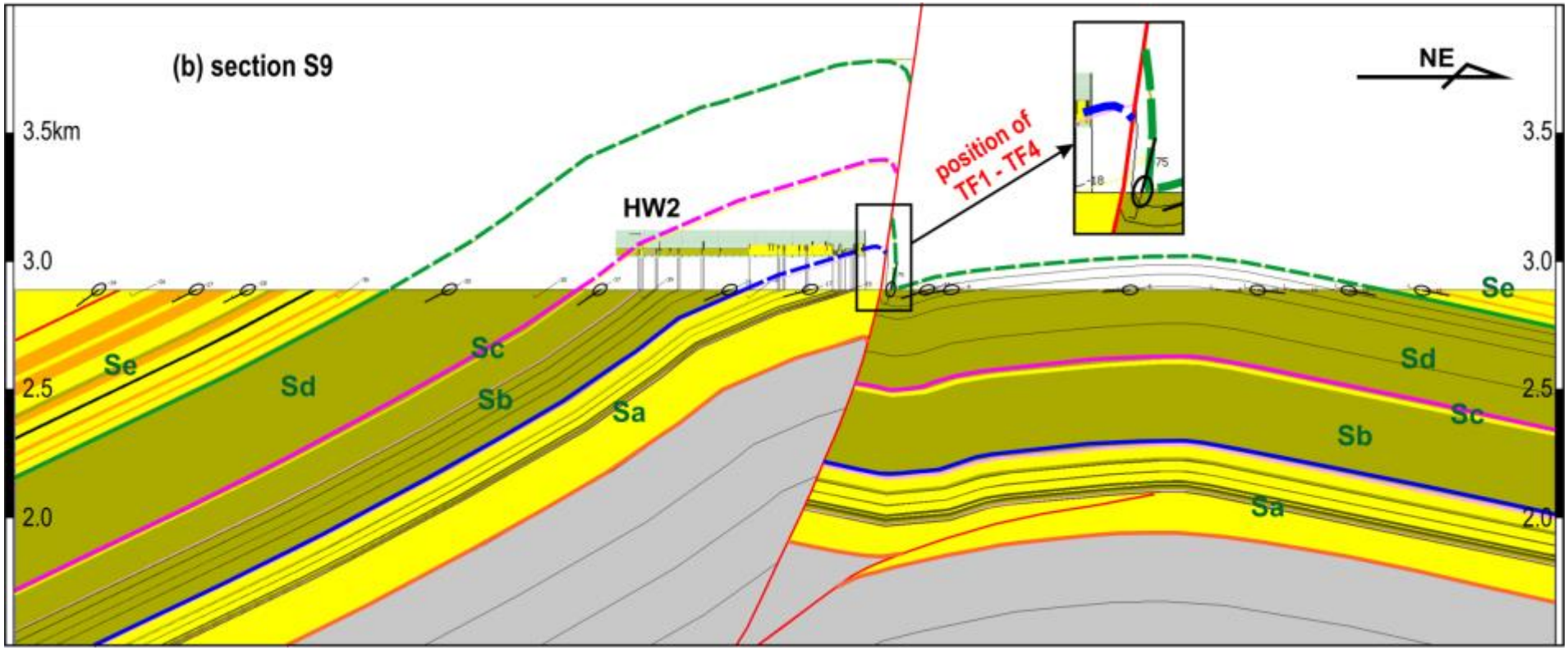

Figure 5.1 The structural map (a) and cross section (b) show the locations of outcrops selected for detailed outcrop mapping.

5.3.1. Main Reverse Faults: TF1

The main reverse fault TF1, ~40m wide and ~30m high, is well exposed and located in the southern end of the Lenghu5 structure (Figure 5.1). Based on the section analysis (Chapter 4), the fault throw of this main reverse fault is 700-800m (Figure 5.1b), which is large enough to be imaged on seismic reflection data. However, the field observation suggests that the main reverse fault TF1 is not a single-plane fault, but comprises several splay faults with varying amounts of strain.

Figure 5.2b shows the general structural domains present in this outcrop, i.e.,

(i). a high strain domain: intensively deformed main reverse faults with fault lenses in the fault zone;
(ii). a medium strain domain: minor peripheral reverse faults within footwall;
(iii). a low strain domain: slightly deformed hanging wall.

According to this classification, the fault splays within the outcrop TF1 can be divided into three groups:

(i). high strain domain splay faults TF1-4/TF1-5 and TF1-6;

(ii). medium strain domain splay faults TF1-3 and TF1-2;

(iii). low strain domain splay fault TF1-1.

The individual outcrops of the high to low strain reverse faults are mapped in detail and have been integrated into a composite map (Figure 5.2c). The majority of deformation is concentrated into the two high strain reverse faults TF1-4/TF1-5 and TF1-6. The throws of these faults cannot be measured because of the unmatchable stratigraphy in the two walls of the fault domain (minimum hundreds of meters based on section analysis in Chapter4). The interval between the two high strain reverse faults experienced medium strain deformation (TF1-3). In the footwall of TF1-6, another medium strain reverse fault TF1-2 is developed, of which the throw reaches up to 2m. A low strain reverse fault TF1-1 is observed in the further footwall of TF1-6. The undeformed or slightly deformed part is the sub-horizontal hanging wall to the left of TF1-4/TF1-5.

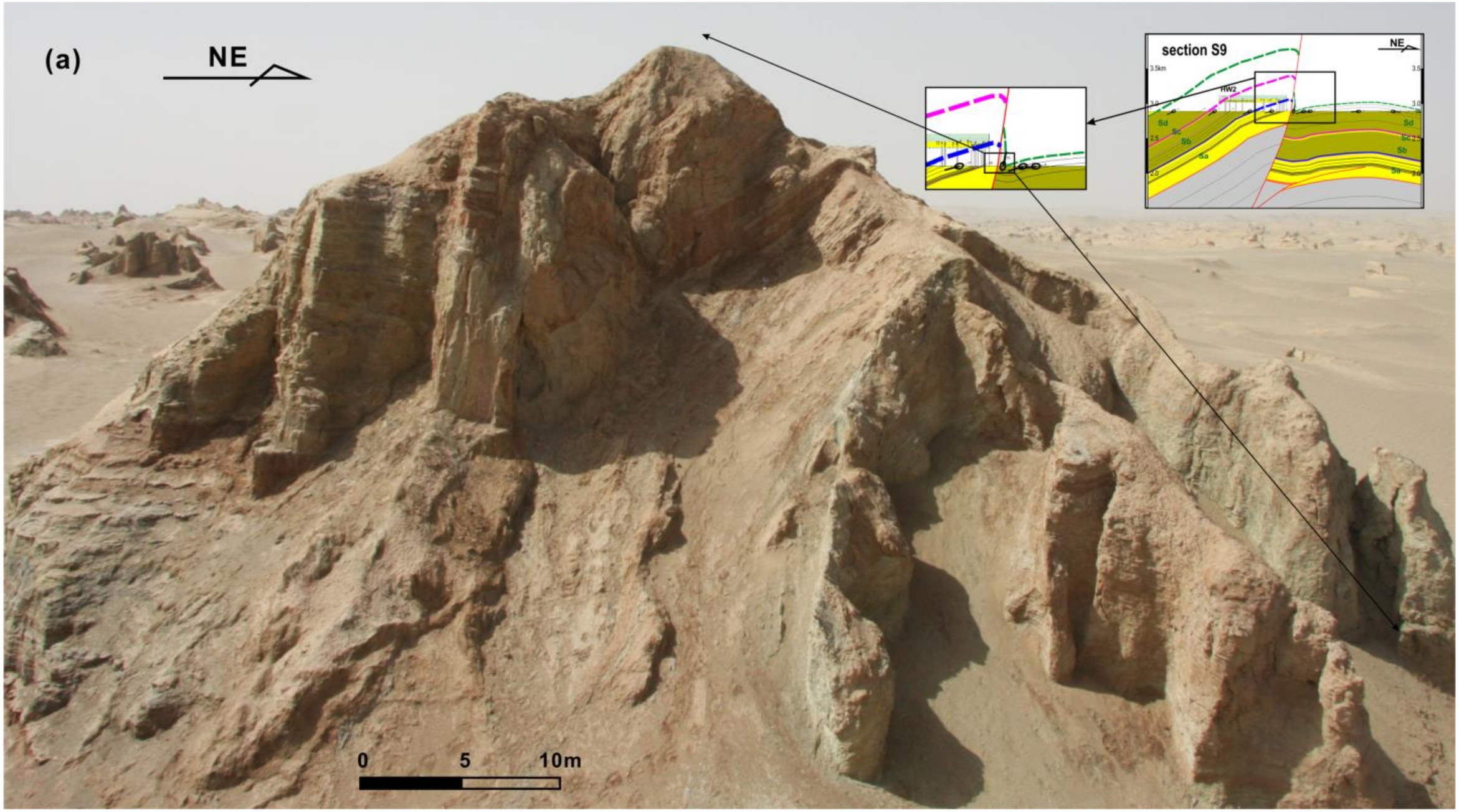
(a)
NE
section S9
NE
HW2
Sd
Sc
Sb
Sa
0
5
10m

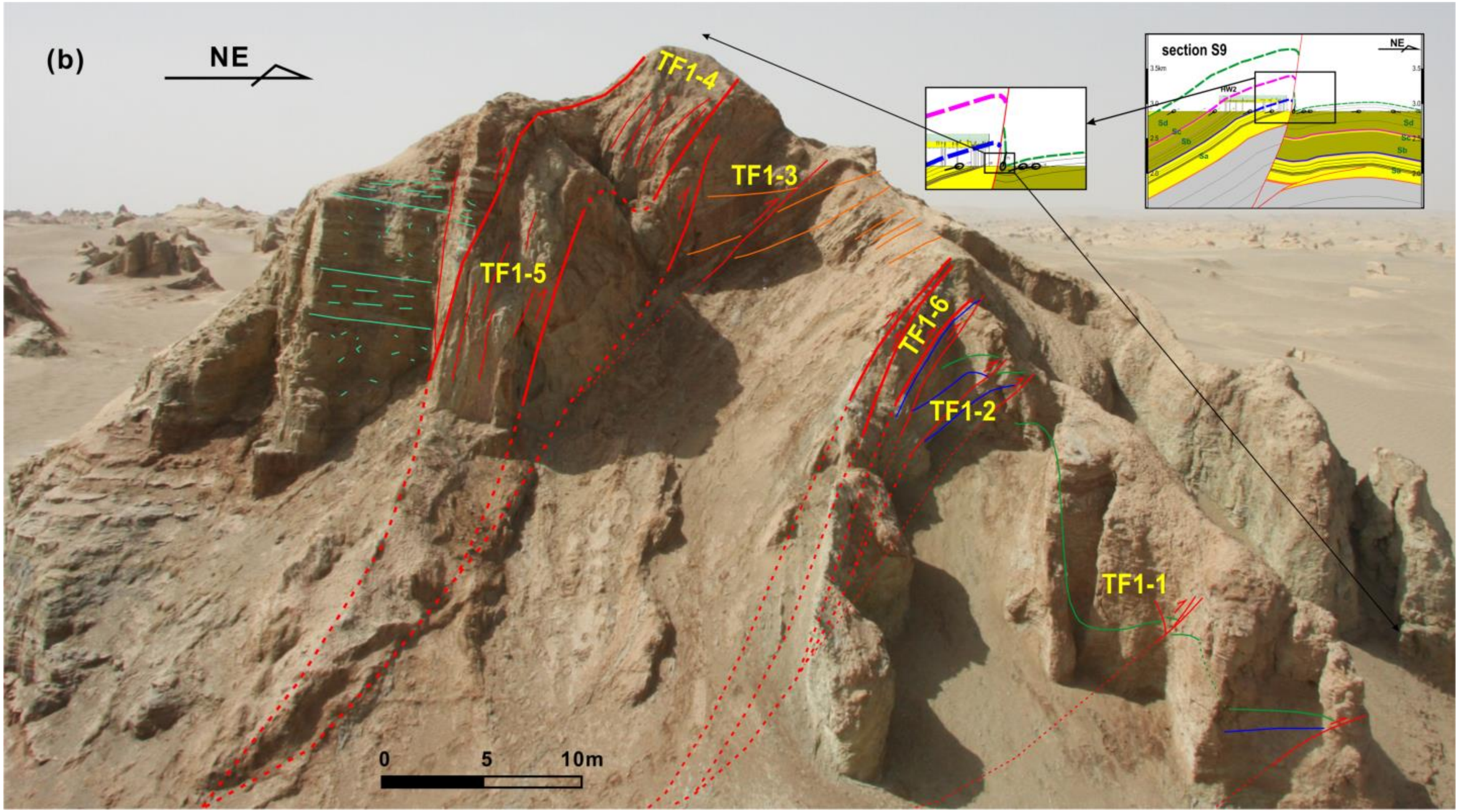
(b)
NE
TF1-4
TF1-3
TF1-5
TF1-6
TF1-2
TF1-1
section S9
NE
HW2
Sd
Sc
Sb
Sa
0
5
10m

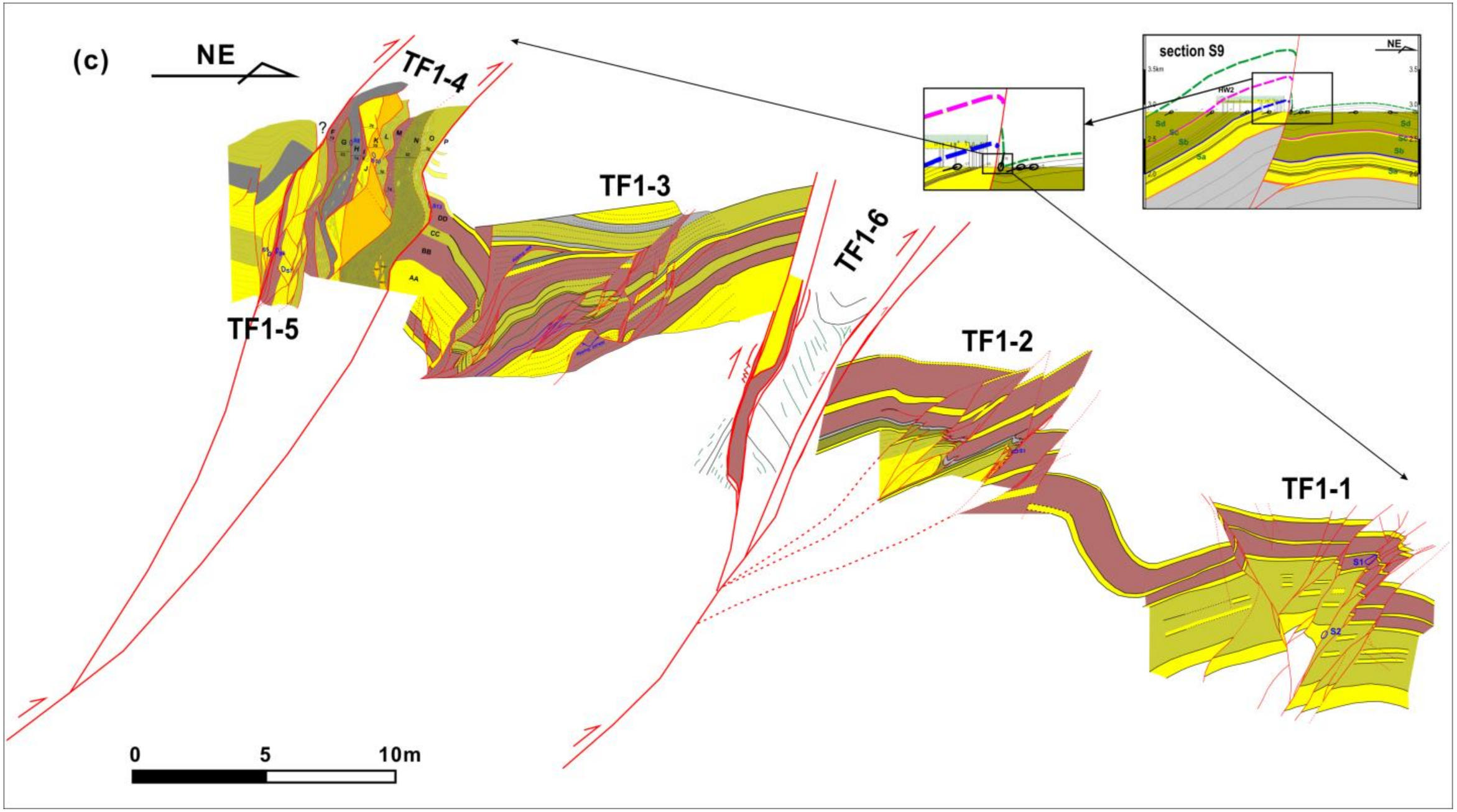

Figure 5.2 The well-exposed outcrop TF1 (a) comprises high strain splay faults TF1-4/TF1-5 and TF1-6; medium strain splay faults TF1-3 and TF1-2; and low strain splay fault TF1-1 (b). (c): A composite of detailed outcrop maps of TF1. In the composite outcrop map (c), the filled colour represents the lithology of the rocks (i.e., yellow for sandstones; greyish-yellow for impure sandstones; grey/red for mudstones/shales).

(1). High Strain Splay Faults: TF1-4/TF1-5 and TF1-6

The outcrop TF1-4 is directly in contact with the slightly deformed hanging wall (left hand side of Figure 5.2) and has a steeply dipping fault zone (70-80°) with sheared stratigraphy comprising foliated fault rocks of primarily shales and some sandstones (Figure 5.3). The shales are vertically smeared into this fault zone from the hanging wall stratigraphy (e.g., unit A, F, H, N, etc.), while the sandstones are faulted and thinned by fault offsets (e.g., unit K and E) forming boudins in the attenuated layers. Although the fault rock domains are vertical in the fault zone, the bedding cannot be identified because the original bedding is destroyed by the intense smearing and faulting. In the NE (right) end of TF1-4, the sub-horizontal footwall bedding shows no or only slight deformation. A primary slip surface separates the steeply dipping and sheared fault zone from the footwall sequence, which suggests this slip surface forms the NE boundary of the fault zone. There are also some boudins derived from the footwall stratigraphy, e.g., the segments of unit AA in unit N.

As shown in Figure 5.2, the outcrop TF1-5 is located ~5m to the SE of TF1-4. TF1-5 is composed of the SW (left) hanging wall with slight or no deformation and the NE (right) intensely deformed reverse fault zone that is similar to the high strain fault zone of TF1-4. The steeply dipping fault zone presents foliated fault rocks of highly sheared pink shales and faulted sandstones. The sandstones attenuate with fault-bounded boudins that become encased within the clay smear. A discrete slip surface separates the steeply dipping fault zone from the sub-horizontal beddings in the hanging wall, which suggests it forms the left boundary of the fault zone. The bedding in the hanging wall adjacent to the fault shows the development of a shear zone into the fault zone.

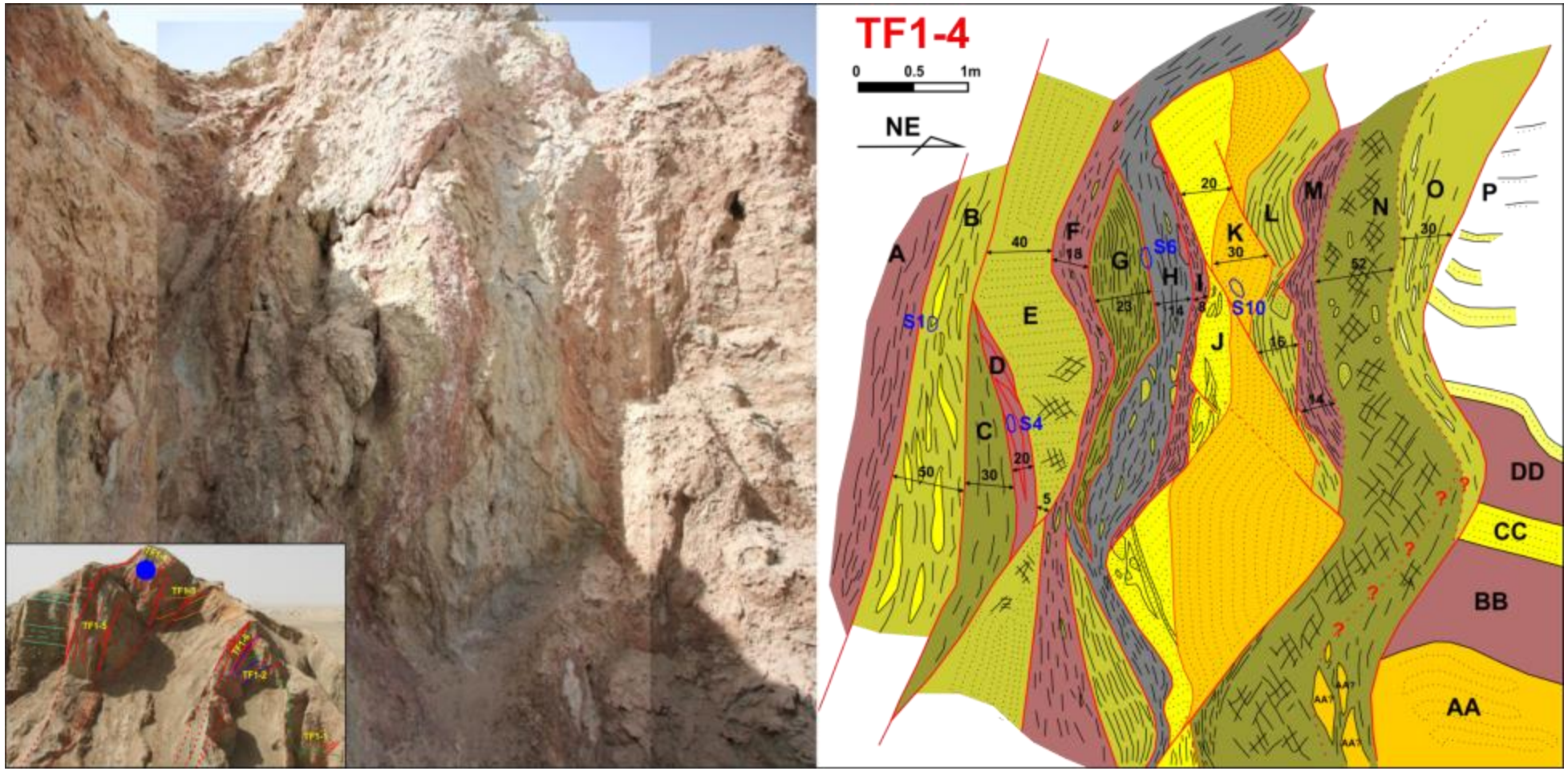

Figure 5.3 Detailed outcrop map of TF1-4 showing highest strain in TF1 (see position in Figure 5.2). In TF1-4, bedding cannot be identified because of the intense deformation. The mudstones together with sandstones are smeared into this fault zone from the hanging wall. In the right end, it becomes the more gentle bedding that is the same as the bedding in the left end of TF1-3.

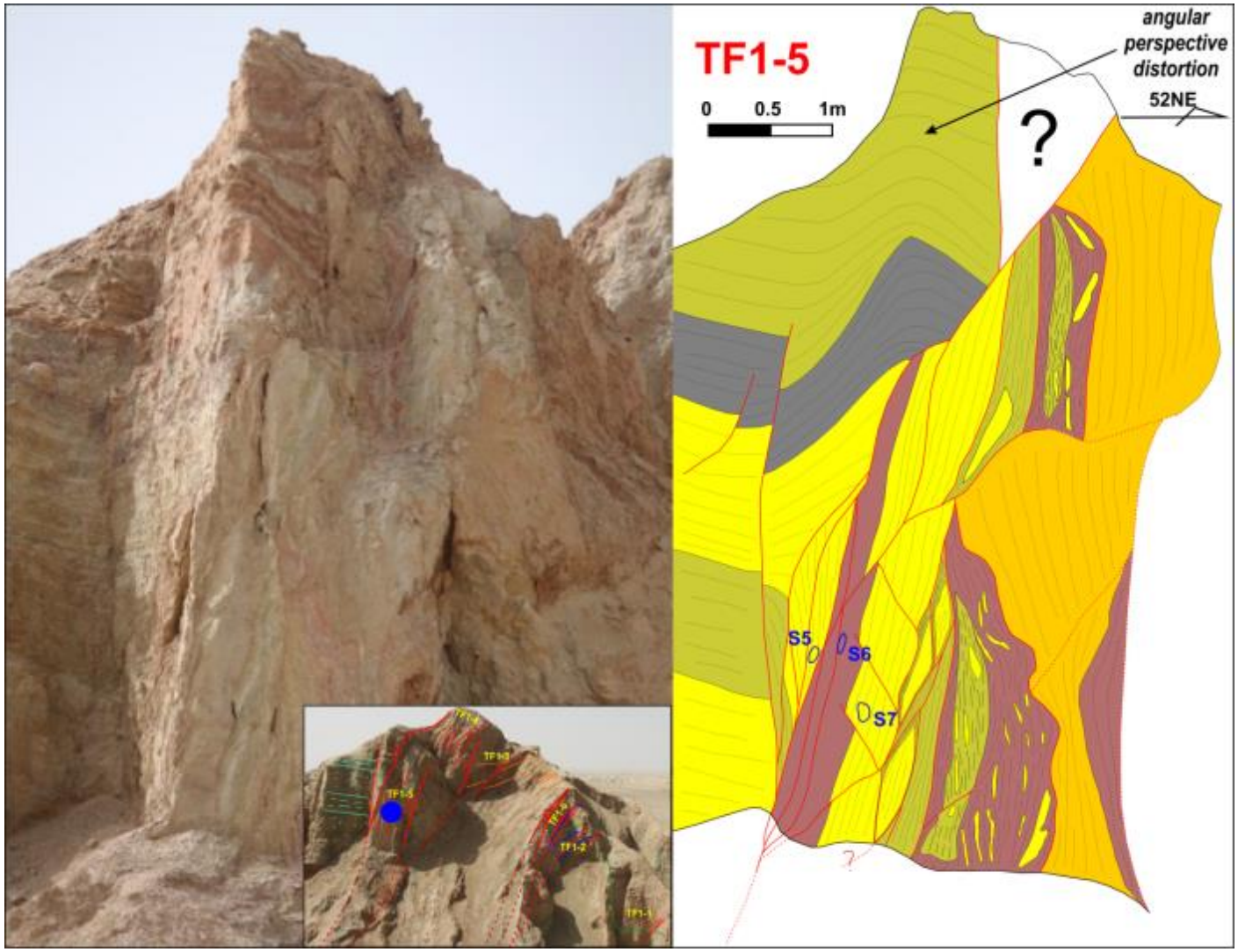

Figure 5.4 The splay fault TF1-5 (position in Figure 5.2) comprises two parts: the SW (left) slightly deformed or undeformed beddings and the NE (right) intensely deformed zone which is similar to TF1-4. A slip surface separates the low strain hanging wall (left) and the high strain fault zone (right). The sub-horizontal beddings in the hanging wall are curved because of angular perspective.

Because of the limited exposure, the outcrop TF1-6 was only mapped in a sketch (Figure 5.5). TF1-6 is a high strain fault zone domain (50-100cm wide) with highly sheared fault rocks including sand lenses encased in a clay rich matrix. In this highly sheared fault zone, the original bedding cannot be identified because of the very intense deformation. Several sandstone blocks are captured in the smeared clay/shale. The shape and distribution of the sandstone blocks suggest that the sandstones and surrounding smearing shales are derived from the hanging wall. The clay smearing from hanging wall into the fault zone cannot be observed because of the very large fault displacement (hundreds of meters based on section analysis in Chapter4), which is similar to that observed in outcrops TF1-4 and TF1-5. On the NE (right) footwall, the reverse faults of outcrop TF1-2 merge into the outcrop TF1-6. Discrete slip surfaces separate the high strain deformation of TF1-6 from the adjacent medium strain reverse faults of TF1-2.

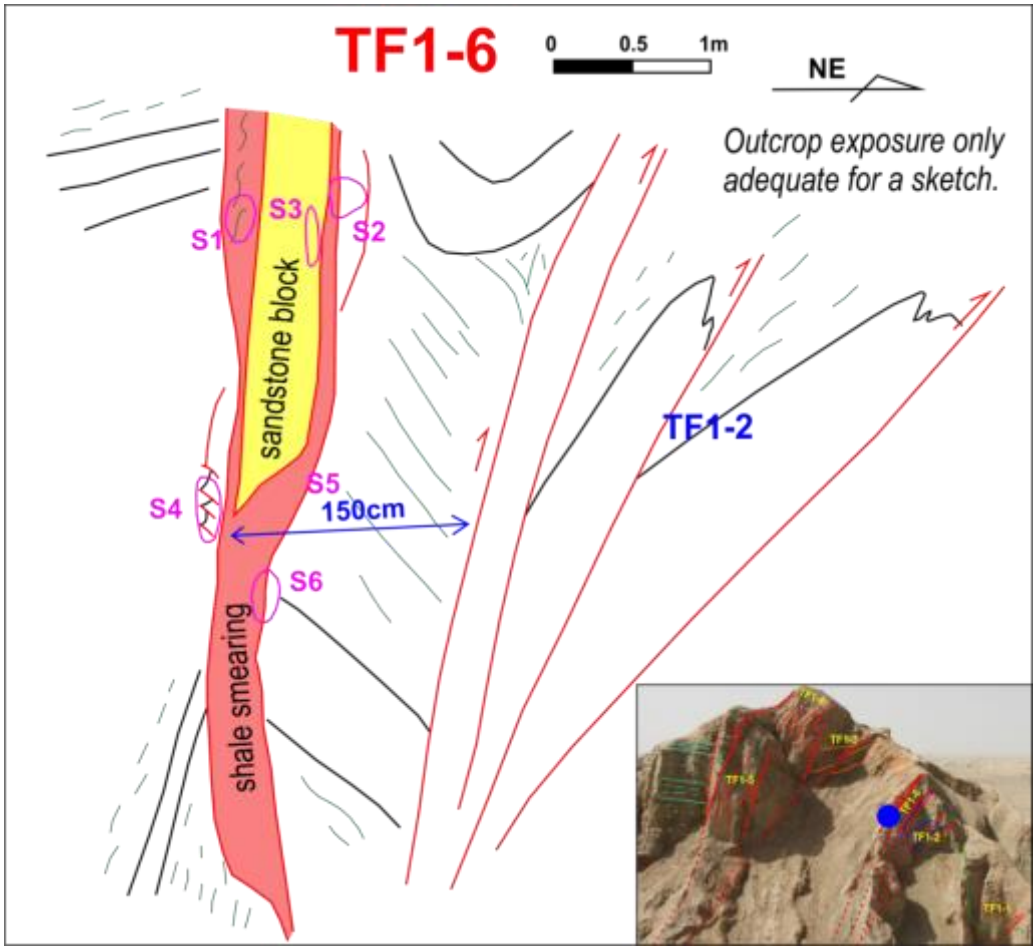

Figure 5.5 Detailed outcrop map of TF1-6 with high strain. The fault core is dominated by the smeared shales with some faulted sandstone blocks bounded within the smear zone. Sharp slip surfaces separate TF1-6 from the medium strain splay fault TF1-2 to its right.

(2). Medium Strain Splay Faults: TF1-3 and TF1-2

The medium strain domain outcrop TF1-3 is located between the two high strain fault zones TF1-4/TF1-5 and TF1-6 (Figure 5.2b). The stratigraphy of TF1-3 is mainly composed of brown mudstones and grey sandstones. Reverse faults with measurable fault throws (5cm-5m) are abundantly developed in this outcrop. The cumulative throw on these reverse faults is approximately 5-10m. The bedding adjacent to the fault core dips steeply and is folded. However, in contrast with TF1-4/TF1-5 and TF1-6, this outcrop contains low angle reverse faults (30-50°) that offset beds in a tightly folded zone. Through-going faults are developed in the thick homogeneous units (either the thick sandstone or the mudstone beds in the top or bottom of the section) while fault segments and lenses are developed where the stratigraphic heterogeneity increases (e.g., interbedded thin sandstones and mudstones/shales in the central section).

A stack of small reverse faults with medium strains are developed in the immediate footwall of TF1-6, which is also the hanging wall of TF1-2. The maximum throw reaches up to 2m within the imbricated reverse faults. More folding is shown in the clay-rich layers than in the sandy layers, which may be attributed to the physical properties of rocks with high clay/sand ratio. The strain decreases away from the reverse fault to the edge of the fault zone. Reverse fault imbricates form at lower angles than the bounding reverse faults and are mostly discrete faults, but shearing into fault zone is also locally present. Fault lenses are also evident along the reverse faults, particularly where the fault leaves the top of clay-rich layers. Fault lenses are also structural elements that absorb a great amount of fault throw. As the lithology is clay-rich, the fault rocks are dominated by shales/mudstones that have been smeared into the fault zone.

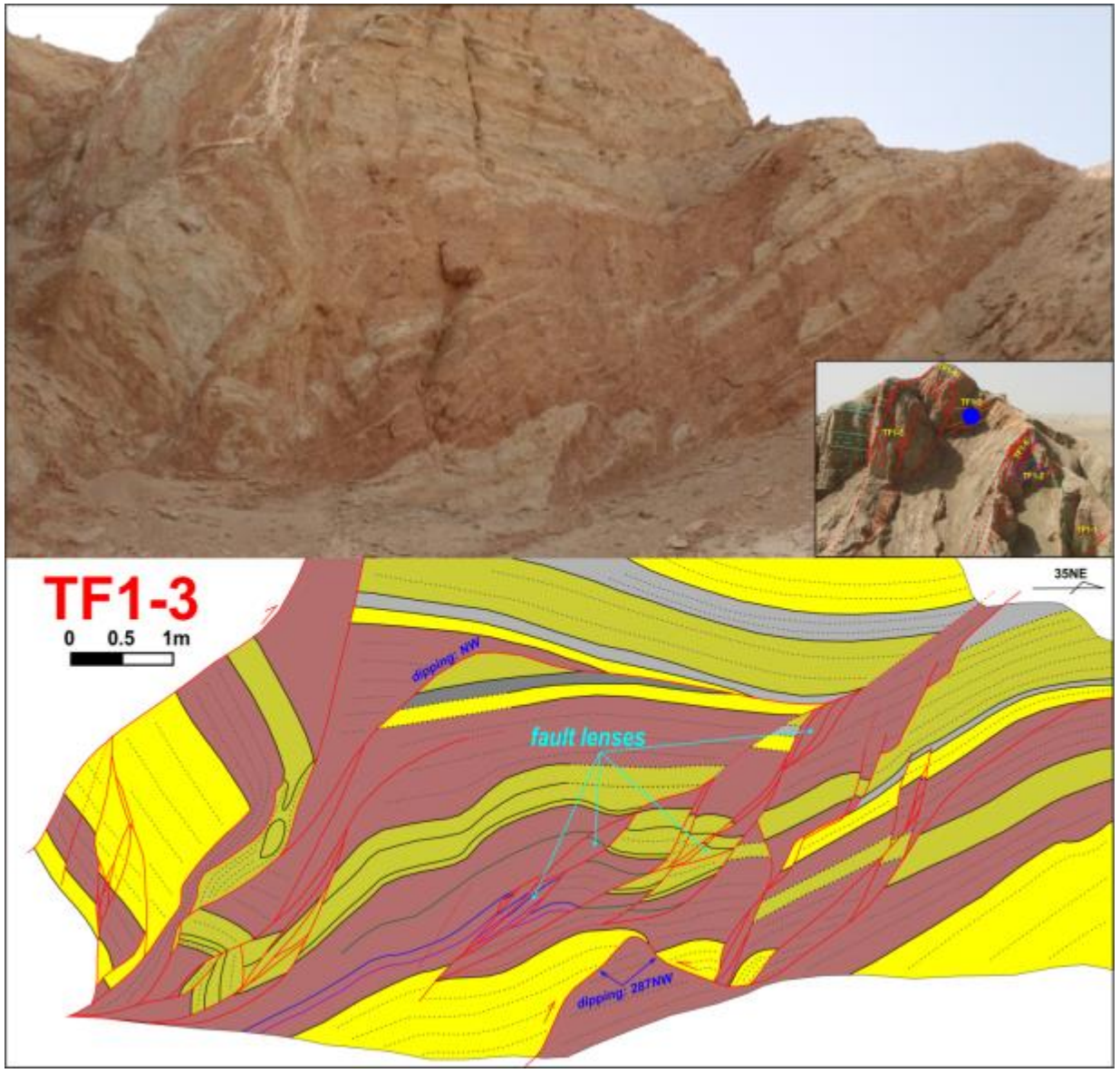

Figure 5.6 Detailed outcrop map of TF1-3, an outcrop with medium strain. The faults are not perpendicular to the cross section.

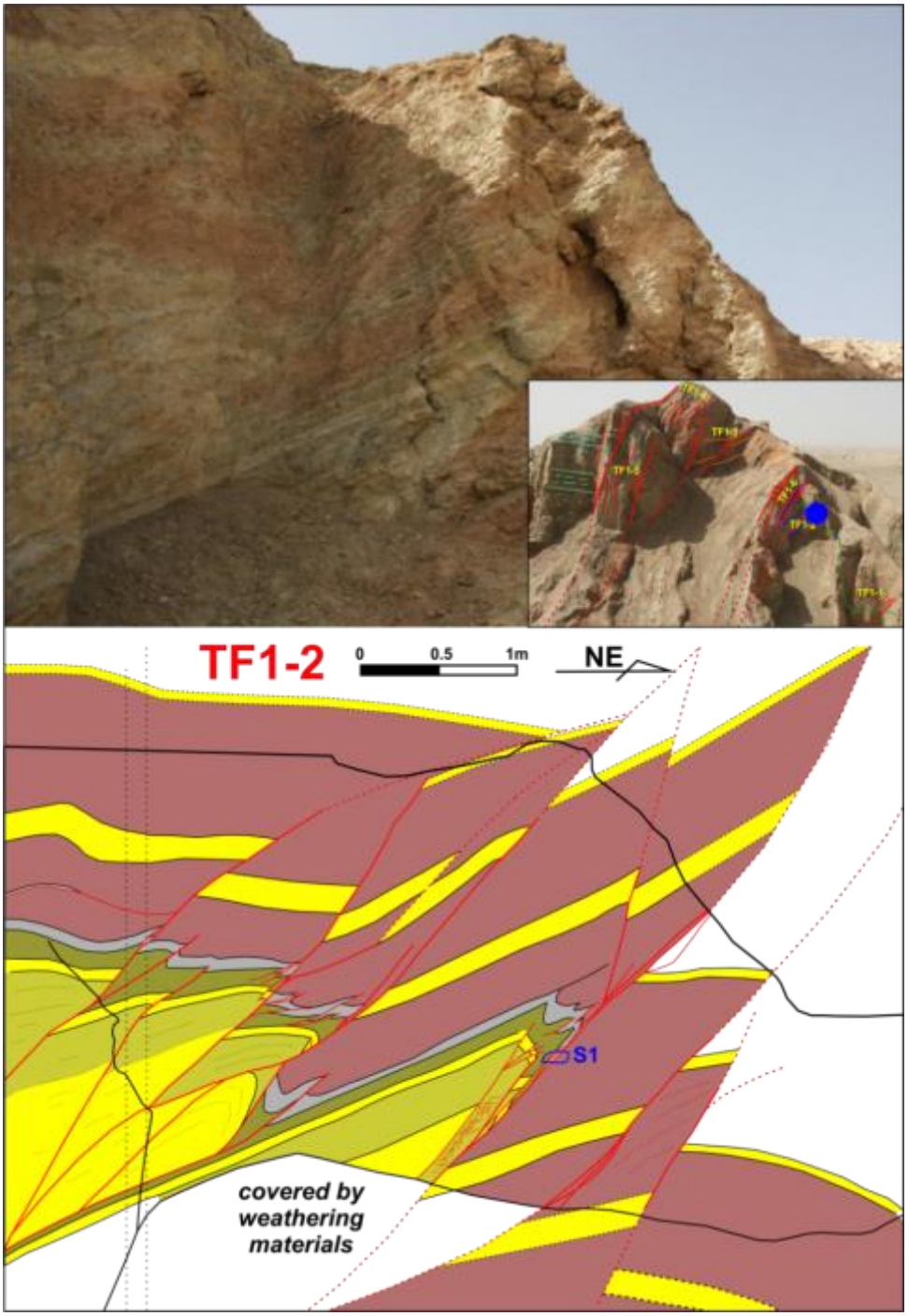

Figure 5.7 The medium strain splay fault TF1-2 that is controlled by a series of NE-directing reverse faults with measurable fault throws.

(3). Low Strain Splay Fault: TF1-1

Low strain reverse fault TF1-1 is a small pop-up structure along the minor fold axis in the footwall beds with low dips away from main reverse fault (Figure 5.8). The lower layers involved are mainly sandstones while the top layers are mudstone-dominated. TF1-1 is a structure composed of a series of sub-parallel NE-directing reverse faults and SW back-thrusting faults. In both the reverse faults and back-thrusts, the top clay-rich layers show more

folding than the lower sandy layers, which is similar to that observed in TF1-2. Fault lenses are generated along the reverse faults and back-thrusts similarly form as in TF1-2; particularly where the faults cut the top clay-rich layers. In these fault lenses, the fault rocks are dominated by clay-rich shales/mudstones.

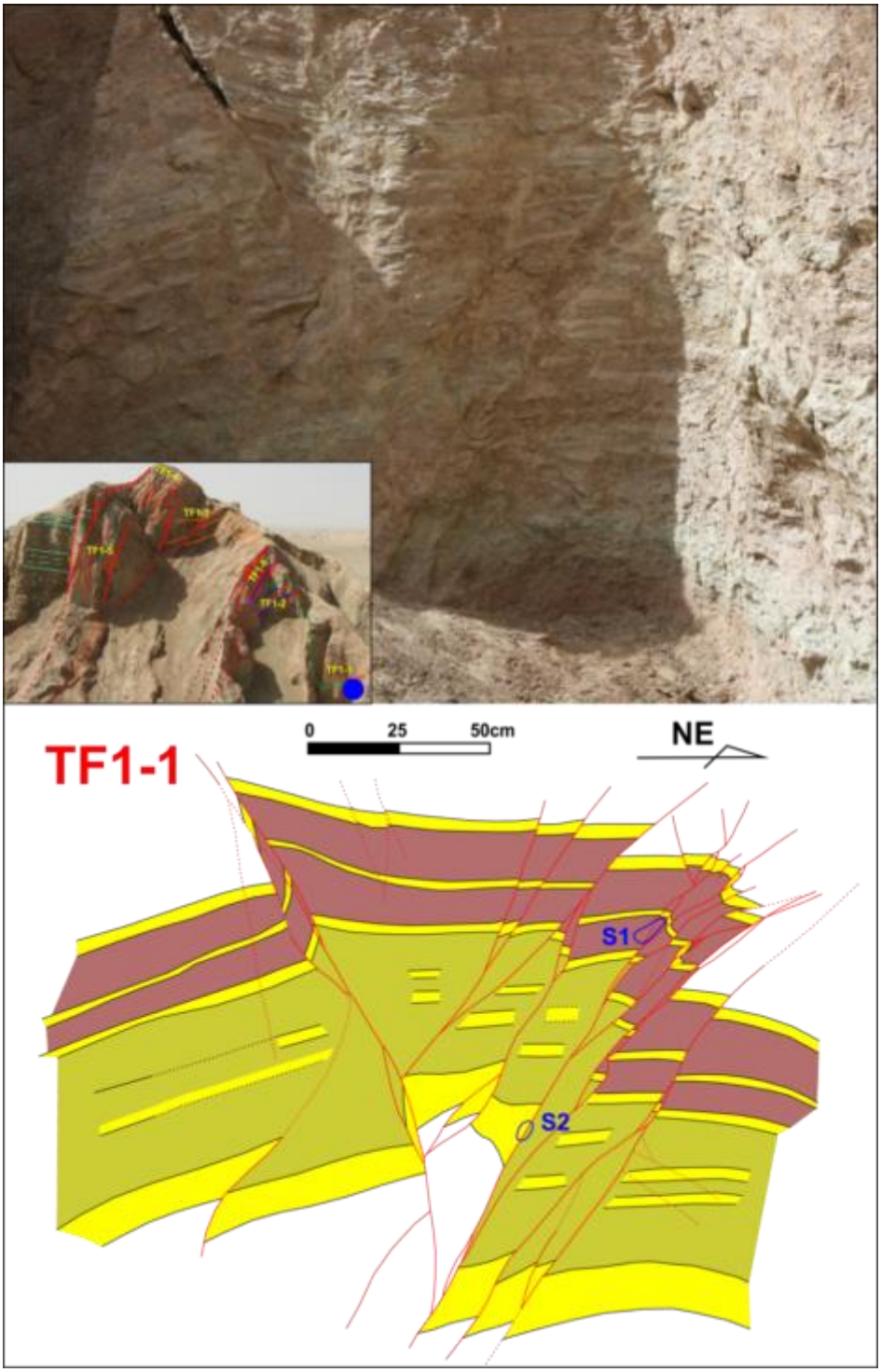

Figure 5.8 Detailed outcrop map of TF1-1 with medium strain which is controlled by a series of NE-directing reverse faults and back-thrusting faults with measurable fault throws.

As a summary of the outcrops of main reverse fault TF1, the majority of the deformation concentrates in the two high strain fault cores TF1-4/TF1-5 and TF1-6 (the left and central parts of Figure 5.2c); the medium strain faults TF1-3 and TF1-2 are located in the intermediate hanging walls or footwalls of the high strain splay faults; and the low strain splay fault TF1-1 is developed as an isolated structure in the far footwall of the high strain fault TF1-6 (right end of Figure 5.2c). In terms of the fault zone geometry, the high strain faults form steeper fault zones than the medium and low strain faults. Moreover, the fault zone width may be attributed to the fault displacements, as high strain faults have generated wider fault zones than medium and low strain faults.

5.3.2. Main Reverse Fault: TF2, TF3 and TF4

Apart from the main reverse fault TF1, three more well-exposed outcrops of the main reverse fault were also mapped in detail: TF2, TF3 and TF4.These three faults cut through the hanging wall of the reverse fault ~50m apart, which are distributed sub-parallel to a NW-SE direction (see position in Figure 5.1). Although these three outcrops are distributed ~2km northwest to the TF1, they all cut the main reverse faults of Lenghu5 structure in a similar way to TF1.

Therefore, the three outcrops present very similar structural geometries that are tectonically controlled by a main reverse fault with small splays. An anticline with a flat crest forms against the reverse fault in the hanging wall, in both the outcrops TF2, TF3, TF4 (Figure 5.9) and TF1 (Figure 5.2). The steeply dipping fault zone has sheared stratigraphic units comprising foliated fault rocks (primarily shales and some sandstones), which accounts for the majority of the fault deformation. The shales are vertical as they are smeared into the fault zone from the hanging wall stratigraphy; while the sandstones are faulted and thinned by fault offsets. Although the fault domains are vertical, the bedding cannot be identified within the central fault zones, because the intense deformation has destroyed the original bedding by smearing and faulting. Shearing into high strain fault zones generates clay smears and sand inclusions.

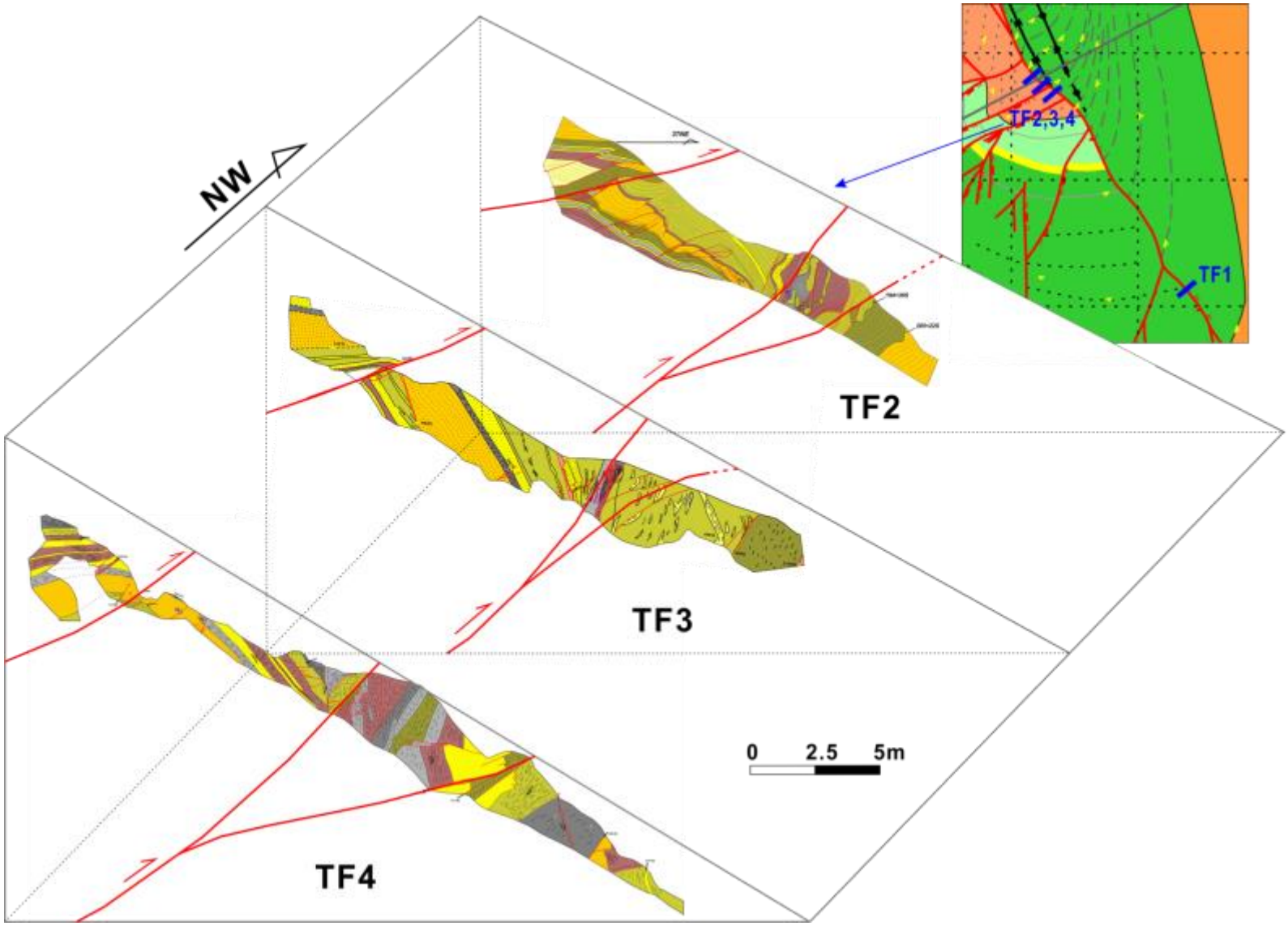

Figure 5.9 The distribution of TF2, TF3 and TF4 through the hanging wall of the Lenghu5 reverse fault ~50m apart (a) and the basic structural geometry (b).

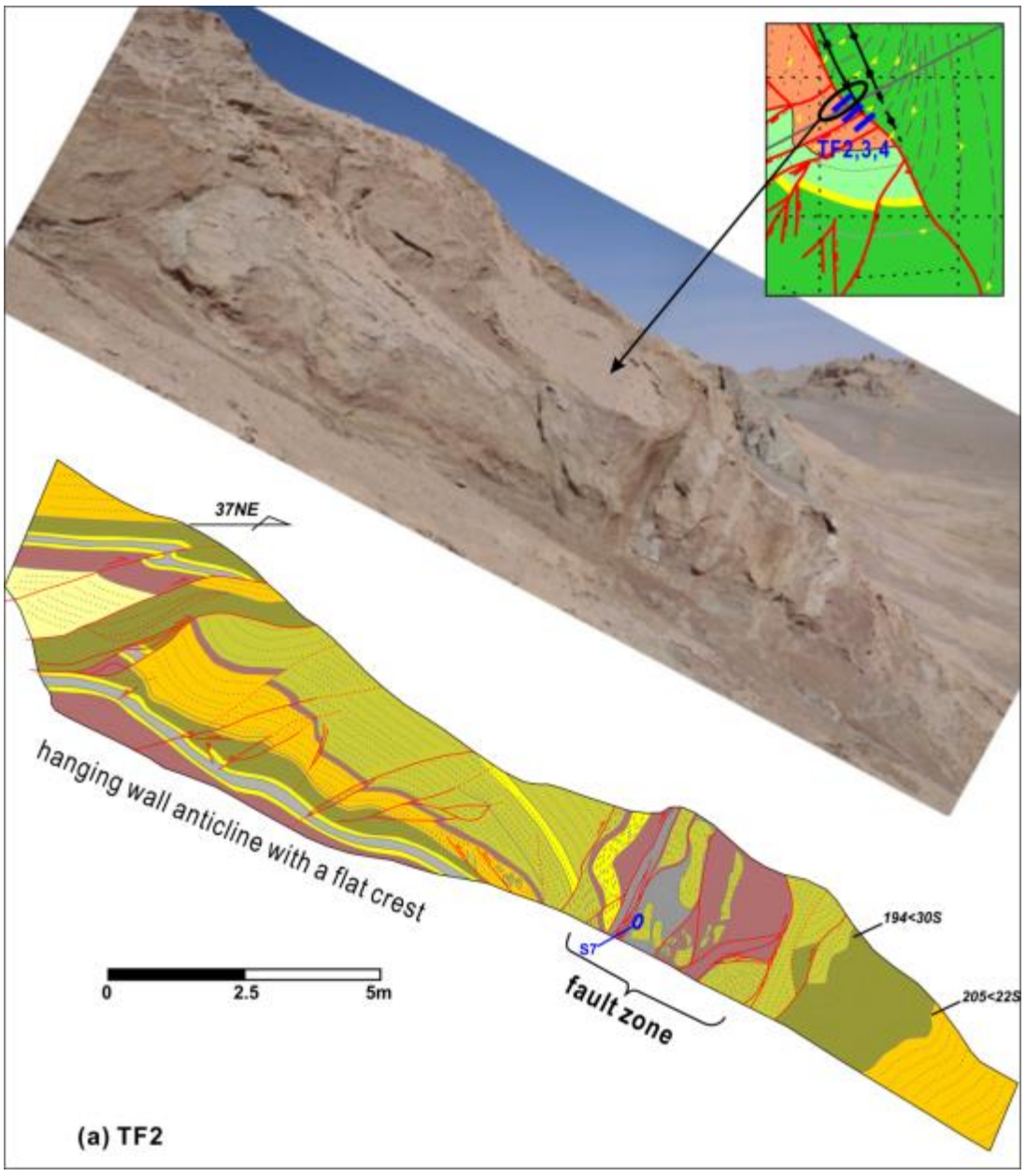

Figure 5.10 The photos and detailed outcrop maps of TF2 (a), TF3 (b) and TF4 (c). A hanging wall anticline with a flat crest can be found in the left-top part of these outcrops. The core of the main reverse fault is just next to the anticline on the left.

(**Figure 5.10** continued)

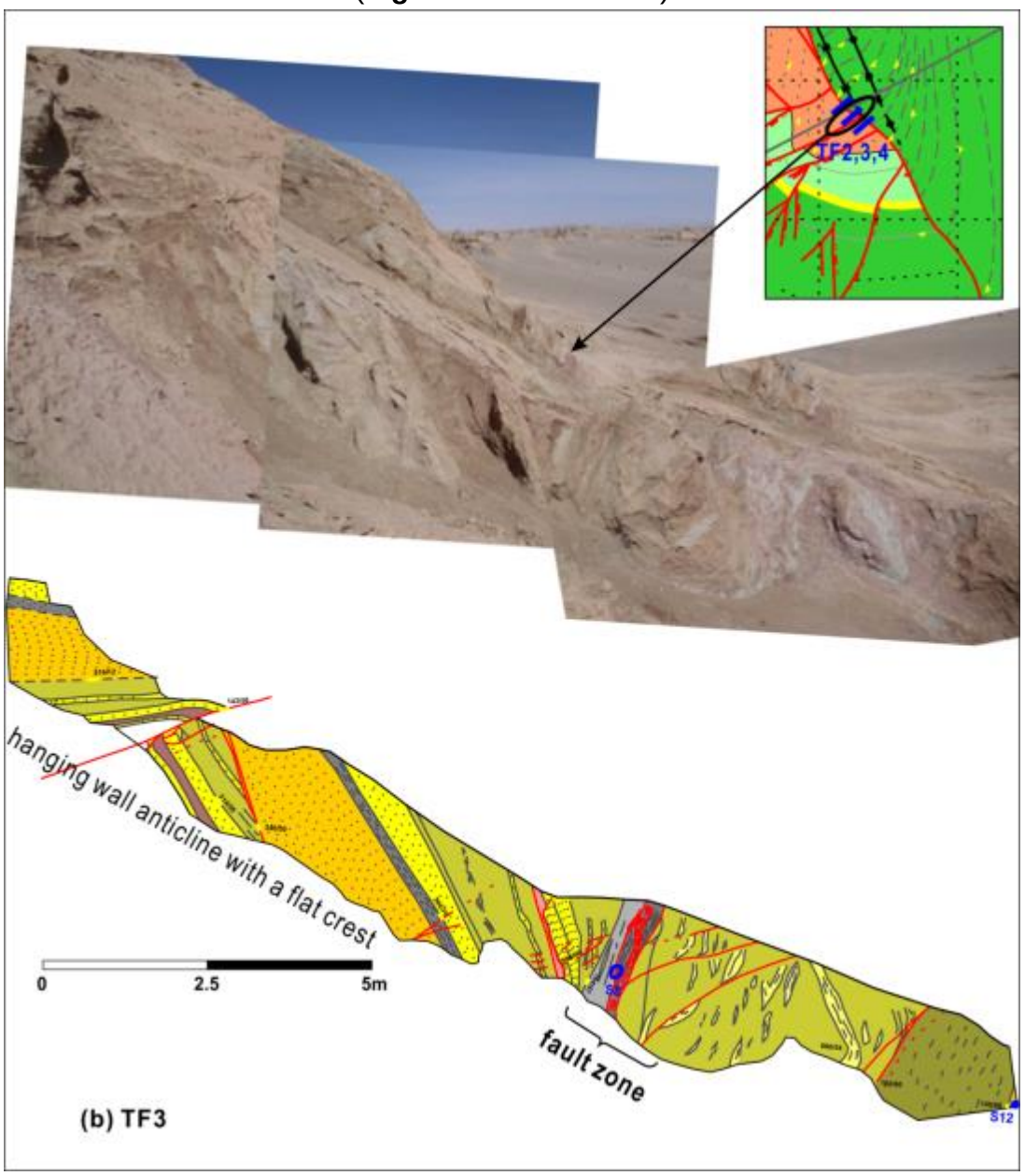

(**Figure 5.10** continued)

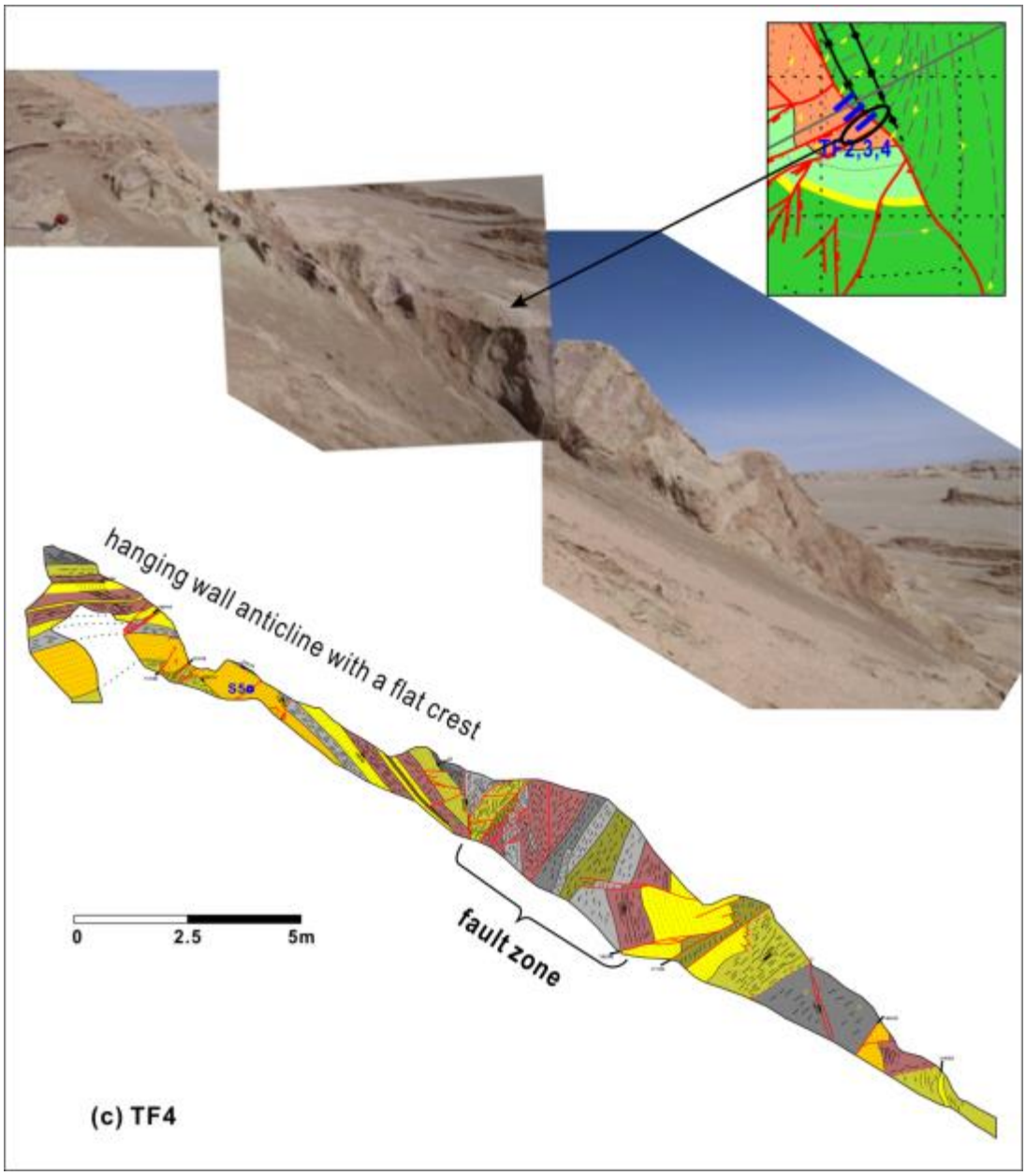

5.4. Fault Architecture Characterization - Accommodation Faults in the Hanging Wall

In addition to the outcrops of the main reverse fault, abundant reverse faults and normal faults with smaller fault throws (10cm-10m) are dominantly formed in the hanging wall of the Lenghu5 structure. These represent a concentration of strain into the two fold cores of the two hanging wall anticlines (Figure 5.1a). As discussed in Chapter4, these reverse faults and normal faults with small fault throws are generated to accommodate the strain required in the hanging wall. Two sets of well-exposed outcrops (minor reverse

faults and normal faults) have been mapped, to understand the deformation features of fault zones with small fault throws. Finally, the similarities and differences between these accommodation faults and the main reverse faults are considered.

5.4.1. Minor Reverse Faults

In the northern end of the Lenghu5 structure (Figure 5.1a), three well-exposed outcrops of minor reverse faults were mapped: F1, F2 and F3, all with fault throws not exceeding 5m. As these are fold-core-concentrated strains (Figure 5.1a), it is assumed that these minor reverse faults may have formed in response to a local perturbation in the stresses along the NW-SE trending main reverse faults. These three outcrops are used to identify the effects of the small fault throws on the deformation features by making a comparison with the above main reverse faults TF1-TF4 with large fault throws.

(1). Minor Reverse Fault F1 with Mudstone-dominated Stratigraphy

The minor reverse fault F1 is a SW-directing reverse fault with a throw of ~1m, and is located in the northern end of Lenghu5 reverse fault zone (see position in Figure 5.1a). This outcrop can be used to investigate the deformation features of a mudstone-dominated sequence (Figure 5.11).

The stratigraphy of F1 is mainly composed of a relative thick mudstones (25-40cm) and thin sandstones (5-10cm). Small chevron folds are developed in the central part of the mapped area as pop-up structures. The fold hinges are cut by two sets of reverse faults. Fault lenses are formed by the left set of reverse faults while the right reverse fault shows steeper fault dips and forms several back-reverse faults. The left hand reverse faults, which cut through the left edge of the anticline, initiates from a bed-parallel flat to a ramp across the fold hinge. The left reverse faults may continue to another bed-parallel flat higher in the section. The shortening of the beds is primarily achieved from the imbricated reverse faults and layer-parallel shearing.

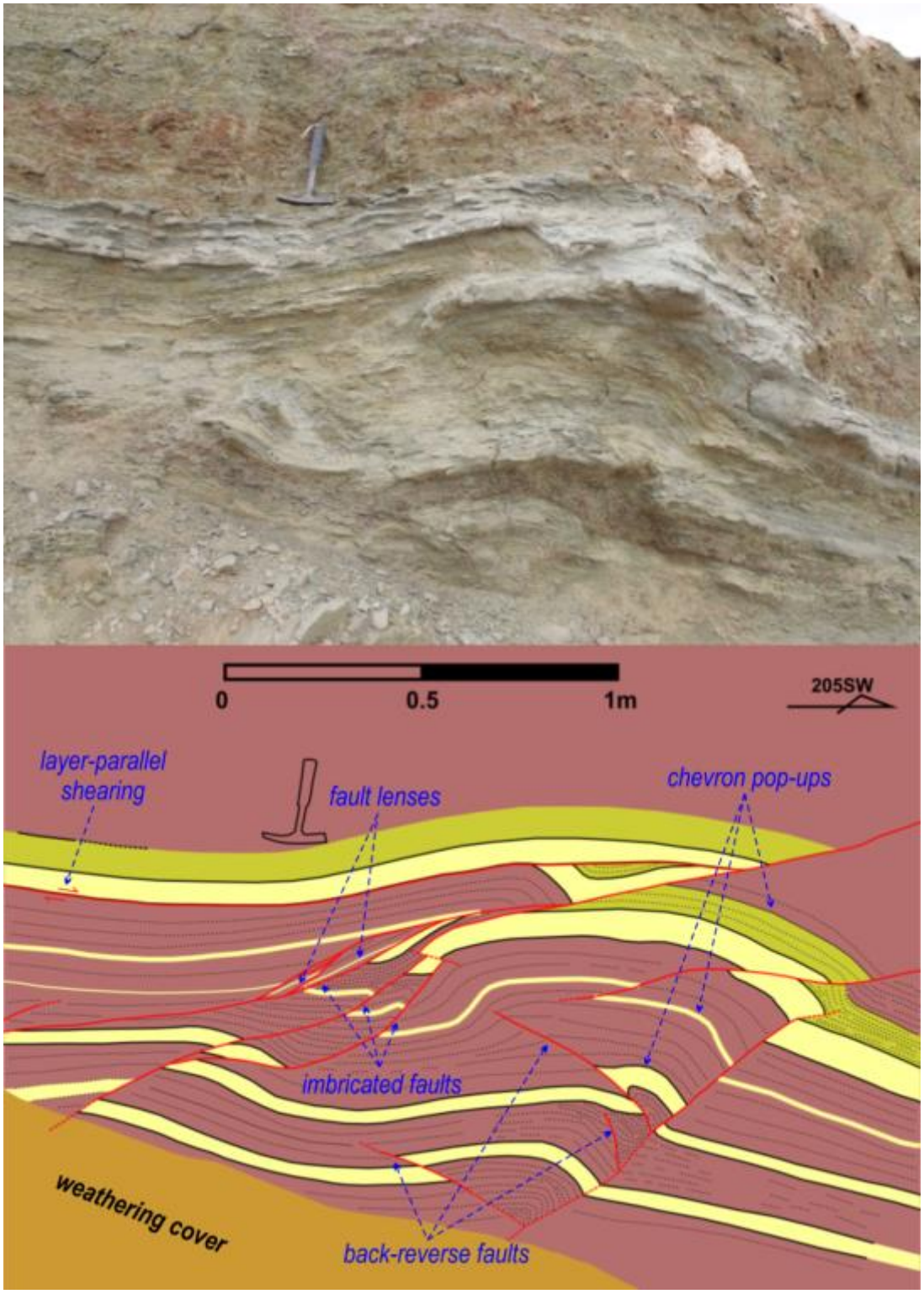

Figure 5.11 The fault F1 (position in Figure 5.1a), located in the northern end of Lenghu5 structure, presents fault throw of ~1m. The deformation is concentrated in the left fault zone, while the right reverse fault and its back-reverse faults accommodate the overall strain in the footwall.

Compared with the previous main reverse faults (e.g., TF1 in Figure 5.2), the reverse fault F1 shows much lower strain and corresponds to a relatively thinner fault zone of 30-40cm, although the stratigraphy of F1 is similar to

that of the previous main reverse faults. Therefore, the fault displacement may be linked to the width of fault zones, which will be discussed in detail later in section 5.6.

(2). Minor Reverse Fault F2 with Sandstone-dominated Stratigraphy

The outcrop F2 was selected to consider the deformation features of a sandstone-dominated sequence. As with F1, the minor reverse fault F2 is located in the hanging wall of the northern Lenghu5 structure (see position in Figure 5.1a). F2 covers two suites of minor reverse faults: F2A and F2B (Figure 5.12). The two sets of reverse faults cut the same stratigraphy and their deformation styles are similar to each other. Compared with the mud-stone-dominated stratigraphy of F1 (Figure 5.11), the outcrop F2 shows a sandstone-dominated stratigraphy. The stratigraphy continues across the two walls of F2A and F2B indicate fault throws of 50-60cm for F2A and 120-130cm for F2B. Compared with the deformation style of F1, the reverse faults have much steeper dips (~70-80°W) than the reverse fault F1. Clay smearing is not as well-developed as in the reverse fault F1.

Small splay faults and fault lenses are also observed along the fault zones. However, both faults F2A and F2B show fault zones present with very limited widths (<30cm), which reflects the low mechanical heterogeneity and small fault throws. There is also very limited clay shearing into the fault zones. Apart from the faults in the central high strain domain, the peripheral fractures or faults with smaller throws are thus also formed in the outer foot-wall/hanging wall.

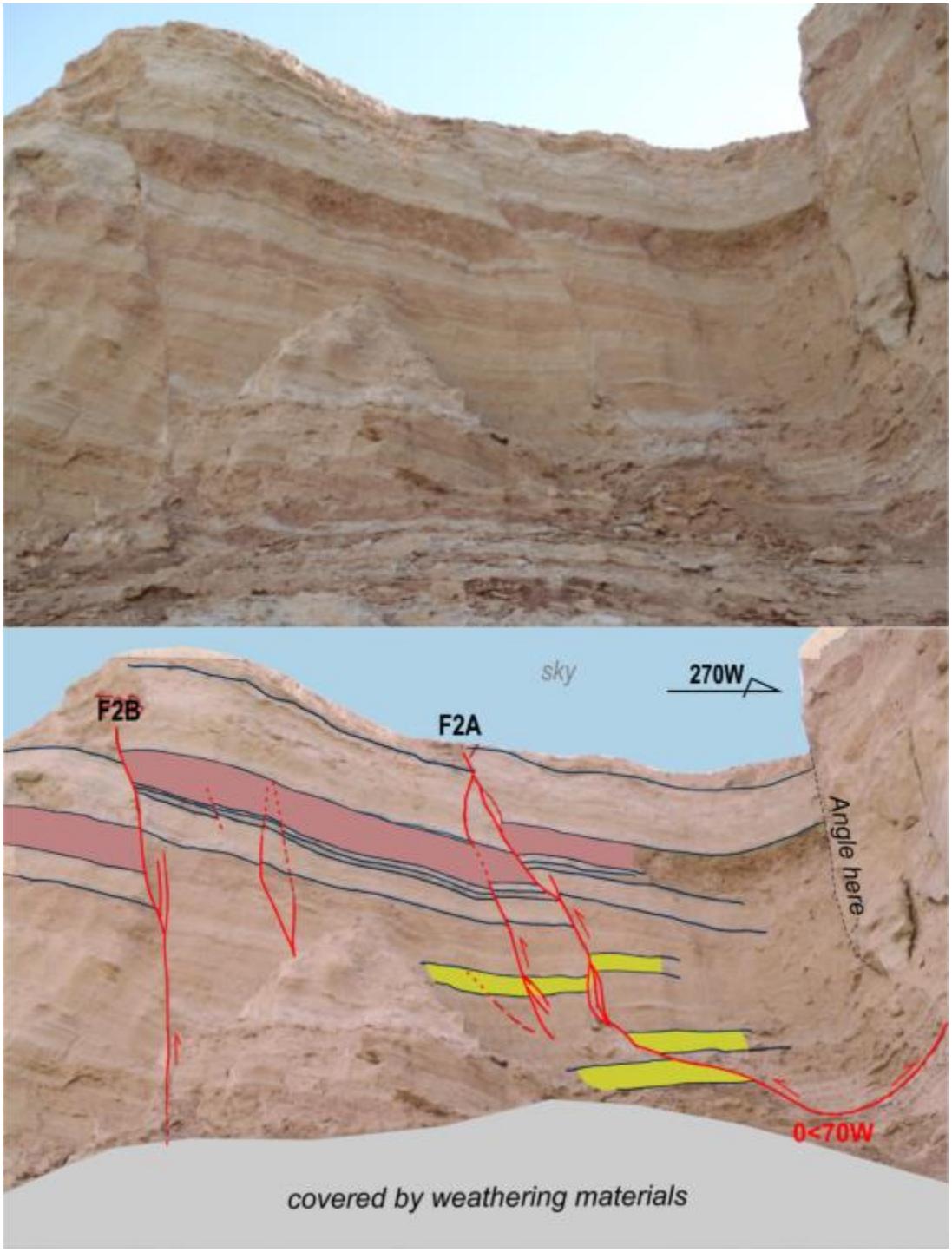

Figure 5.12 The field photo and schematic interpretation of the minor reverse fault F2, in which two sets of steep faults are developed. The fault throws are estimated: 50-60cm for F2A and 120-130cm for F2B.

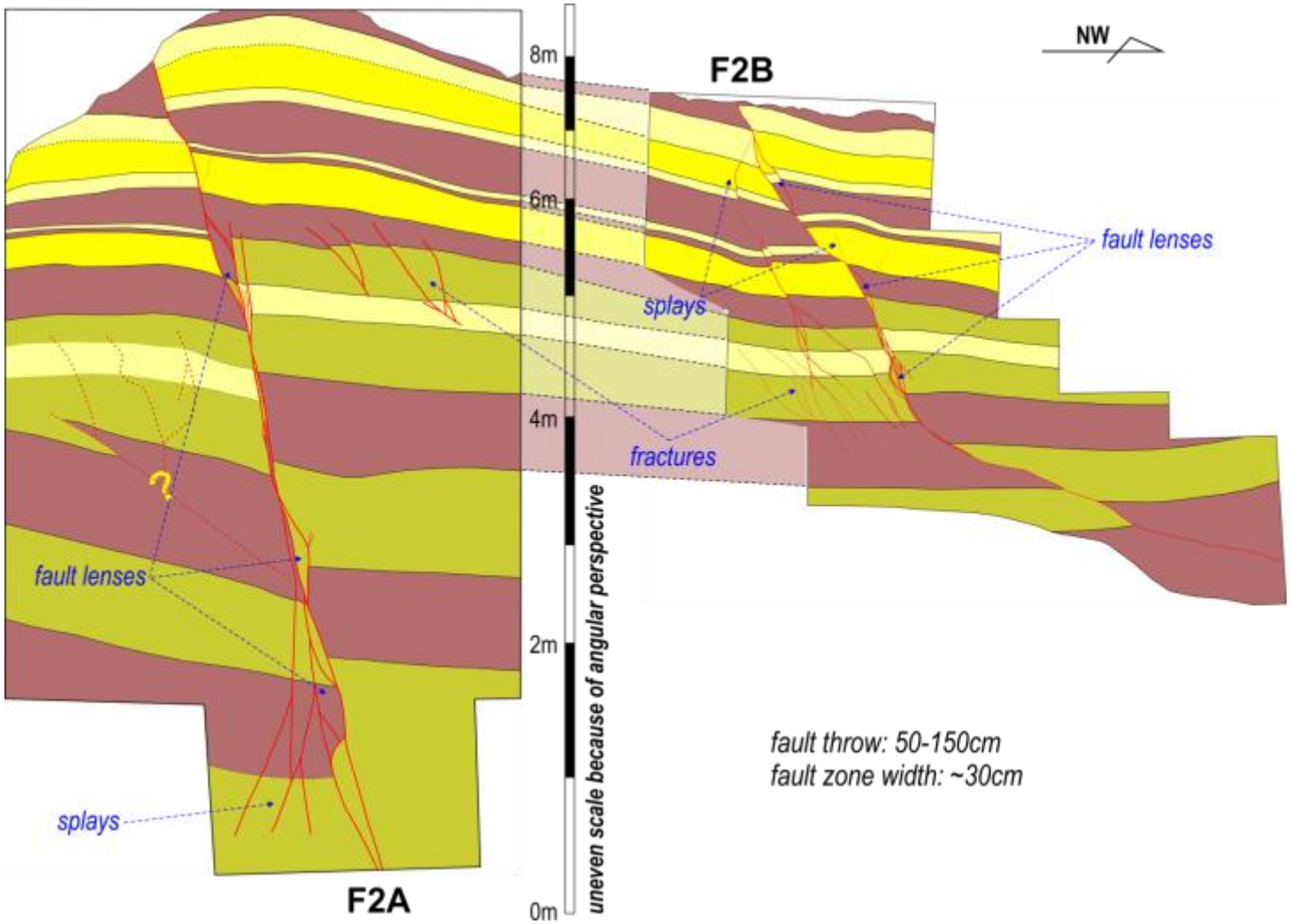

Figure 5.13 The detailed outcrop map of F2 with steep reverse faults. Fault lenses are formed along the fault plane. The fault throw in this outcrop is between 50cm to 130cm.

(3). Minor Reverse Fault F3 with Interbedded Stratigraphy

The minor reverse fault F3 was selected to analyse the deformation features of a sequence with interbedded lithologies and an intermediate degree of mechanical heterogeneity between F1 and F2. The reverse fault F3 is located in the hanging wall of northern Lenghu5 structure (Figure 5.1a). F3 shows a fault zone 80-90cm wide (Figure 5.14), where the cumulative fault throw reaches up to 1.5m. The faults cut a sequence of fine sandstones and mudstones each with low stratigraphic and mechanical heterogeneity. The fault zone has several major through-going faults that bound a fractured but unfaulted fault lens. Based on the geometry of the top sandstone layer, it is assumed that the sequence was initially folded and then cut by the later through-going faults.

As a summary of the three minor reverse faults, faults F1, F2 and F3 all show small fault throws cutting a sequence of beds with low to moderate mechanical heterogeneity. The fault throws do not exceed 1.5m and form a limited fault zone width of 30-50cm. Splay faults, fault lenses and smearing of mudstones/shales are commonly observed along the fault zones, which increases the fault zone complexity. However, as observed, the dominant lithology in the stratigraphy of the three faults varies; the sandstone-dominated stratigraphy in F2 forms steeper faults but less continuous clay smears than the mudstone-dominated stratigraphy in F1.

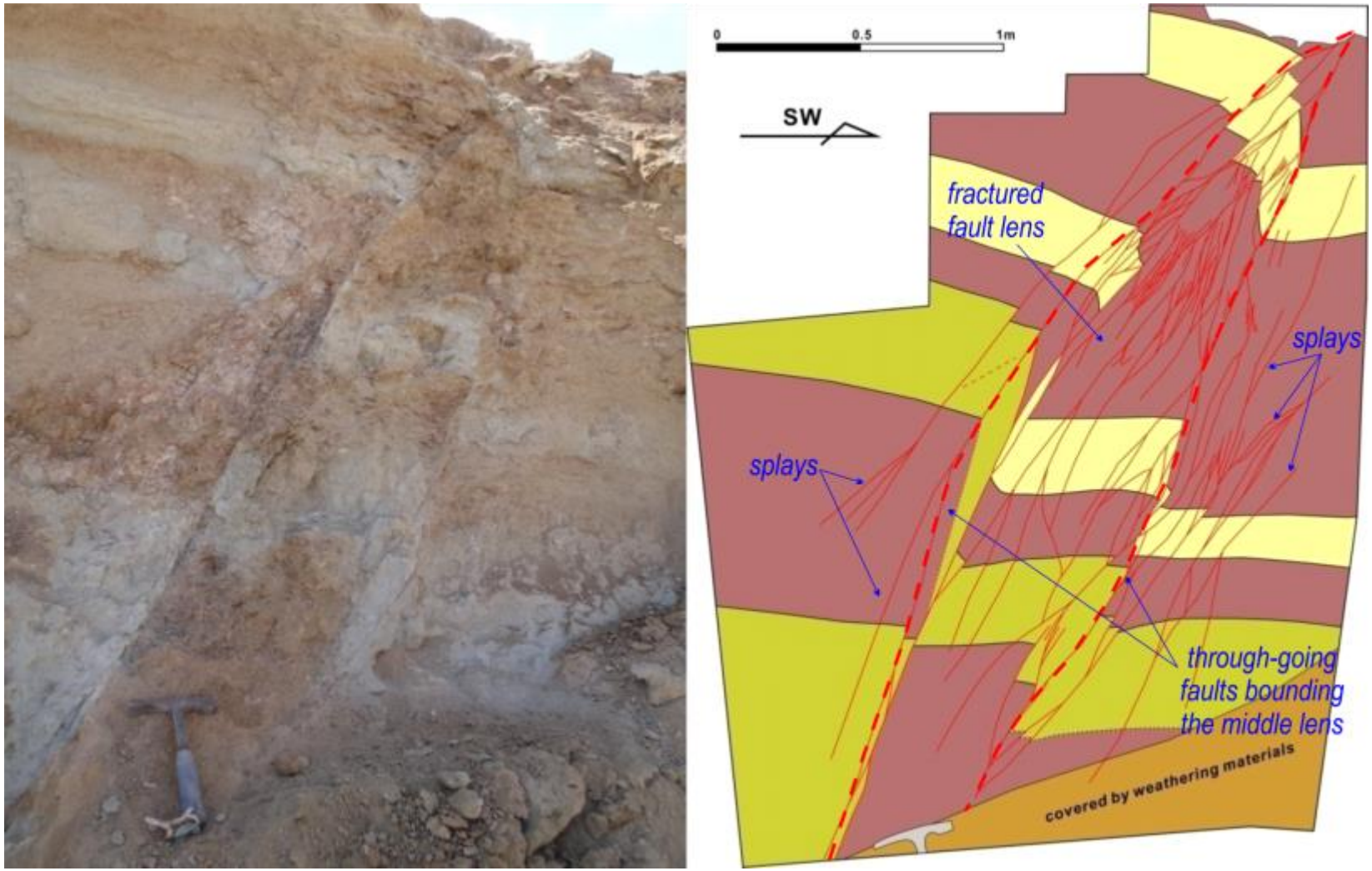

Figure 5.14 The field photo and detailed map of minor reverse fault F3, in which fault lenses are formed in the fault core zone of F3. The reverse fault F3 forms mainly fractures and fault lenses with very limited clay smearing into the fault zone.

5.4.2. Normal Faults

Apart from the reverse faults, abundant normal faults with small fault throws are also developed in Lenghu5. As discussed in Chapter 4, the majority of these normal faults are concentrated within the anticline cores to accommodate the local strain. Although these faults demonstrate extensional regimes, they are not isolated faults but are associated with the overall contractional strain in the Lenghu5 structure. Similar to the above minor reverse faults, here two typical outcrops were selected for detailed study: normal faults NF1 and NF2 (Figure 5.1a), and to investigate the effects of fault throw and mechanical heterogeneity on the fault deformation features. The outcrop NF1 includes two sets of normal faults with fault throws of >6m and ~20cm respectively. The outcrop NF1 presents low to moderate-heterogeneous stratigraphy with thick sandstones and thin mudstones; while the outcrop NF2 cuts a moderate heterogeneous stratigraphy with both thick sandstones and mudstones.

(1). Normal Fault: NF1

The outcrop NF1 includes two sets of normal faults: the central normal fault with a minimum throw of 6m and the NW normal faults with throws of only 20-50cm. The smear in the central core was mapped in detail and sampled. The meso-scale detailed maps are created in order to understand the deformation mechanism of the intense smearing into the fault zone.

NF1 covers a section with low-moderate mechanical heterogeneity. The central fault core, dipping 46°SE, is primarily a zone of continuous mudstone shearing into the fault zone, which probably relates to the low to moderate mechanical heterogeneity. Several inclusions of small sandy blocks are also observed in the lower part of the fault core zone. The ~6m long sheared mudstone along the fault core zone is bounded by two discrete slip surfaces that separate the hanging wall from the footwall. Comparatively, the hanging wall shows sandstone dominated stratigraphy with low heterogeneity forming small fractures rather than through-going faults; while an outer damage zone formed in the footwall as a result of the higher mechanical heterogeneity (although the faults in the outer damage zone have small throws of 20-50cm). These small normal faults also form their own fault zones with very limited width and sub-structures. The thin mudstone beds are also sheared into the narrow fault zones.

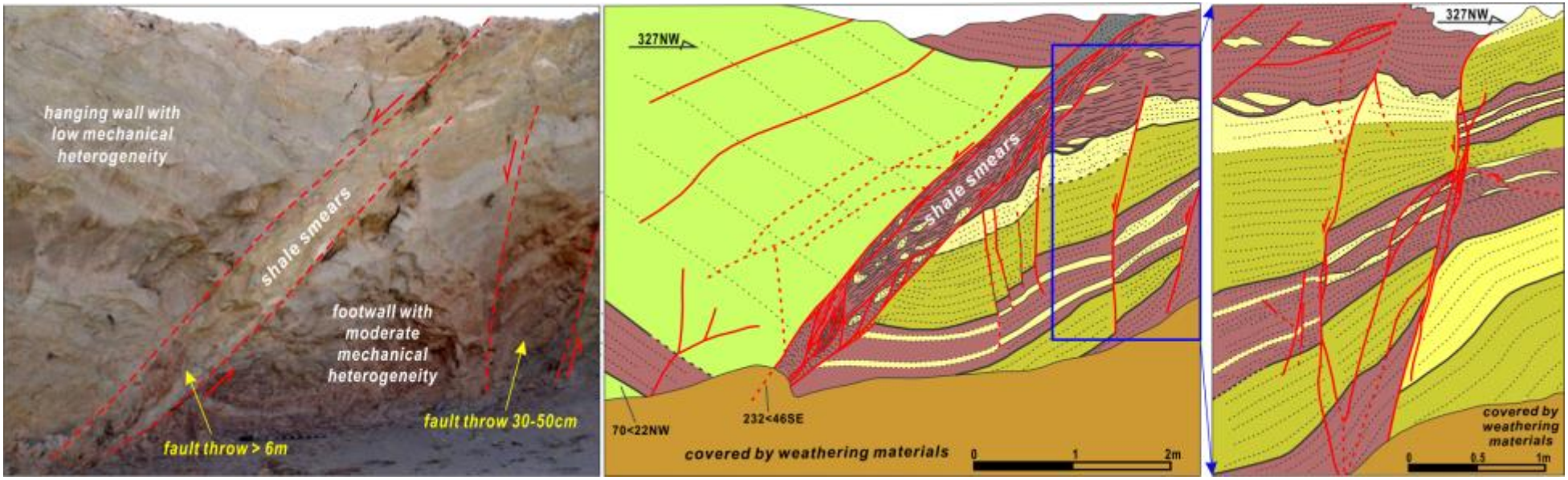

Figure 5.15 The field photo and detailed maps of the outcrop NF1. The intense smearing of mudstone is observed in the central fault zone with a minimum throw of 6m. The highest strain deformation focuses in the central smear zone, while the lenses bounded by the small normal faults in the NW end are accommodation structures with low strain.

(2). Normal Fault: NF2

The outcrop NF2, with a fault dip of 70°-80°NW, has similar stratigraphy to the outcrop NF1 and its deformation style is mudstone smearing dominated. Because of the unmatchable stratigraphy on the two walls, an accurate fault throw cannot be measured (>3m).

The majority of deformation is localized in the central fault zone. Both the sandstone and mudstone beds are sheared into the fault zone. However, the shearing is accomplished by faulting in the more brittle beds (i.e., sandstone beds) and by ductile flow or smearing in soft beds (i.e., mudstone beds). The faulting in sandy beds forms faulted sandstone blocks in the central fault zone, while the muddy beds results in continuous smearing domains along the fault zone.

At the observed scale, the hanging wall shows a higher mechanical heterogeneity. The low strain outer damage zone is concentrated into the hanging wall, while a few of fractures are observed in the footwall with lower stratigraphic and mechanical heterogeneity. In the hanging wall outer damage zone, the thin sandstone beds shear and break into small boudins; while the mudstone beds smear to bound the sandstone boudins. Based on observations in both the central fault core zone and the hanging wall outer damage zone, it is suggested that the thin sandstone beds interbedded within mudstone dominated sequence form more complex structures, e.g., discrete sandstone boudins.

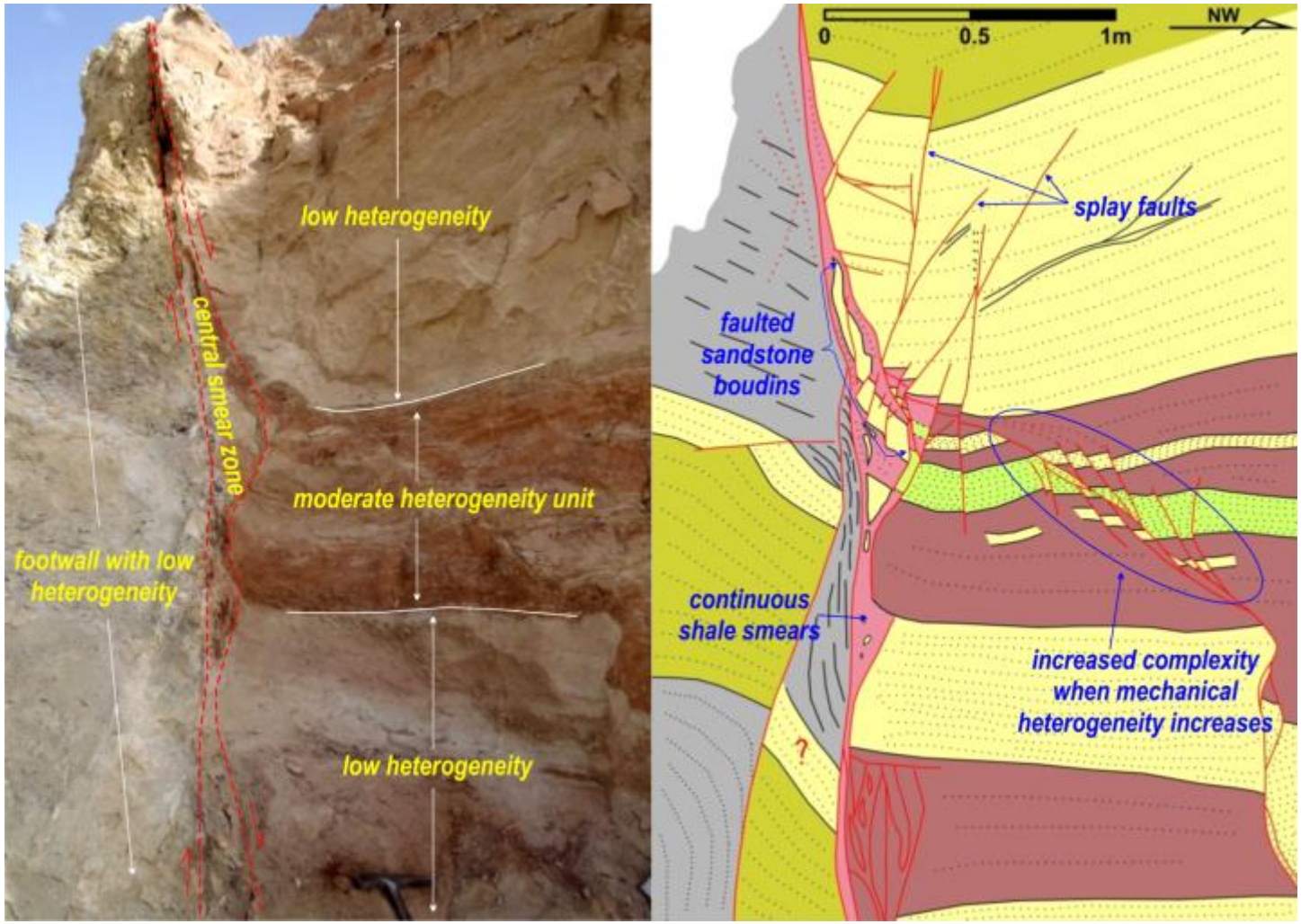

Figure 5.16 (a) Field photo of minor reverse fault NF2. Smears of mudstone can be observed in the central core. (b) Detailed outcrop map interprets the fault zone geometry of NF2.

5.5. Dynamic Fault Evolution and Deformation Mechanisms

5.5.1. Dynamic Fault Evolution

Based on the detailed outcrop maps, a fault zone evolution model is presented here and includes the development of both the reverse faults (Figure 5.17) and normal faults (Figure 5.18). The minor reverse fault F3 and normal fault NF2 are selected as templates because the fault outcrops with small fault throw preserve the majority of the fault zone elements.

(1). Reverse Fault Evolution

The fault zone geometry of the minor reverse fault F3 (Figure 5.14) shows a very high similarity with both the kinematic models and natural examples in the Cedar Mountain Thrust in Utah presented in the study of Welch et al. (2009). Here the schematic models (Figure 5.17) are created based on the geometry and stratigraphy observed in the F3, in order to understand the evolution and the effects of the stratigraphic and mechanical heterogeneity on the resultant geometries. The sequence cut by the reverse fault comprises of competent sandy beds (in yellow) and weak muddy/silty beds (in brown). Both the top and bottom of the section are thick homogeneous sandy layers, while the package sandwiched between them is comprised of thin interbedded sandy and muddy layers. Comparatively, the middle sandwiched package shows lower competency than the top and bottom packages; therefore it is inferred that the fractures/faults tend to form within the top/bottom packages initially and the middle sandwiched package is likely to deform passively to accommodate the overall strain. This evolution is also suggested by previous studies (Eisenstadt and De Paor, 1987; Peacock and Sanderson, 1992; McGrath and Davison, 1995; Childs et al., 1996a; Schöpfer et al., 2006).

The interpretation in Figure 5.17 shows the through-going faults form initially within the top and bottom homogeneous packages, and then propagate both up and down section into the more mechanically heterogeneous package sandwiched between them. The development of single-plane faults within the top and bottom packages forms a lensoid shear zone between the top and bottom packages. Within the shear zone, small faults form in the sandy

layers, while the weak muddy layers passively form folds to accommodate the strain in the sandy layers. As the throw increases, the faults propagate both upward and downward into the weak muddy layers, leading to the muddy layers' ductile deformation that is well-described by the trishear algorithm (Erslev, 1991; Hardy and Ford, 1997; Welch et al., 2009). Additionally, the internal smaller scale lithology units nucleate additional smaller scale lenses (Figure 5.17b, c). It is inferred that multi-scale mechanical heterogeneity can form multi-scale fault lenses, e.g., the section scale lensoid strain zone (Figure 5.17a) and smaller scale fault lenses confined within the thin layers of the middle sandwiched package (Figure 5.17b, c).

The schematic models presented in Figure 5.17 suggest that the shear-zone width is determined by the large-scale stratigraphic packages being subject to stress (Figure 5.17a, b): the homogeneous brittle top and bottom packages form single-plane faults or narrow fault zones; in contrast, the relatively heterogeneous packages sandwiched between them form a much wider fault zone. The competent packages have high fault propagation/slip ratios, while the weak packages have low fault propagation/slip ratios (e.g., Erslev, 1991; Hardy and Ford, 1997; Allmendinger, 1998). Therefore, the fractures or through-going faults with narrow fault zone widths tend to form within the brittle packages; while the weak/ductile packages form wider shearing zone because of low fault propagation/slip ratios.

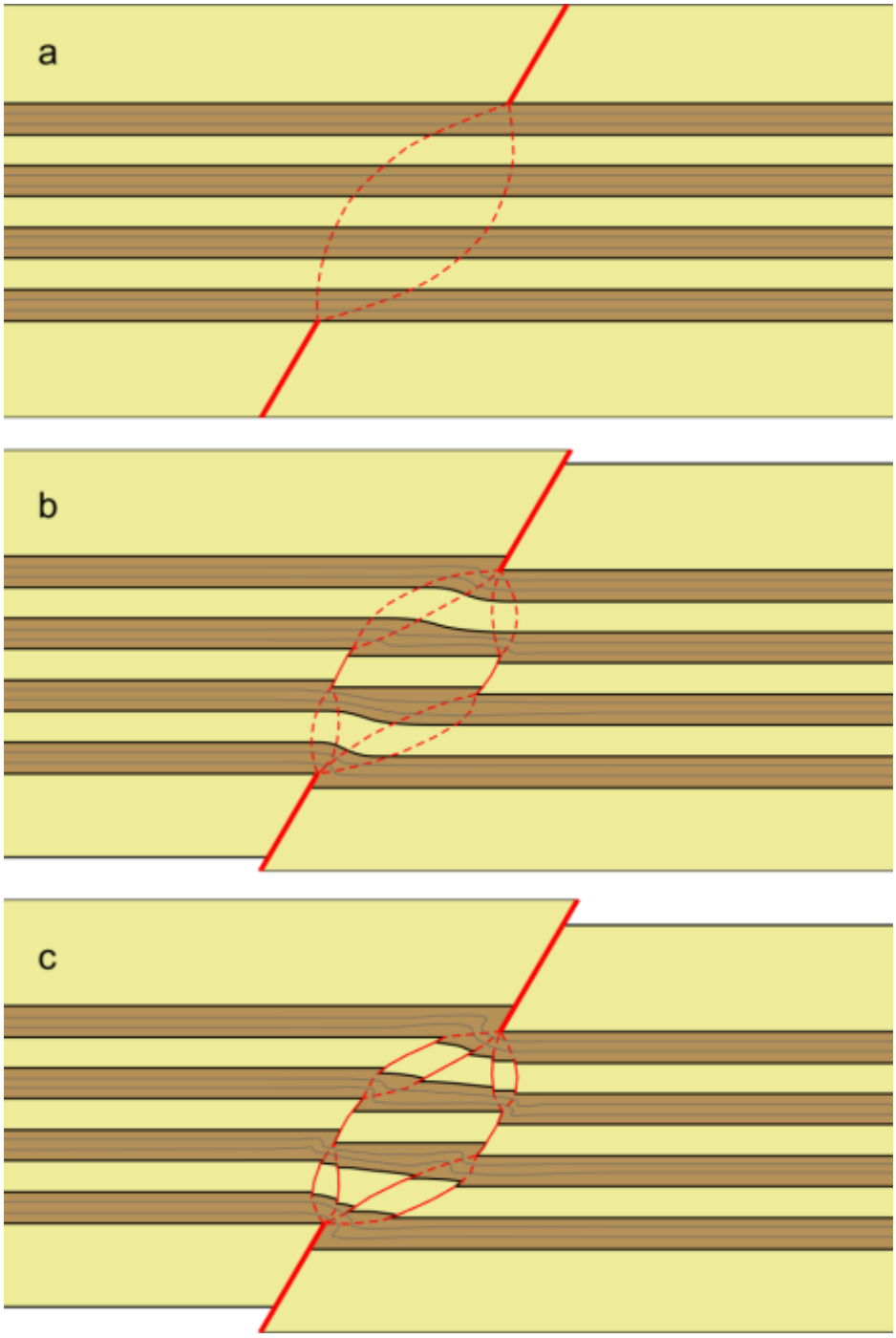

Figure 5.17 Schematic fault evolution within a mechanically layered sequence of beds (yellow: brittle sandy layer; brown: weak muddy layer). Multi-scale fault lenses are formed during the fault deformation as a result of the multi-scale mechanical heterogeneity.

(2). Normal Fault Evolution

The evolution of the normal faults in the Lenghu5 structure is considered in Figure 5.18, where the beds subject to stress comprise of interbedded thin layers of mudstones (brown) and sandstones (yellow) with low-moderate mechanical heterogeneity.

The schematic models suggest the shear zones form as the precursors to the development of through-going faults (Davies and Knipe, 2008; Davies et al., 2012). The sheared multi-layered sequence of beds form wide fault cores of clay smear encasing the boudins broken from the attenuated sandy layers. The geometry of the fault zones is suggested to be dominated by the vertical mechanical heterogeneity. Early monoclinal geometries are commonly observed in the beds that are attenuated into the shear zone (Figure 5.18b, c), in the form of either the ductile folding/shearing in weaker layers (mudstones) or the faulted folds in stronger layers (sandstones). The through-going faults are developed with increasing fault displacement, which may make the clay smears discontinuous or semi-continuous along the fault zone. Finally, a fault zone is formed with fault rocks comprising the blocks derived from the incorporated sandy layers and the clay smears.

The sandy layers generally form fractures initially and faults later, while the muddy layers generally shear into the fault zone either cut by discrete faults or as a ductile shearing in the muddy layers. In the first scenario, the thinner muddy layer sandwiched between thick sandy layers is cut by discrete faults and develops limited folding; in the second scenario, the thicker muddy layers with a lower mechanical heterogeneity is sheared into the fault zone and shows limited faulting. However, the deformation style of an individual layer is scale-independent. For example, a thin ductile layer sandwiched within a thick sequence dominated by brittle layers still locally behaves as a ductile layer on the layer-scale, although it has limited folding on the overall sequence scale; similarly, a thin brittle layer sandwiched within a thick sequence dominated by ductile layers still locally forms fractures or small faults on the layer-scale, although the faulted boudins presents a smearing-like distribution towards the fault core zone (e.g., see the distribution of the sandy boudins entrained by the smearing zone within the fault core zone in NF2, Figure 5.16).

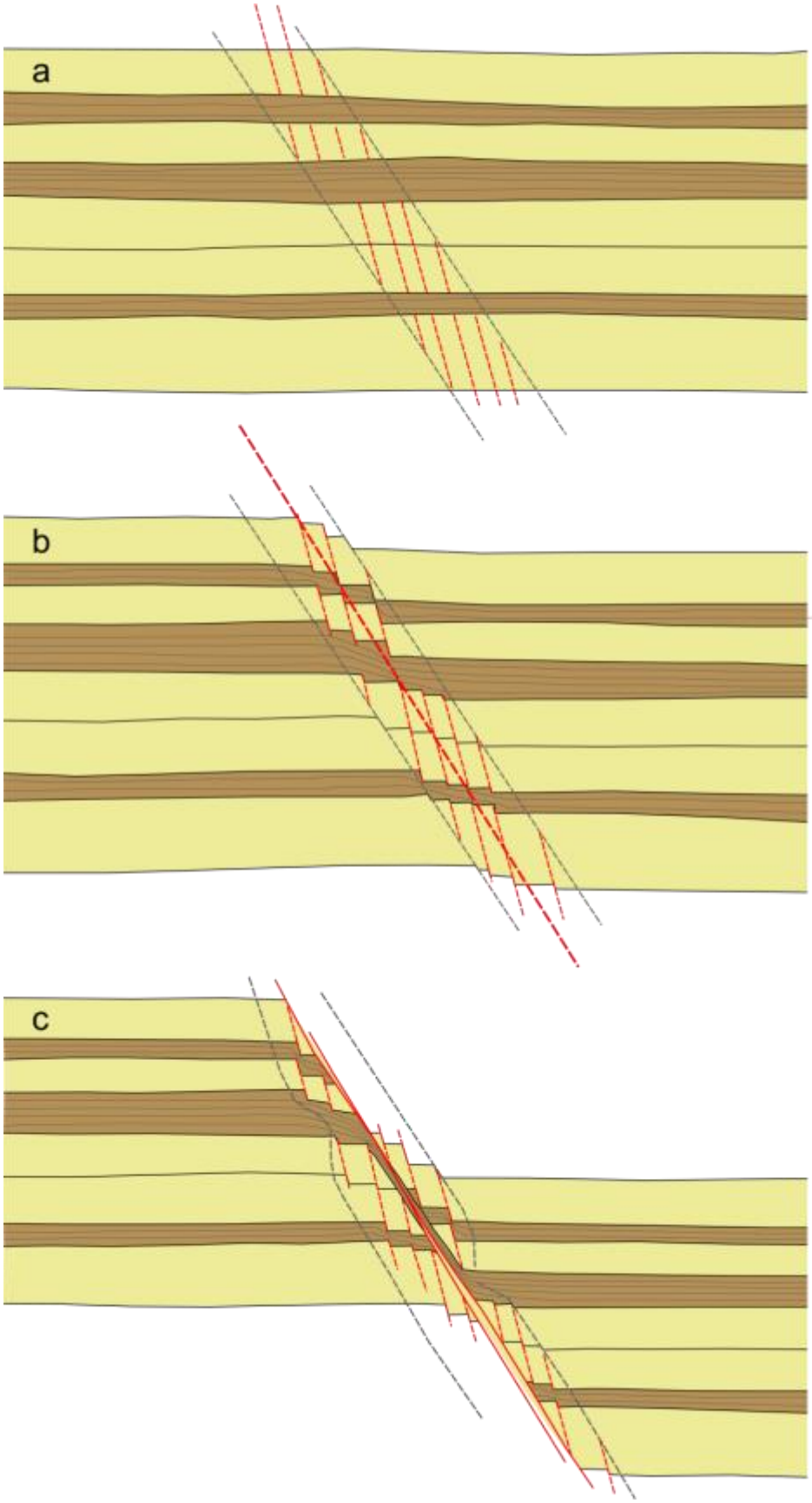

Figure 5.18 Schematic fault architecture of normal faults. The small faults form initially within the brittle beds (yellow), while the ductile folding of weak beds (brown) accommodates the strain. Finally, a large through-going fault forms within the fault zone.

5.5.2. Deformation Mechanisms

Based on the detailed maps of the well-exposed outcrops together with the structural evolution models presented, the deformation mechanisms associated with the reverse faulting deformation are now considered. The deformation mechanisms of strong/brittle beds, weak/ductile beds, and mechanically layered sequence are discussed.

(1) The **strong/brittle beds**, e.g., sandstones, are prone to brittle deformation, e.g., fractures or faults in the study area. The fractures with minor offsets tend to form initially when the stress is applied; the through-going faults then develop later in the strain history (Figure 5.19a). Although this is a continuous process, both the fractures and the through-going faults can be observed in a single outcrop. This is because a single outcrop includes a high strain fault core zone and several outer damage zones with very low strain (as observed in the above outcrops, e.g., TF1, F2 and F3). The deformation of competent beds is linked to a very high fault propagation/slip ratio. Moreover, the fault lenses can also form in the fault core zone, which may have resulted from fault linkage (Peacock and Sanderson, 1991; Childs et al., 1996a; Walsh et al., 2003) or from asperity reduction on the fault surface (Childs et al., 1996b; Walsh et al., 1999).

(2) The **weak/ductile beds**, such as mudstones or shales in the study area experience ductile deformation, e.g., folding or smearing. The ductile folding is always observed when the stress is initially applied on the weak/ductile beds; the continuous smearing is then developed when the increasing strain offsets the weak/ductile beds (Figure 5.19b), (e.g., TF1-1, TF1-2, F2 and F3). The progress of smearing is linked to a relative low fault propagation/slip ratio, which is well-described by the trishear algorithm (Erslev, 1991; Hardy and Ford, 1997). Finally, when the offset is high enough, the smearing of the weak/ductile beds becomes discontinuous and leaves some clay or shale gouge patches along the fault surface, e.g., TF1-4 and TF1-6. This is in agreement with the studies in Childs et al. (1996a) and Solum et al. (2010).

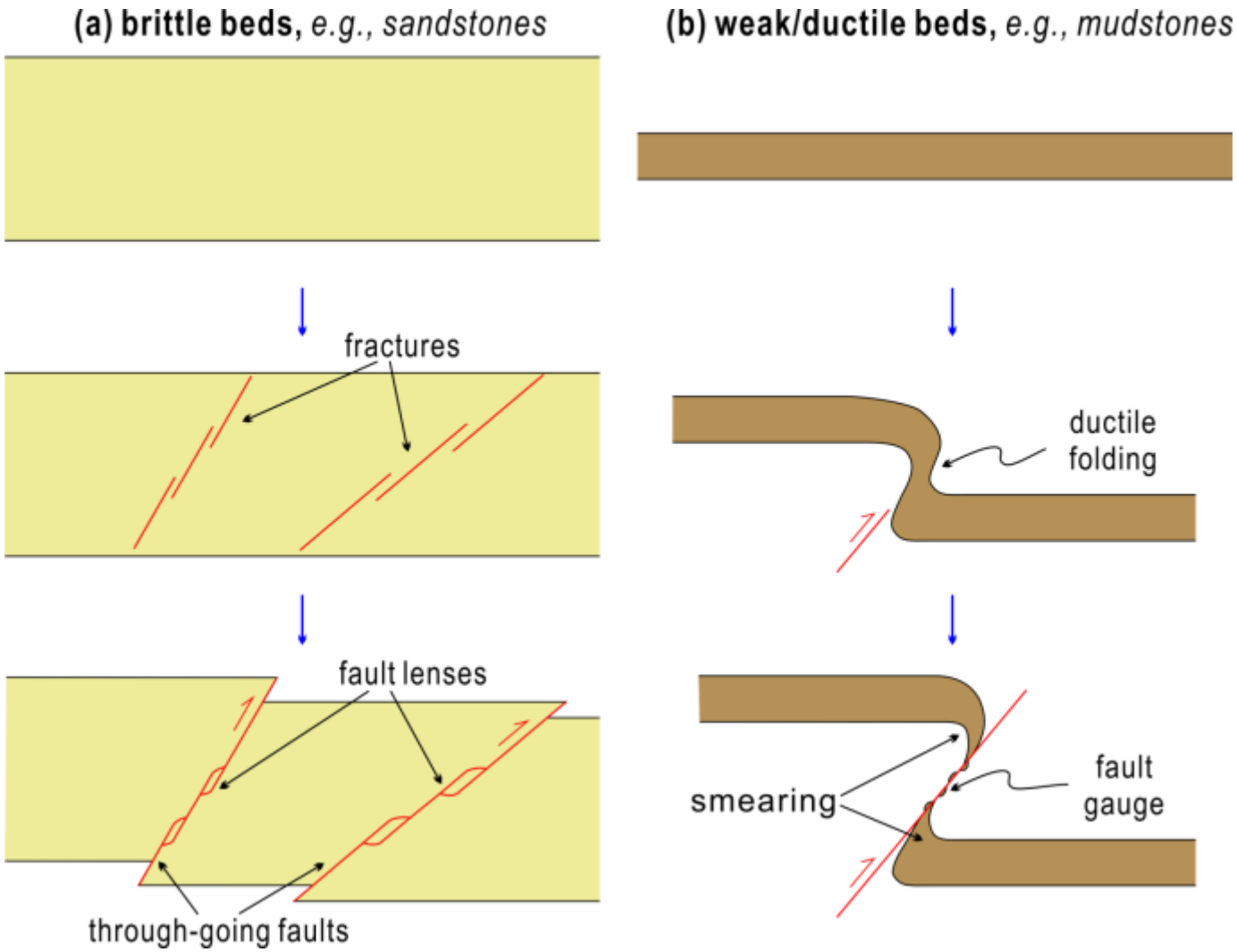

Figure 5.19 Schematic cartoons to demonstrate the strain in competent beds (a) and weak/ductile beds (b), respectively.

(3) It is common that the beds define a **mechanically layered sequence**, e.g., interbedded sandstones and mudstones. As shown in the natural examples above, when the mechanically layered sequence of beds are subject to stress, the fractures or small faults form in the brittle beds (e.g., sandstones in the Lenghu5 structure) while the weak/ductile beds (e.g., mudstones in the Lenghu5 structure) are folded or sheared to accommodate the overall strain. This observation concurs with the previous studies focusing on the deformation of layered sequence (Eisenstadt and De Paor, 1987; Peacock and Sanderson, 1992; McGrath and Davison, 1995; Childs et al., 1996a; Schöpfer et al., 2006). As the strain increases, the fractures or small faults confined within the brittle beds will grow until they eventually propagate the weak/ductile beds (Peacock and Sanderson, 1991; Childs et al., 1996a; Walsh et al., 1999; Walsh et al., 2003), forming clay/shale smearing or clay/shale gauge along the fault surfaces, e.g., TF1, F2, F3 and NF2.

By applying the trishear algorithm (Erslev, 1991; Hardy and Ford, 1997), the detailed process of the propagation from brittle beds into the interbedded weak/ductile beds is analysed (Figure 5.20). This pattern defines the Quadshear concept (Welch et al., 2009). As Figure 5.20, when a mechanically layered sequence of beds are subject to stress, the fractures or small faults tend to form in the brittle beds, e.g., sandstones (yellow). As the fault throw increases, the fractures or small faults will grow by propagating into the weak/ductile beds, e.g., mudstones or shales (brown). The propagation of the fracture or small faults from brittle beds into the weak/ductile beds can be well-described by the trishear algorithm. However, as the weak/ductile beds are sandwiched by the brittle beds, there can be divergent trishear within the weak/ductile beds both from upper and lower brittle beds. In contrast, convergent trishear within the brittle beds can be found to propagate into the upper and lower weak/ductile beds. The convergent and divergent trishear may form a very complex fault core zone. This result agrees with the study of Welch et al. (2009), in which a Quadshear model is proposed to demonstrate the shearing deformation in a weak/ductile layer sandwiched between two brittle layers. It is suggested that small through-going faults form initially in the brittle layers accommodated by the folding of the weak/ductile layer sandwiched between them. As the fault throw increases,

a shear zone forms as the faults propagate into the weak/ductile layer from both the upper and lower brittle layers.

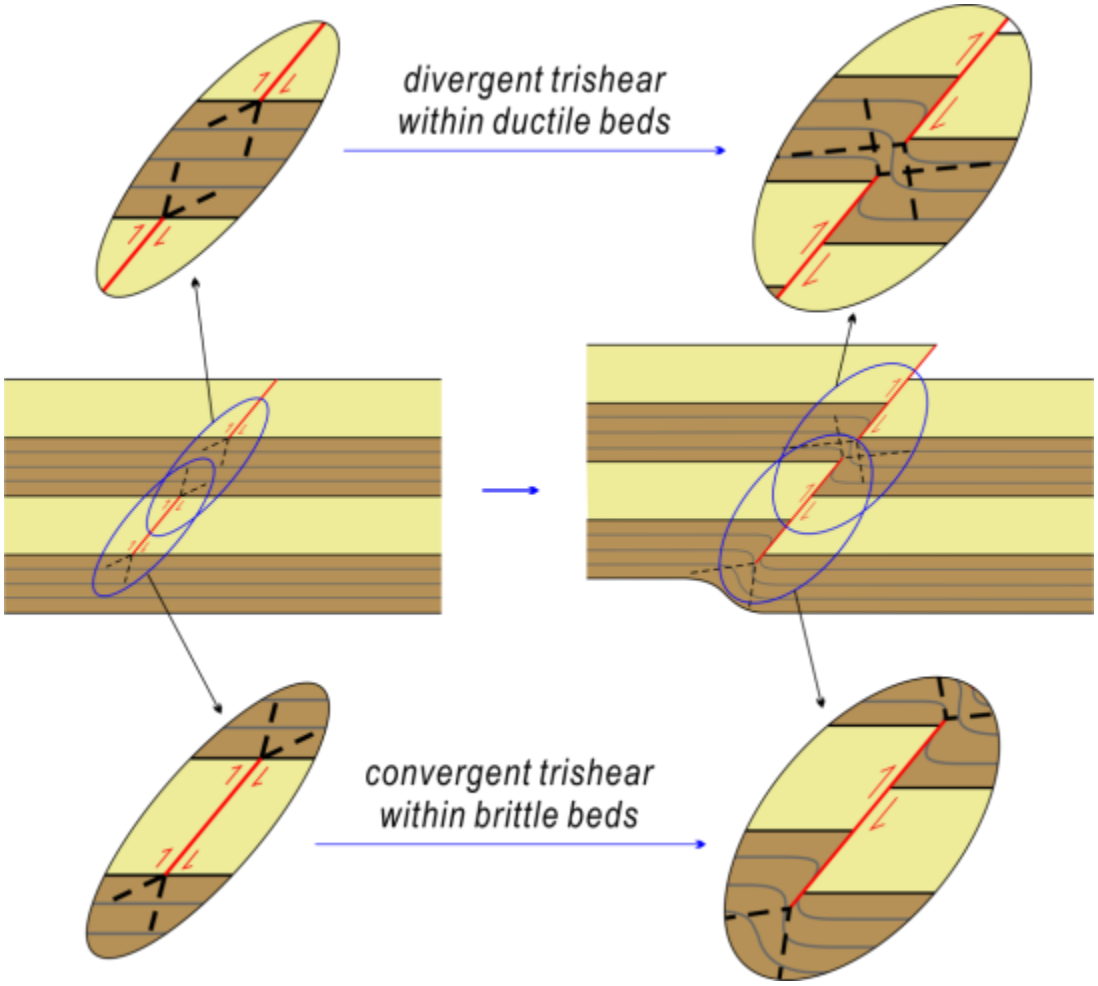

Figure 5.20 Schematic cartoons to illustrate the divergent trishear within the weak/ductile beds and convergent trishear within the brittle beds, when a mechanically layered sequence of beds is subject to stress.

5.6. Reverse Fault Model to Define the Fault Zone Elements

Based on the detailed maps of the outcrops in the Lenghu5 structure, here a more detailed reverse fault growth model is presented in Figure 5.21, in which the fault zone grows in a mechanically layered sequence of beds. As above, the yellow and brown units represent brittle layers and weak/ductile layers, respectively. The interbeds of brittle and weak/ductile layers with different thickness are chosen in order to evaluate the effects of mechanical heterogeneity on the final fault zone geometry.

As shown in Figure 5.21, according to the magnitude of the strain in the deformed beds, the fault has been divided into three zones: **Fault Core (FC),**

Inner Damage Zone (IDZ) and Outer Damage Zone (ODZ) outward from the centre. This division concurs with the outcrop observation, e.g., TF1, F2, NF1 and NF2.

The Fault Core (FC) is located in the most central position of the faulted section, which accounts for the majority of the fault displacement and is usually confined by two discrete slip surfaces that are sub-parallel to each other, e.g., TF1-4 , TF1-5 and TF1-6 (Figure 5.3-Figure 5.5). This observation is in an agreement with the study of Childs et al. (1996b). The fault rocks between the two discrete slip surfaces experience the highest strain. It is found that the final geometry of a FC is highly dependent on the mechanical heterogeneity of the sequence. For example, the FC is very poorly developed in a mechanically homogeneous sequence (e.g., F2 in Figure 5.13); in contrast, the more ductile layers are incorporated into a smear zone within the FC in a mechanically heterogeneous sequence (e.g., F3 in Figure 5.14).

The detailed outcrop maps suggest that the mechanical strength of a layered sequence is scale-dependent. For example, the thin sandstones within thick mudstones do not have a large impact on the bulk strength and become entrained into the smear zone within the FC. The degree of disassociation of entrained sandstone beds depends on the thickness/strength of the sandstone beds. The thick sandstone beds may form continuous faulted sand boudins defining a smearing-like distribution towards the FC, but thin sandstone beds just break down to form isolated boudins.

The Inner Damage Zone (IDZ) is located directly at the two sides of the FC. In reverse fault model (Figure 5.21), the folds, splay faults and fault lenses dominate the IDZ, presenting the highest strain except in the FC. The splay faults and fault lenses form within the mechanically stronger units, and link through the weaker units. The smaller-scale heterogeneities of the sequence generating smaller-scale fault arrays or lenses (e.g., the reverse fault F3, Figure 5.14), which presents the scale independency in terms of the deformation styles. The splay faults branch into the undeformed or slightly deformed beds, which creates more fault complexity. The asperity reduction during later deformation may potentially form new fault lenses, which can increase the width of the IDZ.

The Outer Damage Zone (ODZ) is usually located in the further side adjacent to the Inner Damage Zone (IDZ) (Figure 5.21). The ODZ is often developed in the mechanically stronger units in the study area, e.g., the reverse fault F2 (Figure 5.13) and the thick sandy packages in the hanging wall of the normal fault NF1 (Figure 5.15). In the ODZ, fractures or small faults can form but do not propagate far enough to link together.

Based on the field observation, the FC and IDZs are commonly observed in all the outcrops. However, the ODZs are usually observed in the outer portion of the hanging wall and footwall of a high strain FC. This is because the FC and IDZs account for the majority of the strain accommodated in a sequence and the low strain deformation is not capable to create ODZs in the two walls.

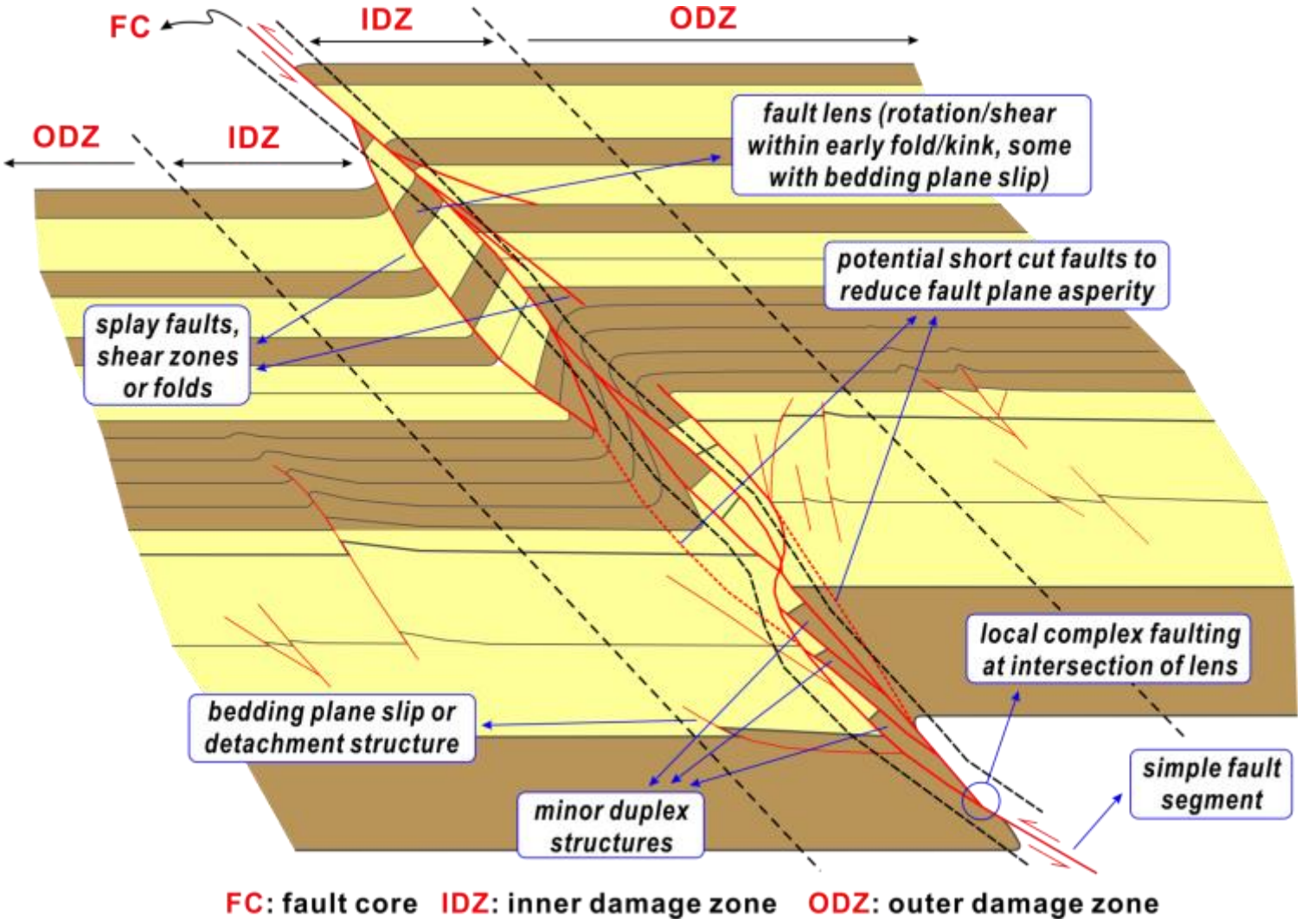

Figure 5.21 The conceptual model to define the elements of the reverse fault zone.

The mapped outcrops in Lenghu5 structure cover reverse faults with different amounts of fault throw, ranging from 50cm (e.g., F1) to hundreds of meters (e.g., TF1). The high range of fault throws generates fault zones with very different widths. The outcrops with different fault throws suggest that the FC, IDZ and ODZ are not static but dynamically evolve with the growing fault displacement. The schematic model In Figure 5.22 demonstrates the FC, IDZ and ODZ evolving with the growing fault displacement. As described above, the IDZ usually comprises many splay faults and fault lenses. The growing fault displacement will effectively increase the strain of these splay faults and fault lenses within the IDZs. Therefore the portions adjacent to the FC are likely to be entrained into the FC, which increases the width of the FC significantly (Figure 5.22). When the fault displacement increases to a very large amount, the current IDZs may be entrained into the FC completely. Similarly, the developing IDZs extend towards the hanging wall and footwall by creating more splay faults and fault lenses in the adjacent undeformed rocks (see the extension in Figure 5.22b). Meanwhile, the ODZs also extend by creating more fractures or small faults in the outer undeformed hanging wall and footwall.

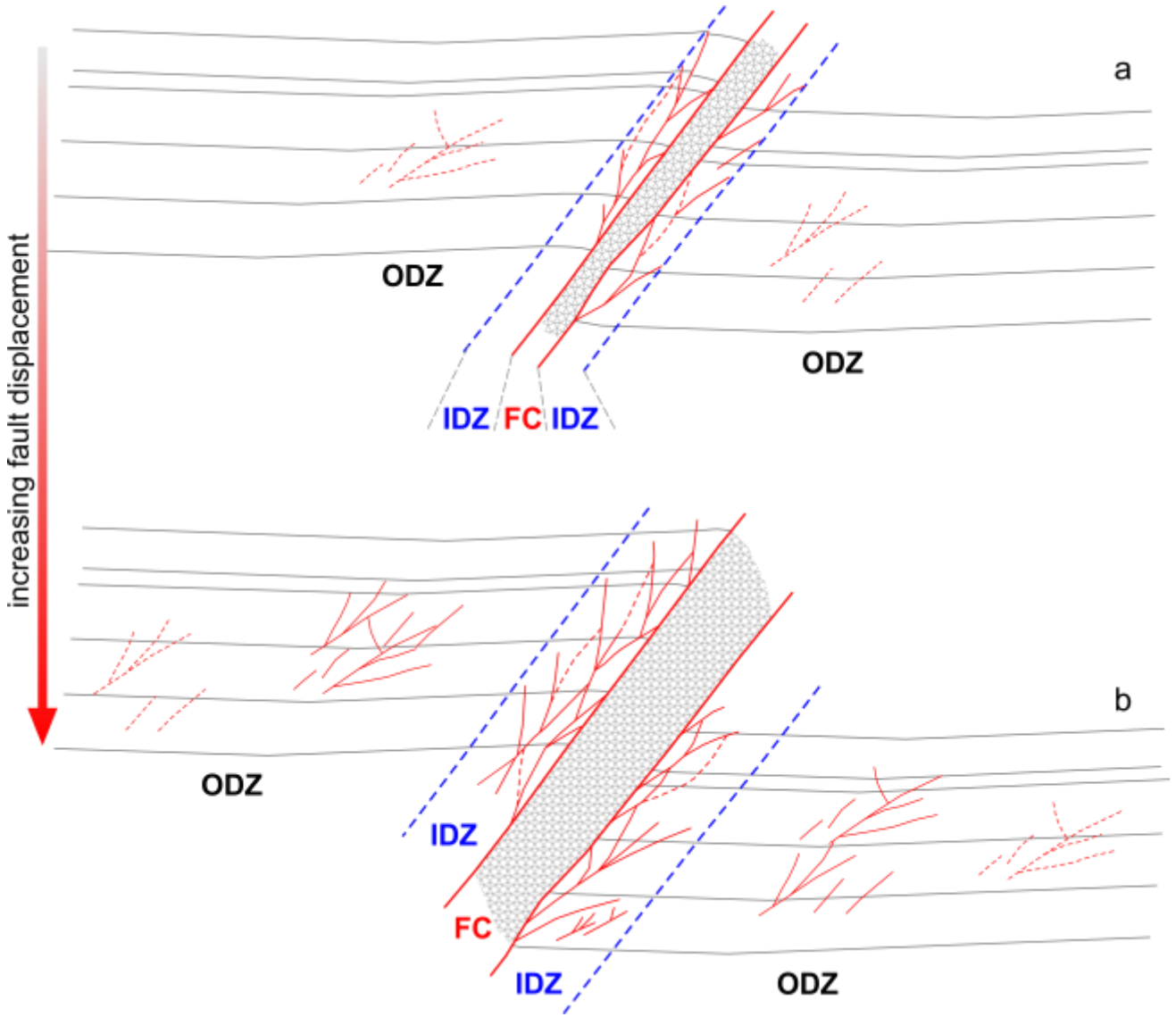

Figure 5.22 Schematic models to demonstrate the dynamic evolution of FC, IDZ and ODZ with growing fault displacement.

5.7. Discussion and Conclusions

Previous studies reported that the generation and distribution of fault rocks are affected by several factors, e.g., the fault displacement, lithology, deformation mechanism and internal fault structure (e.g., Hull, 1988; Blenkinsop, 1989; Loveless et al., 2011). Through integrating the observation of natural structures from the Lenghu5 structure, the effects of the fault displacement, the bed thickness, the stratigraphic sequence and the mechanical heterogeneity on the reverse fault architecture are discussed.

(1). Fault Displacement and Bed Thickness

Based on the detailed outcrop maps, it is proposed that larger displacements develop wider FC and IDZs. In the Lenghu5 outcrops, the high strain reverse faults, e.g., TF1-4/TF1-5 with displacements of >200m, form fault zones of >5m wide FCs (Figure 5.3 and Figure 5.4); while the low strain reverse faults, e.g., F3 with cumulative displacement of ~1.5m, form ~50cm wide FCs (Figure 5.14). This observation concurs with many of the previous studies (e.g., Otsuki, 1978; Robertson, 1983; Hull, 1988; Evans, 1990; Knott, 1994; Childs et al., 2009; Bastesen and Braathen, 2010), although the general rules describing the relationship between FC width and fault displacement still have not yet been quantitatively formulated. The smears of weak/ductile beds, e.g., mudstones, are commonly observed along the FCs in the outcrops of reverse faults. Large fault displacement renders the smears more discontinuous, although clay gauges may be formed along the FCs. This can be quantitatively verified by the previously proposed tools that are used to evaluate the effectiveness of generating continuous clay/shale smears, such as CSP (Bouvier et al., 1989; Fulljames et al., 1997), SSF (Lindsay et al., 1993), SGR (Yielding et al., 1997) and SSGR (Ciftci et al., 2013).

The strength of beds is influenced by the bed thickness, which imposes an important impact on the FC width. The FCs with similar fault displacements are compared to identify the effects of the bed thickness on the fault architecture. The reverse fault TF1-1 (Figure 5.11) comprises both thick sandstone beds in the lower section and thin sandstone beds in the upper section. The lower section forms discrete reverse faults and several narrow fault

lenses, while the reverse faults developed in the upper section mostly define wider FCs. This effect of the bed thickness on the fault architecture is also observed in the reverse fault TF1-3 (Figure 5.6). The degree of disruption of entrained sandstone beds depends on the thickness/strength of the sandstone beds: thick beds form continuous faulted layers, but thin beds break down to isolated boudins. For mudstone beds, thick mudstone beds can assist the generation of wider FCs than thin mudstone beds, because the thick mudstone beds can provide more mudstones to be attenuated or smeared into the FCs. The thicker mudstone beds are likely to generate more continuous smears in the FCs, which may form barriers for fluid migration.

(2). Stratigraphy

Hull (1988) pointed out that lithology is an important controlling factor on the fault rock generation and distribution in a fault zone. Here the effect of stratigraphic heterogeneity on the rock deformation behaviour in reverse faults is considered. The four sets of schematic cartoons in Figure 5.23 present the fault zone evolution of a layered sequence with different stratigraphic heterogeneities. Four sets of different sequences have been considered, which are (i). thick brittle beds; (ii). thin weak/ductile beds sandwiched within thick brittle beds; (iii). thin brittle beds sandwiched within thick weak/ductile beds; and (iv). thick weak/ductile beds, respectively.

Concurring with the previous studies (Eisenstadt and De Paor, 1987; Peacock and Sanderson, 1992; McGrath and Davison, 1995; Childs et al., 1996a; Schöpfer et al., 2006), the sequence of brittle beds form a strain zone evolving from fractures, small faults to through-going faults (Figure 5.23a); while the sequence of weak/ductile beds experiences folding-dominated deformation (Figure 5.23d). When the stratigraphic heterogeneity increases, the final geometry of a deformed sequence is determined by the dominant beds. For example, the sequence shown in Figure 5.23b is brittle-beds dominated, it presents a deformation behaviour similar to that in Figure 5.23a; similarly, the weak/ductile-beds dominated sequence in Figure 5.23c experience deformation features similar to that in Figure 5.23d.

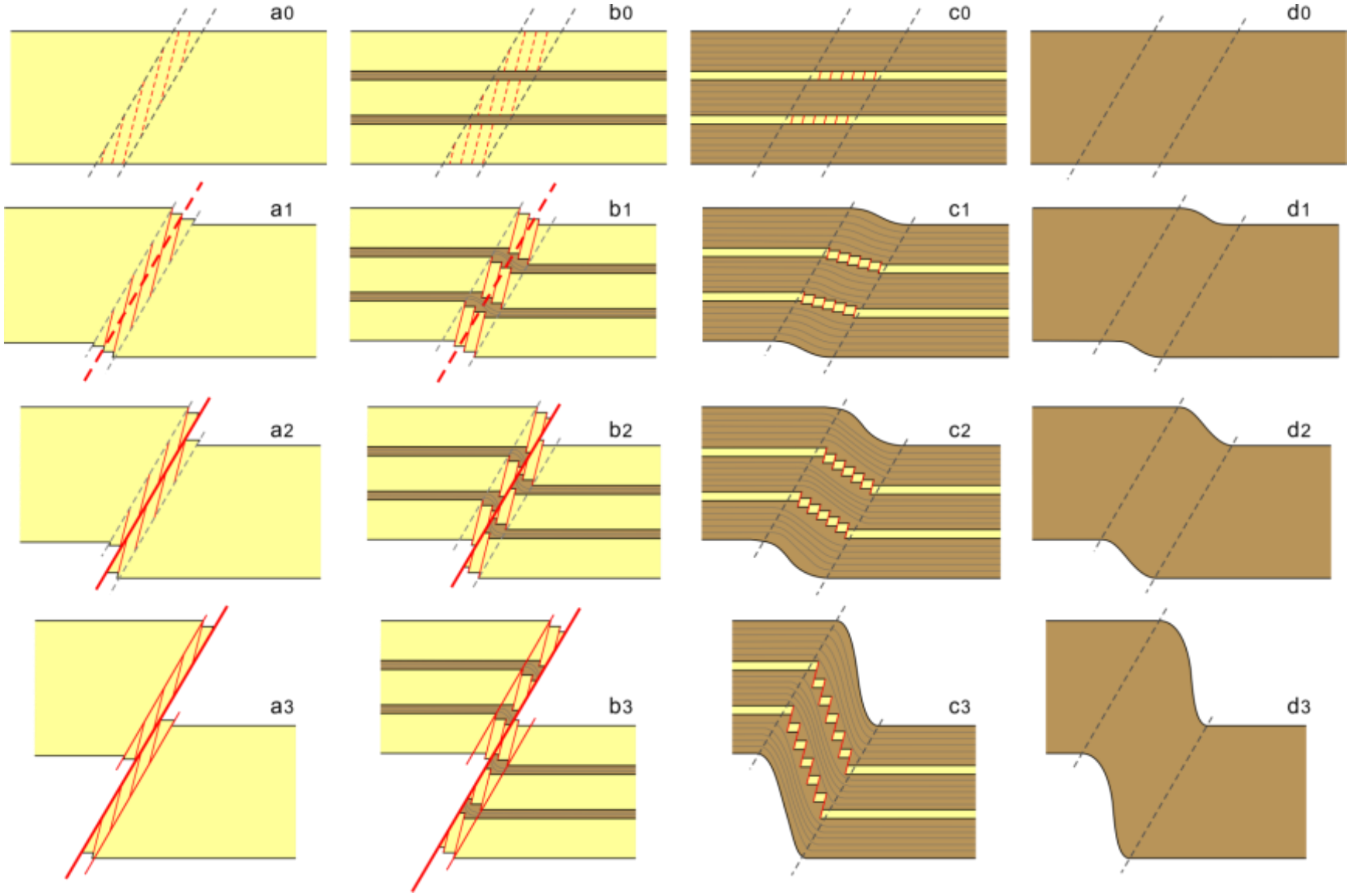

Figure 5.23 Schematic cartoons showing the effects of stratigraphy on the fault zone architecture in compressional structures.

The deformation behaviour of the beds also define a scale-independency. For example, although the sequence of thin weak/ductile beds sandwiched within thick brittle beds (Figure 5.23b) presents a deformation behaviour similar to that of the sequence of brittle beds (Figure 5.23a), the thin weak/ductile beds still tend to form ductile folds in the layer-scale; similarly, the thin brittle beds sandwiched within thick weak/ductile beds (Figure 5.23c) form layer-scale through-going faults, although the faulted boudins show an overall folding-like distribution.

(3). Mechanical Heterogeneity.

The term ‘mechanical stratigraphy’ has been widely accepted in structural geology to subdivide rocks into discrete mechanical units defined by properties such as tensile strength, elastic stiffness, brittleness and fracture mechanics properties (e.g., Corbett et al., 1987; Tyler and Finley, 1991; Cooke, 1997; Laubach et al., 2009). A mechanical stratigraphy with high heterogeneity may increase the complexity of the fault zone architecture in thrust systems (e.g., Woodward and Rutherford Jr, 1989; Woodward, 1992; Pfiffner, 1993; Davies et al., 2012). Therefore, the effect of mechanical heterogeneity needs to be considered when a sequence of multi-layered beds is subject to stress, e.g., the interbedded sandstone and mudstone observed in the Lenghu5 structure. In this scenario, apart from the fault displacement, bed thickness and stratigraphical/lithological stacking sequence, the reverse fault architecture also depends on the level of the vertical mechanical heterogeneity of the host stacking sequences.

The detailed outcrop studies in the Lenghu5 structure suggest that the high mechanical contrasts produce locally complex fault arrays; while the low mechanical contrasts generate more planar faults with narrow or absent damage zones, which concurs with the study of Davies et al. (2012). Figure 5.24 presents two sets of deformed sequences with the same stratigraphy but different mechanical heterogeneity. The sequence of thick interbedded brittle beds and weak/ductile beds (Figure 5.24a) presents lower mechanical heterogeneity than the sequence of thinly interbedded brittle beds and weak/ductile beds (Figure 5.24b).

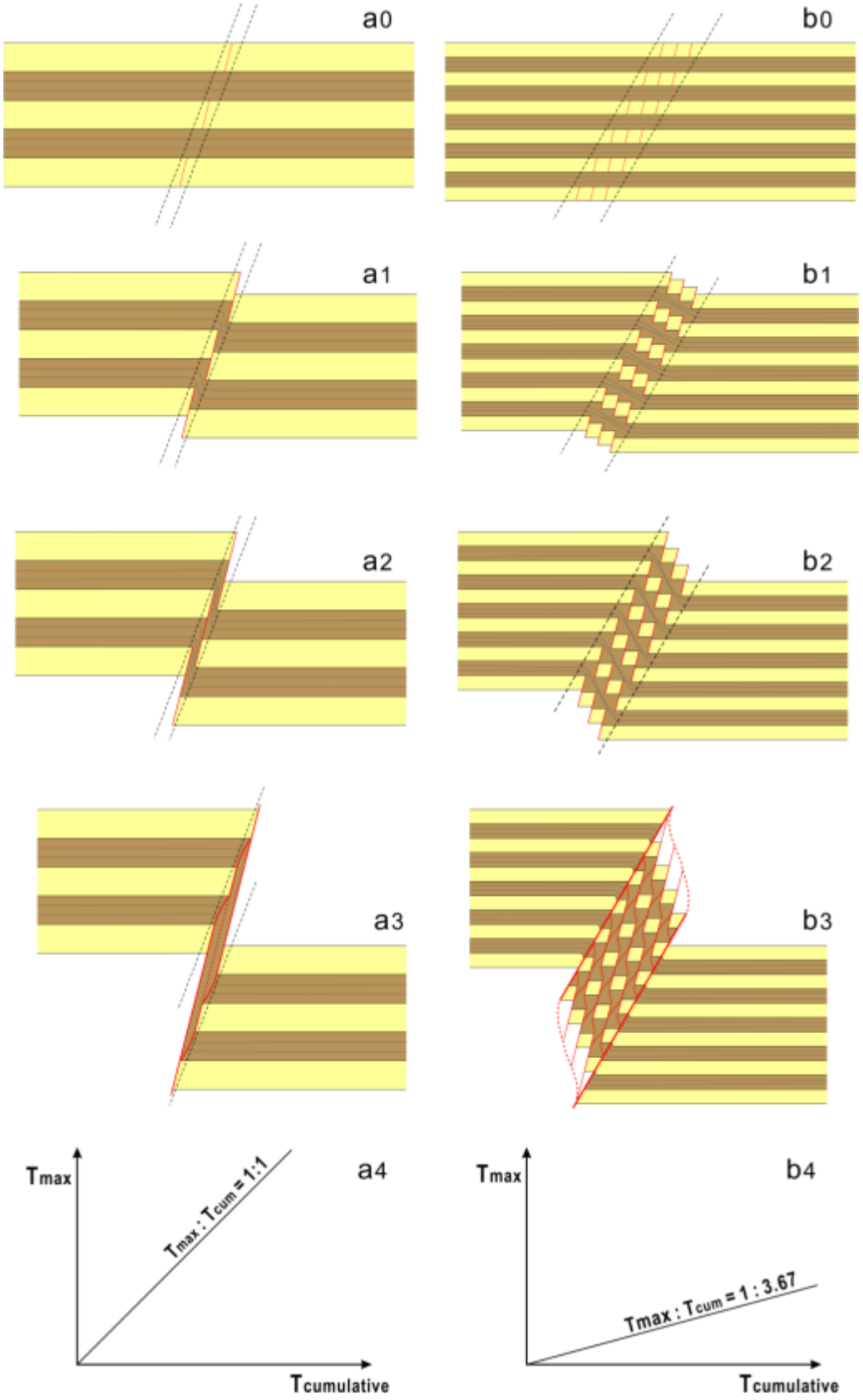

Figure 5.24 Schematic cartoons and plots showing the effects of mechanical heterogeneity on fault zone architecture in compressional structures. The plots are built based on the cartoon a3 and b3. T_{max} is the maximum throw along fault planes, and $T_{cumulative}$ is the cumulative throws of all fault planes.

A sequence of multi-layered beds with low mechanical heterogeneity is predicted to form narrow fault zones with a limited number of slip planes (Figure 5.24a); while a sequence of multi-layered beds with high mechanical heterogeneity usually forms wide fault zones that are composed of many small slip palnes (Figure 5.24b). In the first scenario, the maximum throw of slip planes is likely to be close to the cumulative throw (e.g., minor thrust fault F2). In the latter scenario, the maximum throw of the slip planes is usually much smaller than the cumulative throw of the fault zones (e.g., minor thrust fault F3). The sequence with lower mechanical heterogeneity tends to form narrow fault zones or single-plane faults with low degree of fault zone complexity (Figure 5.24a); in contrast, the sequence with higher mechanical heterogeneity is likely to form fault zones with high degree of fault zone complexity, e.g., splay faults, small folds, clay/shale smears and fault lenses (Figure 5.24b).

Having understood the meso-scale fault zone architecture of the Lenghu5 structure, the next chapter will present the micro-scale deoformation features of rocks both in and out of the fault zones. The micro-structural SEM analysis will demonstrate the deformation mechanisms and their effects on the fluid flow properties of the fault rocks, such as porosity, permeability and capillary threshold pressure.

Chapter 6
Micro-scale Analysis to Identify the Micro-scale Deformation Mechanisms and their Effects on Fault Sealing Capacity

6.1. Introduction

Faults increase the heterogeneity in sedimentary sequences and may perform as barriers or conduits for the entrapment and movement of hydrocarbons on both geological and production time scales (Smith, 1966; Berg, 1975; Smith, 1980; Watts, 1987). The barriers to fluid flow can be formed by the juxtaposition of reservior rocks against low permeability rocks (e.g., Allan, 1989; Knipe, 1997). Therefore, juxtaposition seal has been widely recognized as one of the most important hydrocarbon traps, which has been frequently targeted by the petroleum exploration. However, it is common to have fault zones formed when the beds are subject to stress, either extension or contraction (as discussed in Chapter 5). The rocks entrained into the fault zone have experienced deformation and develop different physical properties that may affect the fluid flow behaviour (e.g., Knipe, 1993a, 1997; Knipe et al., 1997; Fisher and Knipe, 1998; Ottesen Ellevset et al., 1998; Fisher et al., 2001; Fisher and Knipe, 2001; Fisher et al., 2009). The generation of fault rocks with high sealing capacity can effectively decrease the porosity and permeability of the fault zones, which may form traps when the reservior rocks are truncated by these fault rocks (Knipe, 1993a; Knipe et al., 1997; Fisher and Knipe, 1998; Ottesen Ellevset et al., 1998). The fundamental processes that result in the generation of fault-related barriers for hydrocarbon migration have been addressed by Mitra (1988) and Knipe (1989, 1992a, 1993b). In these studies, the deformation mechanisms and their effects on the fluid flow properties (e.g., porosity, permeability, capillary pressure) are investigated based on SEM micro-structural and petrophysical analyses.

In the Lenghu5 structure, the rock samples have been collected from the mapped outcrops (meso-scale analysis in Chapter 5), in both the fault zones

and the undeformed hanging walls/footwalls. SEM micro-structural analysis has been conducted on these fault rocks in order to:

(i). determine the diagenetic history of both inside and outside of the fault zones;

(ii). identify the deformation processes and the sealing mechanisms involved;

(iii). constrain the timing of deformation relative to the burial and diagenetic histories.

6.2. Methods

The detailed maps of outcrops (Chapter 5) provide good understanding in the detailed fault zone architecture. The rocks samples are then collected in both the fault zones and the undeformed hanging walls/footwalls of these mapped outcrops in the Lenghu5 structure. The microstructures of these rock samples are studied by Scanning Electron Microscope (SEM), in order to identify the deformation mechanisms and their influences on the fluid flow properties of the fault rocks.

(1) Fault rock sample preparation

The samples in both the fault zones and the undeformed hanging walls/footwalls of the well-exposed outcrops have been collected in the fieldwork, with the necessary marks noting the sample orientation and shearing sense. In the cutting lab, the rock samples are cut perpendicular to the fault plane along the shearing direction, in order to expose the maximum deformation features in the cutting planes (Figure 6.1). As the rock samples are poorly to moderately lithified, the samples are resin-impregnated before cutting and polishing. These resin-impregnated polished blocks are then coated by carbon for the SEM micro-structural analysis.

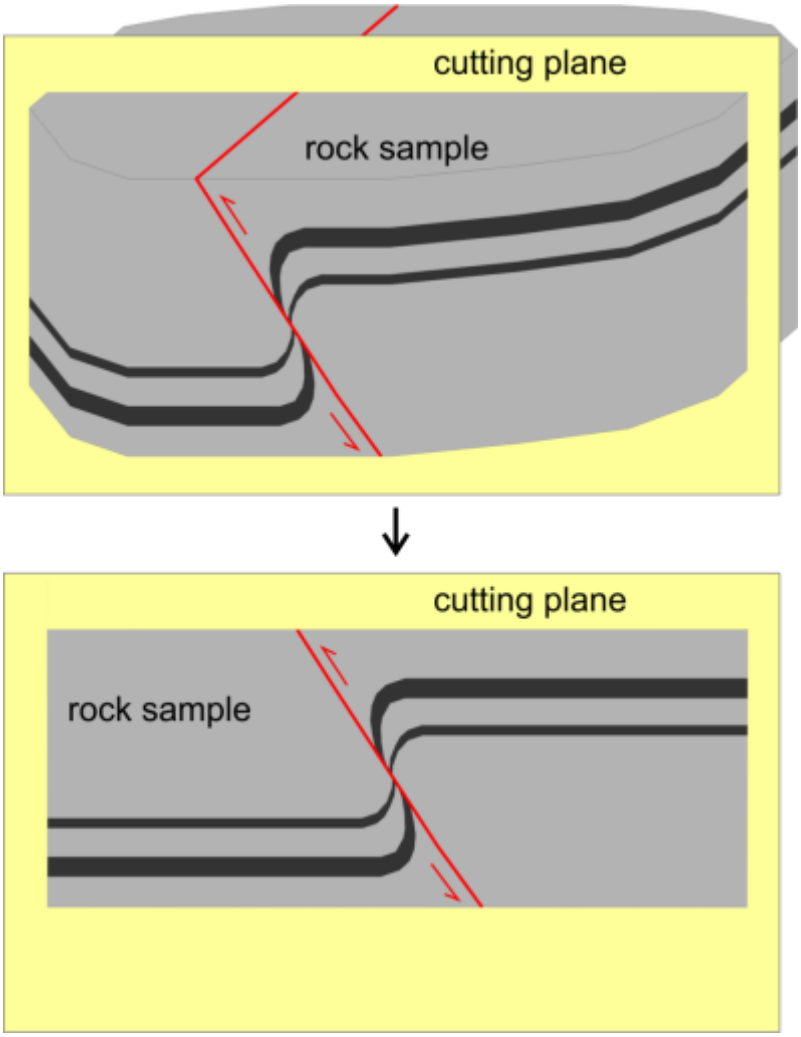

Figure 6.1 The sketch delineating the best cutting plane to the rock samples selected for SEM micro-structural analysis. The bottom sketch shows the maximum deformation features in the best cutting plane.

(2) SEM micro-structural analysis

Polished blocks were examined by a CAMSCAN CS44 high performance Scanning Electron Microscope (SEM) equipped with detectors of Secondary Electron (SE), Back-Scattered Electron (BSE), Cathodeluminescence (CL) and an EDAX Energy Dispersive X-ray Spectrometer (EDX). The BSE signal is directly proportional to the mean atomic number of the mineral; so phases of different mass have different brightness levels. The CL signal is extremely sensitive to trace element abundances and provides information on the growth zonation (e.g., the quartz overgrowth).

The diagenetic history of both inside and outside the fault zones are determined and used to establish the timing of deformation in relation to the major diagenetic events. The microstructures of the deformation features are used

to assess/identify the active rock deformation mechanisms (e.g. diffusive mass transfer, grain-fracturing etc.) and the history of deformation. Representative BSE and CL images are taken from inside and outside of the fault zones as well as traverses across the border zone areas. These images are saved in 8-bit (256 grey-levels) digital form, and then imported into an image analysis package to estimate the porosity and the mineral abundance of the rock samples. This data set is then used to assess the effect of deformation on the porosity/permeability relations, and deformation/ diagenetic history of the rock.

6.3. Micro-Structural Analysis of the Fault Rocks

Fourteen rock samples (Table 6.1) collected from the Lenghu5 central fault zone were selected for the micro-structural analysis. Based on the detailed cross section S9 in Chapter 4 (also in Figure 6.2), the maximum displacement of the Lenghu5 reverse fault zone is ~800m. As shown in the structural map (Figure 6.2), the outcrops where these rock samples were collected are TF1 and TF2-TF4. The outcrops are all located within the central fault zone to highlight the maximum deformation happened to the Lenghu5 structure. The outcrop TF1 is located in the southern end of the Lenghu5 structure; while the outcrops TF2-TF4 are located within the southern anticline core. The detailed micro-structural analyses of these rock samples are presented in the following sub-sections (Figure 6.4 to Figure 6.17).

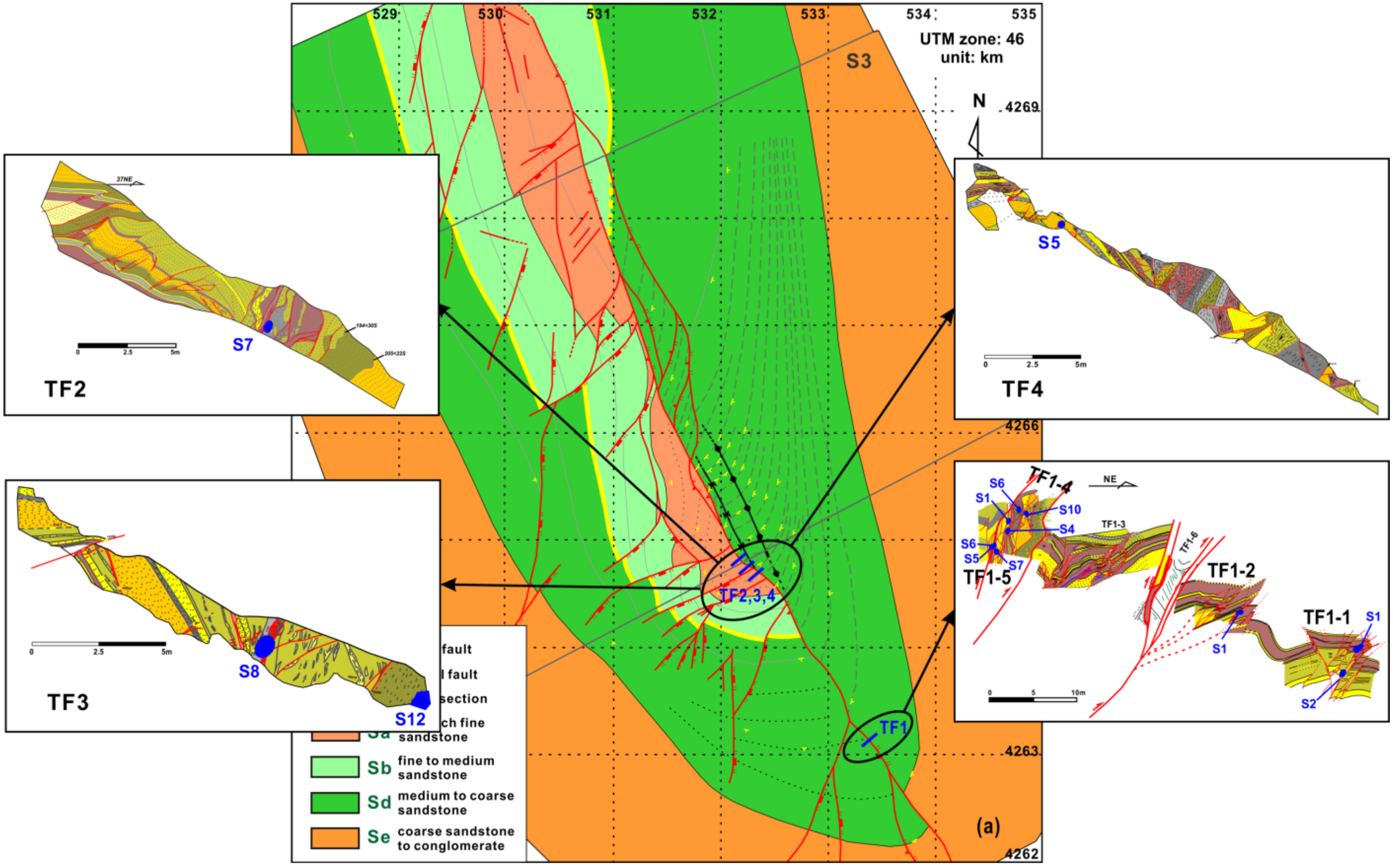
529
530
531
532
533
534
535
UTM zone: 46
unit: km
N
4269
4266
4263
4262
S3
TF2,3,4
TF1
(a)
TF2
37NE
S7
0
2.5
5m
TF3
S8
S12
TF4
S5
TF1-5
TF1-4
TF1-3
TF1-6
TF1-2
TF1-1
NE
S6
S1
S10
S4
S5
S7
S2
0
5
10m
fault
l fault
section
ch fine
sandstone
Sb fine to medium sandstone
Sd medium to coarse sandstone
Se coarse sandstone to conglomerate

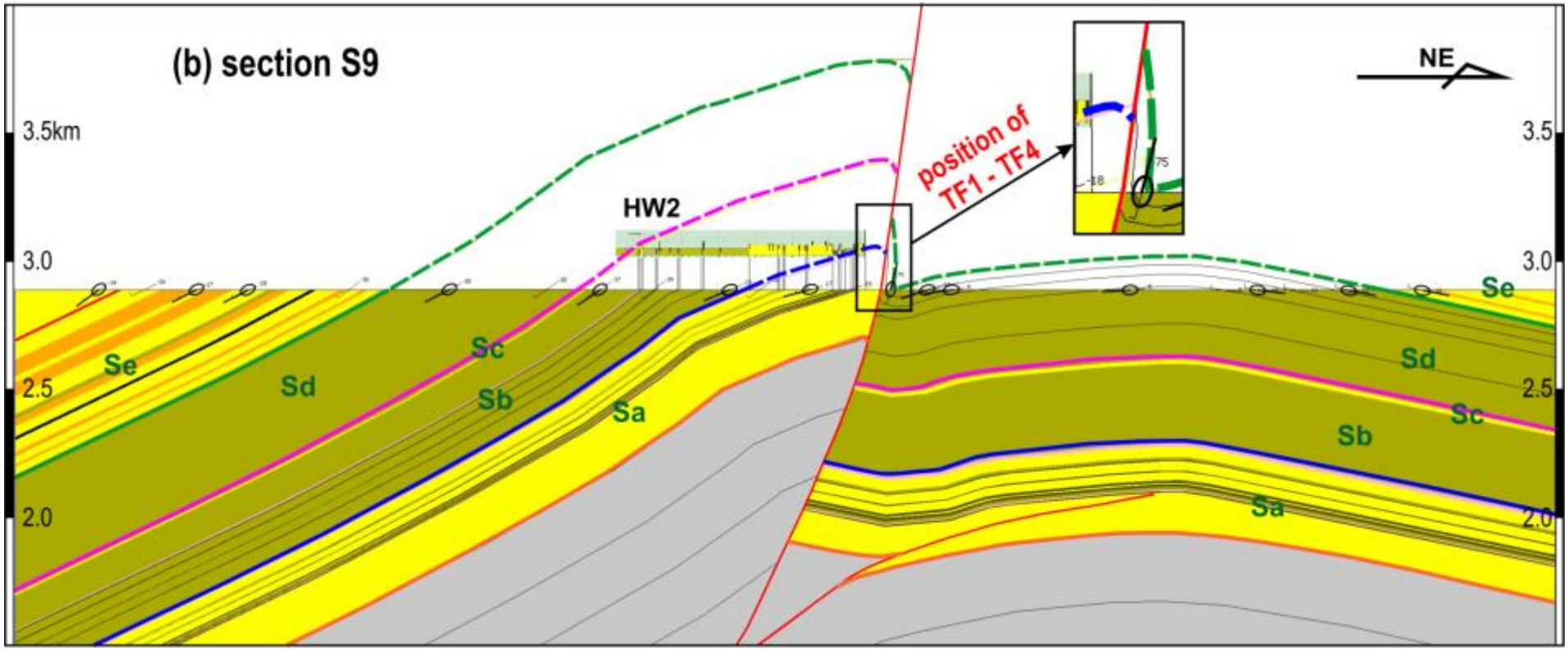

Figure 6.2 The structural map and cross section showing the locations of the outcrops where fault rocks were sampled for micro-structural analysis.

Table 6.1 The list of fault rock samples collected in the Lenghu5 structure for the SEM micro-structural analysis. Abbreviations: HR (host rock) and FR (fault rock).

Fault	Sample ID	Sampling Position	Rock Types	Formation
TF1-1	TF1-1-S1	hanging wall & fault zone	HR & FR	N_2
	TF1-1-S2	hanging wall & fault zone	HR & FR	N_2
TF1-2	TF1-2-S1	fault zone	FR	N_2
TF1-4	TF1-4-S1	central fault zone of the main fault	FR	N_2
	TF1-4-S4	central fault zone of the main fault	FR	N_2
	TF1-4-S6	central fault zone of the main fault	FR	N_2
	TF1-4-S10	central fault zone of the main fault	FR	N_2
TF1-5	TF1-5-S5	fault zone	FR	N_2
	TF1-5-S6	fault zone	FR	N_2
	TF1-5-S7	sandstone block in fault zone	HR	N_2
TF2	TF2-S7	fault zone	FR	N2
TF3	TF3-S8	hanging wall & fault zone	HR & FR	N2
	TF3-S12	deformation bands in sandstone	FR	N2
TF4	TF4-S5	fault zone in impure sandstone	FR	N2

A classification scheme for fault rocks as a function of the grain-size reduction, the post-deformation lithification and the clay/phyllosilicate content is presented in Figure 6.3 (Fisher and Knipe, 1998). With reference to this diagram, the deformation features present in the investigated fault rock samples from the Lenghu5 central fault zone include:

(i). Clay smears (six samples);

(ii). Phyllosilicate-framework fault rocks (three samples);

(iii). Cataclastic fault rocks (two samples);

(iv). Cemented fractures (three samples).

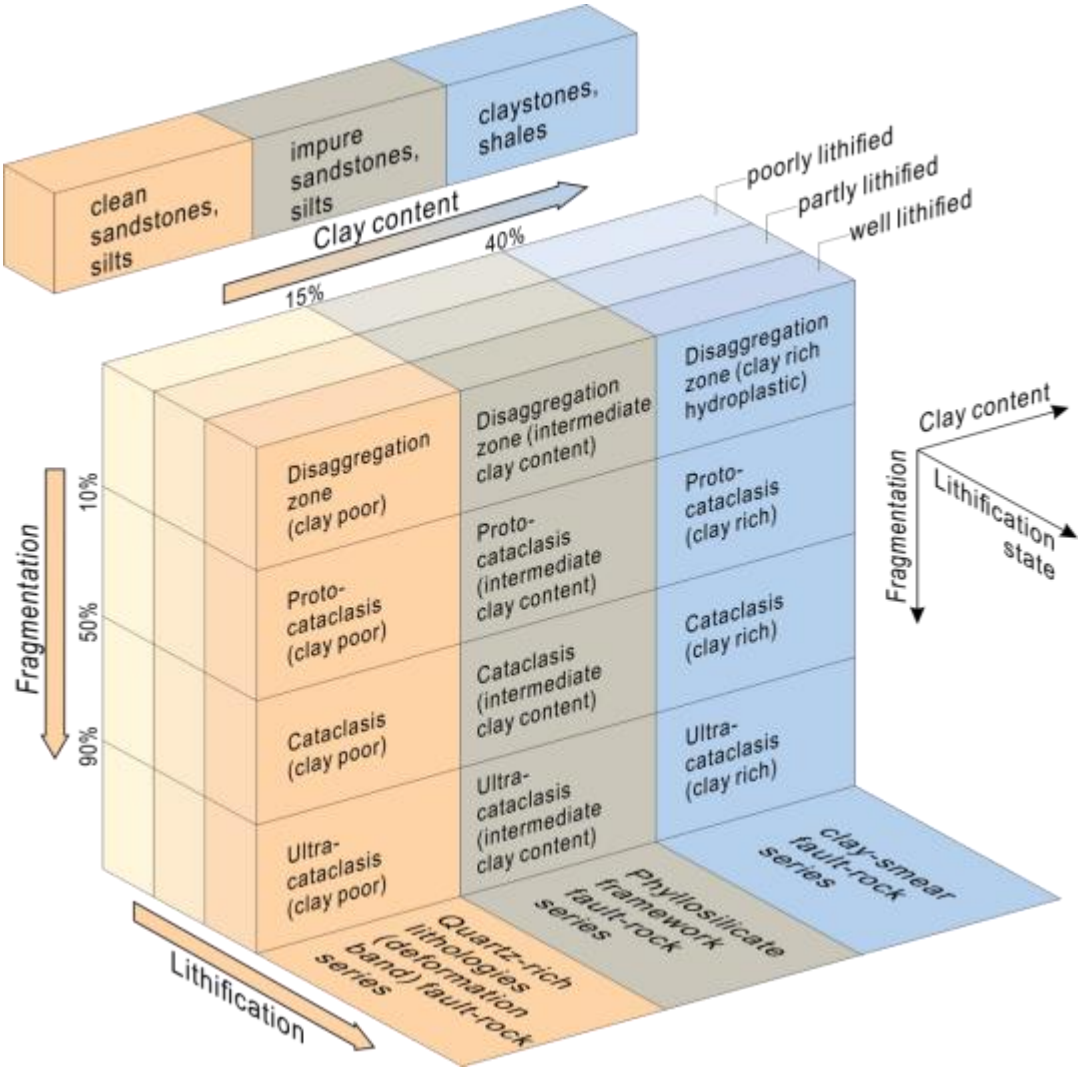

Figure 6.3 The fault rock classification based on the clay content, the grain-size reduction and the post-deformation lithification. The arrows point towards decreased permeability and increased threshold pressure (Fisher and Knipe, 1998).

6.3.1. Clay Smears

The clay smears are fault rocks that contain coherent domains of aligned phyllosilicates with over 40% total fine-grained phyllosilicates formed by the smearing of phyllosilicate-rich laminae along the faults. The term ‘clay smear’ is generally used to describe the incorporation of clay/phyllosilicate materials into a fault zone between the hanging wall and footwall cut-offs of the mudstone horizons. The presence of a clay domain along the fault plane produces a zone of very fine-grained material with limited pore throat connectivity; as a result, the clay smears have very low permeabilities and high threshold pressures.

In the previous studies (e.g., Bouvier et al., 1989; Lindsay et al., 1993; Gibson, 1994; Yielding et al., 1997; Yielding, 2002; Jolley et al., 2007; Ciftci et al., 2013), the clay smear has been widely used to describe the shearing of clay-rich units (e.g., clay soils, shales and mudstones) induced by the fault zone deformation. Three mechanisms of clay/phyllosilicate smearing have been proposed by Lindsay et al. (1993):

(i) by the abrasion of clay/phyllosilicate when it moves past brittle beds, e.g., sandstones;

(ii) by the shearing and ductile deformation of high clay content beds (e.g. shale/mudstone beds) between the hanging wall and footwall;

(iii) by the injection of clay/phyllosilicate materials during fluidisation.

In the Lenghu5 structure, six samples associated with clay smears were observed: TF1-2-S1, TF1-4-S4, TF1-4-S1, TF1-4-S6, TF1-5-S6 and TF3-S8 (Table 6.1). The clay smear domains form where the phyllosilicate-rich laminae or shale units were displaced by being dragged into the fault zone. They are mainly present in the sections of clay-rich units. The clay smear fault rocks have the lowest permeabilities. Therefore, these clay smears, if developed across the reservoir sandstone sections, can be significant barriers to fluid flow.

(1). Sample TF1-2-S1

Sample TF1-2-S1 is located within the reverse fault zone of TF1-2, a low strain splay fault of the main reverse fault outcrop TF1 in the southern end of the Lenghu5 structure (Figure 6.2).

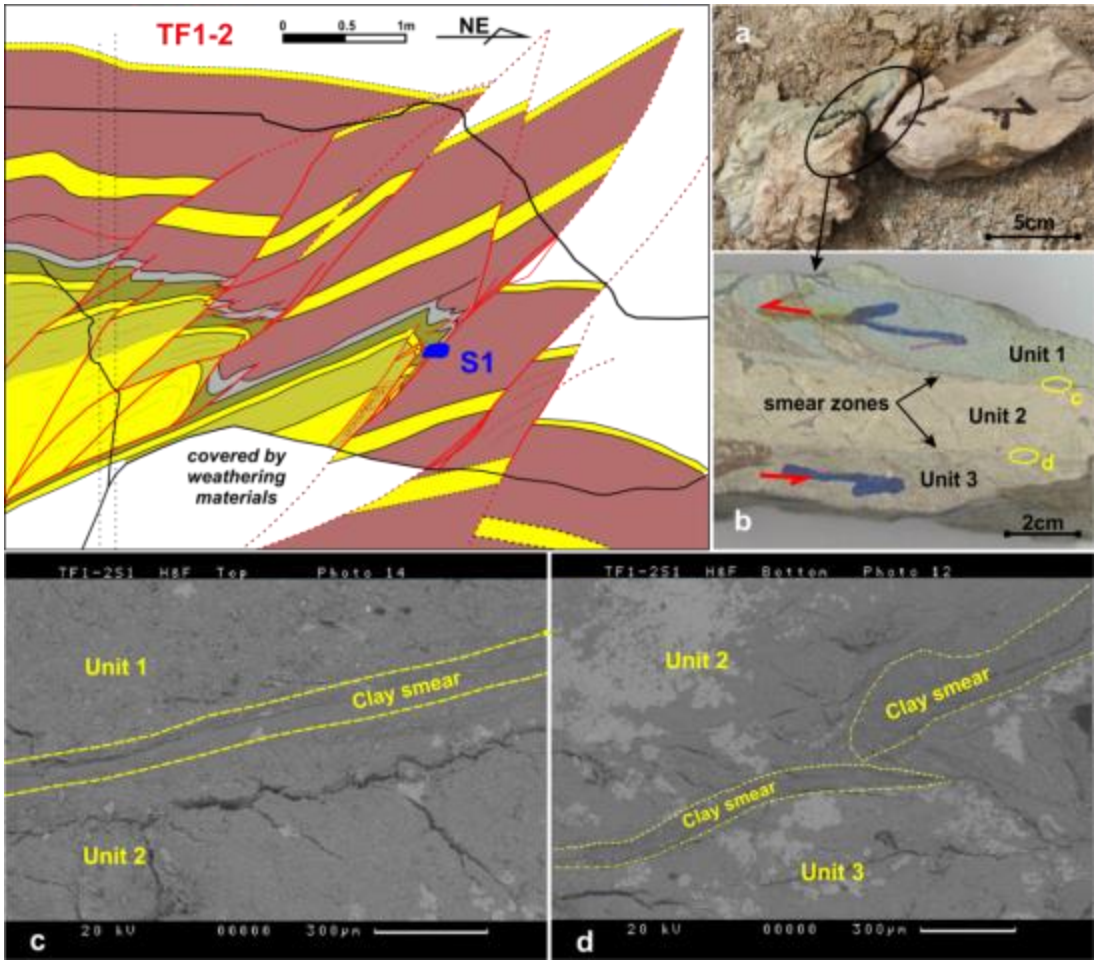

Figure 6.4 The sample photos (a, b) and BSE micrographs (c, d) showing the clay smear-dominated fault rocks in the sample TF1-2-S1. Note the high clay contents (75-85%) and low porosity (<5%) of the clay smear fault rocks formed in the interfaces between the sub-units (b-d).

The cumulative fault throw of TF1-2 is ~2m. More folding is shown in clay-rich layers than the sandy layers, which may be attributed to the physical properties of rocks with high clay/sand ratio. The reverse fault imbricates form at lower angles than the bounding reverse faults and mostly as discrete fault traces but shearing into fault zone except the frontal faults. Fault lenses are also generated along the reverse faults, particularly when the fault comes across the top clay-rich layers. Fault lenses are also the structures that absorb a great amount of fault throw. As the lithology is clay-rich, the

fault rocks are dominated by shales/mudstones that have been smeared into the fault zone.

As the detailed outcrop map (Figure 6.4) shows, the sample TF1-2-1 is collected in the fault zone where the hanging wall mudstone (grey) juxtaposes against the footwall mudstone (brown). The host rock is a mudstone with up to 75-85% clay contents, showing very low porosity (<5%) and permeability. A series of clay smears are observed in the SEM micro-structural analysis on this sample, particularly in the interfaces between the three sub-units (Figure 6.4b-d).

(2). Sample TF1-4-S4

Sample TF1-4-S4 is located within the fault zone of TF1-4, the central high strain fault zone of the main reverse fault outcrop TF1 in the southern end of the Lenghu5 structure (Figure 6.2). TF1-4 is a steeply dipping fault zone with sheared stratigraphy comprising foliated fault rocks of primarily mudstones and some sandstones (Figure 6.5). The mudstones are vertically distributed as they are smeared into this fault zone from the hanging wall stratigraphy; while the sandstones are faulted and thinned by fault offsets forming boudins in the attenuated layers. Although the fault rocks are apparently vertically distributed in the fault zone, bedding cannot be identified because the original bedding is destroyed by the intense shearing and faulting. The fault throw of TF1-4 is not measurable as it exceeds the outcrop size (hundreds of meters based on the section analysis in Chapter 4). Similar to the sample TF1-2-S1 (Figure 6.4), sample TF1-4-S4 has a lithology of mudstone with up to 75-80% clay contents; and the primary deformation features are clay smears that have very low porosity <5% (Figure 6.5d, e).

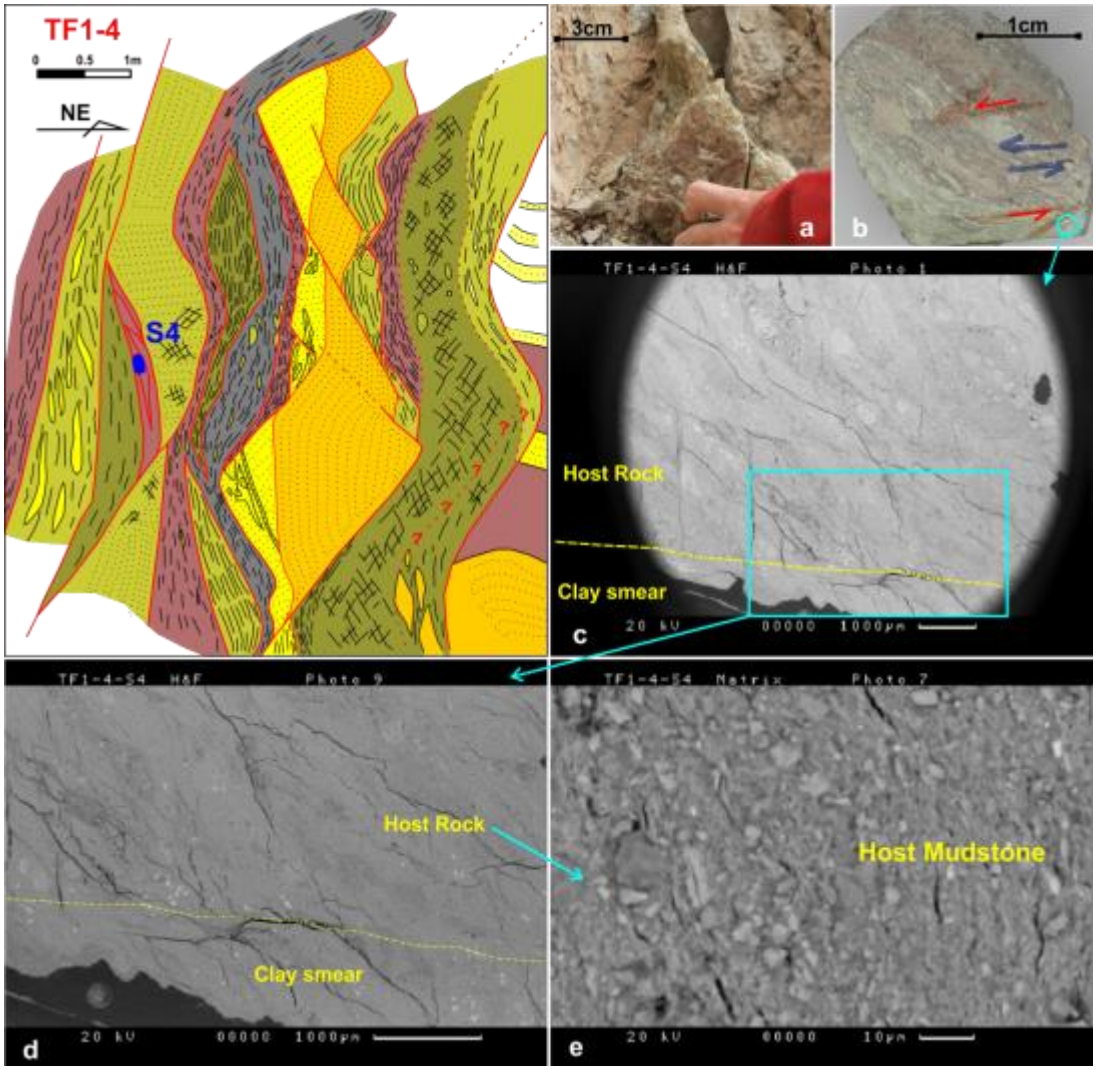

Figure 6.5 The sample photos (a, b) and BSE micrographs (c-e) showing the clay smear-dominated fault rocks in the sample TF1-4-S4. Note the high clay contents (75-80%) and low porosity (<5%) of the clay smear fault rocks (d).

(3). Sample TF1-4-S1

Sample TF1-4-S1 is located in the fault zone of TF1-4, the central high strain fault zone of the main reverse fault outcrop TF1 in the southern end of the Lenghu5 structure (Figure 6.2). This sample is collected from mixed mud-stones and sandstone boudins. It comprises lithologies of sandy mudstone (in grey) and mudstone (in brown), with clay contents of 50-60% and 70-75%, respectively (Figure 6.6a). This sample presents clay smear-dominated fault rocks with low porosity <5% (Figure 6.6c, d, f). However, in some fault rock domains, the sandy boudins are contained in the clay matrix (Figure 6.6e).

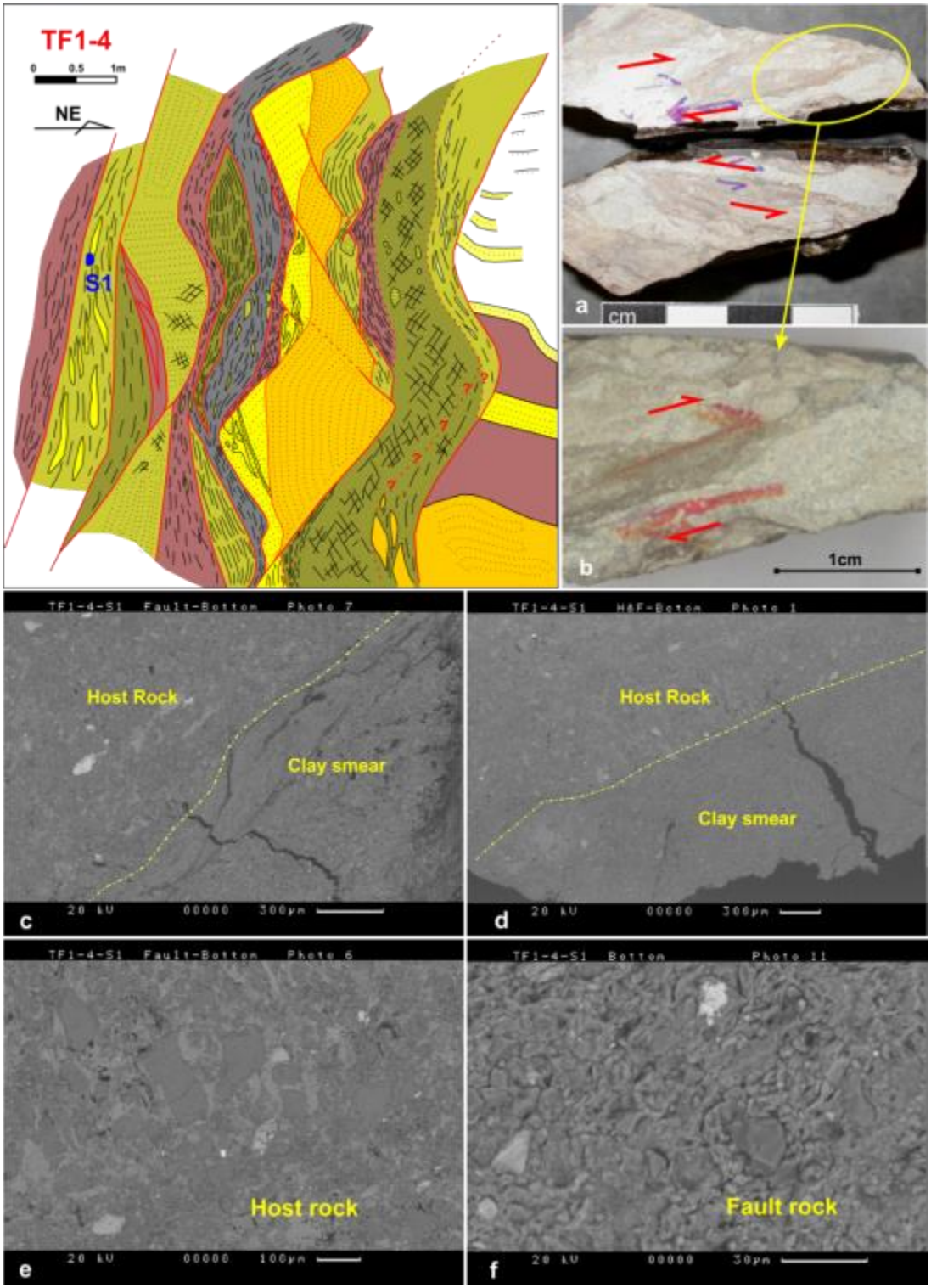

Figure 6.6 The sample photos (a, b) and BSE micrographs (c-f) showing the clay smear-dominated fault rocks in the sample TF1-4-S1. Note the high clay contents (50-75%) and low porosity (<5%) of the clay smear fault rocks (f).

(4). Sample TF1-4-S6

Sample TF1-4-S6 is located within the outcrop TF1-4, the central high-strain fault zone of the main reverse fault outcrop TF1 in the southern end of the Lenghu5 structure (Figure 6.2). This sample was derived from a sandstone-dominated bed (the left greyish-yellow sandstone in Figure 6.7); however, the mixing between the left sandstone and the right grey shale increased the clay content of the fault rock (>50%) (Figure 6.7). The dominating deformation features observed in the SEM micro-structural analysis are clay smear zones, which have very low porosity <5% (Figure 6.7d, e).

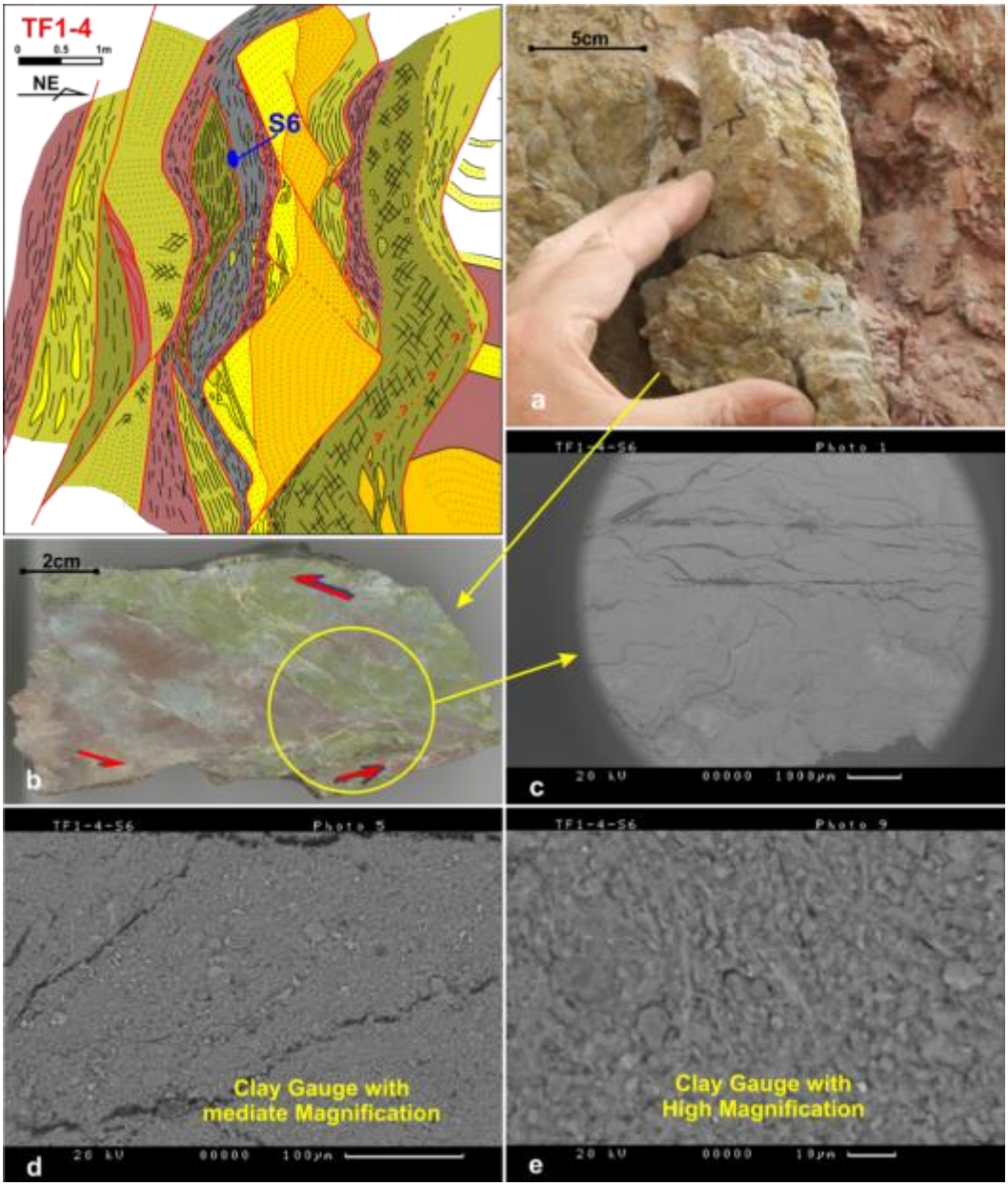

Figure 6.7 The sample photos (a, b) and BSE micrographs (c-e) showing the clay smear-dominated fault rocks in the sample TF1-4-S6. Note the high clay contents (>50%) and low porosity (<5%) of the clay smears.

(5). Sample TF1-5-S6

Sample TF1-5-S6 is located within the fault zone of TF1-5, a central high strain fault zone of the outcrop TF1 in the southern end of the Lenghu5 structure (Figure 6.2). Similar to the above TF1-4, the fault throw is not measurable as it exceeds the outcrop size (hundreds of meters based on the section analysis in Chapter 4). The host lithologies of this sample are mud-stone (Unit 1, 3, clay contents of 70-75%) and sandy mudstone (Unit 2, 4, clay contents of 50-60% (Figure 6.8b). The deformation features present in the SEM micro-structural analysis are clay smears that has low porosity <5% (Figure 6.8c).

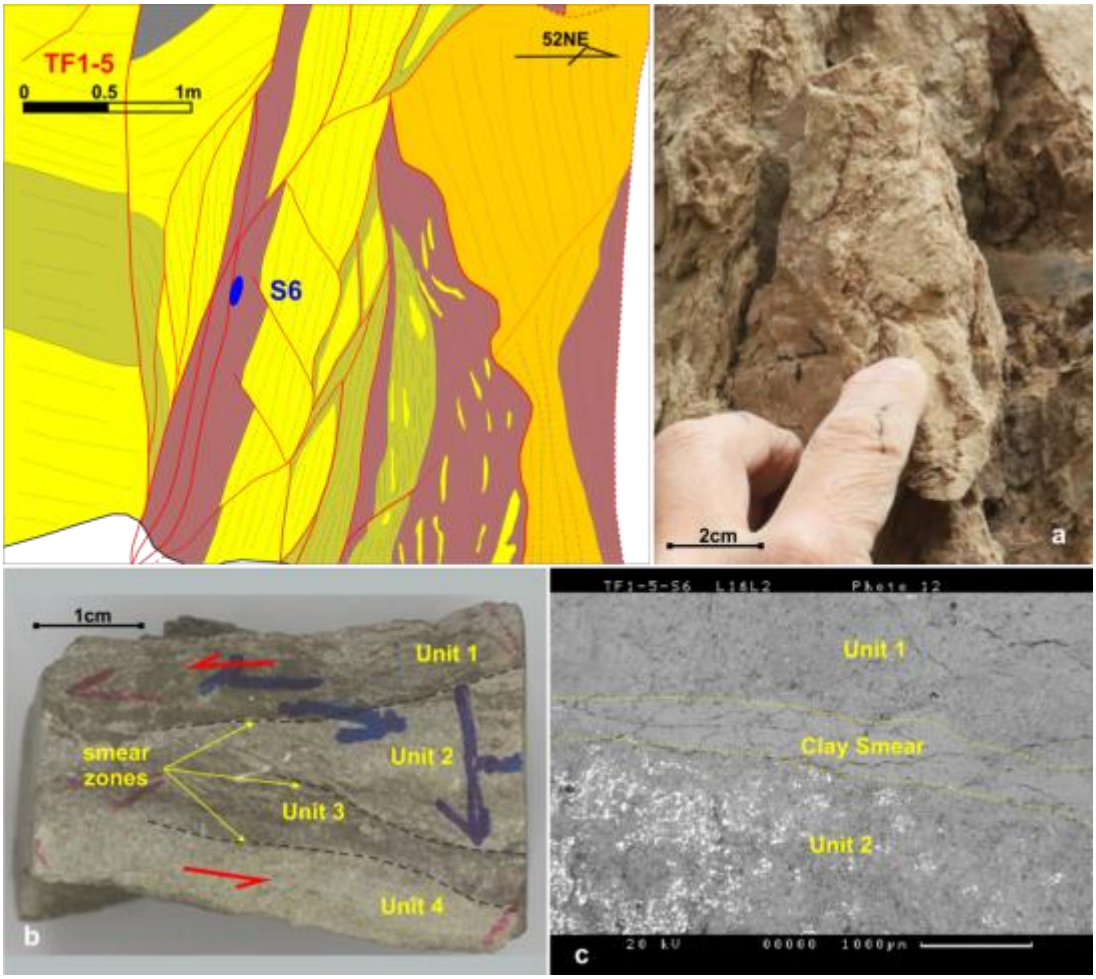

Figure 6.8 The sample photos (a, b) and BSE micrograph (c) showing the clay smear-dominated fault rocks in the sample TF1-5-S6. Note the high clay contents (70-75% for units 1&3 and 50-60% for units 2&4) and low porosity (<5%) of the clay smear fault rocks in the interfaces between the sub-units (c).

(6). Sample TF3-S8

Sample TF3-S8 is located within the central fault zone of TF3, a main reverse fault outcrop in the southern anticline core of the Lenghu5 structure (Figure 6.2). As the detailed outcrop map of TF3 (Figure 6.9) shows, an anticline with a flat crest forms against the reverse fault in the hanging wall. The steeply dipping central fault zone presents sheared stratigraphy comprising foliated fault rocks of primarily mudstone and some sandstones. Similar to TF1-4/TF1-5 outlined above, the fault throw for the central fault zone is not measurable as there are no matching stratigraphic units in the two walls (700-800m based on section S9 in Chapter 4, also Figure 6.2b).

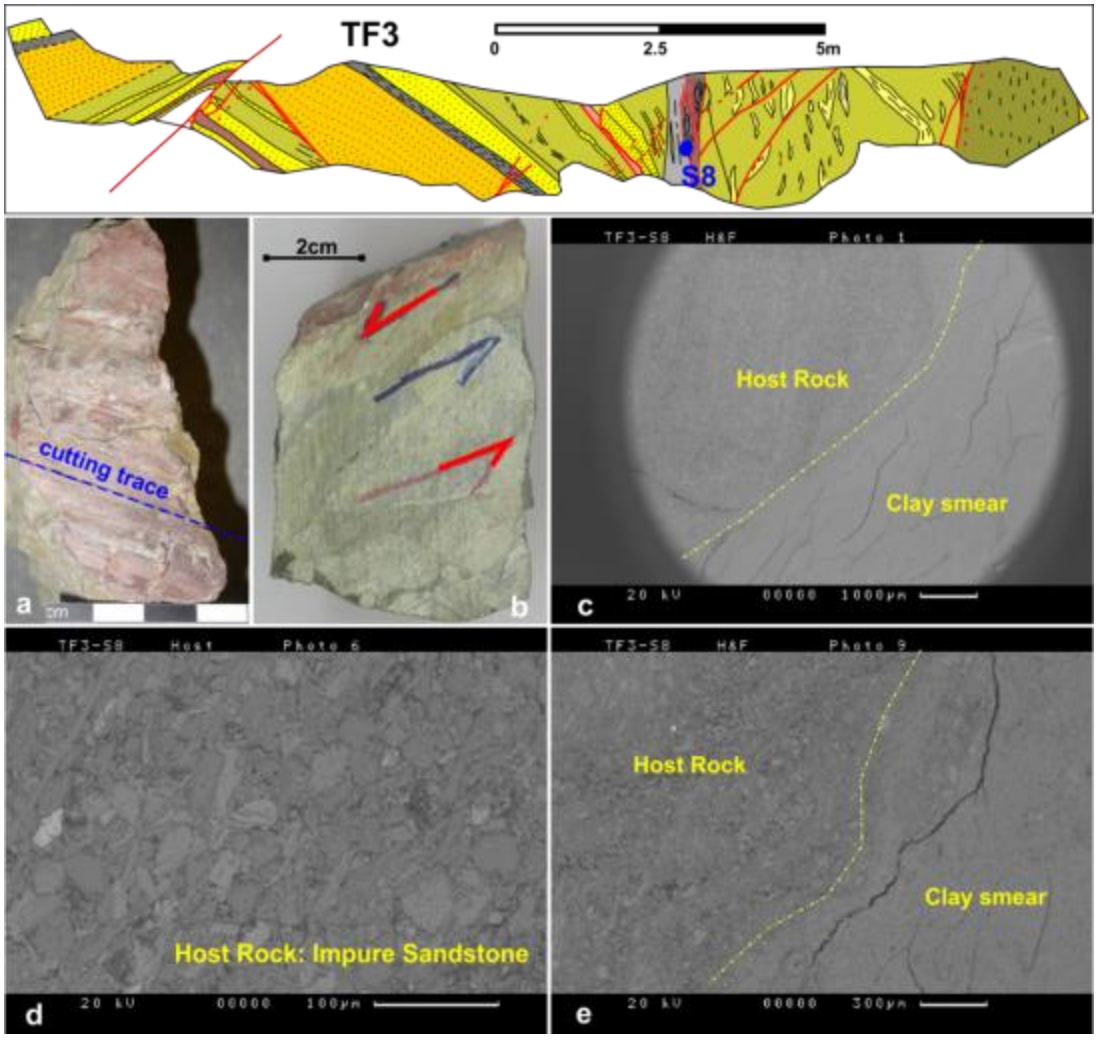

Figure 6.9 The sample photos (a, b) and BSE micrographs (c-e) showing the clay smear-dominated fault rocks in the sample TF3-S8. Note the high clay contents (55-75%) and low porosity (<10%) of the clay smear fault rocks (e).

The host lithologies of this sample are mudstone with 70-75% clay contents (the brown top surface of Figure 6.9a; top brown portion of Figure 6.9b) and

impure sandstone with 55-65% (the residual greenish-grey portion in Figure 6.9a, b). The deformation features present in this sample are clay smear fault rocks with a very low porosity <10% (Figure 6.9c, e).

6.3.2. Phyllosilicate-Framework Fault Rocks (PFFRs)

The phyllosilicate-framework fault rocks (PFFRs) are fault rocks with 15-40% clay contents (Knipe, 1997). The PFFRs typically occur within fault zones developed from impure sandstones (~15-40% phyllosilicates) or from clean sandstones interlaminated with phyllosilicate-rich layers, by generating anastomosing networks of micro-smears around the framework silicates. These micro-smears within the anastomosing networks can present similar properties to clay/phyllosilicate smears. Therefore, the PFFRs commonly have reduced permeabilities and increased capillary threshold pressures relative to their host rocks (Fisher and Knipe, 1998; Ottesen Ellevset et al., 1998). The main processes responsible for decreasing porosity and permeability and increasing threshold pressure within the PFFRs can conclude:

(i) the mixing of phyllosilicates and framework grains during deformation, which results in the homogenisation and the replacement of macro-porosity by micro-porosity;
(ii) the enhanced post-deformation grain-contact quartz dissolution.

In the Lenghu5 structure, PFFRs were observed in the micro-structural analysis of three rock samples: TF1-4-S10, TF1-5-S7 and TF4-S5 (Figure 6.9 to Figure 6.11). In these samples, the fault rock domains are dominated by mixing of fine-grained phyllosilicates and framework grains. They are mainly present within the intervals of sandstones laminated with clay-rich layers or the impure sandstone intervals.

(1). Sample TF1-4-S10

Sample TF1-4-S10 is located within the fault zone of TF1-4, a central high strain fault zone of the main reverse fault outcrop TF1 in the southern end of the Lenghu5 structure (Figure 6.2).

Fault TF1-4 is a steeply dipping fault zone with sheared stratigraphy comprising foliated fault rocks primarily of mudstones and some sandstones (Figure 6.10). The mudstones are vertically distributed as they are smeared into fault zone from the hanging wall; while the sandstones are faulted and thinned by fault offsets forming boudins in the attenuated layers. The fault throw of TF1-4 is not measurable as it exceeds the outcrop size (hundreds of meters based on the section analysis in Chapter 4).

This sample is collected from a faulted fine-grained impure sandstone with 7-13% clay contents (Figure 6.10). A series of PFFRs (20-35% clay contents) are formed in the shear zones or deformation bands. The host grain size experiences a small reduction in the fault rocks. The BSE micrographs demonstrate the relatively high content of fine-grained phyllosilicates, pressure solution and low porosity in the fault rocks (20-35% clay contents and 5-10% porosity) when compared to the surrounding host rocks (7-13% clay contents and 15-25% porosity).

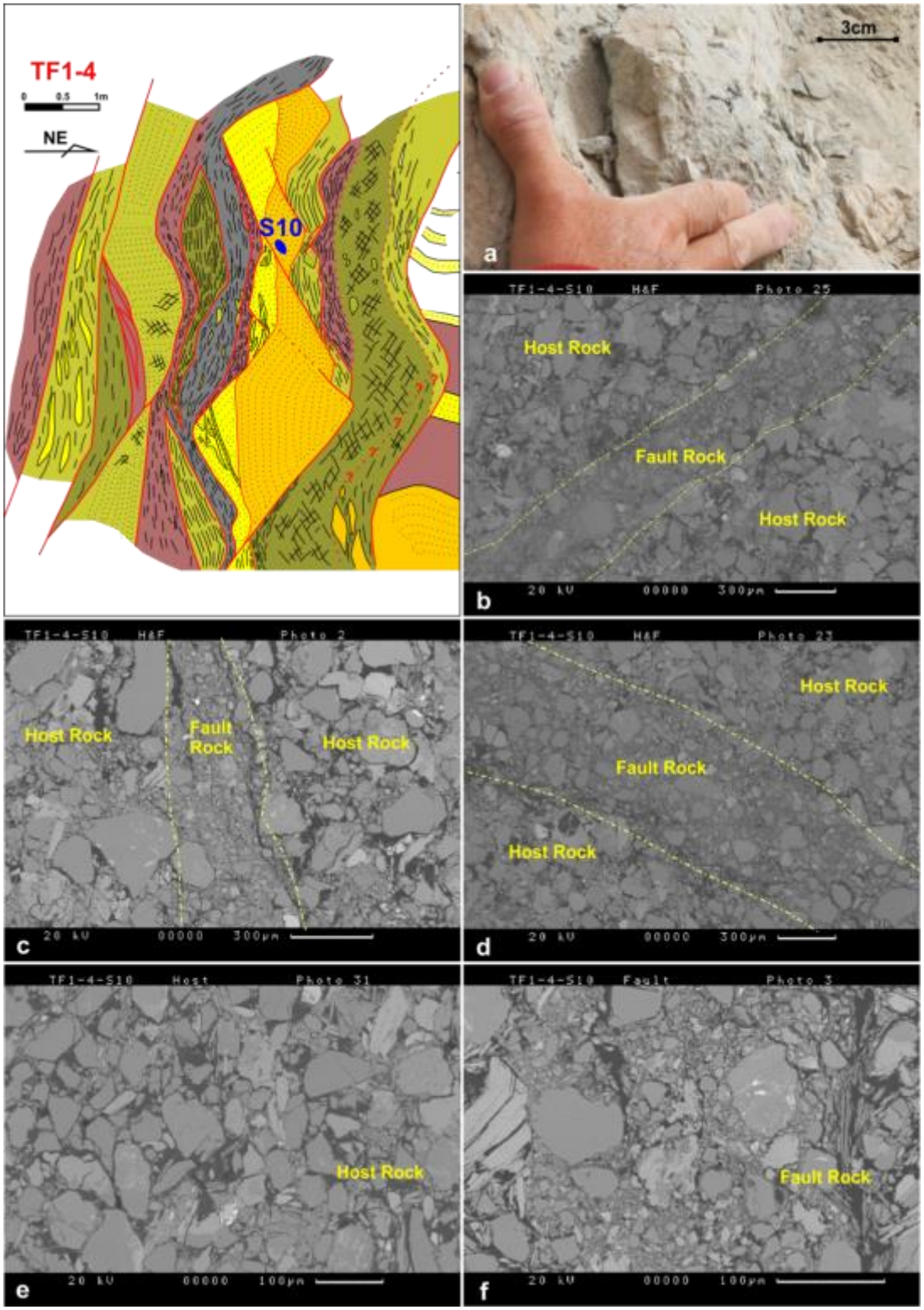

Figure 6.10 The sample photo (a) and BSE micrographs (b-f) showing the PFFRs developed in impure sandstones in the sample TF1-4-S10. The micrographs (b), (c) and (d) show domains covering both host rocks and fault rocks. The fault rocks (f) have relatively higher content of fine-grained phyllosilicates (20-35%) and lower porosity (5-10%) when compared to the surrounding host rocks with 7-13% clay contents and 15-25% porosity (e).

(2). Sample TF1-5-S7

Sample TF1-5-S7 is located in the fault zone of TF1-5, a central high-strain fault zone within the outcrop of TF1 in the southern end of the Lenghu5 structure (Figure 6.2). Similar to the above TF1-4, TF1-5 shows a steeply dipping fault zone composed dominantly of mudstones and some sandstones. The fault throw is not measurable as it exceeds the outcrop size. This sample is collected within a sandstone unit (Figure 6.11).

The dominating host rock lithology of this sample is a fine-grained impure sandstone (8-15% clay contents). A series of deformation bands are observed in the hand specimen (Figure 6.11a). The deformation features in BSE micrographs are PFFRs (20-35% clay contents) that have a small grain size reduction compared to the host rocks (Figure 6.11b-d). The BSE micrographs demonstrate the relatively high content of fine-grained phyllosilicates, pressure solution and low porosity in the fault rocks (20-35% clay contents and <5% porosity) when compared to the surrounding host rocks (8-15% clay contents and 15-20% porosity) (Figure 6.11b, c). Some fault rock domains containing post-deformation calcite precipitation is also observed (crushed calcite cement, the light phase in BSE photograph in Figure 6.11d).

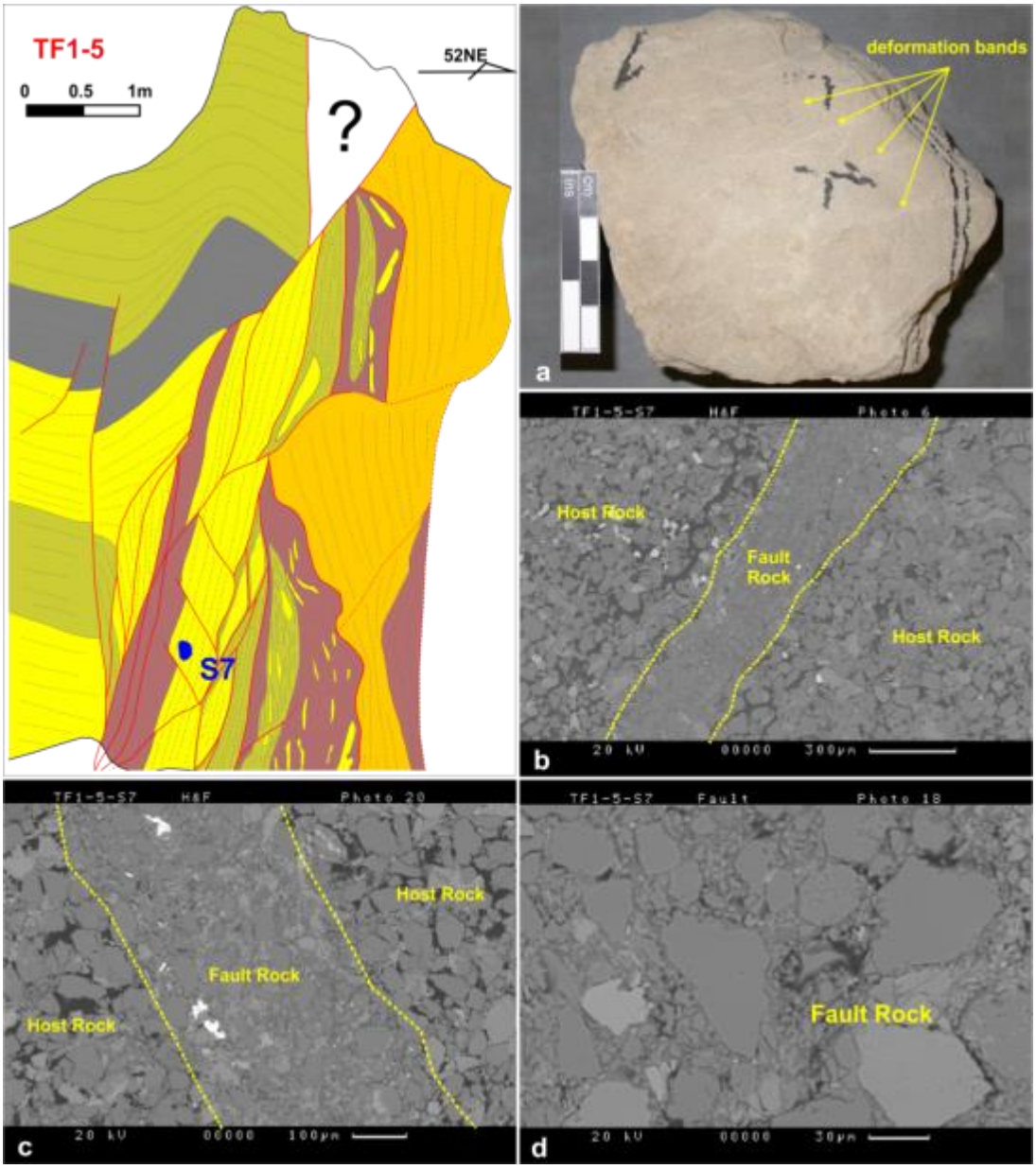

Figure 6.11 The sample photo (a) and BSE micrographs (b-d) showing the PFFRs developed in impure sandstones in the sample TF1-5-S7. The micrographs (b) and (d) show deformation features of both host rocks and fault rocks. The fault rocks (d) have relatively higher content of fine-grained phyllosilicates (20-35%) and low porosity (<5%) than the surrounding host rocks with 8-15% clay contents and 15-20% porosity (b, c).

(3). Sample TF4-S5

Sample TF4-S5 is located within the fault zone of TF4, a main reverse fault outcrop in the southern anticline core in the Lenghu5 structure (Figure 6.2). The outcrop TF4 comprises an anticline with a flat crest against the reverse fault in the hanging wall and a steeply dipping central fault zone. The central fault zone consists of sheared stratigraphy comprising foliated fault rocks of

primarily mudstones and some sandstones. The fault throw for the central fault zone is not measurable as there are no matching stratigraphic units in the two walls (Figure 6.12).

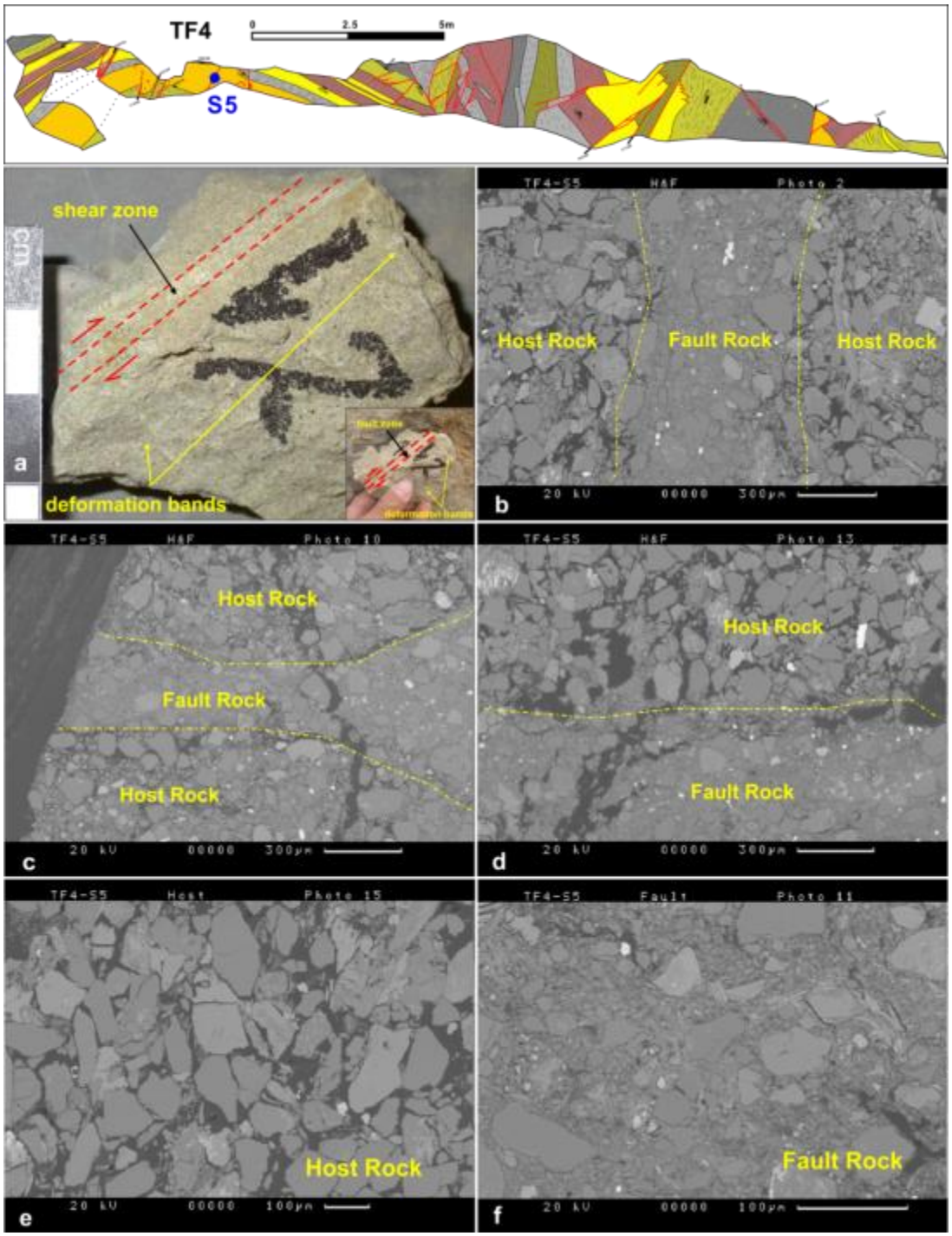

Figure 6.12 The sample photo (a) and BSE micrographs (b-f) showing the PFFRs developed in impure sandstones in the sample TF4-S5. The micrographs (b), (c) and (d) show domains covering both host rocks and fault rocks. The fault rocks (f) have relatively higher content of fine-grained phyllosilicates (25-40%) and lower porosity (<5%) than the surrounding host rocks with 8-15% clay contents and 15-25% porosity (e).

This sample is collected in a sandstone-dominated unit in the hanging wall anticline. The lithology is dominated by a fine-grained impure sandstone with 8-15% clay contents. Similar to the sample TF1-5-S7 in Figure 6.11, deformation bands are observed in the impure sandstones (Figure 6.12a). A series of PFFRs (25-40% clay contents) are formed in the shear zones or deformation bands (Figure 6.12b-d). The host grain size experiences a small reduction in the PFFRs. The high magnification BSE micrographs enable the comparison between the host rocks and fault rocks in terms of the clay content and porosity (Figure 6.12e, f). These BSE micrographs demonstrate the relatively high content of fine-grained phyllosilicates, pressure solution and low porosity in the fault rocks (25-40% clay contents and <5% porosity) when compared to the surrounding host rocks (8-15% clay contents and 15-25% porosity).

As a summary, the key observations/conclusions from the SEM microstructural analyses (Figure 6.9 to Figure 6.11) on these PFFRs samples are:

(i). the phyllosilicate-framework fault rocks are developed from sandstones containing phyllosilicate-rich laminae at the time of deformation;

(ii). the fault rocks have relatively high content of fine-grained phyllosilicates, pressure solution and low porosity when compared to the surrounding host rocks;

(iii). the main processes that are responsible for the observed microstructural modifications and porosity collapse are: (a) the mixing of the fine-grained phyllosilicates and framework grains during deformation; (b) the enhanced post-deformation grain-contact quartz dissolution; and (c) the slight cataclasis.

6.3.3. Cataclasites

Fault rocks where the processes of grain fracturing and frictional sliding dominate and induce a reduction in both permeability and porosity are grouped together as cataclastic fault rocks (Knipe, 1989; Knipe and Lloyd, 1994; Knipe et al., 1997; Fisher and Knipe, 1998; Fossen et al., 2007; Rotevatn et al., 2008). Cataclasis is the main process responsible for porosity collapse in clean porous (>15%) sandstones where the phyllosilicate content is low (<15%). The petrophysical properties of cataclastic faults developed from clean sandstones are usually reduced in comparison to the host sandstones as a result of three processes, which are:

(i). The reduction in grain-size and grain-sorting during deformation produces the collapse of macro-porosity and allows the grain fragments to be compacted more efficiently than the host sandstone (Antonellini and Aydin, 1994, 1995).

(ii). The cataclastic faults can experience enhanced quartz cementation following deformation. It should be emphasized that the cement does not usually precipitate from exotic fault-related fluids but instead is generated by local reactions (such as quartz dissolution at clay-quartz contacts) and preferentially precipitates within the fault rocks due to the presence of new quartz fracture surfaces which are usually unpolluted compared to the grain surfaces within the host sandstone (Fisher and Knipe, 1998).

(iii). Following the deformation, some fault rocks experience grain-to-grain dissolution. The fault rocks susceptible to enhanced grain-to-grain dissolution are those that formed from sandstones containing small quantities of phyllosilicates at the time of deformation. The emplacement of the phyllosilicates at the grain-to-grain contacts enhances the rate of quartz dissolution (e.g., Bjorkum, 1996; Oelkers et al., 1996).

During the process of cataclasis, the porosity and permeability are reduced effectively because cataclasis results in the collapse of porosity; reduction of grain size; and grain-sorting becomes poorer by fracturing (Fisher and Knipe, 1998). The micro-structural analysis undertaken by Fisher and Knipe (1998) suggests that concentrations of clay/phyllosilicate materials inhibit the prob-

ability of occurrence of cataclasis. The cleaner the sandstones are, the more dominant the cataclasis is as a deformation process within fault zones, the reason being that within clay/phyllosilicate-rich sandstones deformation by grain sliding and rotation is easier than by fracturing.

In the Lenghu5 structure, the cataclastic fault rocks were observed in two samples: TF2-S7 (Figure 6.13) and TF3-S12 (Figure 6.14).

(1). Sample TF2-S7

Sample TF2-S7 is located within the fault zone of TF2, an outcrop of the main reverse fault in the southern anticline core in the Lenghu5 structure (Figure 6.2). Similar to the previous TF3 and TF4, the outcrop TF2 comprises a hanging wall anticline with a flat crest and a steeply dipping central fault zone (Figure 6.13). The central fault zone presents a highly sheared stratigraphy comprising foliated fault rocks of primarily mudstones and some sandstones. The fault throw for the central fault zone is not measurable as there are no matching stratigraphic units in the two walls (Figure 6.13).

This sample is collected in a shale-contained sand boudin within the central fault zone, with main lithologies comprising mixed sandstone and mudstone. The undeformed host rocks have 7-12% clay contents in sandstone (in grey) and 75-85% clay contents in mudstone (in brown) (Figure 6.13a, b). The deformation features present in this sample include cataclasis in the sandstone section (5-10% porosity, Figure 6.13c, d) and clay smears in the mudstone section (<5% porosity, Figure 6.13f). The cataclastic fault rocks experienced moderate grain size reduction and the reduction in poroperm properties occurred as a result of deformation-induced grain fracturing and porosity collapse. The lack of significant post-deformation quartz cementation may indicate that the cataclasites formed prior to the main phase of quartz cementation, allowing the contamination of fracture surfaces and restricting quartz cementation. This cataclastic fault rock also experienced post-deformation minor barite cementation (Figure 6.13e).

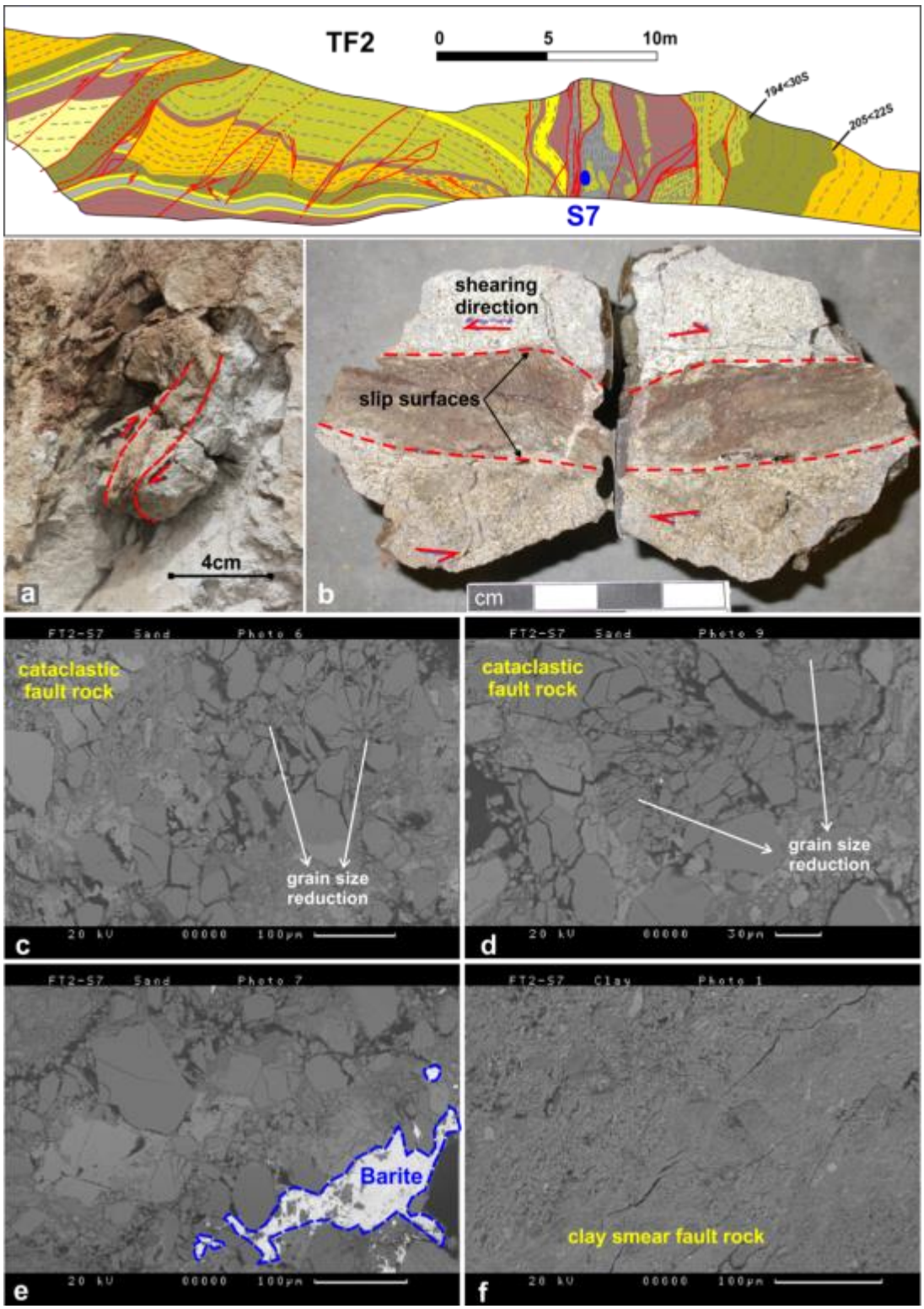

Figure 6.13 The sample photos (a, b) and BSE micrographs (c-f) showing both cataclastic and clay smear fault rocks present in the sample TF2-S7. The micrographs (c) and (d) indicate moderate grain size reduction within the cataclastic fault rocks. Minor barite cementation (e) and clay smear fault rocks (f) are also observed within several domains.

(2). Sample TF3-S12

Sample TF3-S12 is located within the fault zone of TF3, a main reverse fault outcrop in the southern anticline core in the Lenghu5 structure (Figure 6.2). The outcrop TF3 comprises a hanging wall anticline with a flat crest and a steeply dipping fault zone (Figure 6.14). The central fault zone presents a sheared stratigraphy comprising foliated fault rocks of primarily mudstones and some sandstones. The fault throw of the central fault zone is not measurable as there are no matching stratigraphic units in the two walls (Figure 6.14).

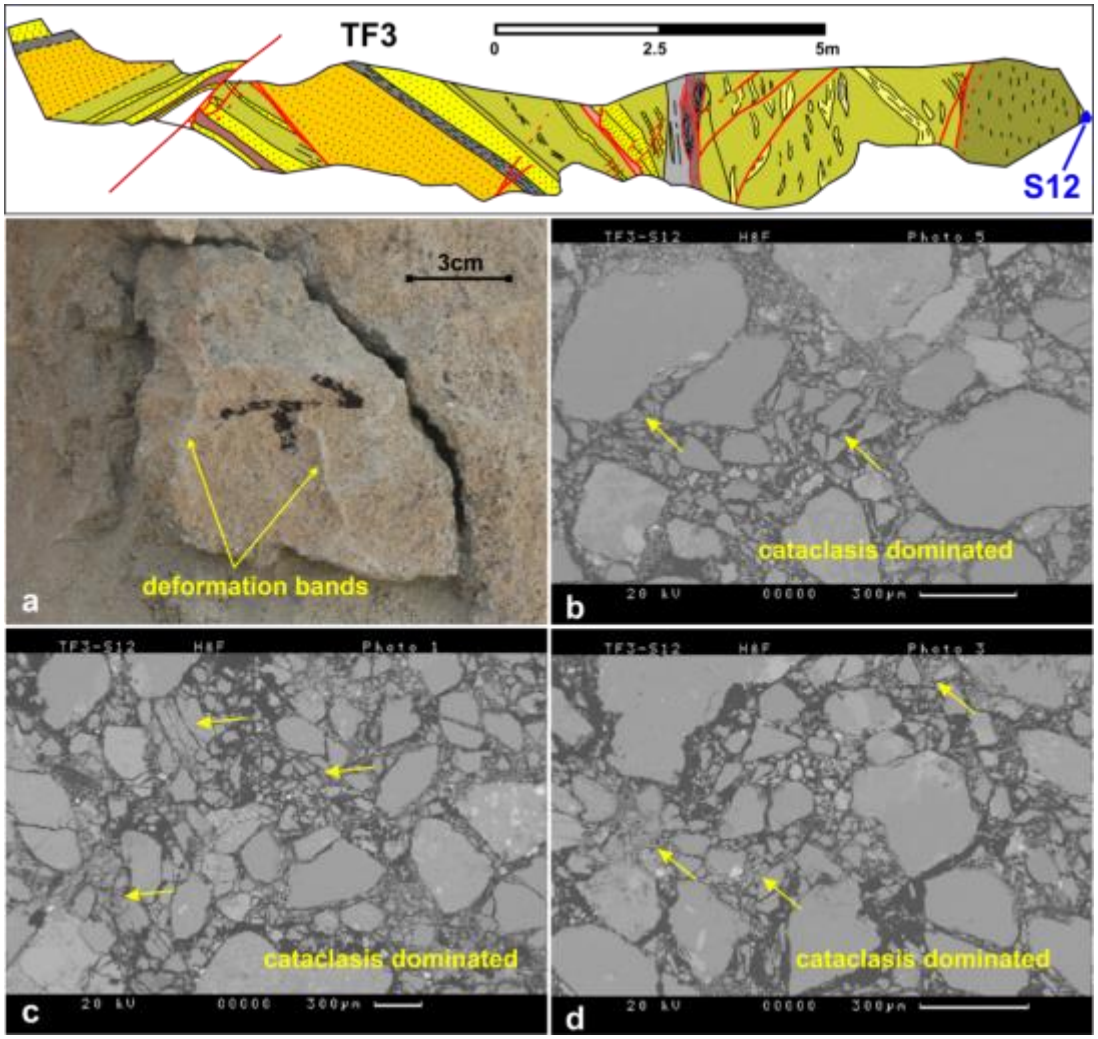

Figure 6.14 The sample photo (a) and BSE micrographs (b-d) showing the general microstructure of the cataclastic fault rocks present in the sample TF3-S12. Deformation bands (a) are observed in the specimen. The cataclasites experienced low to moderate grain size reduction (arrows in b-d).

This sample is collected in the right end of the outcrop TF3. The sample has a sandstone-dominated lithology (5-10% clay contents) and deformation

bands are observed in the hand specimen (Figure 6.14a). Based on the BSE micrographs, cataclastic fault rocks are formed within the shear zones or deformation bands. The cataclastic fault rocks have experienced a moderate grain size reduction, presenting 35-45% porosity (Figure 6.14b).

As a summary, the key observation/conclusions from the SEM microstructural studies (Figure 6.13 and Figure 6.14) on these two samples are:

(i). The cataclasites developed in clean sandstones (<15% detrital clay) and formed by the deformation-induced grain-fracturing and porosity collapse.

(ii). The fault rocks experienced small to moderate grain size reduction. The lack of significant post-deformation quartz cementation may indicate that the cataclasites formed prior to the main phase of quartz cementation, allowing contamination of the fracture surfaces.

(iii). It should be stressed that these sampled cataclasite faults are low displacement features. The higher levels of cataclasis, corresponding to lower permeabilities and higher threshold pressures, can be expected on larger throw (seismic scale) faults.

6.3.4. Cemented Fractures

The cemented faults and fractures are defined here as those containing authigenic cements which precipitated from fluids as they flowed through dilatant fault-fracture networks. The fault/fracture cements commonly encountered in siliciclastic reservoirs include kaolin, carbonates, sulphates and sulphides. The cemented fractures present in the Lenghu5 structure are mainly calcite or halite-cemented fractures (Figure 6.15 to Figure 6.17). The cemented deformation features can create fault rocks with very low porosity/permeability, and high capillary threshold pressure, but it is unlikely that they will be laterally continuous at a large scale. Therefore, the cemented fractures are unlikely to influence large-scale fluid flow now.

(1). Sample TF1-1-S1

Sample TF1-1-S1 is located within the fault zone of TF1-1, a low strain splay fault of the main reverse fault outcrop TF1 in the southern end of the Lenghu5 structure (Figure 6.2). TF1-1 is a small pop-up structure developed in the footwall away from the main reverse fault. The stratigraphy is mudstone-dominated, but presenting decreasing clay contents downward (Figure 6.15).

TF1-1 is composed of a series of sub-parallel NE-directing reverse faults and SW back-thrusting faults. Both in the reverse faults and back-thrusts, the top clay-rich layers show more folding than the bottom sandy layers. Fault lenses are generated along the reverse faults and back-thrusts, particularly when the faults cut the top clay-rich layers.

This sample is collected in the upper portion of the TF1-1, with a lithology of mudstone with 70-85% clay contents. It comprises several shear zones dominated by clay smears (Figure 6.15a, b). Two polished blocks were cut from this sample for the micro-structural analysis (Figure 6.15b-d). Figure 6.15e and Figure 6.15h show the low magnification SEM micrographs of the two polished blocks, which present clay smear fault rocks with a series of calcite/halite-cemented fractures. The cementation of calcite/halite can effectively decreases the porosity of the fractures.

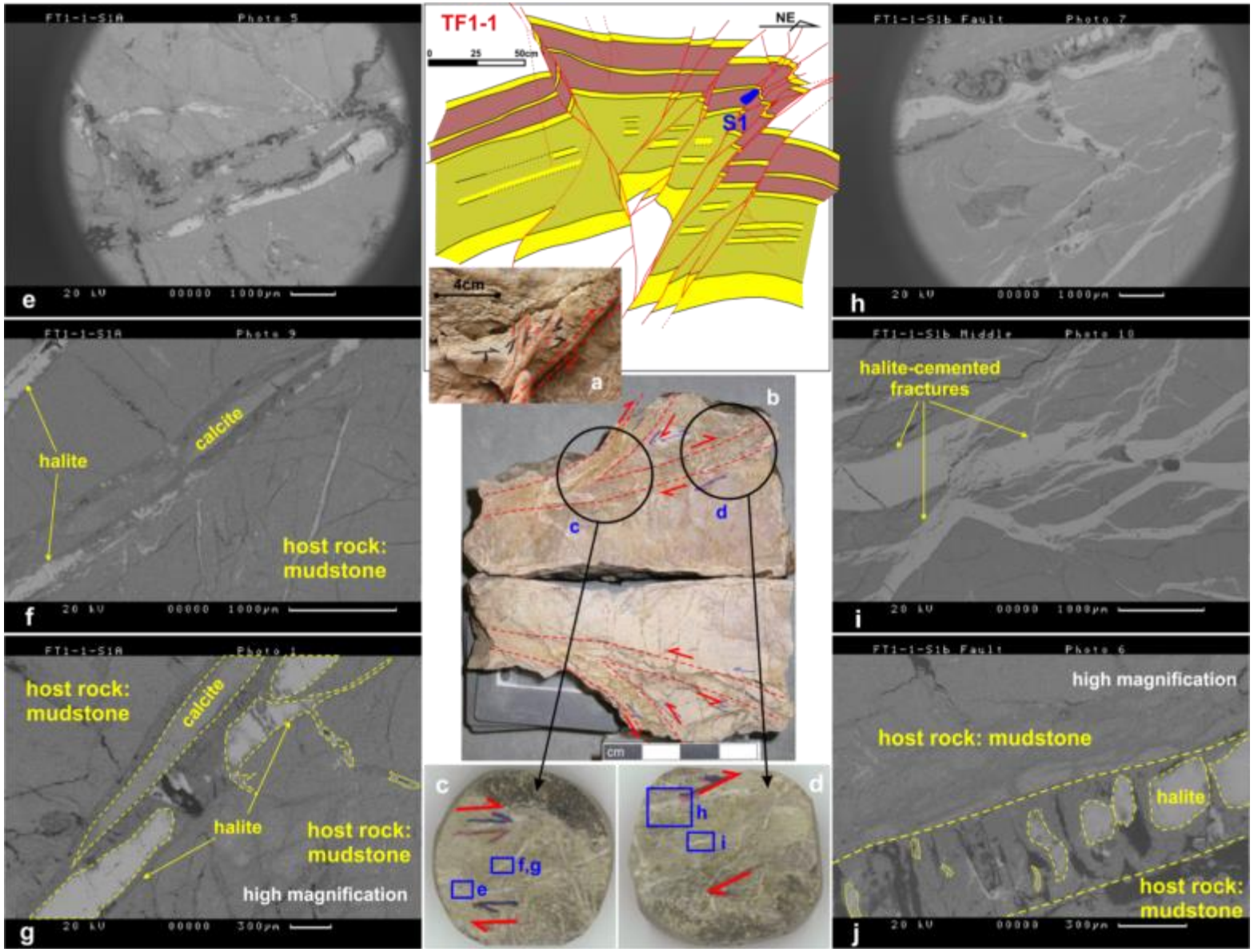

Figure 6.15 The sample photos (a-d) and BSE micrographs (e-j) showing the calcite/halite-cemented micro-fractures in the sample TF1-1-S1. The calcite/halite-cemented fractures significantly decrease the permeability of the fractures (f, g, i, j).

(2). Sample TF1-1-S2

As with the above sample TF1-1-1, sample TF1-1-S2 is also located within the fault zone of the outcrop TF1-1 (Figure 6.2). This sample is collected from the bottom section of TF1-1, with host lithology of mudstone (65-80% clay contents). The sample comprises a ~1cm wide shear zone (Figure 6.16a, b). The SEM micrograph in Figure 6.16d shows clay smears with a series of calcite/halite-cemented micro-fractures present in this sample (intermediate magnification in Figure 6.16e and high magnification in Figure 6.16f). Similar to the sample TF1-1-S1 (Figure 6.15), the porosity and permeability of the micro-fractures are effectively reduced by the cementation of calcite/halite (Figure 6.16e, f).

(3). Sample TF1-5-S5

Sample TF1-5-S5, fault gouge at the hanging wall edge, is located within TF1-5, a central fault zone of the main reverse fault outcrop TF1 in the southern end of the Lenghu5 structure (Figure 6.2). This sample is collected in the interface between the slightly deformed hanging wall and the high strain fault zone.

As a result of faulting and mixing of the sandstones and mudstones, this sample comprise three units (Figure 6.17a): mudstone (e.g., Unit1 and 3) and fault breccia (e.g., Unit 2). The slickensides in the specimen indicate the existence of an oblique fault displacement. The mudstone has 70-80% clay contents; while the fault breccia has only 45-60% clay contents. The micro-fractures in the interfaces are cemented by halite (Figure 6.17b, c). The high magnification micrographs (Figure 6.17d, f) show the composition of Unit 1 and 3 in high magnification; while the petrography in low magnification shows that the fault breccia is composed of fault clasts mixed with clay matrix (Figure 6.17e).

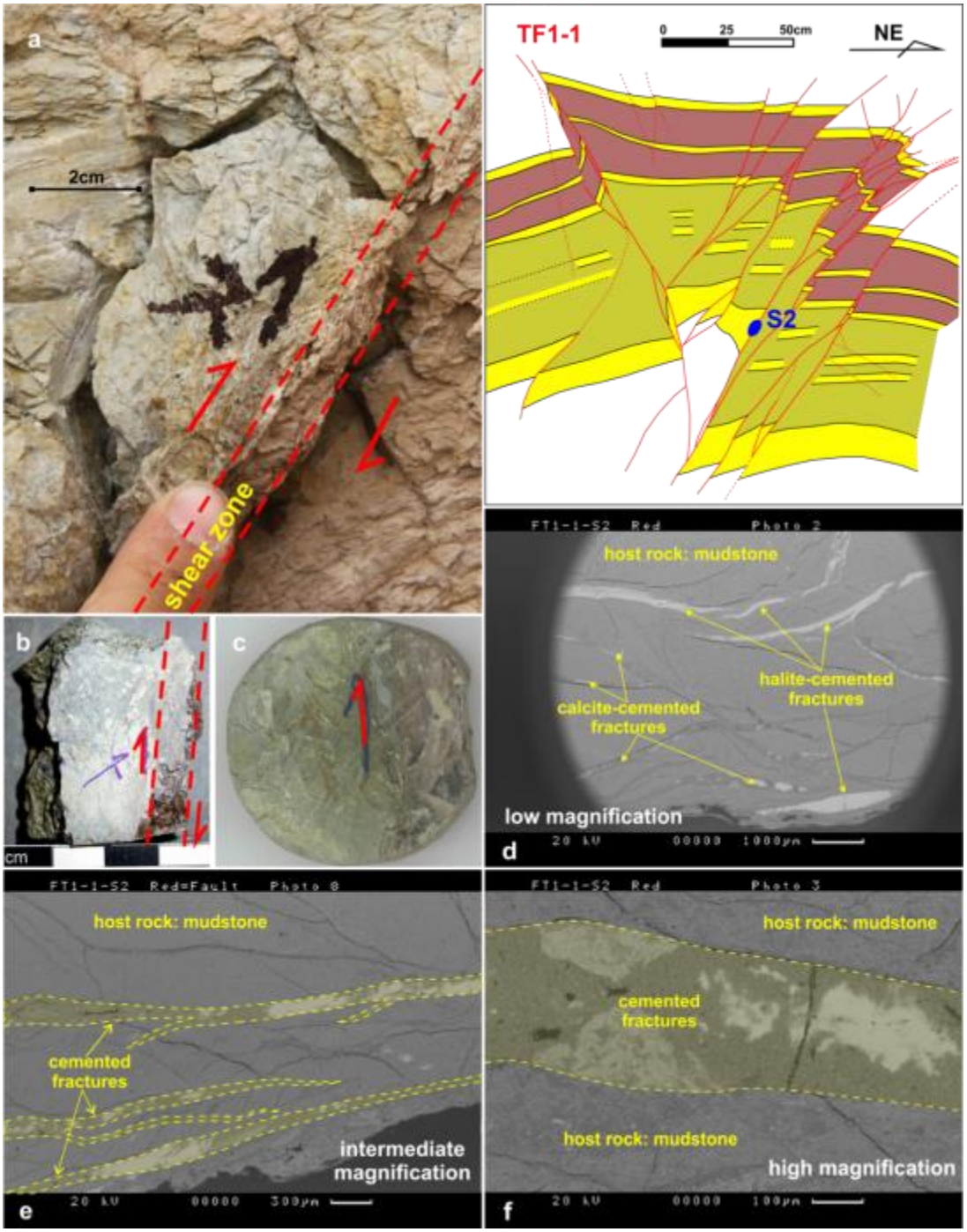

Figure 6.16 The sample photo (a-c) and BSE micrographs (d-f) showing the general microstructure of the calcite/halite-cemented micro-fractures in the sample TF1-1-S2. The permeability of these micro-fractures is significantly decreased by the calcite/halite cementation.

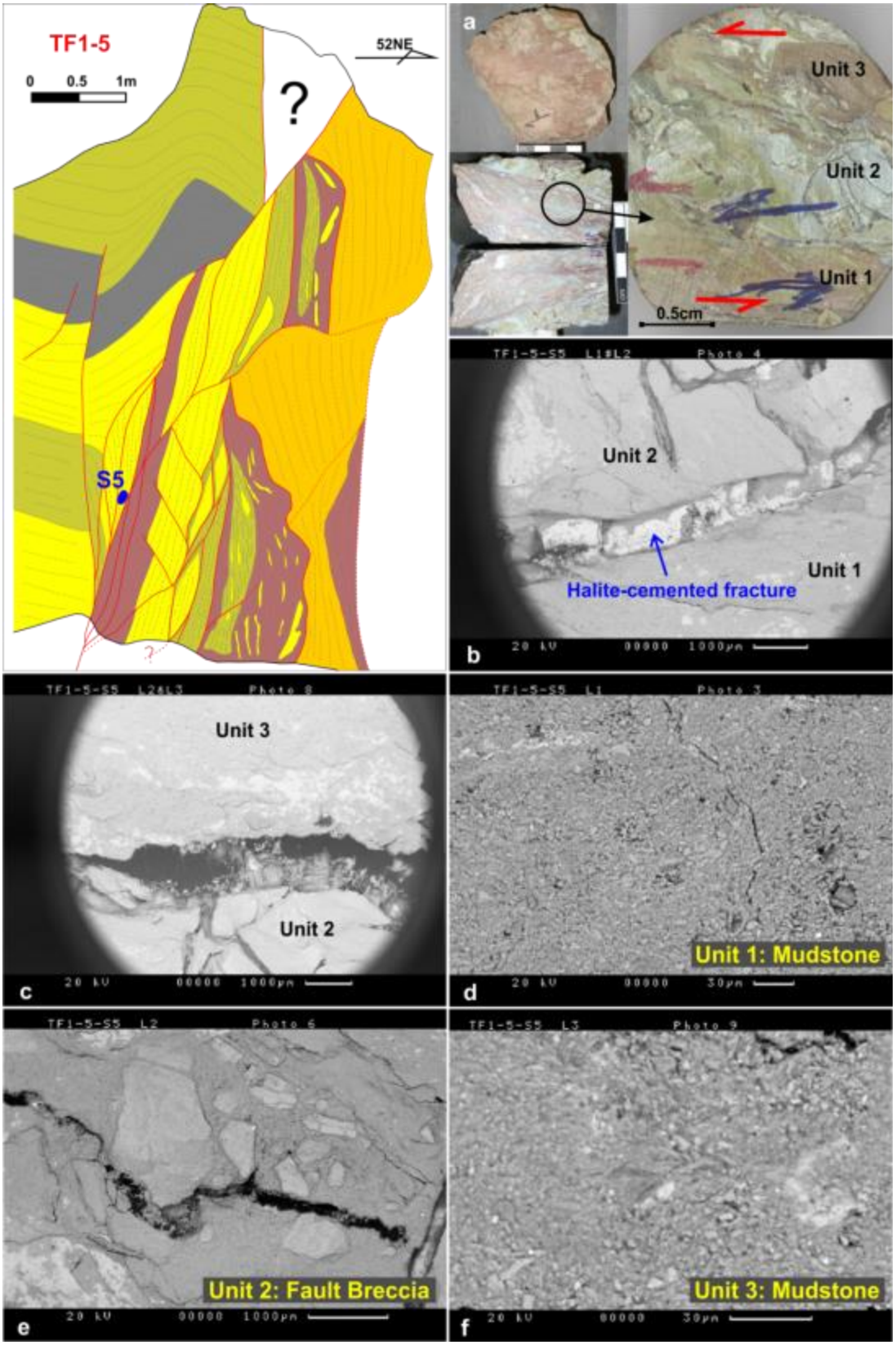

Figure 6.17 The sample photo (a) and BSE micrographs (b-f) showing the general microstructure of the halite-cemented micro-fractures in the sample TF1-5-S5, particularly at the interfaces between the sub-units 1, 2 and 3 (b, c).

6.4. Discussion and Conclusions

6.4.1. Fault Rock Types and their Relationship to Phyllosilicate Contents of the Lenghu5 Central Fault Zone

The micro-structural analysis presented in this chapter suggests the dominating deformation mechanisms are clay smears and the generation of PFFRs in the Lenghu5 structure, although some other mechanisms such as cataclasis and cementation are also observed in the SEM micrographs of the fault rock samples.

Based on the analysed rock samples, a chart of 'Fault Rock Type vs. Phyllosilicate Content' is generated to describe the relationship between the fault rock types and their clay/phyllosilicate contents (Figure 6.18). Statistically, the cataclastic fault rocks have clay contents of <15%; the PFFRs have clay contents of 15-40%; while the clay smear fault rocks have clay contents of >40%. This statistical result is in agreement with previous studies (e.g., Knipe et al., 1997; Fisher and Knipe, 1998; Ottesen Ellevset et al., 1998). However, the clay contents of fault rocks cannot accurately reflect the clay contents of their host rocks, because passing a different lithology during faulting deformation may increase or decrease the clay contents of the fault rocks. For example, when a mudstone unit passes a sandstone unit, the clay contents of generated fault rocks are likely to be lower than the mudstone and higher than the sandstone, and vice versa. Therefore, it is not possible to directly predict the generated fault rock types just based on the clay contents of host rocks.

However, it is assumed that the clay contents of fault rocks are similar to the clay contents of their host rocks if there are only low fault throws that are less than the thickness of the host unit. This is because in this scenario the host rock unit is self-juxtaposed and the clay contents are only determined by the host rocks. Therefore, when the fault throw is less than the host unit thickness, a direct prediction of fault rock types is possible based on the clay contents of host rocks. For example, host rocks with <15% clay content primarily form cataclastic fault rocks (e.g., clean sandstones); host rocks with 15%-40% clay content tend to form phyllosilicate-framework fault rocks (PFFRs) (e.g., impure sandstones); and host rocks with >40% clay content

incline to form clay smear-dominated fault rocks (e.g., shale or mudstones). In all other cases where the fault throws are larger than the host rock beds thickness, the fault rock clay contents have to be predicted from both the host rock lithologies and the fault throws involved in faulting deformation, e.g., the Shale Gouge Ratio (SGR) algorithm considers both the fault throw and the shale/clay percentage of each individual unit (Yielding et al., 1997).

As Knipe (1997) pointed out, the different types of deformation mechanisms can either perform individually during deformation or interactively interplay with each other. For example, in the Lenghu5 SEM microstructural analysis, sample TF1-1-S2 shows a combination of deformation mechanisms of both clay smears and calcite-cemented fractures; sample TF2-S7 shows a combination of deformation mechanisms of both clay smears and generation of PFFRs. A case study from Brent Province in northern North Sea also suggests that these deformation mechanisms that lead to fault rock porosity and permeabilty reduction can interplay with each other interactively as a function of the clay/phyllosilicate content and the burial depth (Figure 6.19) (Jolley et al., 2007). The burial depth is positively related to the lithification state of sediments, effective stress and temperature at the time of faulting deformation (Fisher and Knipe, 2001; Jolley et al., 2007). As the dominating deformation mechanisms in Lenghu5 are clay smearing, generation of PFFRs and minor cataclasis, i.e., the green ellipse in Figure 6.19 represents the primary deformation features of the fault rocks that are generated in the Lenghu5 structure. The ellipse suggests that the Lenghu5 structure has a stratigraphy containing 40-80% clay/phyllosilicate and has experienced faulting deformation at a shallow burial depth of <3km (low to moderate lithification), which shows good agreement with our field observations and the reported burial history of the Qaidam basin (Ritts et al., 1999; Xia et al., 2001).

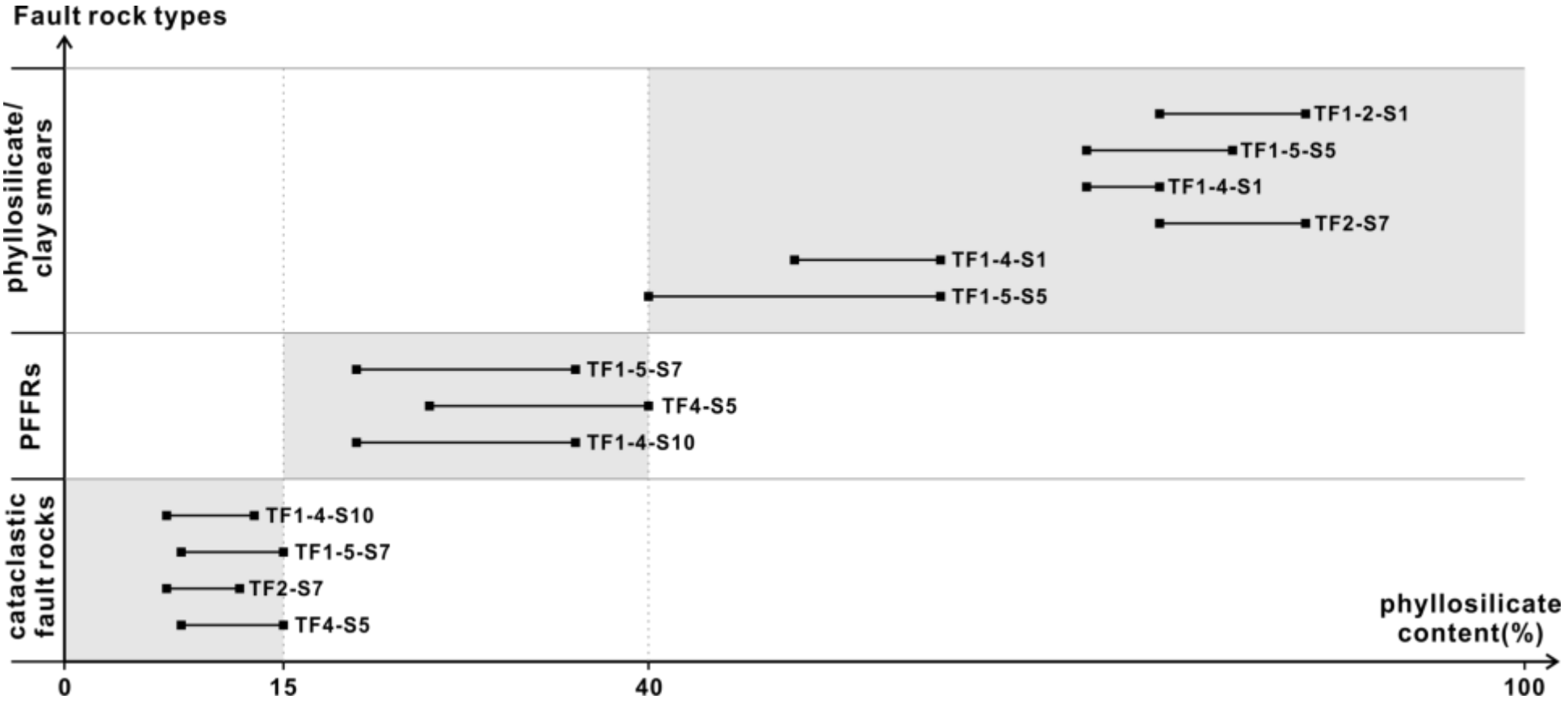

Figure 6.18 A chart delineating the relationship between the fault rock types and their phyllosilicate content studied in the Lenghu5 structure. It indicates that the fault rock types are determined by the phyllosilicate contents of the fault rocks: cataclastic fault rocks with phyllosilicate content <15%; PFFRs with 15-40% phyllosilicate; and phyllosilicate/clay smears with phyllosilicate content >40%.

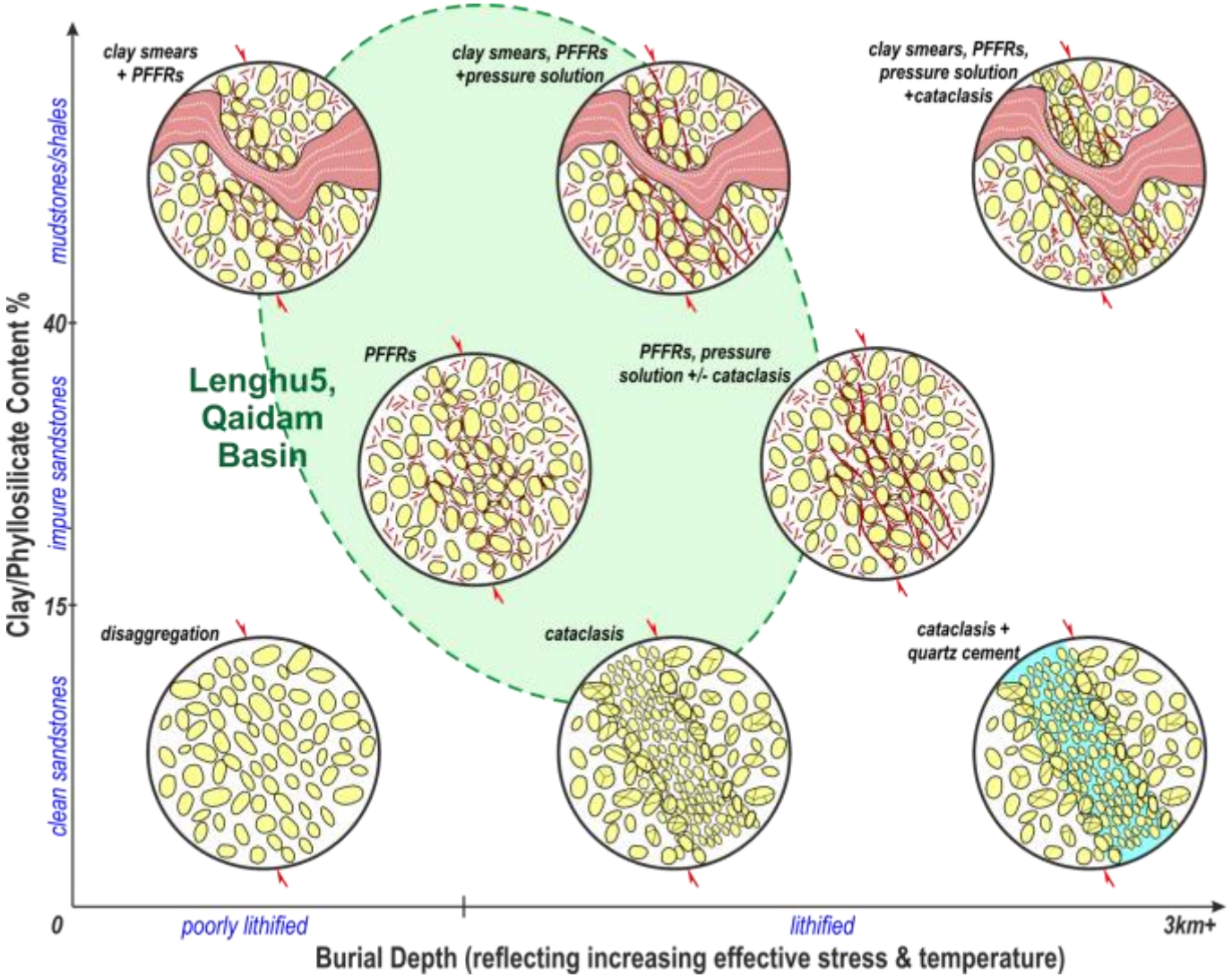

Figure 6.19 Schematic cartoons of micro-structural deformation mechanisms with various fault rocks generated in different geological settings, e.g., clay content of the host rocks and burial depth (reflecting increasing effective stress and temperature) (modified from Jolley et al., 2007).

6.4.2. Fault Sealing Processes and their Sealing Capacity

Two main types of fault seals have been widely recognized, which are juxtaposition seals and fault rock seals (Knipe, 1992a; Knott, 1993; Knipe, 1997). When the fault zone is formed, the entrained stratigraphy can form fault rocks with different physical properties, which may affect the fluid flow properties of the fault zone. This process of forming fluid flow seals has been termed fault rock seals (Knipe, 1992a), which may form fault rocks with different petrophysical properties within the fault zones, e.g., cataclastic fault rocks, clay smears, phyllosilicate-framework fault rocks (PFFRs), cemented fractures, etc.

At the observed scale (outcrop scale) in the Lenghu5 structure, the outcrops are not simple single-plane faults, but comprise fault zones within which fault rocks are formed derived from the entrained host rocks. Therefore, the fault seal processes associated with the Lenghu5 structure are primarly fault rock seals rather than simple juxtaposition seals. The analyses on the microstructures of the fault rocks formed within the fault zones are important to understand the sealing capacity of the Lenghu5 central fault zone. From the above micro-scale analysis based on SEM, two main types of fault rock seals/flow retarders are identified in the Lenghu5 fault zone, which are clay smears and PFFRs. There are also some other fault rocks observed within the Lenghu5 central fault zone, such as the cataclasitic fault rocks and cemented fractures. However, these fault rocks are not extensively developed thoughout the Lenghu5 central fault zone. This can be attributed to the deformation conditions and lithification state that do not promote extensive occurance of cataclasis or cementations, e.g., high clay contents, low to moderate lithification state and shallow burial depth (Ritts et al., 1999; Xia et al., 2001).

(1). Clay Smear Fault Rocks

The fault rocks with high clay content usually have low permeability and high sealing capacity, which may form barriers for hydrocarbon migration. It is reported that the permeability of fault rocks can be reduced up to seven orders of magnitude by incorporating high clay content units, e.g., mudstone or shale (Crawford et al., 2002; Solum et al., 2010). As the clay minerals are mechanically weak, they tend to be sheard by ductile processes when being subject to stress. Clay smears formed by the smearing of phyllosilicate-rich

laminae along the faults when mudstone/shale units pass the sandstone units during faulting (Jev et al., 1993). Previous studies focusing on physical property analysis suggest that the clay smears usually have very low permeability of <0.001mD and high capillary threshold pressure of >1500psi (Fisher and Knipe, 1998; Ottesen Ellevset et al., 1998). Thus the concentration of clay-rich fault rocks tends to determine the permeability and sealing capacity (Yielding et al., 1997; Knipe et al., 1998; Walsh et al., 1998; Fisher and Knipe, 2001; Aydin and Eyal, 2002; Solum and van der Pluijm, 2009). Given the important control of clay smears on the fault sealing property, quantitative methods are proposed to evaluate the potential of forming clay smears along the fault zones, which are the Clay Smear Potential (CSP) (Bouvier et al., 1989; Fulljames et al., 1997), the Shale Smear Factor (SSF) (Lindsay et al., 1993), the Shale Gouge Ratio (SGR) (Yielding et al., 1997) and Scale Shale Gouge Ratio (SSGR) (Ciftci et al., 2013). It is assumed that clay smears will be continuous along the fault zone until the fault throw is larger than some multiple of the shale unit thickness, e.g., three times was suggested by Knipe et al. (1997). Therefore, if the fault throw does not reach three times the shale unit thickness, a continuous impermeable clay smear has a high probability of being formed along the fault zone, which performs as a good barrier for the hydrocarbon migration across the fault zone. If the fault throw continues to increase, the potential of forming continuous clay smears along faults is likely to decrease.

(2). Phyllosilicate-Framework Fault Rocks (PFFRs)

PFFRs usually form from impure sandstones entrained into the fault zone during faulting. Commonly, impure sandstones contain a mixture of phyllosilicates (i.e., clay minerals, e.g., kaolinite, smectite, illite, chlorite, etc.) and framework silicates (also termed tectosilicates, e.g., quartz, feldspars, zeolites, etc.). In impure sandstones (15-40% clay content), the anastomosing networks of micro-smears can be generated around framework silicates, which creates phyllosilicate-framework fault rocks (PFFRs) (Knipe, 1997). These micro-smears within the anastomosing networks can present similar properties to clay/phyllosilicate smear, although on a smaller scale (micro-scale). The petrophysical properties (e.g. permeability and porosity) of the PFFRs are determined by the micro-smears generated around the framework silicates. A case study from the Sleipner Vest Field (Ottesen Ellevset et al., 1998) reported that

the permeability of PFFRs ranges from 0.3 to 0.004mD and capillary pressure of >120psi for the deformation and diagenesis conditions experienced. Another case study in the North Sea and Norwegian Continental Shelf (Fisher and Knipe, 2001) suggests permeabilities in the range of 0.3mD to 0.00003mD are possible for PFFRs. Therefore, as pointed out by Knipe (1992a), it is not necessary to have thick clay units for creating low permeable fault rocks where the sealing properties are determined by the continuity and structure of deformed clay minerals/phyllosilicates, e.g., PFFRs can be generated within impure sandstones. In order to accurately evaluate the sealing capacity of PFFRs, the microstructural analyses of the fault rocks need to be considered as the micro-smears and clay/phyllosilicate mixing determine the fault sealing properties of the fault rocks in this scenario.

Fisher and Knipe (1998) propose that it is the mixing of clay minerals and framework silicates that effectively reduces the porosity and permeability of PFFRs. Natural examples from Norwegian Continental Shelf confirm that the occurrence of PFFRs can have great effects on the sealing behaviour (Ottesen Ellevset et al., 1998). Based on the BSE micrographs of the rock samples in this study, it is suggested that the potential of PFFRs to produce barriers for fluid flow is determined by the continuity of PFFRs along the fault zone. For the PFFRs induced by micro-smears of phyllosilicates, the continuity of PFFRs along the faults is likely to decrease with increasing fault throws, because the continuity of PFFRs is determined by the micro-smears that are sensitive to increasing fault throws. In this scenario, the continuity of PFFRs is likely to be inversely proportional to the fault throws. However, in some cases where PFFRs have a more uniform distribution of phyllosilicates (with 15-40%), there may not be extensive micro-smears to develop reduced PFFRs continuity by increasing fault throws. Therefore, unlike the clay smears, there is not a simple inverse proportion relationship between the PFFRs continuity and fault throws, as the generation of PFFRs is much more complex than that of clay smears.

6.4.3. Effectiveness of using Small-Offset Faults to Evaluate the Fault Sealing Capacity of Seismic-Scale Faults

It is important to evaluate the petrophysical properties of fault rocks to improve the fluid flow prediction, particularly in petroleum reservoirs with high structural complexity (e.g., Jolley et al., 2007; Zijlstra et al., 2007). As the small-offset

faults allow geologists to identify the deformation mechanisms in fault rocks, many recent studies have evaluated the fluid flow properties of seismic-scale faults based on the fault seal analyses on the fault rocks sampled from nearby small-offset faults (e.g., Knai and Knipe, 1998; Ottesen Ellevset et al., 1998; Jolley et al., 2007; Zijlstra et al., 2007; Tueckmantel et al., 2010). Fisher and Knipe (2001) suggested that the fault rocks within sesimic-scale faults usually present porosity and permeability reduction that are similar to the nearby small-offset faults, which can be attributed to two aspects of reasons: (i) the grain-size reduction and porosity collapse may be more importantly determined by the effective stress at the time of faulting deformation rather than the degree of final strain; (ii) all the seismic-scale movements also result in deformation of fault rocks within the nearby small-offset faults.

When using small-offset faults to evaluate the fault sealing capacity of seismic scale faults, the critical issue is the impact of the small-offset faults on the over-all fluid flow properties across the fault zone of the seismic-scale faults. As the schematic sections in Figure 6.20a shows, the seismic-scale fault (***F***) has a large fault throw, which is not a throw along a single-plane fault, but actually a cumulative throw of a series of meso-scale small-offset faults (***f_1-f_5***) within the fault zone. Therefore, the fluid flow properties of the seismic-scale fault (***F***) can be estimated by considering the cumulative impacts of these small-offset faults (***f_1-f_5***) present on the overall sealing capacity across the fault zone of the seismic-scale fault (***F***). In the Lenghu5 example, the seismic-scale fault in the regional cross section (***TF1*** in Figure 6.20b) are composed of a series of meso-scale small-offset faults (***TF1-1*** to ***TF1-6*** in Figure 6.20c), which shows similar relationship between the schematic cartoon sections shown in Figure 6.20a. This research has studied the meso-scale small-offset faults to evaluate the fluid flow properties of the main reverse fault within the Lenghu5 structure. The fluid flow properties across the fault zone of the seismic-scale Lenghu5 thrust fault have been well constrained by analysing the cumulative impacts of each individual small-offset faults on the overall fault zone fluid flow properties (e.g., TF1-1, TF1-2, TF1-4/TF1-5, see details in Chapter 5).

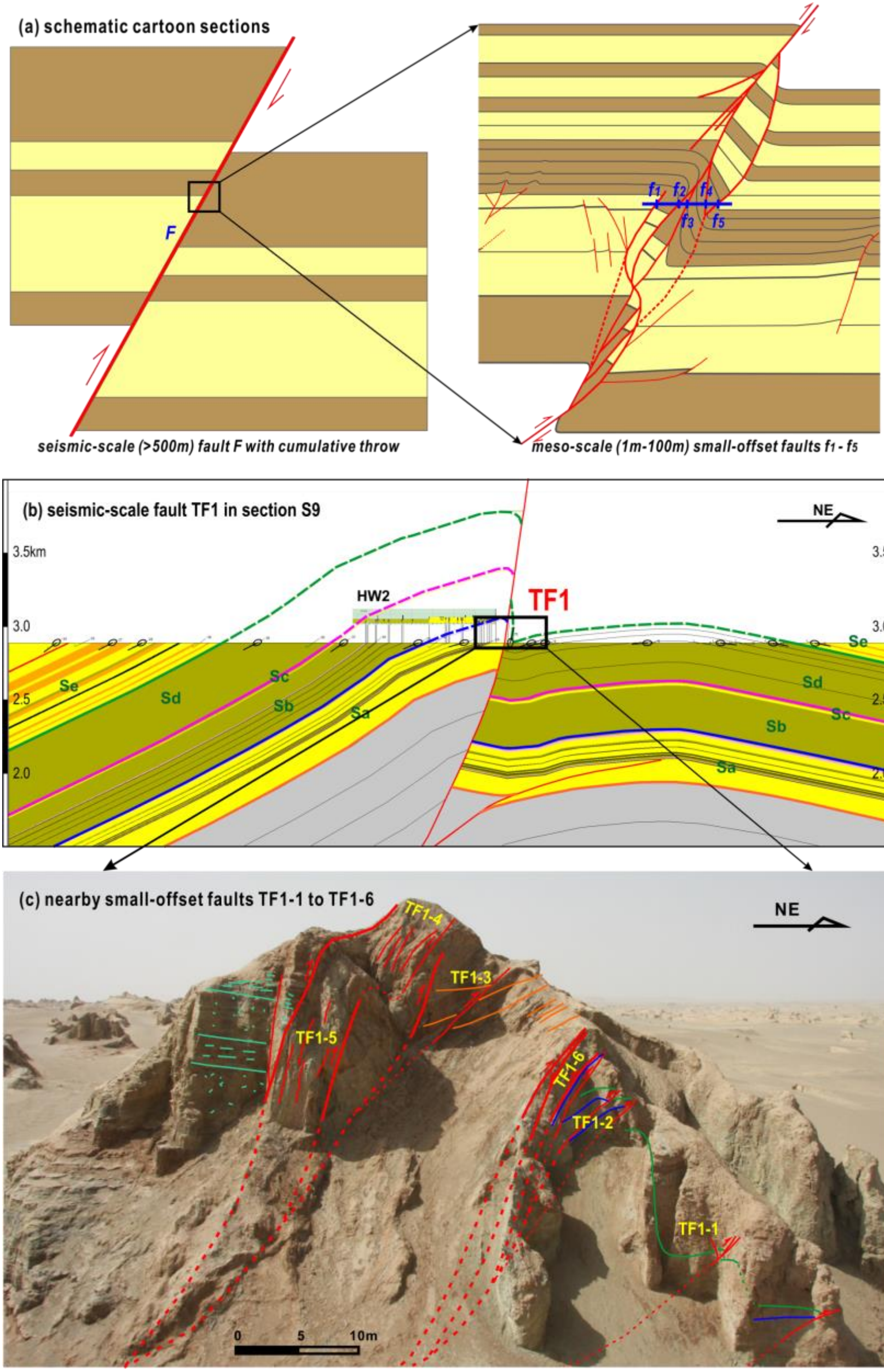

Figure 6.20 Schematic sections (a) and the Lenghu5 examples (b and c) depicting why the small-offset faults can be used to evaluate the fluid flow properties of the seismic-scale faults.

Having analyzed the multi-scale fault zone deformation features in the Lenghu5 structure (Chapter 3 - 6), the next chapter will conclude the key findings and discuss the effects of controlling parameters on the fault zone evolution and hydrocarbon sealing behaviour in the Lenghu5 structure.

Chapter 7
Discussion and Conclusions

Based on the multi-scale study in the Lenghu5 structure in Qaidam basin (Chapter 3 - Chapter 6), this chapter aims to:

(i). Summarise the findings on thrust fault architecture at each scale;

(ii). Consider how the fault evolution impacts on fault sealing behaviour.

In particular, the effects of controlling parameters on the thrust fault evolution and hydrocarbon sealing behaviour are also discussed.

7.1. Thrust Fault Architecture

7.1.1. Multi-Scale Thrust Fault Architecture

In this study, we have employed a multi-scale approach to investigate the fault related deformation involved in the Lenghu5 structural evolution at different scales (Figure 7.1).

(1). Regional-scale (1km-10km)

Based on regional seismic interpretation and the theoretical trishear modelling presented in Chapter 3, the first-order geometry of the Lenghu5 structure can be accurately modelled using trishear mechanisms (Erslev, 1991; Hardy and Ford, 1997). A 3D parameter space has been presented to evaluate the effects of different trishear parameters on the geometries of trishear models; a 3D dynamic space is built to evaluate the deformation evolution of the structures. The Lenghu5 structure is then interpreted based on the trishear parameter/dynamic space and the strain level (Figure 7.1c). The results of Chapter 3 provide a new workflow for applying trishear algorithm to complex natural structures, which are summarised below:

- The 3D parameter space is used to evaluate the effects of different trishear parameters on the resultant structural geometry. The clusters of plotted natural examples in the 3D parameter space are best de-

scribed by propagation/slip (p/s) ratio of 2-3, fault dips of 25°-45° and trishear apical angles from 30° to 100°.

- The 3D dynamic space is built to evaluate the deformation evolution of natural structures. The deformation stage $\boldsymbol{R_i}$ of a structure is not unique, but varies for different reference layers.
- As the deformation associated with the trishear algorithm is always constrained within the triangle zone in front of the fault tip, the strain ($\boldsymbol{e}$) of the folded beds is quantified by the ratio of the hanging wall uplift ($\boldsymbol{h}$) to the width of folded beds ($\boldsymbol{w}$). The strain plots can narrow the inferred range of the key variables, particularly when the surface and subsurface data provide better constraints to the variables.
- Complex trishear geometries resulting from fault-dip change and role of pre-existing fault(s) have been considered to explain complex structural styles in nature.
- A natural example from the Lenghu5 structure in Qaidam basin is selected to test the applicability of trishear modelling. The successful application of the trishear algorithm provides a useful workflow of applying trishear algorithm to the complex natural structures.

High-resolution fieldwork studies were well undertaken to understand the detailed fault architecture in the Lenghu5 structure (Chapter 4). The cross sections cutting the hanging wall anticlines contain reverse faults with upward-decreasing fault displacements that are in close agreement with the theoretical trishear models (Figure 7.1c). However, the Lenghu5 structure shows a high degree of lateral structural variability in both 2D sections and 3D models; these are not accounted for in the trishear models in Chapter 3. A simplified model is then proposed to simulate the strain distribution of the Lenghu5 structure, which also provides information for predicting second-order structures. By comparing the predicted strain distribution and the second-order structures observed in nature, an evaluation of the simplified model has been made. Moreover, the effects of critical parameters on the detailed fault development have also been considered, e.g., fault throws, stratigraphy, mechanical heterogeneity, etc.

- The first-order geometry of the Lenghu5 structure is constrained by seismic interpretation, suggesting a geological history composed of three stages: (i) the initial extensional faulting; (ii) the inversed SW-directing reverse faulting in the early compression; and (iii) the NE-directing reverse faulting in the middle and late compression.
- The stratigraphic columns are generated based on the high-resolution fieldwork studies in the Lenghu5 structure. The good stratigraphic correlation between the hanging wall and footwall enables the estimation of fault displacement along the reverse fault zone, which is ~500m in the northern anticline of the Lenghu5 structure.
- A series of high-resolution transects are constructed to understand the 3D structural geometry of the Lenghu5 structure, particularly the lateral variability of the structure. The 3D fault architecture suggests: (i). the main reverse fault reaches local maximum displacements at cores of the two hanging wall anticlines; (ii). the reverse fault beneath the southern anticline shows maximum fault displacement of ~850m, which is ~450m larger than that shown in the northern anticline (maximum displacement of ~400m); and (iii). the middle saddle between the two anticlines, which locally presents smallest fault displacement, acts as a stress-concentrated area because of the rapidly increasing displacement both northward and southward.
- By measuring the 3D model of the Lenghu5 structure, the throw vs. distance chart quantitatively delineates the nonuniform fault throw along the fault zone, which is in close agreement with field observation. The 3D model is restored in 3D MOVE (Midland Valley), providing an improved structural evolution of the Lenghu5 structure.
- A simplified model is proposed to simulate the strain distribution of the Lenghu5 structure, e.g., the total movement, extensional strain (e1), compressional strain (e3) and strain ratio (1+e1)/(1+e3). The second-order normal faults observed in the Lenghu5 structure are investigated statistically to verify the local strain distribution predicted from strain analysis on the simplified model.

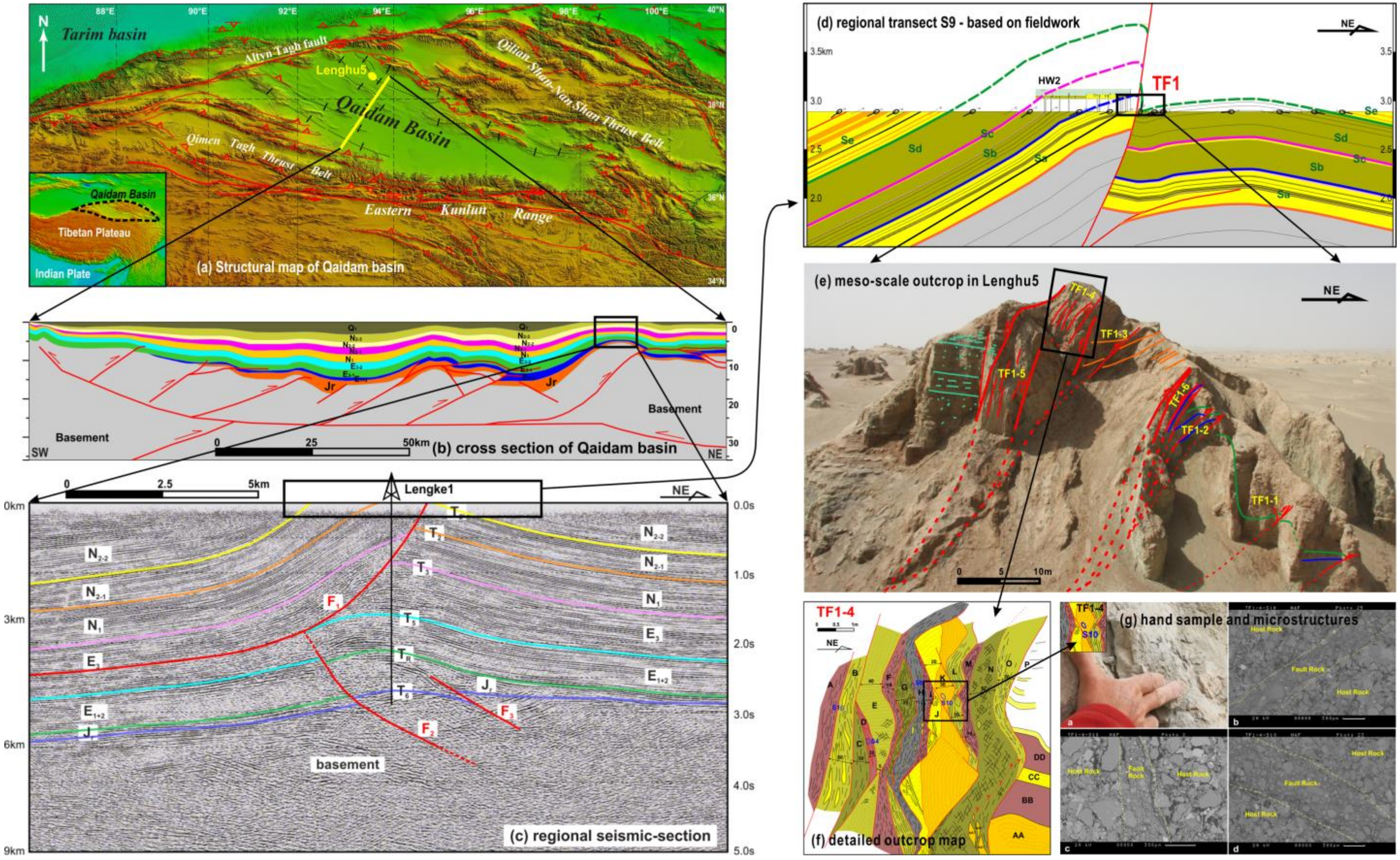

Figure 7.1 The multi-scale approach of studying the detailed thrust fault architecture in the Lenghu5 structure, Qaidam basin.

(2). Meso-scale (10cm-1km)

In order to understand the detailed meso-scale fault architecture and structural evolution of fault zones in compressional systems, the fault zone elements of the key outcrops have been mapped, including reverse and normal faults developed in low to moderate consolidated sediments with different stacking sequences (Chapter 5) (Figure 7.1e&f). The deformation mechanisms associated with reverse faults and the dynamic fault zone evolution are then considered. The detailed outcrop maps are used to provide new details for a reverse fault zone model. The effects of the critical factors on the reverse fault architecture are finally evaluated, e.g., the fault displacements, bed thickness, stratigraphic heterogeneity and mechanical heterogeneity.

- The main reverse fault TF1, with cumulative fault displacement of ~850m, includes high strain splay faults TF1-4/TF1-5 and TF1-6; medium strain splay faults TF1-3 and TF1-2; and low strain splay fault TF1-1. The other three reverse fault outcrops TF2, TF3 and TF4 show similar deformation features.
- The fault architecture of accommodation faults (e.g., minor reverse faults and normal faults) is characterized to compare with the main reverse faults. The factors controlling the fault development are also considered, e.g., bed thickness, stacking sequence, fault displacement, etc.
- The dynamic fault zone evolution of both reverse faults and normal faults are then considered. The dynamic evolution models demonstrate the detailed fault development, e.g., fault linkage, generation of fault lens and splay faults.
- Based on the detailed outcrop studies, the deformation responses are then drawn for different stacking sequences, e.g., strong/brittle beds, weak/ductile beds and mechanically layered sequences. When a mechanically layered sequence is subject to stress, the weak/ductile beds experience divergent trishear from upper and lower brittle beds.
- The detailed reverse fault model is then proposed, which subdivides a fault zone into: (i) fault core (FC), (ii) inner damage zone (IDZ) and (iii)

outer damage zone (ODZ). From FC, IDZ to ODZ, the rocks experience decreasing magnitude of deformation.

(3). Micro-scale (10μm-10cm)

The rock samples from the mapped outcrops (Figure 7.1f) were collected during fieldwork in order to investigate the micro-deformation features and to evaluate their effects on the fault rock sealing properties, e.g., porosity, permeability and capillary threshold pressure. A high performance Scanning Electron Microscope (SEM) investigation was employed to identify the micro-deformation mechanisms (Figure 7.1g). The relationship between fault rock types and their host rock composition has been revealed by the statistics related to clay/phyllosilicate content. The factors that may control the fault rock types are also evaluated, for example, the compaction state; the rock lithology; the fault throws; etc. The effects of the fault rocks on the fluid flow properties are then evaluated based on the magnitude of the porosity reduction during the micro-deformation.

- Four types of fault rocks are identified in the collected rock samples, including (i). clay smears/clay fault gouge; (ii). Phyllosilicate-framework fault rocks; (iii). cataclastic fault rocks; and (iv). fault breccia & cemented fractures. The SEM studies suggest the dominant micro-deformation mechanisms in the Lenghu5 structure are associated with clay smears and generation of PFFRs (Phyllosilicate-Framework Fault Rocks).
- Based on the SEM studies of rock samples, the fault rocks vs. phyllosilicate content chart is generated to reveal the relationship between the fault rock types and the clay content of host rocks. For low throws which preserve self-juxtaposition of units, host rocks with <15% clay content primarily form cataclastic fault rocks, e.g., clean sandstones; host rocks with 15%-40% clay content tend to form phyllosilicate-framework fault rocks (PFFRs), e.g., impure sandstones; and host rocks with >40% clay content incline to form clay smear-dominated fault rocks, e.g., mudstones.

The multi-scale approach enables us to understand the reverse fault architecture of the Lenghu5 structure from regional-scale (1km-10km) to micro-

scale (10μm-10cm), which provides a useful workflow of investigating reverse fault architecture in other natural structures. Firstly, the regional-scale analysis (1km-10km) can be employed to understand the first-order geometry, deformation timing and dynamic evolution of a target structure. Secondly, the meso-scale analysis (10cm-1km) can be then used to investigate the detailed features of fault zones, e.g., splay faults, fault lenses, clay smears and sand boudins. Finally, the micro-scale analysis (10μm-10cm) can be used to consider the micro-deformation mechanisms and their influences on the petrophysical properties of fault rocks, e.g., porosity, permeability and capillary pressure.

7.1.2. Parameters Controlling Fault Zone Architecture in the Lenghu5 Structure

Having summarised the key findings from the chapters, here the findings are integrated across scales. Based on the multi-scale analyses on fault zone architecture, several parameters have been identified as controlling the architecture of thrust fault zones, and these are the sequence competency, the fault throw, the mechanical heterogeneity, etc. The effects of these parameters on the thrust fault architecture have been described in a 3D parameter space (Figure 7.2).

(1). Sequence Competency

The competency of a sequence is determined by the lithology of comprising rocks. For example, a sequence dominated by sandstone beds usually has high competency; a sequence dominated by mudstone beds often has low competency; and a sequence of interbedded sandstone and mudstone beds shows intermediate competency (Figure 7.2b). Many previous studies have found that a strong bed-dominated sequence (high competency) tends to be fractured or faulted when being subject to stress; while a weak bed-dominated sequence (low competency) is likely to be deformed by ductile deformation (e.g., Eisenstadt and De Paor, 1987; Peacock and Sanderson, 1992; McGrath and Davison, 1995; Childs et al., 1996a; Schöpfer et al., 2006). The results of the outcrop studies in the Lenghu5 structure confirm that the competency of the deformed sequence plays an important role in determining the thrust fault architecture. When being subject to stress, the

sandstone-dominated sequence is prone to form fractures/TGFs (through-going faults). The mudstone-dominated sequence is likely to form folds or clay smears by ductile deformation of beds. In between these two end scenarios, a sequence of interbedded sandstone and mudstone can form fractures within sandstone beds and clay smears within mudstone beds. In this intermediate scenario, as discussed in Chapter 5, the sandstone beds experience convergent trishear deformation while the mudstone beds experience divergent trishear deformation. The contrast of deformation behaviour results in the high complexity of fault zones developed in a sequence with interbedded units of different properties.

(2). Fault throw

The well-exposed outcrops with different fault throws mapped in the Lenghu5 structure suggest that fault throw plays an important role in controlling the local level of faulting deformation. Generally, small fault throws usually form simple fault zones, while large fault throws mostly produce fault zones with high level of complexity (Figure 7.2b). For example, in the Lenghu5 structure, the minor reverse faults F1, F2 and F3 with cumulative fault throw up to 5m present low fault zone complexity; while the main reverse faults TF1, TF2, TF3 and TF4 with cumulative fault throws of hundreds of meters present much higher fault zone complexity (Chapter 5). In terms of details within a fault zone, very small fault throws may only form discrete fractures within strong beds and continuous clay smears within weak beds; while large fault throws are likely to form TGFs (through-going faults) by linking the preformed fractures in strong beds (Childs et al., 1996a) and semi-continuous clay smears in weak beds (see forward models in Chapter 5). If fault throw increases, fault lenses can be produced and clay smears can become discontinuous along the fault zone.

(3). Mechanical heterogeneity

The term ‘mechanical stratigraphy’ has been widely accepted in structural geology to subdivide rocks into discrete mechanical units defined by properties such as tensile strength, elastic stiffness, brittleness and fracture behaviour (e.g., Corbett et al., 1987; Cooke, 1997; Laubach et al., 2009). Mechanical stratigraphy with a high degree of heterogeneity may increase the com-

plexity of the fault zone architecture in thrust systems (Woodward and Rutherford Jr, 1989; Woodward, 1992; Pfiffner, 1993). Therefore, the effects of mechanical heterogeneity need to be considered when a sequence of multi-layered beds is subject to stress, e.g., the interbedded sandstone and mudstone observed in the Lenghu5 structure (Chapter 5). In this scenario, apart from the fault displacement, the bed thickness and the stacking sequence, the reverse fault architecture also depends on the level of mechanical heterogeneity of the host layers (Figure 7.2c). Based on the detailed outcrop studies in Lenghu5, in a mechanically homogeneous sequence (low mechanical heterogeneity), the fault zone is poorly developed or confined within a very limited width; while in a mechanically heterogeneous sequence, the fault zone has a wider width and a higher complexity. In the latter scenario, the mechanical contrasts present results in a high level of mixing of both brittle deformation in strong beds and ductile deformation in weak beds. The higher the mechanical heterogeneity of a sequence, the more ductile beds are folded or smeared into a fault zone.

As a summary, in the Lenghu5 structure, the fault zone develops increasing complexity as the mechanical heterogeneity and fault throw increases. The resultant elements within a fault zone can be fault segments, fault lenses, clay gouges, etc. These parameters are not independent factors but also interact with each other, which may result in more uncertainties than that demonstrated in Figure 7.2. Therefore, when studying the fault zone architecture of a natural structure at meso-scale (10cm-1km), it is necessary to consider the effects of those controlling parameters, which are the sequence competency, the fault throw and the mechanical heterogeneity.

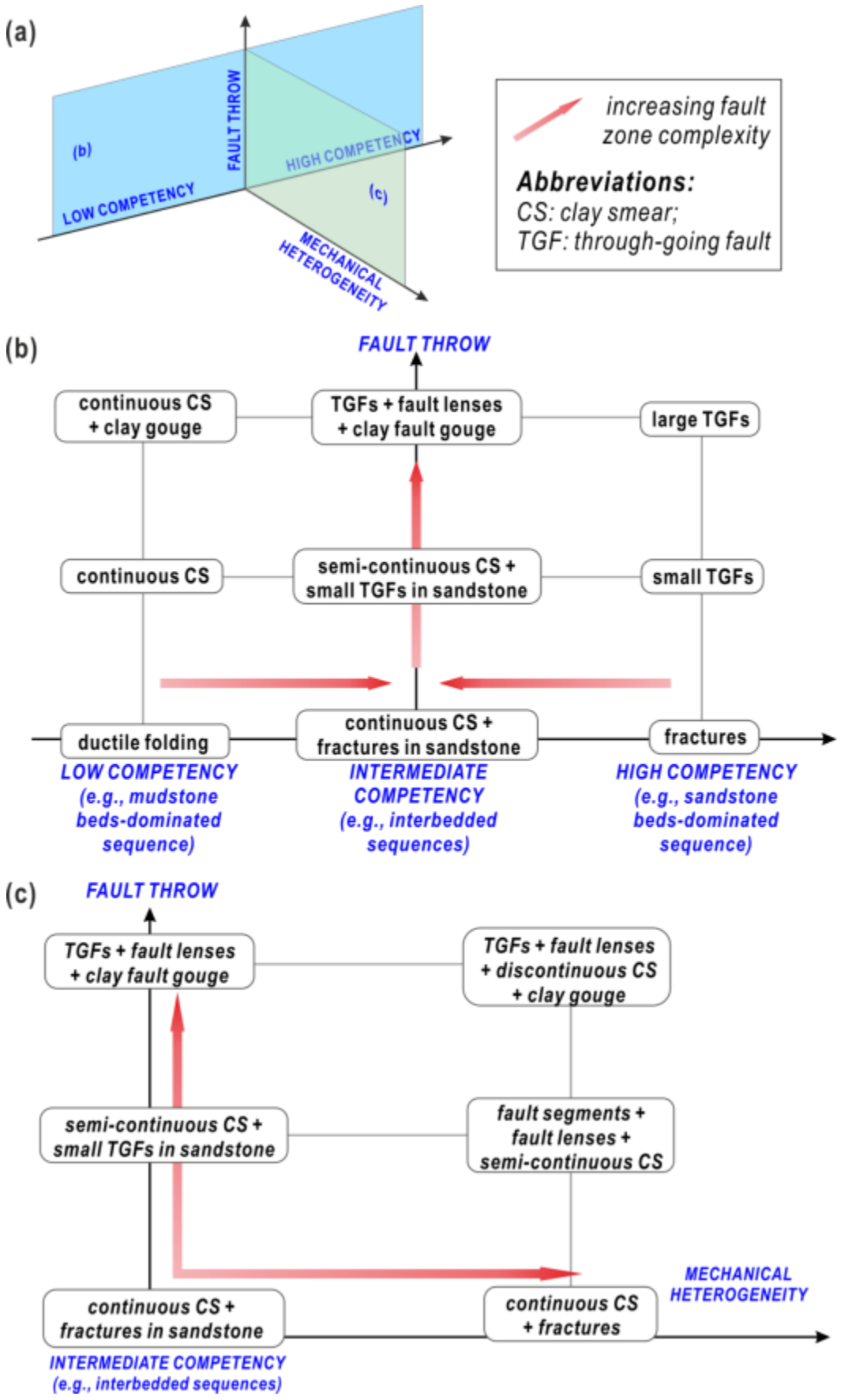

Figure 7.2 A 3D parameter space delineates the effects of key parameters on the thrust fault architecture, which are sequence competency, fault throw and mechanical heterogeneity.

7.2. Hydrocarbon Sealing Behaviour

7.2.1. Fault Seal Analysis at Multi-Scales

Corresponding to the multi-scale investigation on the fault zone architecture, the approaches of fault seal analysis at regional-scale, meso-scale and micro-scale are employed to evaluate the fault sealing capacity in the Lenghu5 structure (Figure 7.3).

(1). Regional-scale (1km-10km)

At a regional-scale (1st column in Figure 7.3), the detailed stratigraphic correlation and high-resolution transects enable the 3D fault architecture of the Lenghu5 structure in the Qaidam basin. The 3D fault architecture and dynamic evolution can be used to define the sediment compaction state, the faulting and deformation timing, the strain distribution and the burial history, which are critical for evaluating the fault sealing properties.

(2). Meso-scale (10cm-1km)

Fault seal analysis at a meso-scale normally focuses on juxtaposition seals, e.g., the Allan maps (Allan, 1989) and Juxtaposition Diagrams (Knipe, 1997) that predict the stratigraphic seals between the hanging wall and footwall. The juxtaposition between impermeable beds (e.g., shales, mudstone, etc.) can form good seals for fluid flow across a fault (2nd column in Figure 7.3). It is particularly useful to employ Allan maps or Juxtaposition Diagrams to define petroleum-leaking windows generated by stratigraphic juxtaposition between high-permeable sandstone beds in hanging wall against high permeable sandstone beds in footwall. However, these methods treat a fault as a single-plane surface, which is not in agreement with the widely observed fault zone architecture with a defined width and array of small structures.

The fault seal analysis at meso-scale focuses on the potential of forming continuous clay/shale smears along a fault plane, which may form effective barriers for the hydrocarbon migration across a fault zone. Quantitative methods are proposed to evaluate the effectiveness of forming continuous clay/shale smears or clay mixing along a fault zone (right bottom of 2nd column in Figure 7.3), e.g., Clay Smear Potential (CSP) (Bouvier et al., 1989), Shale Smear Factor (SSF) (Lindsay et al., 1993), Shale Gouge Ratio (SGR)

(Yielding et al., 1997) and Scaled Shale Gouge Ratio (SSGR) (Ciftci et al., 2013). These methods evaluate the effectiveness of forming continuous clay rich fault rocks / shale smears along a fault zone by considering both the thickness and the distribution of clay/shale-rich beds in the stratigraphy of a fault outcrop. At the meso-scale, the evaluation of fault sealing properties by smearing depends on the mudstone/shale bed thickness and fault throw: thick mudstone/shale bed tends to form continuous clay/shale smears along the fault plane with small fault throws.

(3). Micro-scale (10μm-10cm)

The fault seal analysis at micro-scale aims to identify the micro-deformation mechanisms and flow properties in rocks that are entrained into the fault zone during faulting, e.g., clay/phyllosilicate smearing, the generation of PFFRs, cataclasis, cementation, etc. (Knipe et al., 1997; Fisher and Knipe, 1998; Ottesen Ellevset et al., 1998). The micro-scale analysis employs SEM photography to evaluate the effects of micro-deformation mechanisms on the fluid flow properties of fault rocks, e.g., the porosity, the permeability, and the capillary pressure (3rd column in Figure 7.3). The micro-scale analysis provides useful evidence in the respect of fault rock types and their sealing capacities.

As a summary, given the fault seal analysis at a certain scale is not able to cover all aspects of the details associated with fault sealing capacity, the fault seal analysis restricted to a certain scale should not be used in isolation. Multi-scale fault seal analysis is needed to achieve reliable results when evaluating the sealing capacity of a fault zone.

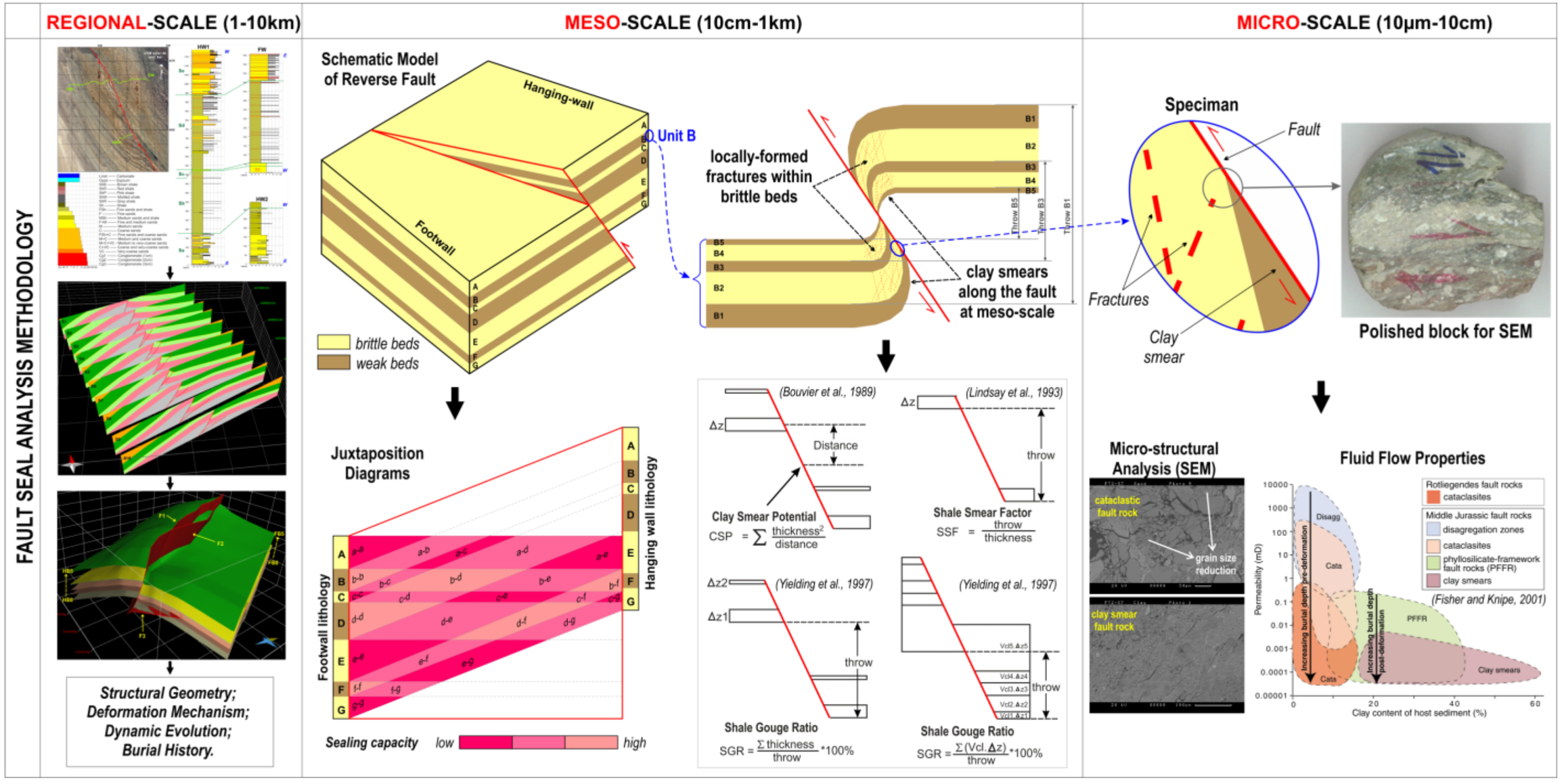

Figure 7.3 A conclusive table demonstrates the multi-scale fault seal analysis approaches, e.g., regional scale, meso-scale and micro-scale. The multi-scale fault seal analysis is needed when evaluating the fault sealing properties in natural structures.

7.2.2. Parameters Controlling the Fault Sealing Capacity in the Lenghu5 Structure

Based on the multi-scale fault seal analyses in the Lenghu5 structure, several parameters have been identified affecting the sealing capacity of thrust fault zones, which are the host rock composition, the fault throw, the stacking sequence, the bed thickness, etc.

(1). Host rock composition

In the Lenghu5 structure, the multi-scale fault seal analysis suggests that:

- Through-going faults are associated with cataclasis in clean sandstone beds (<15% clay content);
- Ductile folding and clay smearing are usually observed in weaker beds (e.g. mudstone/shale beds with >40% clay content);
- Intermediate clay content rocks (e.g., impure sandstone with 15-40% clay content) may generate phyllosilicate-framework fault rocks (PFFRs).

The micro-scale investigation in the Lenghu5 structure indicates that for the geohistory experienced, low permeable fault rocks are most likely to form from host rocks with high clay content. For example, the mudstone beds present good sealing properties; while it is difficult for the clean sandstone beds to form laterally continuous effective seals unless extensive cataclasis or cementation are developed.

(2). Fault displacement

As demonstrated by SEM photography, two types of low permeable fault rocks (clay smears and PFFRs) are observed in the Lenghu5 structure. However, the effectiveness of forming fluid flow barriers also depends on the continuity of low permeable fault rocks along a fault zone. The outcrop studies suggest that the continuity of low permeable fault rocks along fault zones is determined by the fault displacement. Empirically, with a certain bed thickness, large fault throw promotes the continuity of low-permeable fault rocks along fault zones. Although, increasing the throw beyond a critical value may disrupt the continuity of low permeability fault rocks as clay smears break down.

(3). Bed Thickness

Based on the outcrop studies in the Lenghu5 structure, it is suggested that the bed thickness plays an important control on the continuity of low permeable fault rocks. For a sandstone-dominated sequence, the degree of disruption of entrained beds depends on the thickness/strength of the host rocks. Thick sandstone beds form continuous faulted layers, but thin beds break down to isolated boudins. For a mudstone/shale-dominated sequence, the thick mudstone/shale beds generate more continuous clay smears or PFFRs, which may form barriers for hydrocarbon migration across the fault zone, where these fault rocks end up adjacent to sandstone carrier / reservoir units.

Although petrophysical properties of fault rocks are mainly determined by host rock composition, fault displacement, the stacking sequence and the bed thickness, some other factors still affect the petrophysical properties of fault rocks. For example, in some oil/gas fields, the fault rocks, even if generated from sandstones with identical clay/phyllosilicate content, sometimes present different porosity and permeability (e.g. Fisher and Knipe, 2001; Fisher et al., 2003). This can be attributed to the interaction between temperature history and stress history, which can alter the deformation mechanisms and thus the petrophysical properties of fault rocks (Fisher and Knipe, 2001). Therefore, as well as host rock composition, fault displacement and bed thickness, the effects of temperature history and stress history should be taken into account when evaluating fault sealing properties. The fault sealing analysis in the Lenghu5 structure can be applied to other natural structures if the temperature history and stress history are properly considered.

7.3 Summary and Future Work

As a summary, the trishear modelling and multi-scale research have revealed the detailed thrust fault evolution and its effect on the fault sealing properties in the Lenghu5 structure. The parameters that control the thrust fault evolution and fault sealing properties have also been evaluated. This study has properly answered the previously raised questions in the introduc-

tion section (Chapter 1) and provided a good workflow for considering both the fault architecture and fault sealing capacity at multi-scales.

In the future, three aspects of this PhD research can be improved by the following works:

(i). The parameter ‘mechanical heterogeneity’ plays a vital impact in both the fault evolution and fault sealing properties. If the mechanical heterogeneity could be quantitatively described, it will be useful to quantitatively evaluate the effect of mechanical heterogeneity on fault zone evolution, e.g., fault numbers, fault zone width, fault lens width/length ratio etc.

(ii). In this research, the studied rock samples were collected in the outcrops exposed in the ground in the Lenghu5 structure. If the core samples could be studied together, the comparison between outcrop samples and core samples can provide more reliable results, particularly to reveal the effects of the burial depth and consolidation state on fault rock sealing properties.

(iii). The future petrophysical assessment of the fault rock samples can provide precise poroperm properties, e.g., mercury injection porosimetry, water permemetry, XRD (X-ray diffraction) analysis, etc.

List of References

Allan, U. S., 1989, Model for Hydrocarbon Migration and Entrapment within Faulted Structures: American Association of Petroleum Geologists Bulletin, v. 73, no. 7, p. 803-811.

Allen, P. A., and Allen, J. R., 2005, Basin analysis: principles and applications (Second Edition): Oxford, Blackwell.

Allmendinger, R. W., 1998, Inverse and forward numerical modeling of trishear fault-propagation folds: Tectonics, v. 17, no. 4, p. 640-656.

Allmendinger, R. W., Zapata, T., Manceda, R., and Dzelalija, F., 2004, Trishear Kinematic Modeling of Structures, with Examples from the Neuquen Basin, Argentina: in K. R. McClay, eds., Thrust tectonics and hydrocarbon systems: American Association of Petroleum Geologists Memoir, v. 82, p. 356-371.

Alonso, J. L., and Teixell, A., 1992, Forelimb Deformation in Some Natural Examples of Fault-Propagation Folds: in K. R. McClay, eds., Thrust Tectonics. Springer Netherlands, p. 175-180.

Antonellini, M., and Aydin, A., 1994, Effect of Faulting on Fluid-Flow in Porous Sandstones - Petrophysical Properties: American Association of Petroleum Geologists Bulletin, v. 78, no. 3, p. 355-377.

-, 1995, Effect of Faulting on Fluid-Flow Geometry and Spatial-Distribution: American Association of Petroleum Geologists Bulletin, v. 79, no. 5, p. 642-671.

Antonellini, M. A., Aydin, A., and Pollard, D. D., 1994, Microstructure of deformation bands in porous sandstones at Arches National Park, Utah: Journal of Structural Geology, v. 16, no. 7, p. 941-959.

Aydin, A., and Eyal, Y., 2002, Anatomy of a normal fault with shale smear: Implications for fault seal: Aapg Bulletin-American Association of Petroleum Geologists, v. 86, no. 8, p. 1367-1381.

Bally, A. W., Chou, I. M., Clayton, R., Eugster, H. P., Kidwell, S., Mechel, L. D., Ryder, R. T., Watts, A. B., and Wilson, A. A., 1986, Notes on sedimentary basins in China: Report of the American Sedimentary Basins Delegation to the People's Republic of China, US Geological Survey Open-File Report. p. 86-327.

Bally, A. W., Gordy, P., and Stewart, G. A., 1966, Structure, seismic data, and orogenic evolution of southern Canadian Rocky Mountains: Bulletin of Canadian Petroleum Geology, v. 14, no. 3, p. 337-381.

Barclay, J., and Smith, D. G., 1992, Western Canada foreland basin oil and gas plays: in R.W. Macqueen and D.A. Leckie, eds., Foreland Basins and Fold Belts: American Association of Petroleum Geologists Memoir, v. 55, p. 191-228.

Bastesen, E., and Braathen, A., 2010, Extensional faults in fine grained carbonates – analysis of fault core lithology and thickness–displacement relationships: Journal of Structural Geology, v. 32, no. 11, p. 1609-1628.

Belotti, H. J., Saccavino, L. L., and Schachner, G. A., 1995, Structural styles and petroleum occurrence in the Sub-Andean fold and thrust belt of northern Argentina: in A. J. Tankard, R. Sua´rez S., and H. J. Welsink,

eds., Petroleum basins of South America: American Association of Petroleum Geologists Memoir, v. 62, p. 545-555.

Berg, R. R., 1975, Capillary pressures in stratigraphic traps: American Association of Petroleum Geologists Bulletin, v. 59, no. 6, p. 939-956.

Bjorkum, P. A., 1996, How important is pressure in causing dissolution of quartz in sandstones?: Journal of Sedimentary Research, v. 66, no. 1, p. 147-154.

Blenkinsop, T. G., 1989, Thickness — displacement relationships for deformation zones: Discussion: Journal of Structural Geology, v. 11, no. 8, p. 1051-1053.

-, 1991, Cataclasis and processes of particle size reduction: Pure and Applied Geophysics, v. 136, no. 1, p. 59-86.

Borg, I., Friedman, M., Handin, J., and Higgs, D. V., 1960, Chapter 6: Experimental Deformation of St. Peter Sand: A Study of Cataclastic Flow: Geological Society of America Memoirs, v. 79, p. 133-192.

Bose, S., Mandal, N., Mukhopadhyaly, D. K., and Mishra, P., 2009, An unstable kinematic state of the Himalayan tectonic wedge: Evidence from experimental thrust-spacing patterns: Journal of Structural Geology, v. 31, no. 1, p. 83-91.

Bouvier, J. D., Kaarssijpesteijn, C. H., Kluesner, D. F., Onyejekwe, C. C., and Vanderpal, R. C., 1989, Three-Dimensional Seismic Interpretation and Fault Sealing Investigations, Nun River Field, Nigeria: American Association of Petroleum Geologists Bulletin, v. 73, no. 11, p. 1397-1414.

Buchanan, P., and Warburton, J., The influence of pre-existing basin architecture in the development of the Papuan fold and thrust belt:

implications for petroleum prospectivity, *in* Proceedings Petroleum exploration, development, and production in Papua New Guinea: PNG [Papua New Guinea] Chamber of Mines and Petroleum, PNG Petroleum Convention, 3rd, Port Moresby1996, p. 89-109.

Burchfiel, B. C., Quidong, D., Molnar, P., Royden, L., Yipeng, W., Peizhen, Z., and Weiqi, Z., 1989, Intracrustal detachment within zones of continental deformation: Geology, v. 17, no. 8, p. 748-752.

Burliga, S., Koyi, H. A., and Krzywiec, P., 2012, Modelling cover deformation and decoupling during inversion, using the Mid-Polish Trough as a case study: Journal of Structural Geology, v. 42, p. 62-73.

Butler, R., Mazzoli, S., Corrado, S., De Donatis, M., Di Bucci, D., Gambini, R., Naso, G., Nicolai, C., Scrocca, D., and Shiner, P., 2004, Applying thick-skinned tectonic models to the Apennine thrust belt of Italy—Limitations and implications: in K. R. McClay, eds., Thrust tectonics and hydrocarbon systems: American Association of Petroleum Geologists Memoir, v. 82, p. 647-667.

Caine, J. S., Evans, J. P., and Forster, C. B., 1996, Fault zone architecture and permeability structure: Geology, v. 24, no. 11, p. 1025-1028.

Cardozo, N., 2005, Trishear modeling of fold bedding data along a topographic profile: Journal of Structural Geology, v. 27, no. 3, p. 495-502.

-, 2008, Trishear in 3D. Algorithms, implementation, and limitations: Journal of Structural Geology, v. 30, no. 3, p. 327-340.

Cardozo, N., and Aanonsen, S., 2009, Optimized trishear inverse modeling: Journal of Structural Geology, v. 31, no. 6, p. 546-560.

Cardozo, N., Allmendinger, R. W., and Morgan, J. K., 2005, Influence of mechanical stratigraphy and initial stress state on the formation of two fault propagation folds: Journal of Structural Geology, v. 27, no. 11, p. 1954-1972.

Cardozo, N., Jackson, C. A. L., and Whipp, P. S., 2011, Determining the uniqueness of best-fit trishear models: Journal of Structural Geology, v. 33, no. 6, p. 1063-1078.

Cecil, C. B., and Heald, M. T., 1971, Experimental investigation of the effects of grain coatings on quartz growth: Journal of Sedimentary Petrology, v. 41, p. 582-584.

Cerveny, K., Davies, R., Dudley, G., Fox, R., Kaufman, P., Knipe, R. J., and Krantz, B., 2004, Reducing Uncertainty with Fault-Seal Analysis: Oilfield Review, v. 16, no. 4, p. 38-51.

Champion, J., Mueller, K., Tate, A., and Guccione, M., 2001, Geometry, numerical models and revised slip rate for the Reelfoot fault and trishear fault-propagation fold, New Madrid seismic zone: Engineering Geology, v. 62, no. 1-3, p. 31-49.

Chen, W. P., Chen, C. Y., and Nabelek, J. L., 1999, Present-day deformation of the Qaidam basin with implications for intra-continental tectonics: Tectonophysics, v. 305, no. 1-3, p. 165-181.

Chen, Z. Y., Wang, L. Q., Chen, S. P., and Wang, Z. X., 2005, Tectonic model and its deformation feature of Cenozoic in west section of Lenghu structural belt, northern margin of Qaidam basin (in Chinese with English abstract): Xinjiang Petroleum Geology, v. 26, no. 6, p. 614-617.

Childs, C., Manzocchi, T., Walsh, J. J., Bonson, C. G., Nicol, A., and Schöpfer, M. P. J., 2009, A geometric model of fault zone and fault rock thickness variations: Journal of Structural Geology, v. 31, no. 2, p. 117-127.

Childs, C., Nicol, A., Walsh, J. J., and Watterson, J., 1996a, Growth of vertically segmented normal faults: Journal of Structural Geology, v. 18, no. 12, p. 1389-1397.

Childs, C., Walsh, J. J., Manzocchi, T., Strand, J., Nicol, A., Tomasso, M., Schöpfer, M. P. J., and Aplin, A. C., 2007, Definition of a fault permeability predictor from outcrop studies of a faulted turbidite sequence, Taranaki, New Zealand: Geological Society, London, Special Publications, v. 292, no. 1, p. 235-258.

Childs, C., Watterson, J., and Walsh, J. J., 1996b, A model for the structure and development of fault zones: Journal of the Geological Society, v. 153, no. 3, p. 337-340.

Ciftci, N. B., Giger, S. B., and Clennell, M. B., 2013, Three-dimensional structure of experimentally produced clay smears: Implications for fault seal analysis: American Association of Petroleum Geologists Bulletin, v. 97, no. 5, p. 733-757.

Cooke, M. L., 1997, Predicting fracture localization in folded strata from mechanical stratigraphy and fold shape: Case study of east Kaibab Monocline, Utah: International Journal of Rock Mechanics and Mining Sciences, v. 34, no. 3-4, p. 56.e51-56.e12.

Corbett, K., Friedman, M., and Spang, J., 1987, Fracture development and mechanical stratigraphy of Austin Chalk, Texas: American Association of Petroleum Geologists Bulletin, v. 71, no. 1, p. 17-28.

Couzens, B. A., and Wiltschko, D. V., 1996, The control of mechanical stratigraphy on the formation of triangle zones: Bulletin of Canadian Petroleum Geology, v. 44, no. 2, p. 165-179.

Coward, M. P., 1983, Thrust tectonics, thin skinned or thick skinned, and the continuation of thrusts to deep in the crust: Journal of Structural Geology, v. 5, no. 2, p. 113-123.

Coward, M. P., De Donatis, M., Mazzoli, S., Paltrinieri, W., and Wezel, F.-C., 1999, Frontal part of the northern Apennines fold and thrust belt in the Romagna-Marche area (Italy): Shallow and deep structural styles: Tectonics, v. 18, no. 3, p. 559-574.

Cowgill, E., 2007, Impact of riser reconstructions on estimation of secular variation in rates of strike-slip faulting: Revisiting the Cherchen River site along the Altyn Tagh Fault, NW China: Earth and Planetary Science Letters, v. 254, no. 3-4, p. 239-255.

Cowgill, E., Arrowsmith, J. R., Yin, A., Wang, X. F., and Chen, Z. L., 2004a, The Akato Tagh bend along the Altyn Tagh fault, northwest Tibet 2: Active deformation and the importance of transpression and strain hardening within the Altyn Tagh system: Geological Society of America Bulletin, v. 116, no. 11-12, p. 1443-1464.

Cowgill, E., Yin, A., Arrowsmith, J. R., Feng, W. X., and Zhang, S. H., 2004b, The Akato Tagh bend along the Altyn Tagh fault, northwest Tibet 1: Smoothing by vertical-axis rotation and the effect of topographic stresses on bend-flanking faults: Geological Society of America Bulletin, v. 116, no. 11-12, p. 1423-1442.

Cowgill, E., Yin, A., Feng, W. X., and Qing, Z., 2000, Is the North Altyn fault part of a strike-slip duplex along the Altyn Tagh fault system?: Geology, v. 28, no. 3, p. 255-258.

Cowgill, E., Yin, A., Harrison, T. M., and Wang, X. F., 2003, Reconstruction of the Altyn Tagh fault based on U-Pb geochronology: Role of back thrusts, mantle sutures, and heterogeneous crustal strength in forming the Tibetan Plateau: Journal of Geophysical Research, v. 108, no. B7, p. 2346.

Cowie, P. A., Knipe, R. J., and Main, I. G., 1996, Introduction to the Special Issue: Scaling Laws for fault and fracture populations - analyses and applications: Journal of Structural Geology, v. 18, no. 2-3, p. v-xi.

Cowie, P. A., and Scholz, C. H., 1992, Displacement-length scaling relationship for faults: data synthesis and discussion: Journal of Structural Geology, v. 14, no. 10, p. 1149-1156.

Cowie, P. A., Vanneste, C., and Sornette, D., 1993, Statistical physics model for the spatiotemporal evolution of faults: Journal of Geophysical Research, v. 98, no. B12, p. 21809-21821.

Craddock, W. H., Kirby, E., Zheng, D. W., and Liu, J. H., 2012, Tectonic setting of Cretaceous basins on the NE Tibetan Plateau: insights from the Jungong basin: Basin Research, v. 24, no. 1, p. 51-69.

Crawford, B. R., 1998, Experimental fault sealing: shear band permeability dependency on cataclastic fault gouge characteristics: Geological Society, London, Special Publications, v. 127, no. 1, p. 27-47.

Crawford, B. R., Myers, R. D., Woronow, A., Faulkner, D. R., and Rutter, E. H., Porosity-permeability relationships in clay-bearing fault gouge, *in* Proceedings SPE/ISRM Rock Mechanics Conference2002.

Cristallini, E. O., and Allmendinger, R. W., 2001, Pseudo 3-D modeling of trishear fault-propagation folding: Journal of Structural Geology, v. 23, no. 12, p. 1883-1899.

Cristallini, E. O., Giambiagi, L., and Allmendinger, R. W., 2004, True three-dimensional trishear: A kinematic model for strike-slip and oblique-slip deformation: Geological Society of America Bulletin, v. 116, no. 7-8, p. 938-952.

Cruden, A. R., and McCaffrey, K. J. W., 2001, Growth of plutons by floor subsidence: Implications for rates of emplacement, intrusion spacing and melt-extraction mechanisms: Physics and Chemistry of the Earth Part a-Solid Earth and Geodesy, v. 26, no. 4-5, p. 303-315.

Cui, Z. Z., Li, Q. S., Wu, C. D., Yin, Z. X., and Liu, H. B., 1995, The crustal and deep structure in Golmud-Ejin Qi GGT: Acta Geophysica Sinica, v. 38, no. 2, p. 28-34.

Dahlstrom, C. D. A., 1990, Geometric Constraints Derived from the Law of Conservation of Volume and Applied to Evolutionary Models for Detachment Folding: American Association of Petroleum Geologists Bulletin, v. 74, no. 3, p. 336-344.

Davatzes, N., and Aydin, A., 2005, Distribution and nature of fault architecture in a layered sandstone and shale sequence: An example from the Moab fault, Utah: in R. Sorkhabi and Y. Tsuji, eds., Faults, fluid flow, and petroleum traps: American Association of Petroleum Geologists Memoir, v. 85, p. 153-180.

Davies, R., and Knipe, R., 2008, RDR Fault Foundation: Unpublished.

Davies, R. K., Knipe, R. J., and Welch, M. J., 2012, The Role of Vertical Mechanical Heterogeneity in Predicting Fault Zone Architecture: Fault and Top Seals 2012 (EAGE Extended Abstract).

Deng, J., Wu, Z., Yang, J., Zhao, H., Liu, H., Lai, S., and Di, Y., 1995, Crust-mantle petrological structure and deep processes along the Golmud-Ejin Qi geoscience section: Acta Geophysica Sinica, v. 38, no. 2, p. 144-157.

Dewers, T., and Ortoleva, P., 1991, Influences of clay minerals on sandstone cementation and pressure solution: Geology, v. 19, no. 10, p. 1045-1048.

Dewers, T., and Ortoleva, P. J., 1990, Interaction of reaction, mass transport, and rock deformation during diagenesis: mathematical modelling of integranular pressure solution, stylolites, and differential compaction/cementation: in I. D. Meshri and P. J. Ortoleva, eds., Prediction of Reservoir Quality through Chemical Modelling: American Association of Petroleum Geologists Memoir, v. 49, p. 147-160.

Dixon, J. M., 2004, Physical (Centrifuge) Modeling of Fold-thrust Shortening Across Carbonate Bank MarginsTiming, Vergence, and Style of Deformation: in K. R. McClay, eds., Thrust tectonics and hydrocarbon systems: American Association of Petroleum Geologists Memoir, v. 82, p. 223-238.

Egan, S. S., Buddin, T. S., Kane, S. J., and Williams, G. D., 1997, Three-dimensional modelling and visualisation in structural geology: New techniques for the restoration and balancing of volumes, v. 1, no. 7, p. 67-82.

Egholm, D. L., Clausen, O. R., Sandiford, M., Kristensen, M. B., and Korstgård, J. A., 2008, The mechanics of clay smearing along faults: Geology, v. 36, no. 10, p. 787-790.

Eisenstadt, G., and De Paor, D. G., 1987, Alternative model of thrust-fault propagation: Geology, v. 15, no. 7, p. 630-633.

Ellis, S., Schreurs, G., and Panien, M., 2004, Comparisons between analogue and numerical models of thrust wedge development: Journal of Structural Geology, v. 26, no. 9, p. 1659-1675.

Engelder, J. T., 1974, Cataclasis and the Generation of Fault Gouge: Geological Society of America Bulletin, v. 85, no. 10, p. 1515-1522.

Erslev, E. A., 1991, Trishear Fault-Propagation Folding: Geology, v. 19, no. 6, p. 617-620.

Erslev, E. A., and Mayborn, K. R., 1997, Multiple geometries and modes of fault-propagation folding in the Canadian thrust belt: Journal of Structural Geology, v. 19, no. 3-4, p. 321-335.

Erslev, E. A., and Rogers, J. L., 1993, Basement-Cover Geometry of Laramide Fault-Propagation Folds: Geological Society of America Special papers, v. 280, p. 125-146.

Evans, J. P., 1990, Thickness-displacement relationships for fault zones: Journal of Structural Geology, v. 12, no. 8, p. 1061-1065.

Faulkner, D. R., Jackson, C. A. L., Lunn, R. J., Schlische, R. W., Shipton, Z. K., Wibberley, C. A. J., and Withjack, M. O., 2010, A review of recent developments concerning the structure, mechanics and fluid flow properties of fault zones: Journal of Structural Geology, v. 32, no. 11, p. 1557-1575.

Finch, E., Hardy, S., and Gawthorpe, R., 2003, Discrete element modelling of contractional fault-propagation folding above rigid basement fault blocks: Journal of Structural Geology, v. 25, no. 4, p. 515-528.

Finch, E., Hardy, S., and Gawthorpe, R., 2004, Discrete-element modelling of extensional fault-propagation folding above rigid basement fault blocks: Basin Research, v. 16, no. 4, p. 467-488.

Fisher, Q. J., Casey, M., Harris, S. D., and Knipe, R. J., 2003, Fluid-flow properties of faults in sandstone: The importance of temperature history: Geology, v. 31, no. 11, p. 965-968.

Fisher, Q. J., Harris, S. D., McAllister, E., Knipe, R. J., and Bolton, A. J., 2001, Hydrocarbon flow across faults by capillary leakage revisited: Marine and Petroleum Geology, v. 18, no. 2, p. 251-257.

Fisher, Q. J., and Jolley, S. J., 2007, Treatment of faults in production simulation models: Geological Society, London, Special Publications, v. 292, p. 219-233.

Fisher, Q. J., and Knipe, R. J., 1998, Fault sealing processes in siliciclastic sediments: Geological Society, London, Special Publications, v. 147, p. 117-134.

-, 2001, The permeability of faults within siliciclastic petroleum reservoirs of the North Sea and Norwegian Continental Shelf: Marine and Petroleum Geology, v. 18, no. 10, p. 1063-1081.

Fisher, Q. J., Knipe, R. J., and Worden, R. H., 2009, Microstructures of Deformed and Non-Deformed Sandstones from the North Sea: Implications for the Origins of Quartz Cement in Sandstones: in R. H. Worden and S. Morad, eds., Quartz Cementation in Sandstones, Blackwell Publishing Ltd., Oxford, UK, v. 14, p. 129-146.

Fossen, H., Schultz, R. A., Shipton, Z. K., and Mair, K., 2007, Deformation bands in sandstone: a review: Journal of the Geological Society, v. 164, no. 4, p. 755-769.

Fulljames, J. R., Zijerveld, L. J. J., and Franssen, R. C. M. W., 1997, Fault seal processes: systematic analysis of fault seals over geological and production time scales, *in* Møller-Pedersen, P., and Koestler, A. G., eds., Norwegian Petroleum Society Special Publications, Volume 7, p. 51-59.

Gallup, W. B., 1951, Geology of Turner Valley oil and gas field, Alberta, Canada: American Association of Petroleum Geologists Bulletin, v. 35, no. 4, p. 797-821.

Gao, R., Chen, X., and Ding, Q., 1995, Preliminary geodynamic model of Goldmud-Ejin Qi geoscience transect: Acta Geophysica Sinica, v. 38, no. 2, p. 14-27.

Gibson, R. G., 1994, Fault-Zone Seals in Siliciclastic Strata of the Columbus Basin, Offshore Trinidad: American Association of Petroleum Geologists Bulletin, v. 78, no. 9, p. 1372-1385.

Gold, R. D., Cowgill, E., Wang, X. F., and Chen, X. H., 2006, Application of trishear fault-propagation folding to active reverse faults: examples from the Dalong Fault, Gansu Province, NW China: Journal of Structural Geology, v. 28, no. 2, p. 200-219.

Hamilton, W. B., 1988, Laramide crustal shortening: Interaction of the Rocky Mountain foreland and the Cordilleran thrust belt: Geological Society of America Memoir, v. 171, p. 27-39.

Handin, J., Hager Jr, R. V., Friedman, M., and Feather, J. N., 1963, Experimental deformation of sedimentary rocks under confining

pressure: pore pressure tests: American Association of Petroleum Geologists Bulletin, v. 47, no. 5, p. 717-755.

Hardy, S., and Finch, E., 2007, Mechanical stratigraphy and the transition from trishear to kink-band fault-propagation fold forms above blind basement thrust faults: A discrete-element study: Marine and Petroleum Geology, v. 24, no. 2, p. 75-90.

Hardy, S., and Ford, M., 1997, Numerical modeling of trishear fault propagation folding: Tectonics, v. 16, no. 5, p. 841-854.

Hayward, A. B., and Graham, R. H., 1989, Some geometrical characteristics of inversion: Geological Society, London, Special Publications, v. 44, no. 1, p. 17-39.

Heald, M. T., 1955, Stylolites in Sandstones: The Journal of Geology, v. 63, no. 2, p. 101-114.

Heynekamp, M. R., Goodwin, L. B., Mozley, P. S., and Haneberg, W. C., 1999, Controls on fault-zone architecture in poorly lithified sediments, Rio Grande Rift, New Mexico: Implications for fault-zone permeability and fluid flow, Faults and Subsurface Fluid Flow in the Shallow Crust. Washington, DC, AGU, Volume 113, p. 27-49.

Hill, K. C., 1991, Structure of the Papuan Fold Belt, Papua New Guinea (1): American Association of Petroleum Geologists Bulletin, v. 75, no. 5, p. 857-872.

Hill, K. C., Keetley, J. T., Kendrick, R. D., and Sutriyono, E., 2004, Structure and hydrocarbon potential of the New Guinea Fold Belt: in K. R. McClay, eds., Thrust tectonics and hydrocarbon systems: American Association of Petroleum Geologists Memoir, v. 82, p. 494-514.

Homza, T. X., and Wallace, W. K., 1995, Geometric and kinematic models for detachment folds with fixed and variable detachment depths: Journal of Structural Geology, v. 17, no. 4, p. 575-588.

Huang, H. C., Huang, Q. H., and Ma, S., 1996, Geology of Qaidam basin and its petroleum prediction: Geological Publishing House, Beijing.

Hull, J., 1988, Thickness-displacement relationships for deformation zones: Journal of Structural Geology, v. 10, no. 4, p. 431-435.

Huo, G. M., 1990, Petroleum geology of China: in Oil fields in Qianghai and Xizang: Beijing: Chinese Petroleum Industry Press, v. 14, p. 483.

Ingram, G. M., Chisholm, T. J., Grant, C. J., Hedlund, C. A., Stuart-Smith, P., and Teasdale, J., 2004, Deepwater North West Borneo: hydrocarbon accumulation in an active fold and thrust belt: Marine and Petroleum Geology, v. 21, no. 7, p. 879-887.

Jamison, W. R., 1987, Geometric analysis of fold development in overthrust terranes: Journal of Structural Geology, v. 9, no. 2, p. 207-219.

Jev, B. I., Kaars-Sijpesteijn, C. H., Peters, M. P. A. M., Watts, N. L., and Wilkie, J. T., 1993, Akaso field, Nigeria: Use of integrated 3-D seismic, fault slicing, clay smearing, and RFT pressure data on fault trapping and dynamic leakage: American Association of Petroleum Geologists Bulletin, v. 77, no. 8, p. 1389-1404.

Jin, G. H., and Groshong, R. H., 2006, Trishear kinematic modeling of extensional fault-propagation folding: Journal of Structural Geology, v. 28, no. 1, p. 170-183.

Jin, G. H., Groshong, R. H., and Pashin, J. C., 2009, Growth trishear model and its application to the Gilbertown graben system, southwest Alabama: Journal of Structural Geology, v. 31, no. 9, p. 926-940.

Jolivet, M., Brunel, M., Seward, D., Xu, Z., Yang, J., Malavieille, J., Roger, F., Leyreloup, A., Arnaud, N., and Wu, C., 2003, Neogene extension and volcanism in the Kunlun Fault Zone, northern Tibet: New constraints on the age of the Kunlun Fault: Tectonics, v. 22, no. 5, p. 1052.

Jolley, S. J., Dijk, H., Lamens, J. H., Fisher, Q. J., Manzocchi, T., Eikmans, H., and Huang, Y., 2007, Faulting and fault sealing in production simulation models: Brent Province, northern North Sea: Petroleum Geoscience, v. 13, no. 4, p. 321-340.

Kane, S. J., Williams, G. D., Buddin, T. S., Egan, S. S., and Hodgetts, D., 1997, Flexural-slip based restoration in 3D, a new approach: 1997 AAPG Annual Convention Official Program A, v. 58.

Knai, T. A., and Knipe, R. J., 1998, The impact of faults on fluid flow in the Heidrun Field: Geological Society, London, Special Publications, v. 147, no. 1, p. 269-282.

Knipe, R. J., 1989, Deformation Mechanisms - Recognition from Natural Tectonites: Journal of Structural Geology, v. 11, no. 1-2, p. 127-146.

-, 1992a, Faulting processes and fault seal, *in* Larsen, R. M., Brekke, H., Larsen, B. T., and Talleraas, E., eds., Norwegian Petroleum Society Special Publications, Volume 1, p. 325-342.

-, 1992b, Faulting processes, seal evolution, and reservoir discontinuities: An integrated analysis of the ULA Field, Central Graben, North Sea, Abstracts of the Petroleum Group meeting on collaborative research programme in petroleum geoscience between UK Higher Education Institutes and the Petroleum Industry, Geological Society, London.

-, 1993a, The Influence of Fault Zone Processes and Diagenesis on Fluid Flow: Diagenesis and Basin Development, no. 36, p. 135-154.

-, 1993b, Micromechanisms of deformation and fluid flow behaviour during faulting: The mechanical behavior of fluids in fault zones: USGS Open-File Report, p. 94-228.

-, 1994, Fault zone geometry and behaviour: the importance of damage zone evolution: Abstracts of Meetings Modern Developments in Structural Interpretation, Geological Society, London.

-, 1997, Juxtaposition and seal diagrams to help analyze fault seals in hydrocarbon reservoirs: American Association of Petroleum Geologists Bulletin, v. 81, no. 2, p. 187-195.

Knipe, R. J., Fisher, R. J., Jones, G., Clennell, M. R., Farmer, A. B., Harrison, a., Kidd, B., McAllister, E., R., P. J., and White, E. A., 1997, Fault seal analysis: successful methodologies, application and future directions: Norwegian Petroleum Society Special Publications, v. 7, p. 15-40.

Knipe, R. J., Jones, G., and Fisher, Q. J., 1998, Faulting, fault sealing and fluid flow in hydrocarbon reservoirs: an introduction: Geological Society, London, Special Publications, v. 147, no. 1, p. vii-xxi.

Knipe, R. J., and Lloyd, G. E., 1994, Microstructural analysis of faulting in quartzite, Assynt, NW Scotland: Implications for fault zone evolution: Pure and Applied Geophysics, v. 143, no. 1-3, p. 229-254.

Knott, S., 1994, Fault zone thickness versus displacement in the Permo-Triassic sandstones of NW England: Journal of the Geological Society, v. 151, no. 1, p. 17-25.

Knott, S. D., 1993, Fault Seal Analysis in the North-Sea: American Association of Petroleum Geologists Bulletin, v. 77, no. 5, p. 778-792.

Lamerson, P. R., 1982, The Fossil basin and its relationship to the Absaroka thrust fault system, Wyoming and Utah: In Geologic Studies of the

Cordilleran Thrust Belt, vol. 1, ed. R. B. Powers. Rocky Mountain Association of Geologists, p. 279-340.

Laubach, S. E., Olson, J. E., and Gross, M. R., 2009, Mechanical and fracture stratigraphy: American Association of Petroleum Geologists Bulletin, v. 93, no. 11, p. 1413-1426.

Lewis, G., Knipe, R. J., and Li, A., 2002, Fault seal analysis in unconsolidated sediments: a field study from kentucky, USA, *in* Andreas, G. K., and Robert, H., eds., Norwegian Petroleum Society Special Publications, Volume 11, p. 243-253.

Lin, M. L., Wang, C. P., Chen, W. S., Yang, C. N., and Jeng, F. S., 2007, Inference of trishear-faulting processes from deformed pregrowth and growth strata: Journal of Structural Geology, v. 29, no. 7, p. 1267-1280.

Lindsay, N. G., Murphy, F. C., Walsh, J. J., and Watterson, J., 1993, Outcrop Studies of Shale Smears on Fault Surface, The Geological Modelling of Hydrocarbon Reservoirs and Outcrop Analogues, Blackwell Publishing Ltd., p. 113-123.

Liu, D. L., Fang, X. M., Gao, J. P., Wang, Y. D., Zhang, W. L., Miao, Y. F., Liu, Y. Q., and Zhang, Y. Z., 2009, Cenozoic Stratigraphy Deformation History in the Central and Eastern of Qaidam Basin by the Balance Section Restoration and its Implication: Acta Geologica Sinica-English Edition, v. 83, no. 2, p. 359-371.

Loveless, S., Bense, V., and Turner, J., 2011, Fault architecture and deformation processes within poorly lithified rift sediments, Central Greece: Journal of Structural Geology, v. 33, no. 11, p. 1554-1568.

McClay, K., and Whitehouse, P., 2004, Analog modeling of doubly vergent thrust wedges: in K. R. McClay, eds., Thrust tectonics and hydrocarbon systems: American Association of Petroleum Geologists Memoir, v. 82, p. 184-206.

McGrath, A. G., and Davison, I., 1995, Damage zone geometry around fault tips: Journal of Structural Geology, v. 17, no. 7, p. 1011-1024.

McQuarrie, N., 2004, Crustal scale geometry of the Zagros fold-thrust belt, Iran: Journal of Structural Geology, v. 26, no. 3, p. 519-535.

Medwedeff, D. A., and Suppe, J., 1997, Multibend fault-bend folding: Journal of Structural Geology, v. 19, no. 3-4, p. 279-292.

Meng, Q. R., Hu, J. M., and Yang, F. Z., 2001, Timing and magnitude of displacement on the Altyn Tagh fault: constraints from stratigraphic correlation of adjoining Tarim and Qaidam basins, NW China: Terra Nova, v. 13, no. 2, p. 86-91.

Meyer, B., Tapponnier, P., Bourjot, L., Metivier, F., Gaudemer, Y., Peltzer, G., Shunmin, G., and Zhitai, C., 1998, Crustal thickening in Gansu-Qinghai, lithospheric mantle subduction, and oblique, strike-slip controlled growth of the Tibet plateau: Geophysical Journal International, v. 135, no. 1, p. 1-47.

Miller, J. F., and Mitra, S., 2011, Deformation and secondary faulting associated with basement-involved compressional and extensional structures: American Association of Petroleum Geologists Bulletin, v. 95, no. 4, p. 675-689.

Mitra, S., 1988, Effects of deformation mechanisms on reservoir potential in central Appalachian overthrust belt: American Association of Petroleum Geologists Bulletin, v. 72, no. 5, p. 536-554.

-, 1990, Fault-Propagation Folds: Geometry, Kinematic Evolution, and Hydrocarbon Traps (1): American Association of Petroleum Geologists Bulletin, v. 74, no. 6, p. 921-945.

Mitra, S., 2003, A unified kinematic model for the evolution of detachment folds: Journal of Structural Geology, v. 25, no. 10, p. 1659-1673.

Mitra, S., and Namson, J. S., 1989, Equal-area balancing: American Journal of Science, v. 289, no. 5, p. 563-599.

Molnar, P., and Tapponnier, P., 1975, Cenozoic Tectonics of Asia - Effects of a Continental Collision: Science, v. 189, no. 4201, p. 419-426.

Muñoz, J., 1992, Evolution of a continental collision belt: ECORS-Pyrenees crustal balanced cross-section, *in* McClay, K. R., ed., in K. R. McClay, eds., Thrust Tectonics. Springer Netherlands, p. 235-246.

Odling, N. E., Harris, S. D., and Knipe, R., 2004, Permeability scaling properties of fault damage zones in siliclastic rocks: Journal of Structural Geology, v. 26, no. 9, p. 1727-1747.

Oelkers, E. H., Bjorkum, P. A., and Murphy, W. M., 1996, A petrographic and computational investigation of quartz cementation and porosity reduction in North Sea sandstones: American Journal of Science, v. 296, no. 4, p. 420-452.

Otsuki, K., 1978, On the relationship between the width of shear zone and the displacement along fault: Journal of Geological Society of Japan, v. 84, no. 1, p. 661-669.

Ottesen Ellevset, S., Knipe, R. J., Svava Olsen, T., Fisher, Q. J., and Jones, G., 1998, Fault controlled communication in the Sleipner Vest Field, Norwegian Continental Shelf; detailed, quantitative input for reservoir

simulation and well planning: Geological Society, London, Special Publications, v. 147, no. 1, p. 283-297.

Pang, X. Q., Li, Y. X., and Jiang, Z. X., 2004, Key geological controls on migration and accumulation for hydrocarbons derived from mature source rocks in Qaidam Basin: Journal of Petroleum Science and Engineering, v. 41, no. 1-3, p. 79-95.

Peacock, D. C. P., and Sanderson, D. J., 1991, Displacements, segment linkage and relay ramps in normal fault zones: Journal of Structural Geology, v. 13, no. 6, p. 721-733.

-, 1992, Effects of layering and anisotropy on fault geometry: Journal of the Geological Society, v. 149, no. 5, p. 793-802.

-, 1994, Geometry and development of relay ramps in normal fault systems: American Association of Petroleum Geologists Bulletin, v. 78, no. 2, p. 147-165.

Pfiffner, O. A., 1993, The structure of the Helvetic nappes and its relation to the mechanical stratigraphy: Journal of Structural Geology, v. 15, no. 3–5, p. 511-521.

Pfiffner, O. A., Ellis, S., and Beaumont, C., 2000, Collision tectonics in the Swiss Alps: Insight from geodynamic modeling: Tectonics, v. 19, no. 6, p. 1065-1094.

Poblet, J., and Lisle, R. J., 2011, Kinematic evolution and structural styles of fold-and-thrust belts: Geological Society, London, Special Publications, v. 349, no. 1, p. 1-24.

Poblet, J., and McClay, K., 1996, Geometry and kinematics of single-layer detachment folds: American Association of Petroleum Geologists Bulletin, v. 80, no. 7, p. 1085-1109.

Price, R. A., 1981, The Cordilleran forelarid thrust and fold belt in the southern'Canadian Rocky Mountains: in K. R. McClay and R. A. Price, eds., Thrust and Nappe Tectonics, The Geological Society of London, p. 427-448.

Qiu, N. S., 2002, Tectono-thermal evolution of the Qaidam Basin, China: evidence from Ro and apatite fission track data: Petroleum Geoscience, v. 8, no. 3, p. 279-285.

Rawling, G. C., and Goodwin, L. B., 2003, Cataclasis and particulate flow in faulted, poorly lithified sediments: Journal of Structural Geology, v. 25, no. 3, p. 317-331.

-, 2006, Structural record of the mechanical evolution of mixed zones in faulted poorly lithified sediments, Rio Grande rift, New Mexico, USA: Journal of Structural Geology, v. 28, no. 9, p. 1623-1639.

Rawling, G. C., Goodwin, L. B., and Wilson, J. L., 2001, Internal architecture, permeability structure, and hydrologic significance of contrasting fault-zone types: Geology, v. 29, no. 1, p. 43-46.

Rieser, A. B., Liu, Y. J., Genser, J., Neubauer, F., Handler, R., Friedl, G., and Ge, X. H., 2006a, Ar-40/Ar-39 ages of detrital white mica constrain the Cenozoic development of the intracontinental Qaidam Basin, China: Geological Society of America Bulletin, v. 118, no. 11-12, p. 1522-1534.

Rieser, A. B., Liu, Y. J., Genser, J., Neubauer, F., Handler, R., and Ge, X. H., 2006b, Uniform Permian Ar-40/Ar-39 detrital mica ages in the eastern Qaidam Basin (NW China): where is the source?: Terra Nova, v. 18, no. 1, p. 79-87.

Ritts, B. D., Hanson, A. D., Zinniker, D., and Moldowan, J. M., 1999, Lower-middle Jurassic nonmarine source rocks and petroleum systems of the northern Qaidam basin, northwest China: American Association of Petroleum Geologists Bulletin, v. 83, no. 12, p. 1980-2005.

Robertson, E., 1983, Relationship of fault displacement to gouge and breccia thickness: Mining Engineering, v. 35, no. 10, p. 1426-1432.

Roche, V., Homberg, C., and Rocher, M., 2012, Architecture and growth of normal fault zones in multilayer systems: A 3D field analysis in the South-Eastern Basin, France: Journal of Structural Geology, v. 37, no. 0, p. 19-35.

Rojas, L., Muñoz, N., Radic, J., and McClay, K., 1999, The Stratigraphic controls in the transference of displacement from basement thrust to sedimentary cover in the Malargue fold-thrust belt, Neuquén basin, Argentina. The Puesto Rojas Oil fields example: Thrust Tectonics Conference, University of London, p. 119-120.

Rotevatn, A., Torabi, A., Fossen, H., and Braathen, A., 2008, Slipped deformation bands: A new type of cataclastic deformation bands in Western Sinai, Suez rift, Egypt: Journal of Structural Geology, v. 30, no. 11, p. 1317-1331.

Rutter, E. H., 1983, Pressure solution in nature, theory and experiment: Journal of the Geological Society, v. 140, no. 5, p. 725-740.

Schmid, S. M., Pfiffner, O. A., Froitzheim, N., Schönborn, G., and Kissling, E., 1996, Geophysical-geological transect and tectonic evolution of the Swiss-Italian Alps: Tectonics, v. 15, no. 5, p. 1036-1064.

Schmidt, C. J., Chase, R. B., and Erslev, E. A., 1993, Laramide basement deformation in the Rocky Mountain foreland of the western United States, Geological Society of America Special Paper.

Schöpfer, M. P. J., Childs, C., and Walsh, J. J., 2006, Localisation of normal faults in multilayer sequences: Journal of Structural Geology, v. 28, no. 5, p. 816-833.

Schowalter, T. T., 1979, Mechanics of secondary hydrocarbon migration and entrapment: American Association of Petroleum Geologists Bulletin, v. 63, no. 5, p. 723-760.

Scott, T. E., and Nielsen, K. C., 1991, The Effects of Porosity on the Brittle-Ductile Transition in Sandstones: Journal of Geophysical Research, v. 96, no. B1, p. 405-414.

Simpson, G. D. H., 2009, Mechanical modelling of folding versus faulting in brittle–ductile wedges: Journal of Structural Geology, v. 31, no. 4, p. 369-381.

Smith, D. A., 1966, Theoretical considerations of sealing and non-sealing faults: American Association of Petroleum Geologists Bulletin, v. 50, no. 2, p. 363-374.

-, 1980, Sealing and nonsealing faults in Louisiana Gulf Coast salt basin: American Association of Petroleum Geologists Bulletin, v. 64, no. 2, p. 145-172.

Solum, J. G., Davatzes, N. C., and Loaner, D. A., 2010, Fault-related clay authigenesis along the Moab Fault: Implications for calculations of fault rock composition and mechanical and hydrologic fault zone properties: Journal of Structural Geology, v. 32, no. 12, p. 1899-1911.

Solum, J. G., and van der Pluijm, B. A., 2009, Quantification of fabrics in clay gouge from the Carboneras fault, Spain and implications for fault behavior: Tectonophysics, v. 475, no. 3–4, p. 554-562.

Song, T. G., and Wang, X. P., 1993, Structural Styles and Stratigraphic Patterns of Syndepositional Faults in a Contractional Setting - Examples from Quaidam Basin, Northwestern China: American Association of Petroleum Geologists Bulletin, v. 77, no. 1, p. 102-117.

Spiers, C. J., and Schutjens, P. M. T. M., 1990, Densification of crystalline aggregates by fluid-phase diffusional creep, Deformation Processes in Minerals, Ceramics and Rocks, Volume 1, Springer Netherlands, p. 334-353.

Sun, Z., Feng, X., Li, D., Yang, F., Qu, Y., and Wang, H., 1999, Cenozoic Ostracoda and palaeoenvironments of the northeastern Tarim Basin, western China: Palaeogeography, Palaeoclimatology, Palaeoecology, v. 148, no. 1–3, p. 37-50.

Sun, Z. M., Yang, Z. Y., Pei, J. L., Ge, X. H., Wang, X. S., Yang, T. S., Li, W. M., and Yuan, S. H., 2005, Magnetostratigraphy of Paleogene sediments from northern Qaidam Basin, China: Implications for tectonic uplift and block rotation in northern Tibetan plateau: Earth and Planetary Science Letters, v. 237, no. 3-4, p. 635-646.

Suppe, J., 1983, Geometry and Kinematics of Fault-Bend Folding: American Journal of Science, v. 283, no. 7, p. 684-721.

Suppe, J., and Medwedeff, D. A., 1990, Geometry and Kinematics of Fault-Propagation Folding: Eclogae Geologicae Helvetiae, v. 83, no. 3, p. 409-454.

Tada, R., and Siever, R., 1989, Pressure Solution during Diagenesis: Annual Review of Earth and Planetary Sciences, v. 17, p. 89-118.

Tapponnier, P., Meyer, B., Avouac, J. P., Peltzer, G., Gaudemer, Y., Guo, S. M., Xiang, H. F., Yin, K. L., Chen, Z. T., Cai, S. H., and Dai, H. G., 1990, Active Thrusting and Folding in the Qilian-Shan, and Decoupling between Upper Crust and Mantle in Northeastern Tibet: Earth and Planetary Science Letters, v. 97, no. 3-4, p. 382-403.

Tavani, S., Storti, F., and Salvini, F., 2005, Rounding hinges to fault-bend folding: geometric and kinematic implications: Journal of Structural Geology, v. 27, no. 1, p. 3-22.

Tueckmantel, C., Fisher, Q. J., Knipe, R. J., Lickorish, H., and Khalil, S. M., 2010, Fault seal prediction of seismic-scale normal faults in porous sandstone: A case study from the eastern Gulf of Suez rift, Egypt: Marine and Petroleum Geology, v. 27, no. 2, p. 334-350.

Tyler, N., and Finley, R. J., 1991, Architectural controls on the recovery of hydrocarbons from sandstone reservoirs: in A. D. Miall and C. N. Tylers, eds., The Three Dimensional Facies Architecture of Heterogeneous Clastic Sediments and its Implications for Hydrocarbon Discovery and Recovery. Concepts Sedimentol. Palontol., v. 3, p. 44-54.

Walderhaug, O., 1996, Kinetic modeling of quartz cementation and porosity loss in deeply buried sandstone reservoirs: American Association of Petroleum Geologists Bulletin, v. 80, no. 5, p. 731-745.

Walsh, J. J., Bailey, W. R., Childs, C., Nicol, A., and Bonson, C. G., 2003, Formation of segmented normal faults: a 3-D perspective: Journal of Structural Geology, v. 25, no. 8, p. 1251-1262.

Walsh, J. J., Watterson, J., Bailey, W. R., and Childs, C., 1999, Fault relays, bends and branch-lines: Journal of Structural Geology, v. 21, no. 8–9, p. 1019-1026.

Walsh, J. J., Watterson, J., Heath, A. E., and Childs, C., 1998, Representation and scaling of faults in fluid flow models: Petroleum Geoscience, v. 4, no. 3, p. 241-251.

Wang, B. Q., Wang, Q. H., Chen, H. L., and Xiao, A. C., 2006a, Three-D mensional structure modeling and structural analysis of the lenghu area on the northern margin of Qaidam basin: Geotectonica et Metallogenia, v. 30, no. 4, p. 430-434.

Wang, E., Xu, F. Y., Zhou, J. X., Wan, J. L., and Burchfiel, B. C., 2006b, Eastward migration of the Qaidam basin and its implications for Cenozoic evolution of the Altyn Tagh fault and associated river systems: Geological Society of America Bulletin, v. 118, no. 3-4, p. 349-365.

Wang, E. C., and Burchfiel, B. C., 2004, Late cenozoic right-lateral movement along the Wenquan fault and associated deformation: Implications for the kinematic history of the Qaidam Basin Northeastern Tibetan Plateau: International Geology Review, v. 46, no. 10, p. 861-879.

Wang, M., 2001, Three Mesozoic–Cenozoic hydrocarbon-bearing systems and the exploration strategies of them: Journal of Xi’an Petroleum Institute (Natural Science Edition), v. 16, p. 8-12 (in Chinese, with English Abstract).

Wang, X. M., Qiu, Z. D., Li, Q., Wang, B. Y., Qiu, Z. X., Downs, W. R., Xie, G. P., Xie, J. Y., Deng, T., Takeuchi, G. T., Tseng, Z. J., Chang, M. M.,

Liu, J., Wang, Y., Biasatti, D., Sun, Z. C., Fang, X. M., and Meng, Q. Q., 2007, Vertebrate paleontology, biostratigraphy, geochronology, and paleoenvironment of Qaidam Basin in northern Tibetan Plateau: Palaeogeography, Palaeoclimatology, Palaeoecology, v. 254, no. 3-4, p. 363-385.

Watts, N. L., 1987, Theoretical aspects of cap-rock and fault seals for single- and two-phase hydrocarbon columns: Marine and Petroleum Geology, v. 4, no. 4, p. 274-307.

Welch, M. J., Knipe, R. J., Souque, C., and Davies, R. K., 2009, A Quadshear kinematic model for folding and clay smear development in fault zones: Tectonophysics, v. 471, no. 3–4, p. 186-202.

Willingshofer, E., and Sokoutis, D., 2009, Decoupling along plate boundaries: Key variable controlling the mode of deformation and the geometry of collisional mountain belts: Geology, v. 37, no. 1, p. 39-42.

Withjack, M. O., and Peterson, E. T., 1993, Prediction of normal-fault geometries--a sensitivity analysis: American Association of Petroleum Geologists Bulletin, v. 77, no. 11, p. 1860-1873.

Woodward, N. B., 1992, Deformation styles and geometric evolution of some Idaho-Wyoming thrust belt structures: in S. Mitra and G. W. Fisher, eds., Structural Geology of Fold and Thrust Belts, Johns Hopkins University Press, Baltimore, p. 191-206.

Woodward, N. B., and Rutherford Jr, E., 1989, Structural lithic units in external orogenic zones: Tectonophysics, v. 158, no. 1-4, p. 247-267.

Xia, W. C., Zhang, N., Yuan, X. P., Fan, L. S., and Zhang, B. S., 2001, Cenozoic Qaidam basin, China: A stronger tectonic inversed,

extensional rifted basin: American Association of Petroleum Geologists Bulletin, v. 85, no. 4, p. 715-736.

Yang, F., Ma, Z., Xu, T., and Ye, S., 1992, A Tertiary paleomagnetic stratigraphic profile in Qaidam Basin: Acta Petrologica Sinica, v. 13, p. 97-101.

Yang, F., Sun, Z., Cao, C., Ma, Z., and Zhang, Y., 1997, Quaternary fossil ostracod zones and magnetostratigraphic profile in the Qaidam basin: Acta Micropalaeotologica Sinica, v. 14, p. 378-390.

Yang, Y. T., Ritts, B., Zou, C. N., Xu, T. G., Zhang, B. M., and Xi, P., 2003, Upper triassic-middle jurassic stratigraphy and sedimentology in the NE Qaidam Basin, NW China: Petroleum geological significance of new outcrop and subsurface data: Journal of Petroleum Geology, v. 26, no. 4, p. 429-449.

Yielding, G., 2002, Shale Gouge Ratio — calibration by geohistory, *in* Andreas, G. K., and Robert, H., eds., Norwegian Petroleum Society Special Publications, Volume 11, p. 1-15.

Yielding, G., Freeman, B., and Needham, D. T., 1997, Quantitative fault seal prediction: American Association of Petroleum Geologists Bulletin, v. 81, no. 6, p. 897-917.

Yin, A., Dang, Y., Zhang, M., McRivette, M. W., Burgess, W. P., and Chen, X., 2007, Cenozoic tectonic evolution of Qaidam basin and its surrounding regions (part 2): Wedge tectonics in southern Qaidam basin and the Eastern Kunlun Range: Geological Society of America Special Papers, v. 433, p. 369-390.

Yin, A., Dang, Y. Q., Wang, L. C., Jiang, W. M., Zhou, S. P., Chen, X. H., Gehrels, G. E., and McRivette, M. W., 2008a, Cenozoic tectonic

evolution of Qaidam basin and its surrounding regions (Part 1): The southern Qilian Shan-Nan Shan thrust belt and northern Qaidam basin: Geological Society of America Bulletin, v. 120, no. 7-8, p. 813-846.

Yin, A., Dang, Y. Q., Zhang, M., Chen, X. H., and McRivette, M. W., 2008b, Cenozoic tectonic evolution of the Qaidam basin and its surrounding regions (Part 3): Structural geology, sedimentation, and regional tectonic reconstruction: Geological Society of America Bulletin, v. 120, no. 7-8, p. 847-876.

Yin, A., Rumelhart, P. E., Butler, R., Cowgill, E., Harrison, T. M., Foster, D. A., Ingersoll, R. V., Zhang, Q., Zhou, X. Q., Wang, X. F., Hanson, A., and Raza, A., 2002, Tectonic history of the Altyn Tagh fault system in northern Tibet inferred from Cenozoic sedimentation: Geological Society of America Bulletin, v. 114, no. 10, p. 1257-1295.

Yue, Y. J., Ritts, B. D., Graham, S. A., Wooden, J. L., Gehrels, G. E., and Zhang, Z. C., 2004, Slowing extrusion tectonics: lowered estimate of post-Early Miocene slip rate for the Altyn Tagh fault: Earth and Planetary Science Letters, v. 217, no. 1-2, p. 111-122.

Zehnder, A. T., and Allmendinger, R. W., 2000, Velocity field for the trishear model: Journal of Structural Geology, v. 22, no. 8, p. 1009-1014.

Zhou, J. X., Xu, F. Y., Wang, T. C., Cao, A. F., and Yin, C. M., 2006, Cenozoic deformation history of the Qaidam Basin, NW China: Results from cross-section restoration and implications for Qinghai-Tibet Plateau tectonics: Earth and Planetary Science Letters, v. 243, no. 1-2, p. 195-210.

Zhu, L. D., Wang, C. S., Zheng, H. B., Xiang, F., Yi, H. S., and Liu, D. Z., 2006, Tectonic and sedimentary evolution of basins in the northeast of Qinghai-Tibet Plateau and their implication for the northward growth of the plateau: Palaeogeography, Palaeoclimatology, Palaeoecology, v. 241, no. 1, p. 49-60.

Zhu, W. L., and Wong, T. F., 1997, The transition from brittle faulting to cataclastic flow: Permeability evolution: Journal of Geophysical Research, v. 102, no. B2, p. 3027-3041.

Zijlstra, E. B., Reemst, P. H. M., and Fisher, Q. J., 2007, Incorporation of fault properties into production simulation models of Permian reservoirs from the southern North Sea: Geological Society, London, Special Publications, v. 292, p. 295-308.